ISBN 978-82-326-0854-6 (printed version)
ISBN 978-82-326-0855-3 (electronic version)
ISSN 1503-8181

NTNU – Trondheim
Norwegian University of
Science and Technology

Vegard Longva

Doctoral Thesis

Doctoral theses at NTNU, 2015:99

NTNU
Norwegian University of
Science and Technology
Faculty of Engineering
Science and Technology
Department of Marine Technology

NTNU

Doctoral theses at NTNU, 2015:99

Vegard Longva

Formulation and Application of Finite Element Techniques for Slender Marine Structures Subjected to Contact Interactions

NTNU – Trondheim
Norwegian University of
Science and Technology

Vegard Longva

Formulation and Application of Finite Element Techniques for Slender Marine Structures Subjected to Contact Interactions

Thesis for the degree of Philosophiae Doctor

Trondheim, May 2015

Norwegian University of Science and Technology
Faculty of Engineering Science and Technology
Department of Marine Technology

NTNU – Trondheim
Norwegian University of
Science and Technology

NTNU
Norwegian University of Science and Technology

Thesis for the degree of Philosophiae Doctor

Faculty of Engineering Science and Technology
Department of Marine Technology

ISBN 978-82-326-0854-6 (printed version)
ISBN 978-82-326-0855-3 (electronic version)
ISSN 1503-8181

Doctoral theses at NTNU, 2015:99

MILJØMERKET
241 TRYKKSAK 731

Printed by Skipnes Kommunikasjon as

Abstract

The main purpose of this work is to formulate and apply new computational strategies for two contact-governed problems where existing finite element software suffer from poor efficiency and lack of robustness. The first problem is concerned with trawl board pull-over interaction of subsea pipelines while the second deals with reeling analysis of history-dependent flexible pipes.

Previous numerical models for trawl-pipe interaction based on simplified geometry modeling has struggled with contact-related convergence problems. A contact element with a continuous description of the trawl board contact geometry and the pipe geometry was therefore developed. The assumption of a rigid contact geometry for the trawl board and the use of line-line and line-point contact kinematics resulted in good numerical efficiency properties. The ability to predict the pull-over responses depends heavily on the modeling of the trawl board hydrodynamic loads. A fairly advanced six degree of freedom load model with precomputed hydrodynamic coefficients was therefore established.

An extensive simulation work was carried out to validate the trawl-pipe computational strategy and to identify sensitive model parameters. Regarding the former, the proposed numerical model was demonstrated to predict pull-over load impulses within a 10% margin of model test measurements and was thus concluded to be capable of describing the relevant effects of the pull-over. The sensitivity study revealed that the interaction behavior was greatly influenced by the board-pipe friction coefficient, the tension level in the wire between board and trawl net, the towing line drag properties and the direction of over-trawling. Due to the sensitivity of the input parameters, it was concluded that a proper validation against experimental tests is necessary for future work of similar kind. Further studies should aim to quantify the degree of non-conservatism present for non-perpendicular crossings and attempt to improve current design load recommendations by including more model parameters.

Reeling operations with history-dependent material behavior and extensive contact interactions along the material transport route are often not feasible to simulate with conventional finite element software. This relates to contact-related convergence problems and the need for long meshes with small and equal-sized elements giving poor numerical efficiency. These issues were successfully solved by developing a Lagrangian-Eulerian beam formulation that enabled for a virtually fixed mesh in space. The proposed formulation was subjected to various benchmark tests where it was demonstrated to provide similar accuracy as the conventional Lagrangian method.

In recent years, subsea contractors have experienced torsional failures in spoolbase-vessel load-out operations of flexible pipes. An idealized finite element model was therefore established to gain insight into such operations and to identify the mechanisms responsible for the generated torque. Torsional failures were identified for three different mechanisms and strategies to avoid them were proposed. A comparison study against a physical load-out operation should be conducted in future work to quantify the ability to predict the torque and to reveal possible model deficiencies.

Acknowledgements

This 4-year PhD project started in July 2010 and was completed for submission in February 2015, including 3 months of additional teaching assistant work and 4 months of external project work. During this rather long study, several people must be acknowledged for contributing with knowledge, motivation and support.

I would like to express my gratitude to my supervisor, Prof. Svein Sævik, for his excellent guidance during the last years. Our collaboration started in the fall semester of 2009 during a MSc project work, which was continued in the spring semester of 2010 when he supervised my master thesis work. His enthusiasm and encouragement in this period made me realize that the PhD study was the obvious choice for me. In the present work, Prof. Svein Sævik has served as an excellent supervisor with his extensive experience in software development and within nonlinear finite element methods. The main direction of this work was defined by a few novel ideas proposed by him, which upon completion has provided new knowledge that he sincerely must be acknowledged for. Throughout this project he has always been available for discussion and shown great patience in the counseling work, regardless of other employment duties and high work pressure. His impressive feedback efficiency has saved a lot of time for me, especially regarding manuscript proofreading and the work concerned with implementation into MARINTEK's computer programs. Several challenges have been encountered during the last years, where Prof. Svein Sævik has been the main source for motivation, giving me sufficient belief so that I could accomplish the work.

Dr. Philippe Mainçon has throughout this project contributed with fruitful discussions, motivation and guidance. Reflections and findings from his research on torsional failure in flexible pipe load-out operations were in fact the main motivation for developing the Lagrangian-Eulerian formulation. Dr. Erik Levold, Dr. Håvar Ilstad and Dr. Per Teigen, affiliated at Statoil, are acknowledged for arranging financial support for the trawl-pipeline work, where they also contributed with trawl board hydrodynamic mass data and gave admission to valuable model test results. The excellent service of Ann-Johanne Bjørgen at the Marine Technology Library is much appreciated. Ivar Nygaard is acknowledged for providing information about the setup and the execution of the trawl-pipeline interaction model tests at MARINTEK. Likewise, John Willy Valdemarsen at The Institute of Marine Research contributed with valuable information and video recordings of full-scale pipe over-trawling tests. Tore Jacobsen is acknowledged for giving information about the practical aspects of flexible pipe load-out operations. Dr. Harald Ormberg is recognized for his feedback on the trawl board hydrodynamic load model. Support provided by Lidvard Auflem, Joakim Taby and Dr. Janne Kristin Økland Gjøsteen regarding use and implementation of the SIMLA software is also appreciated.

Without being specific, I would like to express my gratitude to my colleagues at the Department of Marine Technology. Several friendships and new connections have been established during the last years, both in my personal and my professional life.

My family must be thanked for their support and encouragement for pursuing and completing this PhD.

List of publications

The following original research papers are included as part of this thesis:

I) V. Longva and S. Sævik. A penalty-based contact element for pipe and 3D rigid body interaction. *Engineering Structures*, Vol. 56, pp. 1580 – 1592, 2013.

II) V. Longva, S. Sævik, E. Levold and H. Ilstad. Dynamic simulation of subsea pipeline and trawl board pull-over interaction. *Marine Structures*, Vol. 34, pp. 156 – 184, 2013.

III) V. Longva and S. Sævik. A Lagrangian-Eulerian formulation for reeling analysis of history-dependent multilayered beams. *Computers & Structures*, Vol. 146, pp. 44 – 58, 2015.

IV) V. Longva and S. Sævik. On prediction of torque in flexible pipe reeling operations using a Lagrangian-Eulerian FE framework. *Submitted for journal publication*, 2015.

In the above papers, the candidate was responsible for developing the numerical models, the computer implementation, the simulation work, interpretation of the results and the manuscript writing. Prof. Svein Sævik contributed with counseling, novel ideas, manuscript proofreading and the preliminary work required for the computer implementation in Papers I) and II). Dr. Erik Levold and Dr. Håvar Ilstad contributed with laboratory test results and trawl board hydrodynamic mass data.

The PhD project resulted also in the following papers which are not regarded as part of the thesis:

i) V. Longva, S. Sævik, E. Levold and H. Ilstad. Dynamic simulation of free-spanning pipeline trawl board pull-over. *Proceedings of the ASME 2011 30th International Conference on Ocean, Offshore and Arctic Engineering*, Rotterdam, The Netherlands, June 19 – 24, 2011, Vol. 4, pp. 561 – 568.

ii) V. Longva and S. Sævik. A penalty-based body-pipeline contact element for simulation of pull-over events. *Proceedings of the ASME 2012 31st International Conference on Ocean, Offshore and Arctic Engineering*, Rio de Janeiro, Brazil, July 1 – 6, 2012, Vol. 3, pp. 241 – 250.

iii) X. Wu, V. Longva, S. Sævik and T. Moan. Simulation of hooking event in fish trawling operation. *Proceedings of the ASME 2013 32nd International Conference on Ocean, Offshore and Arctic Engineering*, Nantes, France, June 9 – 14, 2013, Vol. 4A, 13 pages.

iv) X. Wu, V. Longva, S. Sævik and T. Moan. A simplified approach to estimate the probability of otter board hooking at pipelines. *Submitted for journal publication*, 2015.

In Papers i) and ii), the author contributions were similar to Papers I) and II). For Papers iii) and iv), the candidate contributed with guidance on the simulation work, the trawl-pipe contact model, the trawl board hydrodynamic load model and manuscript proofreading.

Notation and conventions

- Vectors, tensors and matrices are written with bold letters and bold symbols, e.g. $\mathbf{a}$, $\mathbf{A}$, $\boldsymbol{\omega}$ and $\boldsymbol{\Omega}$. Second order tensors and matrices are always in upper case.

- All tensors are represented in a three-dimensional vector space with orthonormal basis vectors.

- The term vector is used both for first order tensors and for matrices with dimension N×1.

- The transpose of a vector, tensor or matrix is denoted by superscript $\top$.

- The Einstein summation convention applies for repeated indices when vectors, tensors and coordinate transformation matrices are written in indicial form. The index range is implicitly assumed to loop over 1, 2 and 3, e.g.,

  $$A_{ij}a_i = A_{1j}a_1 + A_{2j}a_2 + A_{3j}a_3$$

- A first order tensor (vector) in a given coordinate representation is expressed in terms of the coordinate basis vectors $\mathbf{e}_i$ as follows

  $$\mathbf{a} = a_i\mathbf{e}_i$$

  Alternatively, the matrix form is used,

  $$\mathbf{b} = \begin{bmatrix} b_1 & b_2 & b_3 \end{bmatrix}^\top$$

  where the coordinate representation for b_i is regarded arbitrary if not explicitly stated or apparent from the context.

- The vector product is denoted by a cross and reads as follows for two vectors $\mathbf{a}$ and $\mathbf{b}$,

  $$\mathbf{a} \times \mathbf{b} = \epsilon_{ijk}a_ib_j\mathbf{e}_k \qquad \epsilon_{ijk} = \begin{cases} 0 \\ 1 \\ -1 \end{cases} \text{if } \{i,j,k\} \text{ is } \begin{cases} \text{an acyclic sequence} \\ \text{a cyclic sequence} \\ \text{an anticyclic sequence} \end{cases}$$

- The scalar product of two vectors $\mathbf{a}$ and $\mathbf{b}$ is denoted by a dot,

  $$\mathbf{a} \cdot \mathbf{b} = a_ib_i$$

- The tensor product of two vectors $\mathbf{a}$ and $\mathbf{b}$ is denoted by $\mathbf{a} \otimes \mathbf{b}$. Under the action of the tensor product, the vector $\mathbf{c}$ is mapped into a new vector according to,

  $$(\mathbf{a} \otimes \mathbf{b}) \cdot \mathbf{c} = (\mathbf{b} \cdot \mathbf{c})\,\mathbf{a} \qquad \mathbf{c} \cdot (\mathbf{a} \otimes \mathbf{b}) = (\mathbf{a} \cdot \mathbf{c})\,\mathbf{b}$$

- For a given coordinate representation, the second order tensor $\mathbf{A}$ is expressed as a linear combination of the nine tensor products of the coordinate basis vectors $\mathbf{e}_i$ as follows,

  $$\mathbf{A} = A_{ij}\mathbf{e}_i \otimes \mathbf{e}_j$$

  The second order tensor $\mathbf{B}$ is expressed on matrix form as follows,

  $$\mathbf{B} = \begin{bmatrix} B_{11} & B_{12} & B_{13} \\ B_{21} & B_{22} & B_{23} \\ B_{31} & B_{32} & B_{33} \end{bmatrix}$$

  where the coordinate representation for B_{ij} is regarded arbitrary if not explicitly stated or apparent from the context.

- Matrices are distinguished from tensors by context and appearance. Multiplications involving tensor quantities are separated by the dot symbol while matrix quantities are not, e.g.,

  $$\underbrace{\mathbf{a} \cdot \mathbf{B} \cdot \mathbf{a}}_{\text{tensor}} = \underbrace{\mathbf{a}^{\top}\mathbf{B}\mathbf{a}}_{\text{matrix}} = \underbrace{a_i B_{ij} a_j}_{\text{indicial}}$$

- The partial derivative of a quantity f is denoted by a comma in subscript followed by the variable involved in the differentiation,

  $$\frac{\partial f}{\partial x} = f_{,x}$$

- The Euclidean norm of the vector $\mathbf{c}$ is defined as,

  $$||\mathbf{c}|| = \sqrt{c_1^2 + ... + c_n^2} \qquad \mathbf{c} = \begin{bmatrix} c_1 & ... & c_n \end{bmatrix}^{\top}$$

Contents

Chapter 1

Introduction

1.1 Background and motivation

Slender marine structures such as rigid steel pipes, steel risers, flexible pipes, umbilical cables, power cables and mooring lines involve several nonlinearities which are prone to become computationally expensive. From a hydrodynamic viewpoint, slender structures give an insignificant disturbance on the fluid motion and the loading can therefore be predicted by Morison's equation with negligible computational costs. Contrarily, the nonlinearities associated with the structural response result in significantly larger computational expenses. These nonlinearities arise due to history-dependent material responses, three-dimensional motions with large rotations and displacements, external contact interactions and internal cross-sectional contact constraints.

The differential equation that governs the structural response may be solved by numerical techniques such as the finite element (FE) method, finite difference methods or finite volume methods. The FE method has since its first scientific appearance [1, 2] almost six decades ago become the preferred numerical method for structural problems. This relates to features such as the ability to handle complex geometries, flexibility regarding the spatial discretization, the strong mathematical foundation, the treatment of normal derivative boundary conditions and the inherent interpolation of the field variables between the solution points. In this work, the FE method was therefore taken as a prerequisite in order to assure a broad applicability of the scientific contributions and to allow for implementation into state of the art computer programs.

The overall objective of the present work is to develop and apply new computational strategies for two contact-governed problems where commercial computer codes suffer from lack of efficiency and poor robustness. The first problem deals with trawl gear and subsea pipeline interaction as well as the gear hydrodynamic load description, while the second focuses on reeling analysis of history-dependent beams. The thesis is therefore divided into two parts regarding physical problems, however, both parts are concerned with slender marine structures where the contact interactions represents a major challenge.

1.1.1 Trawl gear and pipeline interaction

The coexistence of bottom trawling fisheries and offshore oil exploitation has lead to accidents with severe consequences for both parties. In 1997, the small fishing vessel Westhaven capsized with four casualties in the North Sea during an attempt to release a hooked trawl board from a pipeline [3]. Between 1998 and 2004, there were nine fishing gear interactions that caused damage to subsea production equipment and pipelines on the Norwegian shelf, in which at least one resulted in a major gas leakage [4]. Paradoxically, many of these incidents occurred within the platform safety zones, where the structures are not designed to withstand trawl loads, see Ref. [5]. In the United Kingdom, nearly five hundred claims were raised to the Fishermen's Compensation Fund between 2000 and 2013 in relation to fishing vessel and equipment damages caused by petroleum activities [6]. Considering that interactions without damage remain unreported, the over-trawling frequency is substantial and might lead to trawl-governed designs for pipelines which are routed within fishing grounds. An accurate description of the interference loads is therefore required in order to ensure sufficient structural integrity and to minimize the life cycle costs.

The three standard trawl types for bottom trawling are illustrated in Fig. 1.1. The concepts differ with regard to how the trawl net is kept open during harvesting. For the otter trawl types, the net opening is provided by hydrodynamic forces acting on the trawl boards, whereas beam trawling rely on a transverse steel beam mounted across the net entrance. In the Norwegian sector of the North Sea, the relative use of beam trawls in bottom trawling was less than 1% in the period between 2000 and 2004 [8]. According to DNV GL [7], clump weights typically have masses in the range 2 000 kg to 9 000 kg, while heavy trawl boards can have steel masses up to 6 000 kg with hydrodynamic masses of at least the same magnitude. Combined with a trawling velocity of 2 – 3 m/s, the interference

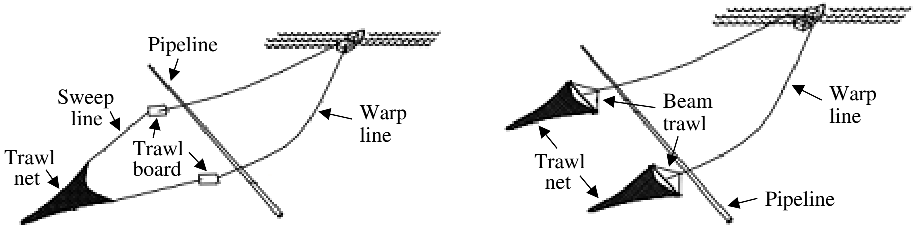

(a) Single otter trawl

(b) Twin beam trawl

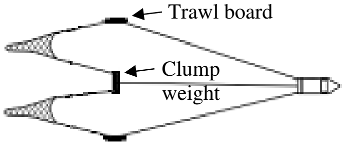

(c) Twin otter trawl with clump weight

Figure 1.1: Bottom trawl gear [7]

loading may therefore lead to a severe utilization of the pipeline capacity.

Nowadays, design of subsea pipelines subjected to trawl loads is in practice based on the DNV-RP-F111 code [7]. This code divides the interaction into three parts according to load characteristics and analysis method. The first part, referred to as the initial impact phase, considers the energy absorbed from the impact load and the local cross-section damage. The subsequent part, which is called the pull-over phase, deals with the global pipe response due to the loads that build up when the gear is forced around and released from the pipe. The third part is the rarely occurring hooking event in which the gear is assumed to get stuck between the seabed and the pipe. Nine incidents with loss of trawl gear, arguably due to pipeline hooking, were reported to the Norwegian Directorate of Fisheries between 2011 and 2013.

With regard to current design practices, the pull-over loading is expected to have the largest potential for improvements. The DNV-RP-F111 code provides fairly general pull-over loads based on simple formulas that have been calibrated against model tests. In view of this, the pipeline designers claim that the recommended pull-over loading is too conservative [9], which also has been demonstrated by FE simulations of pipelines subjected to clump weight interaction [10, 11]. However, the model tests represent a limited number of realizations and the trawl gear has changed in size and geometry since the tests were conducted in 1990. Hence, at present there is no consensus in the subsea industry with regard to the degree of conservatism incorporated in current design practices.

Use of numerical simulations for the trawl-pipe interaction problem represents an attractive alternative since it avoids many of the drawbacks encountered in model testing. Model tests suffer in general from large consumption of time with correspondingly high expenses. Truncated trawl gear wire configurations are unavoidable in laboratory tests and the small models may introduce bias due to scale affects. Furthermore, model tests have low input parameter flexibility and poor ability to effectively reduce the statistical uncertainty. However, to enable use of computer simulations, challenges have to be solved for the trawl gear hydrodynamic load description and the handling of the contact interactions.

The interference loads depend strongly on the modeling of the hydrodynamic loads and the trawl gear interaction behavior. For trawl boards, the interference is particularly challenging due to the non-trivial hydrodynamics and the three-dimensional motions involved. Therefore, the numerical model should preferably be based on an integrated framework of computational fluid dynamics and the structural FE method. In a preliminary work for enabling simulation of trawl board and pipeline interaction in 2009 by Teigen at al. [12], such a framework was concluded to be unfeasible in a foreseeable future due to the extreme computational resources needed. Thus, one is basically left with a six degree of freedom (DOF) rigid body model with precomputed hydrodynamic coefficients for the trawl gear. Such a model was used in work by Reite [13] who developed a trawl board control system for midwater trawling. As opposed to his work, the dependency of the trawl board hydrodynamic mass on the distance and the orientation relative to the seabed must be described, as well as the Coriolis-centripetal loads that arise from the large angular velocities which are present during the interaction. Furthermore, appropriate models must be established for the steady-state fluid loads and the pressure-induced rotational damping loads.

To capture the initial impact response, the pipe and possibly also the trawl gear must be modeled as a flexible continuum with a detailed description of the contact surfaces. Contrarily, for the pull-over and the hooking responses, beam elements suffice to capture the pipe response and a rigid body model can be used for the trawl gear due to its high rigidity compared to the pipe flexural stiffness. Such models have previously been used in trawl board pull-over simulations, however, convergence issues related to loss of contact were reported [14, 15]. The convergence problems occurred because the board contact surface was approximated by cylindrical roller geometries giving disjoint surface regions at the roller connection points. Thus, to avoid similar problems, the contacting surfaces must be given a continuous description. Considering that small time steps are required and that the interaction may last for more than ten seconds, the selected contact surface representation should preferably allow for an efficient contact formulation.

1.1.2 Reeling operations

Slender marine structures undergo processes which involve material transport along a predefined route both during manufacturing and installation. Typical examples are the wounding process used for the cross-section components in flexible pipes and cables, offshore laying operations for steel pipelines, reeling of small-diameter steel pipes at spoolbases as well as offshore installation and spoolbase-vessel load-out operations for flexible pipes and cables, see Fig. 1.2.

Numerical reeling simulations are useful for purposes such as identification of unforeseen events prior to operations, post-analysis of failed operations, estimation of fatigue damage during offshore installation and to provide initial configurations for on-bottom buckling analysis of steel pipes. Use of Lagrangian beam models is considered to be

Figure 1.2: Spoolbase-vessel load-out operation for an umbilical cable [16]

the state of the art simulation method for pipe-laying operations. In work by Økland et al. [17] on pipe-laying, this method was combined with a re-use of element strategy such that the modeled pipe length could be kept constant. Reeling operations of history-dependent flexible pipes and umbilical cables, such as the one illustrated in Fig. 1.2, are far more challenging to simulate with Lagrangian beam formulations. This relates to the extensive contact interactions present along the reeling path and the need for small and equal-sized beam elements. Additionally, internal cross-sectional contact constraints and potential numerical ill-conditioning due to the stick-slip behavior of the cross-section layers represent a complicating factor.

Convergence problems related to the contact interactions are the main challenge in reeling analyses. Therefore, analysts are often forced to apply cumbersome and time-consuming strategies for the problem at hand. For instance, the ABAQUS software was used in simulations of a simple reeling operation in work by Daly and Bell [18], where a multistep procedure involving a large number of load and boundary conditions with reactivation of contact surfaces was required in order to achieve convergence. A similar reeling operation was studied by Jukes et al. [19] who reported that a full reeling analysis was particularly complex to undertake due to convergence issues. Alternatively, at the cost of losing some accuracy, the contact interactions may be completely avoided in certain problems by subjecting the pipe to imposed rotations that simulate the curvature history experienced along the reeling route [20]. Also, the convergence difficulties may be mitigated by using a dynamic analysis method instead of a static analysis method [21]. In summary, the current simulation practices are time-consuming and suffer from lack of generality, even for relatively simple reeling processes.

A secondary challenge in reeling simulations is the poor numerical efficiency present for models with a large number of DOFs. The mesh must often be several times longer than the region of interest to avoid end-effects and to allow the steady-state configuration to be attained. The moving mesh requires use of equal-sized elements whose size must be sufficiently small to capture the response in the large-deformation regions. Furthermore, the frequent changes in contact topology results in time-consuming contact searches and the changing contact conditions might govern the time step size.

In this work, the challenges present in terms of convergence and efficiency are addressed by utilizing a Lagrangian-Eulerian description of motion. The basic idea here is to separate the mesh and the material motions in such a way that the mesh becomes virtually fixed in space. The treatment of the history-dependent material response represents the main challenge for this strategy. There exist so far no examples in the literature where the Lagrangian-Eulerian viewpoint has been utilized in history-dependent beam problems, however, the same challenges as present for arbitrary Lagrangian-Eulerian methods formulated for solid mechanic problems must be dealt with. As stated by Donea et al. [22], the standard Galerkin-based FE method suffer from lack of stability in convection-dominated situations. This is the case with a virtually fixed mesh and thus some kind of stabilization technique must be established. The Lagrangian-Eulerian analysis strategy must further be capable of providing the same accuracy as the conventional Lagrangian formulation. Regarding generality, the development must be formulated to comply with standard beam formulations and the framework of computational elasto-plasticity.

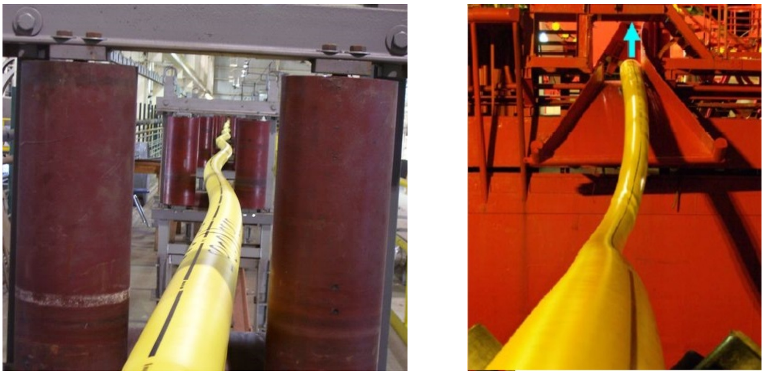

(a) Undesirable deformations of 4.5” umbilical cable during reeling after fabrication

(b) Indication of loop formation at free span between vessel and quay in a flexible pipe load-out operation

Figure 1.3: Incidents with severe torsion

In recent years, extreme torque responses leading to torsional failure in flexible pipe and umbilical cable reeling operations have occurred during installation offshore, in spooling after fabrication and during load-out from onshore spoolbases, see Fig. 1.3. Such failures result in high expenses for the involved parties since the operations must be aborted and new products must be manufactured. Presently, the available design codes [23–25] do not provide any guidance on how to avoid the experienced torsional failure incidents. This is simply because the mechanisms responsible for the failures have not yet been identified, which again relate to the lack of a robust and efficient simulation tool for identification of critical situations during the operation. However, significant torques are known to develop in beams subjected to high curvature if the bending moment vector and the normal vector of the curvature plane are non-aligned. For flexible pipes and umbilical cables, such non-alignments may be introduced due to the hysteretic bending response [26]. Thus, to allow for prediction of the torque in reeling operations the history-dependent bending response, the constitutive coupling introduced by the interlayer contact pressures and the bending-torsional geometric coupling effect must be accounted for.

1.2 Objectives and scope of the work

In the first part of this work, the overall objective is to develop a computational strategy for trawl gear and pipeline interaction able to predict pull-over loads with similar accuracy as model tests. The initial impact response and the hooking event are not considered, however, the proposed simulation tool is expected to handle hooking events. The computational strategy is to be validated against experimental tests for trawl board interaction only. Nevertheless, provided that agreement is demonstrated, the strategy should be applicable for clump weights and beam trawls which have a far simpler hydrodynamic load description. The present work also aims to identify sensitive model parameters, in particular parameters which are difficult to examine in experimental tests. Thus, for Papers I and II which address the trawl-pipe interaction problem, the main objectives can be stated as follows,

- Develop a robust and efficient contact model capable of describing the pull-over interaction behavior in trawl gear and subsea pipeline interferences. [Paper I]
- Propose and calibrate a six DOF trawl board load model with precomputed hydrodynamic coefficients able to capture the relevant effects of the pull-over interaction phase. [Paper II]
- Validate the trawl-pipe computational strategy against existing model tests of trawl board and pipeline pull-over interaction [27]. [Paper II]
- Identify sensitive model parameters and quantify their influence on the pull-over process. [Paper II]

The overall objective in the second part of the work is to develop a Lagrangian-Eulerian formulation for reeling analysis of history-dependent beams. Based on the torsional failures recently experienced by subsea contractors, the application part of the work focuses solely on spoolbase-vessel load-out operations of flexible pipes. The formulation is therefore expressed in terms of a standard flexible pipe constitutive model. The development is expected to be applicable also for umbilical cables since they have a similar constitutive description. Offshore installation operations and $J2$-plasticity models for rigid steel pipes will not be considered. The aim of the numerical studies is to provide recommendations on how to avoid torsional failures in flexible pipe load-out operations. Hence, the main objectives for Papers III and IV which are concerned with reeling operations are as follows,

- Develop a Lagrangian-Eulerian formulation for reeling analysis of flexible pipes with a virtually fixed mesh in space. The formulation must be capable of providing the same accuracy as the conventional Lagrangian method. [Paper III]
- Enable for prediction of the torque generated in flexible pipe reeling operations. Thus, the hysteretic bending response, the bending-axial-torsional constitutive coupling introduced via the interlayer contact pressures and the bending-torsional geometric coupling effect must be properly described. [Paper III]
- Propose a framework for efficient simulation of reeling operations based on the developed Lagrangian-Eulerian formulation. [Paper IV]
- Identify driving mechanisms and propose mitigation strategies for the extreme torque responses experienced in spoolbase-vessel load-out operations of flexible pipes. [Paper IV]

1.3 Thesis organization

The thesis is composed of a main section and an appended collection of four original research papers. The main section consists of five chapters in which the four remaining are organized as follows,

Ch. 2	Contains a literature review of previous work, state of the art modeling practices and FE formulations relevant for trawl-pipe pull-over interaction and flexible pipe reeling analysis.
Ch. 3	Presents the nonlinear FE program developed for Papers III and IV. The finite elements required for simulation of reeling operations are described. A combined verification and Newton convergence study is also presented.
Ch. 4	Gives an extended summary of the research papers and describes the new FE techniques developed, the numerical modeling and the outcome of the simulation work.
Ch. 5	Presents conclusions and recommendations for future work. The original contributions are listed, limitations of the research are stated and the most important implications of the work are described.

Papers I – IV are presented in full-length versions after the main section. The reader is recommended to study the papers in order to fully comprehend all aspects of the research. For a quick overview of the work one may study Chapters 1, 4 and 5 only.

Chapter 2

Literature survey

The objective of this chapter is to summarize previous work relevant for the trawl-pipe pull-over interaction problem and flexible pipe reeling analysis. The basic concepts of beam contact formulations and arbitrary Lagrangian-Eulerian methods are described as well as state of the art modeling practices for trawl boards and flexible pipes. Note that some of the content is also presented in Papers I – IV.

2.1 Trawl-pipe pull-over interaction

2.1.1 Experimental work

Research on trawl-pipe pull-over interaction was initially based exclusively on model testing. The first efforts can be traced back to a multiphase joint industry project (JIP) in the 1970s [28–30], which was initiated by the oil companies operating in the North Sea. Both small-scale and full-scale tests were conducted, in which the most important findings for trawl board interaction were that spanning pipelines were subjected to larger forces than pipelines resting on the seafloor, skew passings resulted in less severe loads than perpendicular crossings and that pipeline hooking could be regarded as an unlikely event. Additionally, it was concluded that pipelines with diameter 0.4 m and greater were able to withstand trawl loads. In the following decades it therefore became general practice in the North Sea to trench or cover all pipes with diameter less than 0.4 m.

Small-scale tests of protective subsea structures subjected to over-trawling of beam trawls and trawl boards were conducted by Nygaard [31] in 1988. He concluded that the interaction was dependent on the gear geometry, the weight of the towed equipment and that small perturbations of the initial conditions could greatly influence the interaction behavior. Furthermore, the most extreme towing line forces for elevated beam structures were found to be more than twice as large as those measured in the JIP described above.

As heavier trawl gear was put into use during the 1980s and previous model tests had presumed 100 – 150 m water depth and not accounted properly for span flexibility, it was realized that new test data should be obtained with systematic variation of parameters such as span height, pipe lateral support conditions, towing velocity and towing line stiffness. An extensive model test program for trawl board pull-over interaction was therefore conducted by MARINTEK in 1990 on behalf of Statoil [27]. Parametrized load histories suitable for design analysis were established from these tests [32], which in fact form the basis for the pull-over loads recommended by the DNV-RP-F111 code [7] as of today.

Valdemarsen [33, 34] conducted full-scale over-trawling tests of pipes at low span heights from the fishermen's perspective. He concluded that trawl boards were significantly hindered for crossing angles less than 40°. The boards were seen to slide several metres along the pipe before they eventually passed and fell flat onto the seabed in danger of getting stuck on soft bottoms.

2.1.2 Numerical work

The use of numerical methods is motivated by the disadvantages present in model testing such as the lack of input parameter flexibility, the need of truncated models and the high expenses involved, as well as the desire to predict load effects in specific design cases without unnecessary conservatism.

The first numerical model for prediction of pull-over loads appeared in work by Horenberg and Guijt in 1987 [35]. They developed a two-dimensional finite difference model for the interaction between a fixed pipe and a beam trawl, which was shown to predict peak load and duration within a 10% margin of model test results. In 2008, Igland and Søreide [10] used FE analysis to study the interaction between a clump weight and a pipeline resting on the seabed, see Fig. 2.1a. They presented a successful validation study against laboratory tests and demonstrated that the DNV-RP-F111 code was too conservative in case of soft seabeds. Similar clump weight simulations were conducted by Maalø et al. [11] for span heights below 1 m. Their model was found to agree well with laboratory tests and they revealed that the recommended peak design load could be reduced by approximately 50% if span flexibility was taken into account. In summary, these three contributions demonstrate that numerical models are capable of predicting pull-over loads

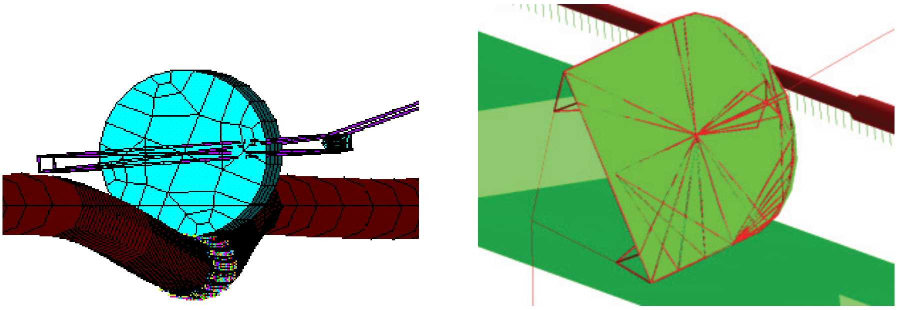
(a) Clump weight simulation by Igland and Søreide [10]

(b) Trawl board model used by Møller and Longva

Figure 2.1: FE simulation of trawl gear pull-over

when the trawl gear interaction behavior is predominantly two-dimensional.

Prediction of trawl board pull-over loads was addressed in a British JIP in the late 1990s with a two-dimensional finite difference model [36]. The simulation strategy predicted unreliable loads which were both conservative and non-conservative when compared against model tests, arguably because of the inability to capture the true three-dimensional interaction behavior. A more general approach based on FE analysis was used in work by Møller [14] and Longva [15]. They used a simplified representation of the board contact geometry based on rigid cylindrical rollers, see Fig. 2.1b, where the presence of disjoint contact surface regions were reported to give convergence issues. No comparison against model tests was considered. Thus, the validity of using numerical simulations for trawl board and pipeline pull-over interaction has not been confirmed yet.

2.1.3 Trawl board hydrodynamic load modeling

The ability to predict realistic pull-over responses depends strongly on the modeling of the hydrodynamic loads. This modeling is particularly challenging for trawl boards as the interaction involves transient motions in all six DOFs. Previously, load estimation has been dealt with by Teigen et al. [12] for bottom trawl boards and by Reite [13] for midwater trawl boards. Since computational fluid dynamics is too slow for time domain simulations, it is common to use six DOF hydrodynamic load models with precomputed coefficients. The loads are then divided into steady-state parts and transient parts and estimated separately.

The steady-state fluid loads are associated with the forces and the moments present when the board travels along a rectilinear path at constant velocity. Regarding estimation of these loads, much data is available in the literature such as the coefficients for the NACA foil series presented in Ref. [37]. If high accuracy is needed, model testing of the actual trawl board is generally required. The available options are wind tunnel experiments as selected by Reite [13] and flume tank testing which was used in the work by Teigen et al. [12], see Fig. 2.2a. The latter option is probably more convenient regarding Reynolds number scale effects.

The transient loads may be divided into loads due to circulation build-up, damping due to angular velocities and hydrodynamic mass loads [13]. Circulation build-up is associated with transient lift loads that arise due to sudden changes of the fluid relative velocity vector, see Ref. [38]. In Reite's work, precomputed coefficients for all three load contributions were established by means of a vortex-lattice potential theory method. In the work by Teigen et al., a standard potential theory method was applied to study a trawl board and a pipe located on the sea bottom, see Fig. 2.2b. They demonstrated that the hydrodynamic mass was dependent on the distance and the orientation relative to the seabed and the pipeline. Worth mentioning is that the hydrodynamic Coriolis-centripetal loads were justifiably neglected in Reite's application, while Teigen et al. did not address these loads since they focused solely on estimation of hydrodynamic mass and steady-state fluid loads.

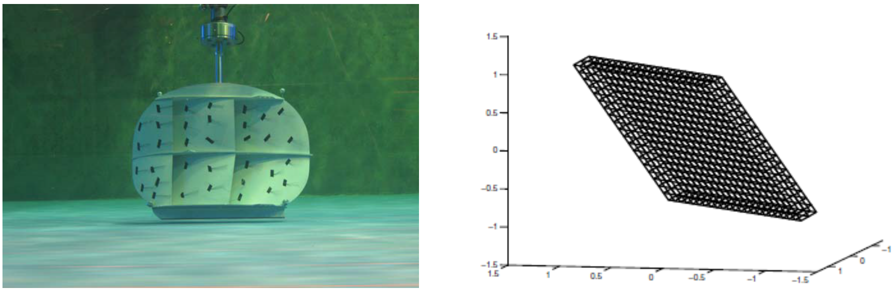

(a) Flume tank testing of multifoil board

(b) Panel model of trawl board

Figure 2.2: Estimation of steady-state fluid loads and hydrodynamic mass [12]

2.1.4 Contact formulations

The rigidity of standard trawl gear is much larger than the pipe flexural stiffness. Consequently, for the purpose of global response prediction, the trawl gear can be modeled as a rigid body and a beam model can be used for the pipe. This modeling assumption was utilized in the previous work described in Sec. 2.1.2, apart from Igland and Søreide who relied on combined use of beam, shell and solid elements, see Fig. 2.1a.

The treatment of beam contact problems differs from the approach used for contact problems involving continuum elements. A key differences is the geometric symmetry which makes distinctions like slave beams and master beams superfluous [39]. The contact is further assumed to occur pointwise and the cross-sections are assumed undeformable [40]. Three-dimensional curves representing the cross-section can therefore be used as basis for the contact kinematics.

The literature on beam contact is sparse in relation to the numerous publications available for conventional contact formulations. One of the first publications was made by Souza de Corsi [41] who addressed a seabed-cable contact problem in analysis of mooring lines. Thereafter, Maker and Laursen [42] proposed a formulation for the interaction between a continuum medium and a rod modeled by beam or truss elements. Contact between two beams was first addressed in 1997 in the work by Wriggers and Zavarise [39]. They developed a contact formulation valid for circular cross-sections, which later was extended to account for friction [43]. Similarly, Litewka and Wriggers presented a contact formulation for two beams with rectangular cross-sections for the frictionless case [44] and thereafter with friction included [45]. The idea of disengaging from the underlying beam formulation was introduced by Litewka [46], who developed a C^1-continuous contact element without involving the beam rotational DOFs. This idea was accomplished for arbitrary three-dimensional curves in the work by Konyukhov and Schweizerhof [47]. They used covariant derivatives to obtain consistent tangent stiffness matrices that were independent of the discretization used for the underlying beam formulation.

In the references cited above, the contact constraints for the frictionless case were imposed by either the penalty method or the standard Lagrange multiplier method [40]. Those concerned with frictional contact applied the penalty method. This is in fact motivated since reversible tangential displacements as observed in experiments [48] can be represented via the penalty regularized stick constraint [40]. As argued by Wriggers [49] and Konyukhov [50], there is a similar motivation for the impenetrability constraint since the penetration-dependent penalty force can be interpreted as a hyper-elastic constitutive law. This is relevant for subsea pipelines as it may be desirable to allow for modeling of elastic coating stiffness properties.

2.2 Flexible pipe reeling analysis

2.2.1 Arbitrary Lagrangian-Eulerian methods

The arbitrary Lagrangian-Eulerian (ALE) concept was introduced in 1964 under the name Coupled Eulerian-Lagrangian by Noh [51] for a two-dimensional hydrodynamic problem with moving fluid boundaries. Two decades later the ALE description was introduced in solid mechanic problems with path-dependent material behavior by Liu et al. [52]. The word *arbitrary* refers to the mesh motion which follows a rule selected for the problem at hand. The ALE formulation reduces into an Eulerian formulation if the mesh velocity is set to zero and into a Lagrangian formulation if the mesh and material motions are equal.

The objective of ALE techniques in solid mechanic problems is usually to avoid severe mesh distortions in large-deformation problems without resorting to re-meshing and updating of the mesh topology. Typical examples are simulation of metal forming processes, necking tests and large-strain impact problems, see Fig. 2.3 and Ref. [53, 54]. The ALE formulation may also function as a mesh adaptive method if the mesh motion rule is defined to give increased element density in regions with strong solution gradients, such as along yield lines in plated structures, see Ref. [55].

In the present work, the purpose is neither mesh regularization nor mesh adaptivity, but rather to obtain a virtually fixed mesh in beam reeling analyses. Lagrangian-Eulerian analysis methods for beams with elastic materials have been developed for problems involving axial mass flow [56], sliding joints [57] and axially moving beams [58]. There exist no examples in the literature where the Lagrangian-Eulerian viewpoint has been utilized in beam problems with path-dependent material behavior. Nevertheless, the basic concepts and the challenges that must be dealt with are similar to those present for

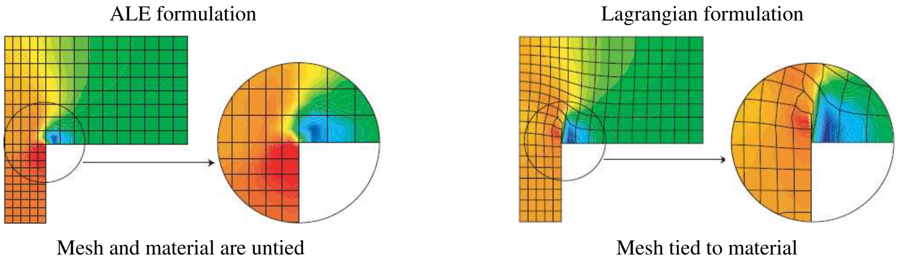

Figure 2.3: ALE mesh regularization in a punch compaction simulation

continuum-based ALE formulations.

ALE stress-update procedures are divided into two categories, coupled and uncoupled methods. In the coupled method, the constitutive rate equation, including the convective term, is integrated forward in time in a single step. This method has been employed for instance by Ghosh and Kicuchi [59] who used an implicit global time-stepping algorithm and in work by Liu et al. [52] for the explicit case.

The uncoupled stress-update method, also referred to as an operator split method, is by far the most common in commercial software. This method can be interpreted to divide the time step into a Lagrangian step, a mesh update step and a convection step, see Ref. [60, 61]. No equilibrium iterations are executed after the convection step and consequently the equilibrium becomes disturbed, however, as described by Donea [22] the unbalance is not severe and can be handled as an extra residual load at the next time step. The uncoupled method is often regarded as more advantageous because simpler and more robust algorithms can be developed [61], it offers greater flexibility for the mesh motion [62] and upgrading of an existing implicit Lagrangian implementation into the ALE description is facilitated since no additional tangent stiffness contributions appear.

Since the material points do not coincide with the quadrature points, the history-dependent constitutive variables must be convected through the mesh. Convection is present also for the inertia term in the momentum balance equation. The spatial gradient of the convected variables is known to introduce spatial oscillations in the Galerkin-based FE method [63]. Such numerical instabilities can be avoided or mitigated by using a stabilization technique on the convective term. Possible candidates are the streamline upwind Petrov-Galerkin method used by Liu et al. [64] and the Taylor-Galerkin method developed by Donea [65]. Other alternatives such as the least-square methods and the characteristic Galerkin method may also be applied [66]. Regarding the present work, spatial instabilities must be anticipated since the virtually fixed mesh represents a strongly convection-dominated situation.

Additional challenges are introduced if the spatial gradient of the convected variables is discontinuous across element borders, such that it cannot be reliably computed on element level [22]. Huétink et al. [67] therefore proposed a strategy based on least square smoothing between quadrature points within the element and simple averaging between elements. In work by Liu et al. [52], the spatial gradient ambiguity was solved by developing a weak formulation for the constitutive rate equation such that the convective term containing the stress gradient transformed into a stress-velocity term. This is relevant for beam models since the constitutive variables are usually assumed constant or interpolated with C^0-functions between the element nodes.

2.2.2 Constitutive modeling

The constitutive model applied for the flexible pipe is important for the ability to predict torque responses in load-out operations. As seen in Fig. 2.4 the composition of the cross-section with metallic and plastic layers is fairly complex. Constitutive models capable of predicting the response of such cross-sections are normally based on separate models for the axial-torsional and bending responses.

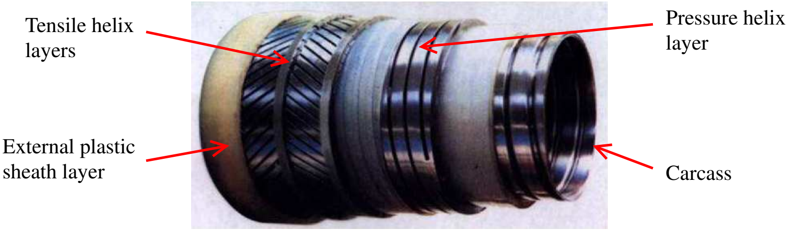

Figure 2.4: Flexible pipe cross-section

Axial-torsional constitutive models, often called axi-symmetric models in the literature, have been addressed in several research efforts the last decades. In 1996, ten institutions participated in a benchmark study initiated by Witz [68], where the response of a flexible pipe subjected to various combinations of tension and torque was considered. The study concluded that the axial-torsional responses can be satisfactorily predicted provided that the interaction between the layers is accounted for. An important contribution to axial-torsional response models is the work pioneered by Féret and coworkers in the late 1980s [69, 70]. Their model is in fact used as basis in current state of the art models which are able to account for effects such as local helix bending moments and torque, material nonlinearity, geometric nonlinearity, formation of radial gaps and tendon circumferential gap closure, see e.g. Ref. [71, 72].

The bending response is characterized by a trivial linear-elastic contribution from the plastic layers and a hysteretic contribution due to the stick-slip behavior of the tensile helix layers. In general, the hysteretic bending response is difficult to predict accurately, which also was concluded in Witz's benchmark study [68]. Several models able to account for the hysteretic bending response have therefore emerged in the literature the last decades. Some of them utilize individual tendon approaches and are not formulated in the framework of computational elasto-plasticity, see e.g. Ref. [73]. Such models can be computationally demanding and are not suitable for use in a general Lagrangian-Eulerian stress-update procedure. Contrarily, the fairly advanced stress resultant based elasto-plastic models proposed by Alfano, Bahtui and coworkers [74, 75] are regarded as applicable. They used detailed FE simulations for calibration of the models and due account was made for radial pressure loads. The disadvantage of their approach is the considerable efforts needed to determine the material parameters and that the models are only valid for a specific cross-section. A more attractive alternative was proposed by Sævik [72], who formulated two elasto-plastic Coulumb bending models valid for generic cross-sections, one detailed and one gross model, which were coupled with a separate axi-symmetric model for determination of the interlayer contact pressures. Both models were shown to predict fatigue damages of flexible pipes in good correlation with laboratory tests. A similar strategy with a gross Coulomb bending model was presented by Skeie et al. [76] for fatigue analysis of umbilical cables and flexible pipes. Although these bending models have been validated for fatigue calculations and gained consensus in the industry, they are still based on simplifying assumptions which strictly speaking must be validated for the problem at hand.

2.2.3 Torsional failure and bending-induced torque

Torsional failure in flexible pipe load-out operations have so far not been addressed in the open literature. According to reports provided by MARINTEK, the failure modes identified in load-out operations are lateral buckling of the tensile helix layers, loop formation and herniation buckling. The radial buckling mode for the tensile helix layers is also relevant.

Lateral and radial buckling of the tensile helix tendons has been studied in work by Vaz and Rizzo [77] with aid of detailed FE analysis. Østergaard et al. [78] developed a mathematical model for global limit load prediction which were able to describe lateral tendon instabilities for zero friction. Design formulas for both the radial and the lateral buckling modes have been proposed by Sævik [79, 80]. Loop formation of risers in catenary configurations have been studied by Ramos and Pesce [81] and Neto et al. [82]. Both studies contributed with design formulas and concluded that Greenhill's equation [83] could be used also for curved configurations. The term herniation buckling above, refers to the extreme situation where the inner tensile helix layer buckles radially through accumulated openings in the outer tensile helix layer. This failure mode has so far not been studied in the open literature.

Significant bending-induced torques are known to develop in flexible pipes because of the hysteretic bending behavior. This phenomenon originates from interlayer friction effects, which allow the bending moment vector to be non-aligned with the normal vector of the curvature plane, such that a torque is needed to fulfill equilibrium. The generation of such torques in flexible pipes has been studied in work by Fylling and Bech [26]. They derived simplified formulas for prediction of the induced torque and compared them against FE results obtained with a corotational beam formulation.

2.2.4 Beam models

Most beam models for flexible pipes are based on a corotational description of kinematics, see Refs. [72, 84, 85]. This is also reflected in analysis software for slender marine structures [86–89]. In brief, the corotational formulation employs element-based reference configurations which rotates and translates with the rigid body motion of the elements. This allows for re-use of linear beam elements in a geometrically nonlinear context under the assumption of small deformations relative to the element-based reference configurations. This assumption represents no limitation, since in case of violation, shorter elements can be applied. Shear deformations in flexible pipes are negligible and thus most corotational pipe models obey the Euler-Bernoulli kinematic relations. If material nonlinearity and higher-order strain terms are accounted for, the formulation is applicable also for plastic collapse analysis [90] and plastic instability analysis [91].

Some examples of geometrically exact beam formulations in marine applications have appeared in recent years, for instance in simulation of pipe-laying operations [93] and in prediction of loop formation of flexible risers [82]. This type of formulation was proposed by Simo [94] based on a generalization of Reissner's two-dimensional finite strain beam formulation [95]. The motion of the beam is described by the displacements of the centroidal line and rotation tensors which give the orientation of the cross-sections. Shear deformations are inherently accounted for and the translations and the rotations along the centroidal line can be independently interpolated. These formulations are coined geometrically exact since they account without any approximations for the total deformation and strains [96]. The beam elements exhibit shear locking for standard discretizations and it is therefore common to use reduced integration [97].

Chapter 3

MATLAB finite element program

The Lagrangian-Eulerian formulation developed in Paper III differs from the conventional Lagrangian method. It would therefore not be feasible with regard to time-consumption, in particular during the development phase, to implement the code into a commercial FE program such as selected in Papers I and II. The available commercial codes [86–89] are neither able to handle the non-symmetric equation system that appears because of the Lagrangian-Eulerian viewpoint. A small FE program was therefore implemented in MATLAB [98]. This software offers a well-designed debugging environment, non-symmetric equation solvers, straightforward post-processing of results and numerous built-in functions.

The MATLAB implementation is representable for the state of the art analysis method for slender marine structures. The intention with this chapter is to describe details that had to be excluded from Papers III and IV and to present a combined verification and Newton convergence study for the implemented corotational beam formulation. The theory presented in the following is relevant also for Papers I and II, where the SIMLA computer program [89] which has a similar beam formulation was used.

3.1 Coordinates, transformations and rotations

The global computational basis is taken to be a fixed Cartesian coordinate system with unit base vectors $\mathbf{E}_i$. For the vector $\mathbf{a}$, the relation between its components in the coordinates associated with $\mathbf{E}_i$ and $\bar{\mathbf{e}}_i$, is defined by the transformation matrix $\mathbf{T}$ according to,

$$\bar{a}_i = T_{ij} a_j \quad T_{ij} = \mathbf{E}_j \cdot \bar{\mathbf{e}}_i \qquad \mathbf{a} = a_i \mathbf{E}_i = \bar{a}_i \bar{\mathbf{e}}_i \quad \mathbf{T}\mathbf{T}^\top = \mathbf{I} \quad i,j = 1,2,3 \tag{3.1}$$

where $\mathbf{I}$ is the identity matrix and the Einstein summation convention, both here and in the sequel, applies for repeated indices. The index range is not stated in the following as it is implicitly assumed to loop over 1, 2 and 3. The components of the second order tensor $\mathbf{A}$ transform according to,

$$\bar{A}_{kl} = T_{ki} A_{ij} T_{lj} \qquad T_{ij} = \mathbf{E}_j \cdot \bar{\mathbf{e}}_i \qquad \mathbf{A} = A_{ij} \mathbf{E}_i \otimes \mathbf{E}_j = \bar{A}_{ij} \bar{\mathbf{e}}_i \otimes \bar{\mathbf{e}}_j \tag{3.2}$$

The nodal rotation state and the orientation of the individual elements are defined by proper orthogonal tensors that give the rotation relative to the global computational basis $\mathbf{E}_i$. For that purpose, the rotation of the vector $\mathbf{a}$ into the vector $\mathbf{b}$, corresponding to the rotation experienced when the $\mathbf{E}_i$-triad is rotated into the $\mathbf{e}_i$-triad, is expressed in terms of the rotation tensor $\mathbf{Q}$ as follows,

$$\mathbf{b} = \mathbf{Q} \cdot \mathbf{a} \qquad \mathbf{Q} = \mathbf{e}_i \otimes \mathbf{E}_i \qquad \mathbf{Q} \cdot \mathbf{Q}^\top = \mathbf{e}_i \otimes \mathbf{e}_i = \mathbf{I} \tag{3.3}$$

3.2 Quaternions

The rotation in Eq. (3.3) can be represented by the vector $\boldsymbol{\psi} = \psi \mathbf{n}$, where ψ denotes the angular rotation about the unit vector $\mathbf{n}$. The corresponding quaternion representation consists of a scalar q_4 and a vector $\mathbf{q}$ defined by the relations,

$$q_4 = \cos\left(\frac{1}{2}\psi\right) \qquad \mathbf{q} = \sin\left(\frac{1}{2}\psi\right)\mathbf{n} \qquad \mathbf{q} = \begin{bmatrix} q_1 & q_2 & q_3 \end{bmatrix}^\top \qquad \boldsymbol{\psi} = \psi \mathbf{n} \tag{3.4}$$

with the following parametrization for the rotation tensor,

$$\mathbf{Q}\left(q_4, \mathbf{q}\right) = \left(q_4^2 - \mathbf{q} \cdot \mathbf{q}\right) \mathbf{I} + 2 q_4 \mathbf{W}\left(\mathbf{q}\right) + 2 \mathbf{q} \otimes \mathbf{q} \tag{3.5}$$

where $\mathbf{W}$ is the skew-symmetric tensor that represents the vector cross product,

$$\mathbf{W}\left(\mathbf{q}\right) = \begin{bmatrix} 0 & -q_3 & q_2 \\ q_3 & 0 & -q_1 \\ -q_2 & q_1 & 0 \end{bmatrix} \tag{3.6}$$

The inverse relation of Eq. (3.5), which gives the quaternion parameters for a specific rotation tensor is in the implementation based on Spurier's algorithm, see Ref. [99]. The major advantage of the quaternion representation is that the parametrization is non-singular for all rotation angles. In the present work, the quaternions are used mainly because compound rotations such as those encountered in the nodal rotation update scheme,

$$\mathbf{Q}\left(q_4, \mathbf{q}\right) = \mathbf{U}\left(u_4, \mathbf{u}\right) \cdot \mathbf{V}\left(v_4, \mathbf{v}\right) \tag{3.7}$$

with $\mathbf{U}$ and $\mathbf{V}$ parametrized according to Eqs. (3.4) and (3.5), can be efficiently computed without matrix multiplications as follows,

$$q_4 = u_4 v_4 - \mathbf{u} \cdot \mathbf{v} \qquad \mathbf{q} = u_4 \mathbf{v} + q_4 \mathbf{u} + \mathbf{u} \times \mathbf{v} \tag{3.8}$$

and requires also less memory since only four parameters need to be stored, rather than all nine tensor components.

3.3 Principle of virtual work and linearization

The principle of virtual work expresses equilibrium in an integrated sense and is derived by developing a weak formulation for the momentum balance equation, see e.g. Ref. [63].

For the quasistatic case, with the nodal displacement state $\mathbf{r}$ and the variation of the nodal displacements $\delta\mathbf{r}$, the virtual work equation can be expressed as,

$$\delta W\left(\delta\mathbf{r},\mathbf{r}\right)=\sum^{N_b}\delta W_b+\sum^{N_c}\delta W_c+\sum^{N_k}\delta W_k-\sum^{N_f}\delta W_{EXT}=0 \qquad (3.9)$$

where the summations are taken over N_b beam elements, N_c active contact constraints, N_k spring elements and N_f external loads. Apart from the trivial load term δW_{EXT}, explicit expressions for the virtual work contributions are presented in Section 3.5 – 3.7.

Equation (3.9) is nonlinear in terms of the displacement state and is therefore linearized and solved with the Newton-Raphson method according to,

$$\left.\frac{d\left(\delta W\right)}{d\mathbf{r}}\right|_{\mathbf{r}^c} d\mathbf{r}=-\delta W\left(\delta\mathbf{r}^c,\mathbf{r}^c\right) \qquad d\mathbf{r}=\begin{bmatrix}d\mathbf{x}_1 & d\boldsymbol{\varphi}_1 & ... & d\mathbf{x}_{N_n} & d\boldsymbol{\varphi}_{N_n}\end{bmatrix}^\top \qquad (3.10)$$

which results in a linear equation system with $6N_n{-}N_u$ unknowns when the arbitrariness of $\delta\mathbf{r}$ is invoked. N_n is the number of nodes, N_u is the number of prescribed displacement DOFs and superscript c refers to the current displacement state. The nodal translation and rotation increments are denoted by $d\mathbf{x}$ and $d\boldsymbol{\varphi}$, respectively. For the case of reeling analysis with a nearly fixed mesh, the following convergence norm is used as termination criterion for the iterative solution process in Eq. (3.10),

$$\epsilon_f>\frac{||\mathbf{R}_R^c||}{\frac{1}{2}||\mathbf{R}_{EXT}^c||+\frac{1}{2}||\mathbf{R}_{INT}^c||} \qquad \mathbf{R}_R^c=\mathbf{R}_{EXT}^c-\mathbf{R}_{INT}^c \quad \delta W=\delta\mathbf{r}^{c\top}\mathbf{R}_R^c \qquad (3.11)$$

where $||{*}||$ refers to the Euclidean norm of the unconstrained translatory DOFs, $\mathbf{R}_{INT}$ is the system internal load vector associated with the beam stress resultants, the contact interactions and the spring elements while $\mathbf{R}_{EXT}$ contains the system external loads.

3.4 Nodal displacement update

The nodal position vectors are updated at each iteration step with the translation increments from the Newton solution procedure in Eq. (3.10) as follows,

$$\mathbf{x}_j=\mathbf{x}_j^p+d\mathbf{x}_j \qquad j=1,...,N_n \qquad (3.12)$$

where superscript p refers to the previous displacement state. The nodal rotation state is updated according to Eqs. (3.7) and (3.8) with $\mathbf{U}(dq_4,d\mathbf{q})$ and $\mathbf{V}(q_4^p,\mathbf{q}^p)$,

$$q_j=q_{4j}^p dq_{4j}-\mathbf{q}_j^p\cdot d\mathbf{q}_j \qquad \mathbf{q}_j=\mathbf{q}_j^p dq_{4j}+q_{4j}^p d\mathbf{q}_j+d\mathbf{q}_j\times\mathbf{q}_j^p \qquad j=1,...,N_n \qquad (3.13)$$

where the quaternions dq_4 and $d\mathbf{q}$ are obtained by inserting the nodal rotation increment, $d\boldsymbol{\varphi}=d\varphi\mathbf{n}$, from Eq. (3.10) into Eq. (3.4).

3.5 Corotational beam formulation

The basic idea in the corotational approach is to decompose the motion of the element into rigid body and pure deformation parts through the use of a reference frame that continuously rotates and translates with the element. The deformation is captured at the level of the corotated reference, while the geometric nonlinearity of the arbitrarily large rigid body motion is incorporated in the local-global transformation matrices. By assuming small deformations relative to the corotated element frames, linear elements can be reused in a geometrically nonlinear context, which in fact is the main motivation for using corotational formulations [100].

The corotational concept is illustrated in Fig. 3.1 where the initial configuration of the element is denoted C_0, the corotated element configuration is labeled C_{0n} and the deformed configuration is denoted C_n. All stress and strain variables are referred to the straight C_{0n}-reference which differs from the initial C_0-configuration by the element rigid body motion. The corotational formulation can therefore be regarded as computationally equivalent to the total Lagrange formulation, however, issues such as membrane-locking and artificial straining are avoided since the eliminated rigid body motion enables use of low-order strain measures [101]. Alternatively, the updated Lagrange formulation which employs C_n as the reference could be used. In that case, the stress and the strains must be transformed to an appropriate computational basis and integrated over the deformed volume. This approach is not preferred in situations where a corotational formulation with high-performance linear elements can be used instead.

The implemented corotational formulation is described in Section 3.5.1 – 3.5.3. The presentation follows closely Ref. [102], apart from the deformation DOFs which are based on the nodal relative rotations rather than the natural deformation modes.

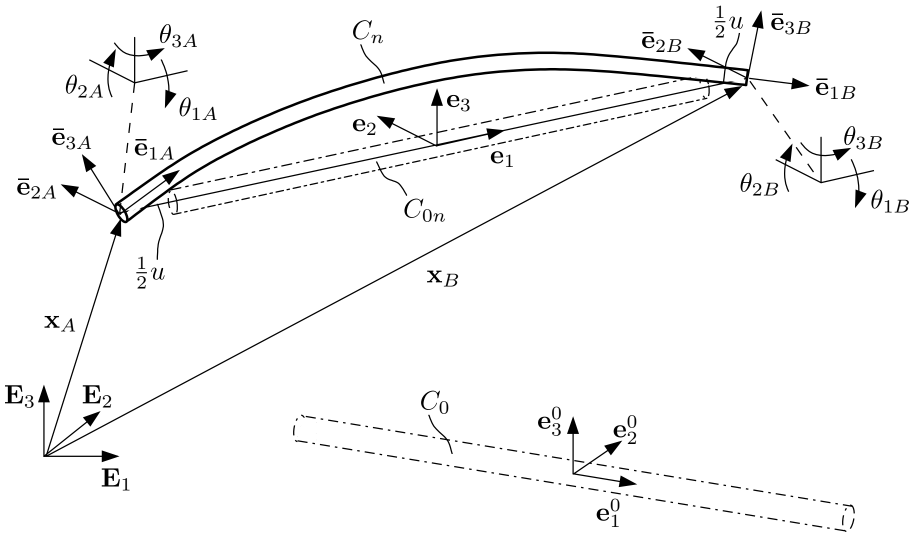

Figure 3.1: Corotated beam element

3.5.1 Deformation DOFs

The Euler-Bernoulli kinematic relations which imply no shear deformations are utilized. As illustrated in Fig. 3.1, the element deformation DOFs therefore consist of the following parameters,

$$\mathbf{v}_d^{\top} = \begin{bmatrix} u\,, & \theta_{1B} - \theta_{1A}\,, & \theta_{2A}\,, & \theta_{3A}\,, & \theta_{2B}\,, & \theta_{3B} \end{bmatrix} \tag{3.14}$$

where the components are referred to the corotated $\mathbf{e}_i$-basis. The axial elongation u is computed from the initial element length L_0 and the current secant length L as follows, see Fig. 3.1,

$$u = L - L_0 \qquad L = ||\mathbf{x}_B - \mathbf{x}_A|| \tag{3.15}$$

The remaining parameters in Eq. (3.14) gives the rotation of the nodal $\bar{\mathbf{e}}_i$-triads relative to the corotated element triad $\mathbf{e}_i$. The latter triad is obtained by a three-step procedure. First, the mean rotation based on the rotation tensors at the element nodes, $\mathbf{Q}_A(q_{4A}, \mathbf{q}_A)$ and $\mathbf{Q}_B(q_{4B}, \mathbf{q}_B)$, is computed,

$$s_4 = \frac{1}{2}\left[(q_{4A} + q_{4B})^2 + ||\mathbf{q}_A + \mathbf{q}_B||^2\right]^{1/2} \tag{3.16}$$

$$\tilde{q}_4 = \frac{1}{2}\left(q_{4A} + q_{4B}\right)/s_4 \qquad \tilde{\mathbf{q}} = \frac{1}{2}\left(q_{4A}\mathbf{q}_B - q_{4B}\mathbf{q}_A + \mathbf{q}_A \times \mathbf{q}_B\right) \tag{3.17}$$

and is thereafter employed to rotate the initial element basis $\mathbf{e}_i^0$ from the C_0-configuration, see Fig. 3.1,

$$\tilde{\mathbf{e}}_i = \mathbf{Q}\left(\tilde{q}_4, \tilde{\mathbf{q}}\right) \cdot \mathbf{e}_i^0 \tag{3.18}$$

At last, the $\tilde{\mathbf{e}}_i$-triad is rotated via the smallest possible angle such that $\mathbf{e}_1$ is directed along the element secant vector,

$$\tilde{\mathbf{e}} = \frac{\tilde{\mathbf{e}}_1 + \mathbf{t}}{||\tilde{\mathbf{e}}_1 + \mathbf{t}||} \qquad \mathbf{t} = \frac{\mathbf{x}_B - \mathbf{x}_A}{L} \tag{3.19}$$

$$\begin{bmatrix} \mathbf{e}_1 & \mathbf{e}_2 & \mathbf{e}_3 \end{bmatrix} = (\mathbf{I} - \tilde{\mathbf{e}} \otimes \tilde{\mathbf{e}}) \cdot \begin{bmatrix} -\tilde{\mathbf{e}}_1 & \tilde{\mathbf{e}}_2 & \tilde{\mathbf{e}}_3 \end{bmatrix} \tag{3.20}$$

which gives the element rotation tensor,

$$\mathbf{Q}_e = \mathbf{e}_i \otimes \mathbf{E}_i \tag{3.21}$$

With the nodal rotation tensors $\mathbf{Q}_j(q_{4j}, \mathbf{q}_j)$ and the element initial rotation tensor $\mathbf{Q}_{e0}$, the rotation of the nodal $\bar{\mathbf{e}}_i$-triads relative to the $\mathbf{e}_i$-triad can now be obtained, see Fig. 3.1 and Eq. (3.3),

$$\mathbf{Q}_j^{rr}\left(q_{4j}^{rr}, \mathbf{q}_j^{rr}\right) = \bar{\mathbf{e}}_{i\{j\}} \otimes \mathbf{e}_i = \mathbf{Q}_j \cdot \mathbf{Q}_{e0} \cdot \mathbf{Q}_e^{\top} \qquad j = A, B \quad \mathbf{Q}_{e0} = \mathbf{e}_i^0 \otimes \mathbf{E}_i \tag{3.22}$$

Equation (3.22) must be projected into the corotated $\mathbf{e}_i$-basis by the transformation matrix $\mathbf{T}_e$. By letting Eq. (3.22) be represented in the $\mathbf{E}_i$-coordinates, Eqs. (3.2) and (3.3) yields $\mathbf{T}_e = \mathbf{Q}_e^{\top}$, and the relative rotation therefore reads,

$$\mathbf{Q}_j^{rrl}\left(q_{4j}^{rr}, \mathbf{q}_j^{rrl}\right) = \mathbf{T}_e \mathbf{Q}_j^{rr}\left(q_{4j}^{rr}, \mathbf{q}_j^{rr}\right) \mathbf{T}_e^{\top} = \mathbf{Q}_e^{\top} \mathbf{Q}_j \mathbf{Q}_{e0} \qquad j = A, B \tag{3.23}$$

where superscript l underlines that the quantities are expressed in the local $\mathbf{e}_i$-basis. With aid of Spurier's algorithm the quaternions are extracted and thereafter inserted into Eq. (3.4) to give the rotational deformation parameters needed in Eq. (3.14),

$$\boldsymbol{\theta}_j = 2\cos^{-1}\big(q_{4j}^{rr}\big)\frac{\mathbf{q}_j^{rrl}}{||\mathbf{q}_j^{rrl}||} \qquad \boldsymbol{\theta}_j = \begin{bmatrix}\theta_{1j} & \theta_{2j} & \theta_{3j}\end{bmatrix}^\top \qquad j = A, B \tag{3.24}$$

In situations where $||\mathbf{q}_j^{rrl}|| << 1$, the rotation parameters are instead obtained from a truncated version of Eq. (3.4),

$$\boldsymbol{\theta}_j = 2\mathbf{q}_j^{rrl} \tag{3.25}$$

3.5.2 Element load vector

The virtual work of a single element in the corotated $\mathbf{e}_i$-basis is expressed in terms of the variation of $\mathbf{v}_d$ from Eq. (3.14) as follows,

$$\delta W_b = \delta\mathbf{v}_d^\top \mathbf{S} \tag{3.26}$$

with the energy-conjugate stress resultants defined as,

$$\mathbf{S} = \begin{bmatrix}N & M_1 & -M_{A2} & -M_{A3} & M_{B2} & M_{B3}\end{bmatrix}^\top \tag{3.27}$$

where the axial force N and the torque M_1 are constant within the element and the bending moments M_2 and M_3 vary linearly between the element nodes. The constant shear forces Q_2 and Q_3 are obtained from bending moment equilibrium as follows,

$$Q_2 = -\frac{M_{B3} - M_{A3}}{L} \tag{3.28}$$

$$Q_3 = \frac{M_{B2} - M_{A2}}{L} \tag{3.29}$$

The stress resultants contained in $\mathbf{S}$ must be assigned a constitutive description. For simplicity, the material behavior is assumed linear-elastic and the stress resultants are therefore obtained from the following constitutive stiffness relation in the corotated $\mathbf{e}_i$-basis,

$$\mathbf{S} = \mathbf{K}_d\,\mathbf{v}_d = \frac{1}{L}\begin{bmatrix} EA & 0 & 0 & 0 & 0 & 0 \\ 0 & GJ & 0 & 0 & 0 & 0 \\ 0 & 0 & 4K_E & 0 & 2K_E & 0 \\ 0 & 0 & 0 & 4K_E & 0 & 2K_E \\ 0 & 0 & 2K_E & 0 & 4K_E & 0 \\ 0 & 0 & 0 & 2K_E & 0 & 4K_E \end{bmatrix}\mathbf{v}_d \tag{3.30}$$

where EA is the axial stiffness, GJ is the torsion stiffness and K_E is the bending stiffness.

When the stress resultants are added into Eqs. (3.9) and (3.10), the element load vector must be on 12×1 format. For that purpose, the element displacement vector $\mathbf{v}$ is introduced, which in terms of variational quantities is expressed as,

$$\delta\mathbf{v} = \begin{bmatrix}\delta\mathbf{w}_A & \delta\mathbf{w}_B\end{bmatrix}^\top \quad \delta\mathbf{w}_j = \begin{bmatrix}\delta x_{1j} & \delta x_{2j} & \delta x_{3j} & \delta\varphi_{1j} & \delta\varphi_{2j} & \delta\varphi_{3j}\end{bmatrix} \tag{3.31}$$

where the variation of the nodal translation and rotation components are denoted by δx_j and $\delta\varphi_j$, respectively. The virtual work in Eq. (3.26) can then be restated,

$$\delta W_b = \delta\mathbf{v}^\top \mathbf{P} \tag{3.32}$$

with the energy-conjugate 12×1 element load vector,

$$\mathbf{P}^\top = \begin{bmatrix} \mathbf{f}_A^\top & \mathbf{m}_A^\top & \mathbf{f}_B^\top & \mathbf{m}_B^\top \end{bmatrix} \tag{3.33}$$

where $\mathbf{f}_j$ and $\mathbf{m}_j$ are 3×1 vectors containing respectively the forces and the moments at the element nodes. A relation between $\mathbf{P}$ and the stress resultants $\mathbf{S}$ is needed. This relation is established with aid of the corotated unit vectors $\mathbf{e}_i$ and Eqs. (3.28) and (3.29),

$$\mathbf{P} = \mathbf{H}\,\mathbf{S} \qquad \mathbf{H} = \begin{bmatrix} -\mathbf{e}_1 & \mathbf{0} & -\frac{1}{L}\mathbf{e}_3 & \frac{1}{L}\mathbf{e}_2 & -\frac{1}{L}\mathbf{e}_3 & \frac{1}{L}\mathbf{e}_2 \\ \mathbf{0} & -\mathbf{e}_1 & \mathbf{e}_2 & \mathbf{e}_3 & \mathbf{0} & \mathbf{0} \\ \mathbf{e}_1 & \mathbf{0} & \frac{1}{L}\mathbf{e}_3 & -\frac{1}{L}\mathbf{e}_2 & \frac{1}{L}\mathbf{e}_3 & -\frac{1}{L}\mathbf{e}_2 \\ \mathbf{0} & \mathbf{e}_1 & \mathbf{0} & \mathbf{0} & \mathbf{e}_2 & \mathbf{e}_3 \end{bmatrix} \tag{3.34}$$

where the 12×6 matrix $\mathbf{H}$ also acts as a transformation for the load vector $\mathbf{P}$ by expressing the corotated unit vectors $\mathbf{e}_i$ in the $\mathbf{E}_i$-basis.

Furthermore, the incremental relation between the element deformations $\mathbf{v}_d$ and the element displacement vector $\mathbf{v}$ is obtained by combining Eqs. (3.26), (3.32) and (3.34)

$$d\mathbf{v}_d = \mathbf{H}^\top d\mathbf{v} \tag{3.35}$$

3.5.3 Element tangent stiffness matrix

The tangent stiffness contribution to Eq. (3.10) is found by linearizing the expression that results when Eq. (3.34) is inserted into Eq. (3.32),

$$d\left(\delta W_b\right) = d\left(\delta\mathbf{v}^\top\right)\mathbf{H}\,\mathbf{S} + \delta\mathbf{v}^\top d\mathbf{H}\,\mathbf{S} + \delta\mathbf{v}^\top\mathbf{H}\,d\mathbf{S} \tag{3.36}$$

The two first terms in Eq. (3.36) contribute to the initial stress stiffness matrix $\mathbf{K}_\sigma$, while the third term gives the constitutive stiffness matrix $\mathbf{K}_c$. By means of Eq. (3.35) and the incremental form of Eq. (3.30), the 12×12 tangent stiffness matrix can be expressed as,

$$\mathbf{K} = \mathbf{K}_c + \mathbf{K}_\sigma \qquad \mathbf{K}_c = \mathbf{H}\,\mathbf{K}_d\mathbf{H}^\top \qquad \mathbf{K}_\sigma = \begin{bmatrix} \mathbf{k}_{11}^\sigma & \mathbf{k}_{12}^\sigma & \mathbf{k}_{13}^\sigma & \mathbf{k}_{14}^\sigma \\ \mathbf{k}_{21}^\sigma & \mathbf{k}_{22}^\sigma & \mathbf{k}_{23}^\sigma & \mathbf{k}_{24}^\sigma \\ \mathbf{k}_{31}^\sigma & \mathbf{k}_{32}^\sigma & \mathbf{k}_{33}^\sigma & \mathbf{k}_{34}^\sigma \\ \mathbf{k}_{41}^\sigma & \mathbf{k}_{42}^\sigma & \mathbf{k}_{43}^\sigma & \mathbf{k}_{44}^\sigma \end{bmatrix} \tag{3.37}$$

The initial stress stiffness matrix $\mathbf{K}_\sigma$ is shown to be important for the convergence properties in Section 3.9. A detailed derivation of the $\mathbf{K}_\sigma$-matrix which opens for three alternative representations is therefore presented in the following.

The contribution to $\mathbf{K}_\sigma$ from the first term in Eq. (3.36) appears because the variation of the rotational DOFs is configuration-dependent. As derived in Ref. [102], the variation of a rotation is linearized as follows,

$$d\left(\delta\boldsymbol{\varphi}\right) = -\frac{1}{2}\delta\boldsymbol{\varphi}\times d\boldsymbol{\varphi} \tag{3.38}$$

with this and the skew-symmetric tensor $\mathbf{W}$ defined in Eq. (3.6), the first term in Eq. (3.36) can be rewritten as follows,

$$d\left(\delta\mathbf{v}^{\top}\right)\mathbf{H}\,\mathbf{S} = \frac{1}{2}\delta\boldsymbol{\varphi}_A\cdot\mathbf{W}\left(\mathbf{m}_A\right)\cdot d\boldsymbol{\varphi}_A + \frac{1}{2}\delta\boldsymbol{\varphi}_B\cdot\mathbf{W}\left(\mathbf{m}_B\right)\cdot d\boldsymbol{\varphi}_B \tag{3.39}$$

which gives the following contributions to $\mathbf{K}_\sigma$,

$${}^{1}\mathbf{k}^{\sigma}_{22} = \frac{1}{2}\mathbf{W}\left(\mathbf{m}_A\right) \qquad {}^{1}\mathbf{k}^{\sigma}_{44} = \frac{1}{2}\mathbf{W}\left(\mathbf{m}_B\right) \tag{3.40}$$

The second term in Eq. (3.36) accounts for the change of element length and the rigid body rotation of the element. This linearization is therefore expressed as follows,

$$\delta\mathbf{v}^{\top}d\mathbf{H}\,\mathbf{S} = \delta\mathbf{v}^{\top}\frac{d\mathbf{H}}{dl}\mathbf{S}\,dl + \delta\mathbf{v}^{\top}\begin{bmatrix} d\boldsymbol{\phi}\times\mathbf{f}_A \\ d\boldsymbol{\phi}\times\mathbf{m}_A \\ d\boldsymbol{\phi}\times\mathbf{f}_B \\ d\boldsymbol{\phi}\times\mathbf{m}_B \end{bmatrix} \tag{3.41}$$

where the first term affects only the translation DOFs according to

$$\delta\mathbf{v}^{\top}\frac{d\mathbf{H}}{dl}\mathbf{S}\,dl = \left(\delta\mathbf{x}_A - \delta\mathbf{x}_B\right)\cdot\frac{1}{L}\mathbf{f}_Q\otimes\mathbf{e}_1\cdot\left(d\mathbf{x}_B - d\mathbf{x}_A\right) \qquad \mathbf{f}_Q = Q_2\mathbf{e}_2 + Q_3\mathbf{e}_3 \tag{3.42}$$

and gives therefore the following contributions to $\mathbf{K}_\sigma$,

$${}^{2}\mathbf{k}^{\sigma}_{13} = {}^{2}\mathbf{k}^{\sigma}_{31} = -{}^{2}\mathbf{k}^{\sigma}_{11} = -{}^{2}\mathbf{k}^{\sigma}_{33} = \frac{1}{L}\mathbf{f}_Q\otimes\mathbf{e}_1 \tag{3.43}$$

An expression for the incremental element rigid body rotation $d\boldsymbol{\phi}$ is derived in Eq. (A.4) in Paper III and reads as follows,

$$d\boldsymbol{\phi} = \boldsymbol{\Omega}\,d\mathbf{v} \qquad \boldsymbol{\Omega} = \begin{bmatrix} -\frac{1}{L}\mathbf{W}\left(\mathbf{e}_1\right) & \frac{1}{2}\mathbf{e}_1\otimes\mathbf{e}_1 & \frac{1}{L}\mathbf{W}\left(\mathbf{e}_1\right) & \frac{1}{2}\mathbf{e}_1\otimes\mathbf{e}_1 \end{bmatrix} \tag{3.44}$$

where $\mathbf{W}$ is the skew-symmetric tensor defined in Eq. (3.6). With aid of Eq. (3.44) and by using $\mathbf{W}(d\boldsymbol{\phi})$ for the vector cross product, the second term in Eq. (3.41) is found to give the following contribution to $\mathbf{K}_\sigma$,

$$\delta\mathbf{v}^{\top}\begin{bmatrix} \mathbf{W}(d\boldsymbol{\phi})\cdot\mathbf{f}_A \\ \mathbf{W}(d\boldsymbol{\phi})\cdot\mathbf{m}_A \\ \mathbf{W}(d\boldsymbol{\phi})\cdot\mathbf{f}_B \\ \mathbf{W}(d\boldsymbol{\phi})\cdot\mathbf{m}_B \end{bmatrix} = \delta\mathbf{v}^{\top}\,{}^{3}\mathbf{K}_\sigma\,d\mathbf{v} \qquad {}^{3}\mathbf{K}_\sigma = -\begin{bmatrix} \mathbf{W}(\mathbf{f}_A\ )\,\boldsymbol{\Omega} \\ \mathbf{W}(\mathbf{m}_A)\,\boldsymbol{\Omega} \\ \mathbf{W}(\mathbf{f}_B\ )\,\boldsymbol{\Omega} \\ \mathbf{W}(\mathbf{m}_B)\,\boldsymbol{\Omega} \end{bmatrix} \tag{3.45}$$

The initial stress stiffness contributions in Eqs. (3.40), (3.43) and (3.45) result in a non-symmetric stiffness matrix $\mathbf{K}_\sigma$. This is a consequence of including three-dimensional rigid body rotations in the virtual work, where only the total force and moment contribute to equilibrium, and thus the distribution of forces and moments on the element nodes is not taken into account. As demonstrated in Ref. [102], a systematic procedure can be applied to restore full symmetry. The procedure relies on the fact that in a rigid body motion,

$$\mathbf{k}_i^{rb} \left(d\boldsymbol{\varphi}_A - d\boldsymbol{\varphi}_B \right) = \mathbf{0} \tag{3.46}$$

because the rotation increments at the ends are equal, $d\boldsymbol{\varphi}_A = d\boldsymbol{\varphi}_B$. Therefore, the non-symmetric $\mathbf{K}_\sigma$-matrix can be made symmetric by modifying the second and the fourth column according to,

$$\mathbf{K}_\sigma^{sym} = \begin{bmatrix} \mathbf{k}_{11}^\sigma & \mathbf{k}_{12}^\sigma + \mathbf{k}_1^{rb} & \mathbf{k}_{13}^\sigma & \mathbf{k}_{14}^\sigma - \mathbf{k}_1^{rb} \\ \mathbf{k}_{21}^\sigma & \mathbf{k}_{22}^\sigma + \mathbf{k}_2^{rb} & \mathbf{k}_{23}^\sigma & \mathbf{k}_{24}^\sigma - \mathbf{k}_2^{rb} \\ \mathbf{k}_{31}^\sigma & \mathbf{k}_{32}^\sigma + \mathbf{k}_3^{rb} & \mathbf{k}_{33}^\sigma & \mathbf{k}_{34}^\sigma - \mathbf{k}_3^{rb} \\ \mathbf{k}_{41}^\sigma & \mathbf{k}_{42}^\sigma + \mathbf{k}_4^{rb} & \mathbf{k}_{43}^\sigma & \mathbf{k}_{44}^\sigma - \mathbf{k}_4^{rb} \end{bmatrix} \tag{3.47}$$

where the $\mathbf{k}_i^{rb}$-matrices are simply selected so that symmetry is achieved. This procedure is, however, not able to provide a unique stiffness matrix. In this work, the symmetrization is selected to be identical with the one presented in Ref. [102], which gives a $\mathbf{K}_\sigma^{sym}$-matrix that is consistent with the initial stress stiffness matrix found by utilizing a geometrically exact beam theory approach. When expressed in the local $\mathbf{e}_i$-basis, the symmetrized matrix entries stemming from Eqs. (3.40), (3.43) and (3.45) reads as follows,

$$\mathbf{k}_{11}^{\sigma l} = \mathbf{k}_{33}^{\sigma l} = -\mathbf{k}_{13}^{\sigma l} = -\mathbf{k}_{31}^{\sigma l} = \frac{1}{L} \begin{bmatrix} 0 & -Q_2 & -Q_3 \\ -Q_2 & N & 0 \\ -Q_3 & 0 & N \end{bmatrix} \tag{3.48}$$

$$\mathbf{k}_{12}^{\sigma l} = \mathbf{k}_{21}^{\sigma l\,\top} = -\mathbf{k}_{32}^{\sigma l} = -\mathbf{k}_{23}^{\sigma l\,\top} = \frac{1}{L} \begin{bmatrix} 0 & 0 & 0 \\ -M_{2A} & M_1 & 0 \\ -M_{3A} & 0 & M_1 \end{bmatrix} \tag{3.49}$$

$$\mathbf{k}_{14}^{\sigma l} = \mathbf{k}_{41}^{\sigma l\,\top} = -\mathbf{k}_{34}^{\sigma l} = -\mathbf{k}_{43}^{\sigma l\,\top} = \frac{1}{L} \begin{bmatrix} 0 & 0 & 0 \\ M_{2B} & -M_1 & 0 \\ M_{3B} & 0 & -M_1 \end{bmatrix} \tag{3.50}$$

$$\mathbf{k}_{24}^{\sigma l} = \mathbf{k}_{42}^{\sigma l\,\top} = \frac{1}{2} \begin{bmatrix} 0 & 0 & 0 \\ 0 & 0 & M_1 \\ 0 & -M_1 & 0 \end{bmatrix} \tag{3.51}$$

$$\mathbf{k}_{22}^{\sigma l} = \frac{1}{2} \begin{bmatrix} 0 & M_{3A} & -M_{2A} \\ M_{3A} & 0 & 0 \\ -M_{2A} & 0 & 0 \end{bmatrix} \tag{3.52}$$

$$\mathbf{k}_{44}^{\sigma l} = \frac{1}{2} \begin{bmatrix} 0 & -M_{3B} & -M_{2B} \\ -M_{3B} & 0 & 0 \\ M_{2B} & 0 & 0 \end{bmatrix} \tag{3.53}$$

Nonlinearity within the corotated element frame can be accounted for by including higher-order strain terms [103, 104] possibly accompanied with higher-order approximations of the local deformational motion [105, 106]. With regard to the present work and the derived stiffness matrix entries in Eqs. (3.48) – (3.53), the stiffness effect caused by the deformation modes for constant internal stresses is not represented. This effect can be included via the linearized internal virtual work from a geometrically exact beam model, in which the terms that are proportional to the internal stress resultants read,

$$d\left(\delta W_{\sigma}\right)=\int_{0}^{L0}\Big[d\left(\delta\epsilon_{1}\right)N+d\left(\delta\epsilon_{2}\right)Q_{2}+d\left(\delta\epsilon_{3}\right)Q_{3}+d\left(\delta\kappa_{i}\right)M_{i}\Big]\mathrm{d}s_{0} \tag{3.54}$$

where L_0 denotes the element initial length, ϵ_1 is the axial strain, κ_1 is the torsion and the bending curvatures are denoted κ_2 and κ_3. The shear strains ϵ_2 and ϵ_3 vanish for the Euler-Bernoulli beam. By means of some intricate manipulations of Eq. (3.54), see Ref. [102], the linearized internal virtual work can be restated as,

$$d\left(\delta W_{\sigma}\right)=\int_{0}^{L_0}\left[\delta\boldsymbol{\theta}_{,s_0}^{\top}\;\;\delta\boldsymbol{\theta}^{\top}\right]\begin{bmatrix}\mathbf{0} & -\frac{1}{2}\mathbf{W}\left(\mathbf{M}\right)\\ \frac{1}{2}\mathbf{W}\left(\mathbf{M}\right) & \frac{L}{L_0}\mathbf{F}\end{bmatrix}\begin{bmatrix}d\boldsymbol{\theta}_{,s_0}\\ d\boldsymbol{\theta}\end{bmatrix}\mathrm{d}s_{0} \tag{3.55}$$

where the skew-symmetric matrix $\mathbf{W}$ is defined in Eq. (3.6) and $\mathbf{M}$ denotes the internal moment vector. The axial component of $\mathbf{M}$ is set equal to the constant torque M while the bending moments vary linearly between the element nodes,

$$\mathbf{M}=M_i\mathbf{e}_i \qquad M_1=M \qquad M_k=\Big(1-\frac{s_0}{L_0}\Big)M_{kA}+\frac{s_0}{L_0}M_{kB} \qquad k=2,3 \tag{3.56}$$

and the matrix $\mathbf{F}$ contains the axial force and the shear forces,

$$\mathbf{F}=\frac{1}{2}\begin{bmatrix}0 & Q_2 & Q_3\\ Q_2 & -2N & 0\\ Q_3 & 0 & -2N\end{bmatrix} \tag{3.57}$$

For the incremental rotation field, linear interpolation is used for the torsion mode while the bending polynomials are obtained by differentiation of the conventional Hermite shape functions for the transverse displacement field,

$$\begin{gathered} d\boldsymbol{\theta}(s_0)=\begin{bmatrix}d\theta_1\\ d\theta_2\\ d\theta_3\end{bmatrix}=\begin{bmatrix}0 & \frac{s_0}{L_0}-\frac{1}{2} & 0 & 0 & 0 & 0\\ 0 & 0 & h_{\theta A} & 0 & h_{\theta B} & 0\\ 0 & 0 & 0 & h_{\theta A} & 0 & h_{\theta B}\end{bmatrix}d\mathbf{v}_d=\mathbf{N}_{d\theta}\,d\mathbf{v}_d\\ h_{\theta A}=1-4\frac{s_0}{L_o}+3\frac{s_0^2}{L_0^2} \qquad h_{\theta B}=3\frac{s_0^2}{L_0^2}-2\frac{s_0}{L_0} \end{gathered} \tag{3.58}$$

The same interpolation polynomials as above are used for the variation $\delta\boldsymbol{\theta}$. Hence, with the 12×6 matrix $\mathbf{H}$ defined in Eq. (3.34), the local initial stress stiffness matrix reads,

$${}^{4}\mathbf{K}_{\sigma}=\mathbf{H}\int_{0}^{L_0}\left[\mathbf{N}_{d\theta,s_0}^{\top}\;\;\mathbf{N}_{d\theta}{}^{\top}\right]\begin{bmatrix}\mathbf{0} & -\frac{1}{2}\mathbf{W}\left(\mathbf{M}\right)\\ \frac{1}{2}\mathbf{W}\left(\mathbf{M}\right) & \frac{L}{L_0}\mathbf{F}\end{bmatrix}\begin{bmatrix}\mathbf{N}_{d\theta,s_0}\\ \mathbf{N}_{d\theta}\end{bmatrix}\mathrm{d}_{s0}\,\mathbf{H}^{\top} \tag{3.59}$$

The ${}^4\mathbf{K}_\sigma$ matrix accounts for changes of the torsion and the bending modes at constant internal stresses and introduces non-trivial coupling terms which are important for torsional buckling phenomenons [102]. When Eq. (3.59) is appended to the ordinary initial stress stiffness matrix in Eqs. (3.48) – (3.53), the total initial stress stiffness matrix reads as follows in the local $\mathbf{e}_i$-basis,

$$\mathbf{k}_{11}^{\sigma l} = \mathbf{k}_{33}^{\sigma l} = -\mathbf{k}_{13}^{\sigma l} = -\mathbf{k}_{31}^{\sigma l} = \frac{1}{L}\begin{bmatrix} 0 & -Q_2 & -Q_3 \\ -Q_2 & \frac{6}{5}N & 0 \\ -Q_3 & 0 & \frac{6}{5}N \end{bmatrix} \tag{3.60}$$

$$\mathbf{k}_{12}^{\sigma l} = \mathbf{k}_{21}^{\sigma l\top} = -\mathbf{k}_{32}^{\sigma l} = -\mathbf{k}_{23}^{\sigma l\top} = \frac{1}{L}\begin{bmatrix} 0 & 0 & 0 \\ -M_{2A} & M_1 & \frac{L}{10}N \\ -M_{3A} & -\frac{L}{10}N & M_1 \end{bmatrix} \tag{3.61}$$

$$\mathbf{k}_{14}^{\sigma l} = \mathbf{k}_{41}^{\sigma l\top} = -\mathbf{k}_{34}^{\sigma l} = -\mathbf{k}_{43}^{\sigma l\top} = \frac{1}{L}\begin{bmatrix} 0 & 0 & 0 \\ M_{2B} & -M_1 & \frac{L}{10}N \\ M_{3B} & -\frac{L}{10}N & -M_1 \end{bmatrix} \tag{3.62}$$

$$\mathbf{k}_{24}^{\sigma l} = \mathbf{k}_{42}^{\sigma l\top} = \frac{L}{30}\begin{bmatrix} 0 & 5Q_2 & 5Q_3 \\ 5Q_2 & -N & \frac{15}{L}M_1 \\ 5Q_3 & -\frac{15}{L}M_1 & -N \end{bmatrix} \tag{3.63}$$

$$\mathbf{k}_{22}^{\sigma l} = \frac{1}{6}\begin{bmatrix} 0 & 2M_{3A} + M_{3B} & -2M_{2A} - M_{2B} \\ 2M_{3A} + M_{3B} & \frac{4L}{5}N & 0 \\ -2M_{2A} - M_{2B} & 0 & \frac{4L}{5}N \end{bmatrix} \tag{3.64}$$

$$\mathbf{k}_{44}^{\sigma l} = \frac{1}{6}\begin{bmatrix} 0 & -2M_{3B} - M_{3A} & -2M_{2B} + M_{2A} \\ -2M_{3B} - M_{3A} & \frac{4L}{5}N & 0 \\ 2M_{2B} + M_{2A} & 0 & \frac{4L}{5}N \end{bmatrix} \tag{3.65}$$

3.6 Pipe-roller contact element

3.6.1 Kinematics and contact search

The contact element consists of a rigid roller geometry and a curved circular pipe, see Fig. 3.2. The pipe geometry is associated with a single beam element and is interpolated by the conventional Hermite shape functions relative to the straight corotated reference configuration. In the $\mathbf{E}_i$-basis the pipe centerline therefore reads,

$$\begin{gathered} \mathbf{x}(\eta) = h_1\mathbf{x}_A + h_2\mathbf{x}_B + \mathbf{T}^\top\mathbf{N}_\theta(h_3)\,\boldsymbol{\theta}_A + \mathbf{T}^\top\mathbf{N}_\theta(h_4)\,\boldsymbol{\theta}_B \qquad 1 \leq \eta \leq 1 \\ h_1 = \frac{1-\eta}{2} \qquad h_2 = \frac{1+\eta}{2} \qquad h_3 = \frac{\eta^3-\eta^2-\eta+1}{8}L \\ h_4 = \frac{\eta^3+\eta^2-\eta-1}{8}L \qquad \mathbf{N}_\theta(h) = \begin{bmatrix} 0 & 0 & 0 \\ 0 & 0 & h \\ 0 & -h & 0 \end{bmatrix} \end{gathered} \tag{3.66}$$

where the rotational deformation parameters at the beam element nodes $\boldsymbol{\theta}_j$ are obtained from Eq. (3.24), and the transformation matrix $\mathbf{T}$ is defined according to Eq. (3.1) with $\bar{\mathbf{e}}_i$ replaced by the beam element corotated unit vectors $\mathbf{e}_i$. The bending modes are included such that a smooth contact geometry is achieved. This is beneficial for avoiding contact search dead zones and issues with the contact force transfer when the contact point moves to neighboring beam elements. The roller centerline is expressed in the $\mathbf{E}_i$-basis in terms of the roller node $\bar{\mathbf{x}}_C$ and the eccentricity vector $\bar{\mathbf{r}}\,(\bar{s})$, see Fig. 3.2,

$$\bar{\mathbf{x}}\,(\bar{s}) = \bar{\mathbf{x}}_C + \bar{\mathbf{r}}\,(\bar{s}) \qquad \bar{\mathbf{r}}\,(\bar{s}) = \bar{s}\,\bar{\mathbf{Q}}_C \cdot \bar{\mathbf{e}}^0 \qquad \bar{s}_1 \leq \bar{s} \leq \bar{s}_2 \tag{3.67}$$

where $\bar{\mathbf{Q}}_C$ is the roller node rotation tensor and $\bar{\mathbf{e}}^0$ is the roller unit tangent vector in the initial configuration.

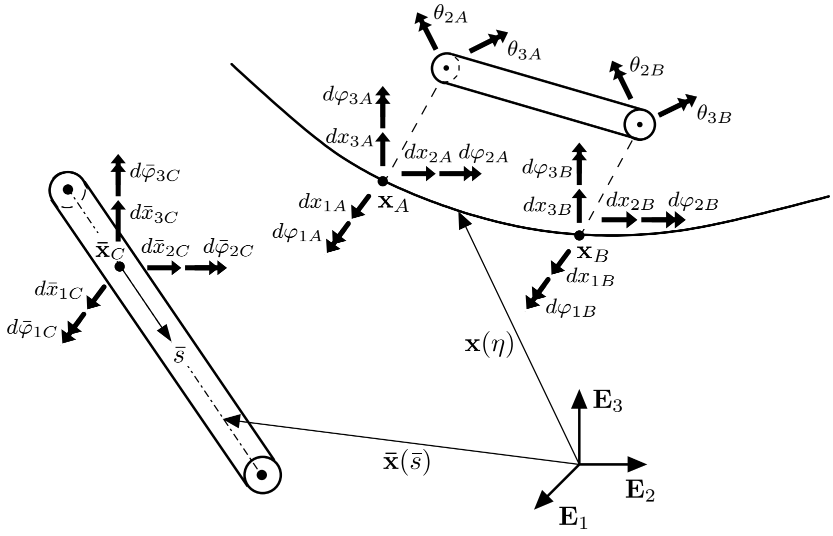

Figure 3.2: Contact kinematics

A predefined range of beam elements is checked for contact at each iteration step. The first step in the contact detection algorithm is to compute the minimum distance points of the pipe and the roller. Because both geometries are circular, the points are computed based on minimization of the centerline coordinates $\mathbf{x}\big(\eta\big)$ and $\bar{\mathbf{x}}\big(\bar{s}\big)$,

$$d = \min\,||\mathbf{x}\,(\eta) - \bar{\mathbf{x}}\,(\bar{s})|| \tag{3.68}$$

which results in the orthogonality conditions,

$$\big[\mathbf{x}(\eta) - \bar{\mathbf{x}}(\bar{s})\big] \cdot \mathbf{x}_{,\eta}\big(\eta\big) = 0 \tag{3.69}$$

$$\big[\mathbf{x}(\eta) - \bar{\mathbf{x}}(\bar{s})\big] \cdot \bar{\mathbf{x}}_{,\bar{s}}\big(\bar{s}\big) = 0 \tag{3.70}$$

where the comma in subscript denotes partial derivative, e.g. $\mathbf{x}_{,\eta} = \frac{\partial \mathbf{x}}{\partial \eta}$. A local Newton scheme must be employed to solve Eqs. (3.69) and (3.70) due to the cubic shape functions used in Eq. (3.66). Details about formulation of the iterative scheme are given in Refs. [39, 44]. The centerline parameters are denoted η_c and $\bar{s}_c$ at the converged solution of the minimum distance problem, and contact is defined to occur if the following inequalities are fulfilled,

$$g_n = ||\mathbf{x}(\eta_c) - \bar{\mathbf{x}}(\bar{s}_c)|| - R - \bar{R} \leq 0 \qquad -1 \leq \eta_c \leq 1 \qquad \bar{s}_1 \leq \bar{s}_c \leq \bar{s}_2 \quad (3.71)$$

where g_n is the normal gap, the pipe radius is denoted R and $\bar{R}$ is the roller radius.

3.6.2 Element load vector and tangent stiffness matrix

The interaction is assumed to be frictionless since the product in reeling operations is transported on rollers with negligible rotational resistance. The penalty method is employed to enforce the impenetrability constraint, $g_n \geq 0$, and the virtual work contribution from a single contact point therefore reads,

$$\delta W_c = F_n(g_n)\, \delta g_n \qquad F_n(g_n) \leq 0 \quad (3.72)$$

where $F_n(g_n)$ is assigned a hyper-elastic relation based on piecewise linear interpolation. By taking the variation of Eq. (3.71) and utilizing the orthogonality conditions in Eqs. (3.69) and (3.70), the normal gap variation can be expressed as,

$$\delta g_n = [\, \delta\mathbf{u}(\eta_c) - \delta\bar{\mathbf{u}}(\bar{s}_c)\,] \cdot \bar{\mathbf{n}} \quad (3.73)$$

where $\delta\mathbf{u}$ and $\delta\bar{\mathbf{u}}$ refer to the variations of the pipe and the roller translations at the contact point, respectively. The roller outward unit normal vector $\bar{\mathbf{n}}$ at the contact point is defined as follows,

$$\bar{\mathbf{n}} = \frac{\mathbf{x}(\eta_c) - \bar{\mathbf{x}}(\bar{s}_c)}{||\mathbf{x}(\eta_c) - \bar{\mathbf{x}}(\bar{s}_c)||} \quad (3.74)$$

The bending curvature and the bending moment must be continuous across element boundaries in the Lagrangian-Eulerian formulation. This implies that contact loads for the pipe rotational DOFs cannot be included. The variation of the relative displacement at the contact point is therefore discretized in terms of the pipe translation DOFs and the six roller DOFs according to, see Fig. 3.2,

$$\delta\mathbf{u} - \delta\bar{\mathbf{u}} = \mathbf{N}_\delta\, \delta\mathbf{v} \quad (3.75)$$

$$\mathbf{N}_\delta = \begin{bmatrix} h_1(\eta_c)\mathbf{I} & h_2(\eta_c)\mathbf{I} & -\mathbf{I} & \mathbf{W}(\bar{\mathbf{r}}(\bar{s}_c)) \end{bmatrix} \quad (3.76)$$

$$\delta\mathbf{v} = \begin{bmatrix} \delta\mathbf{p} & \delta\bar{\mathbf{p}} \end{bmatrix}^\top \quad \begin{aligned} \delta\mathbf{p} &= \begin{bmatrix} \delta x_{1A} & \delta x_{2A} & \delta x_{3A} & \delta x_{1B} & \delta x_{2B} & \delta x_{3B} \end{bmatrix} \\ \delta\bar{\mathbf{p}} &= \begin{bmatrix} \delta\bar{x}_{1C} & \delta\bar{x}_{2C} & \delta\bar{x}_{3C} & \delta\bar{\varphi}_{1C} & \delta\bar{\varphi}_{2C} & \delta\bar{\varphi}_{3C} \end{bmatrix} \end{aligned} \quad (3.77)$$

where the h_i-functions are given in Eq. (3.66) and $\mathbf{W}$ is the skew-symmetric matrix defined in Eq. (3.6). In the $\mathbf{E}_i$-basis the 12×1 element load vector $\mathbf{P}$ therefore reads,

$$\delta W_c = \delta\mathbf{v}^\top \mathbf{P} \qquad \mathbf{P} = \mathbf{N}_\delta^\top \bar{\mathbf{n}}\, F_n(g_n) \quad (3.78)$$

In Paper I, the initial stress stiffness terms that results from $d(\delta g_n)$ was found to give no significant benefits for the convergence properties. The linearization of Eq. (3.72) is therefore established by regarding δg_n as constant in terms of the displacement state,

$$d\left(\delta W_c\right) = \delta g_n \frac{dF_n}{g_n} dg_n \tag{3.79}$$

where dg_n has the same structure as δg_n in Eq. (3.73),

$$dg_n = \left[\, d\mathbf{u}(\eta_c) - d\bar{\mathbf{u}}(\bar{s}_c) \,\right] \cdot \bar{\mathbf{n}} \tag{3.80}$$

The pipe rotational DOFs must be included in the incremental displacement field because the pipe geometry is interpolated in terms of the bending modes in Eq. (3.66). The relative incremental displacement at the contact point is therefore discretized as, see Fig. 3.2,

$$d\mathbf{u} - d\bar{\mathbf{u}} = \mathbf{N}_d \, d\mathbf{v} \tag{3.81}$$

$$d\mathbf{v} = \begin{bmatrix} d\mathbf{p}_A & d\mathbf{p}_B & d\bar{\mathbf{p}} \end{bmatrix}^\top \qquad \begin{aligned} d\mathbf{p}_j &= \begin{bmatrix} dx_{1j} & dx_{2j} & dx_{3j} & d\varphi_{1j} & d\varphi_{2j} & d\varphi_{3j} \end{bmatrix} \\ d\bar{\mathbf{p}} &= \begin{bmatrix} d\bar{x}_{1C} & d\bar{x}_{2C} & d\bar{x}_{3C} & d\bar{\varphi}_{1C} & d\bar{\varphi}_{2C} & d\bar{\varphi}_{3C} \end{bmatrix} \end{aligned} \tag{3.82}$$

$$\mathbf{N}_d = \left[\; \mathbf{T}^\top \mathbf{N} \hat{\mathbf{T}} \quad -\mathbf{I} \quad \mathbf{W}(\bar{\mathbf{r}}\,(\bar{s}_c)) \;\right] \tag{3.83}$$

where $\mathbf{N}_d$ has dimension 3×18, $\mathbf{T}$ is the transformation matrix for the beam element and $\mathbf{W}$ is the skew-symmetric matrix defined in Eq. (3.6). An isoparametric approach is taken and the 3×12 interpolation matrix $\mathbf{N}$ contains therefore the same shape functions as in Eq. (3.66),

$$\mathbf{N} = \left[\; h_1(\eta_c)\mathbf{I} \quad \mathbf{N}_\theta(h_3(\eta_c)) \quad h_2(\eta_c)\mathbf{I} \quad \mathbf{N}_\theta(h_4(\eta_c)) \;\right] \tag{3.84}$$

The 12×12 transformation matrix $\hat{\mathbf{T}}$ in Eq. (3.83) contains the beam element transformation matrix $\mathbf{T}$ on the diagonal and an off-diagonal matrix $\mathbf{Z}$ that accounts for the change of the bending deformation DOFs due to beam node translations, cf. Eq. (3.35),

$$\hat{\mathbf{T}} = \begin{bmatrix} \mathbf{T} & \mathbf{0} & \mathbf{0} & \mathbf{0} \\ \mathbf{Z} & \mathbf{T} & -\mathbf{Z} & \mathbf{0} \\ \mathbf{0} & \mathbf{0} & \mathbf{T} & \mathbf{0} \\ \mathbf{Z} & \mathbf{0} & -\mathbf{Z} & \mathbf{T} \end{bmatrix} \qquad \mathbf{Z}^\top = \frac{1}{L} \left[\, \mathbf{0}_{3\times 1} \quad -\mathbf{e}_3 \quad \mathbf{e}_2 \,\right] \tag{3.85}$$

With this, the 12×18 element tangent stiffness matrix $\mathbf{K}$ is expressed as follows in the $\mathbf{E}_i$-basis,

$$d\left(\delta W_c\right) = \delta\mathbf{v}\, \mathbf{K}\, d\mathbf{v} \qquad \mathbf{K} = \mathbf{N}_\delta^\top \bar{\mathbf{n}}\, \bar{\mathbf{n}}^\top \mathbf{N}_d \tag{3.86}$$

The non-quadratic form of $\mathbf{K}$ makes the system tangent matrix non-symmetric. This is a consequence of not including the pipe rotational DOFs and the $\mathbf{Z}$-matrix in the selected normal gap variation δg_n. This has, however, no practical consequence as the Lagrangian-Eulerian formulation also introduces non-symmetric tangent stiffness matrices.

3.7 Hyper-elastic beam-spring element

At start-up of the Lagrangian-Eulerian analysis strategy, the initial mesh domain is computed by a spline interpolator and thereafter released and subjected to Newton-Raphson iterations until equilibrium is achieved. Transverse springs are needed during this analysis phase to ensure convergence. The spring element may also be used for modeling of load-displacement boundary conditions at the mesh termination points.

The spring element consists of six DOFs associated with a single beam element node. The increment of the spring translation components is computed by projecting the nodal translation increment into the corotated $\mathbf{e}_i$-basis of the beam element,

$$s_i = s_i^p + \mathbf{e}_i \cdot \left(\mathbf{x}_j - \mathbf{x}_j^p\right) \qquad i = 1,2,3 \qquad j = A \vee B \tag{3.87}$$

where superscript p refers to the previous equilibrium state and subscript j denotes the beam element node, either A or B. The load step rotation increment of the nodal $\bar{\mathbf{e}}_j$-triad is measured by the following rotation tensor,

$$\mathbf{Q}_j^{\Delta}\left(q_{4j}^{\Delta}, \mathbf{q}_j^{\Delta}\right) = \bar{\mathbf{e}}_k \otimes \bar{\mathbf{e}}_k^p = \mathbf{Q}_j \cdot \mathbf{Q}_j^{p\top} \qquad j = A \vee B \qquad \mathbf{Q}_j^p = \bar{\mathbf{e}}_k^p \otimes \mathbf{E}_k \tag{3.88}$$

The rotation increment $\Delta\boldsymbol{\omega}$ is extracted from $\mathbf{Q}^{\Delta}$ with aid of Spurier's algorithm and Eq. (3.4). Thereafter, the increment is projected into the corotated $\mathbf{e}_i$-basis of the beam element and added to the accumulated rotation from the previous equilibrium state,

$$\omega_i = \omega_i^p + \mathbf{e}_i \cdot \Delta\boldsymbol{\omega} \qquad \Delta\boldsymbol{\omega} = 2\cos^{-1}\!\left(q_{4j}^{\Delta}\right)\frac{\mathbf{q}_j^{\Delta}}{||\mathbf{q}_j^{\Delta}||} \quad i = 1,2,3 \quad j = A \vee B \tag{3.89}$$

where a truncated version of $\Delta\boldsymbol{\omega}$ similar to Eq. (3.25) is used for $\mathbf{q}^{\Delta} << 1$.

The 6×1 load vector $\mathbf{P}$ for the spring element is defined in terms of the virtual work at the beam element node and reads as follows in the $\mathbf{E}_i$-basis,

$$\delta W_k = \delta\mathbf{v}^\top\mathbf{P} \qquad \delta\mathbf{v} = \begin{bmatrix}\delta x_{1j} & \delta x_{2j} & dx_{3j} & \delta\varphi_{1j} & \delta\varphi_{2j} & \delta\varphi_{3j}\end{bmatrix} \quad j = A \vee B \tag{3.90}$$

$$\begin{aligned} &\mathbf{P} = \tilde{\mathbf{T}}^\top\mathbf{F} \qquad \tilde{\mathbf{T}} = \begin{bmatrix}\mathbf{T} & \mathbf{0}\\ \mathbf{0} & \mathbf{T}\end{bmatrix} \\ &\mathbf{F} = \begin{bmatrix}F_1(s_1) & F_2(s_2) & F_3(s_3) & M_1(\omega_1) & M_2(\omega_2) & M_3(\omega_3)\end{bmatrix}^\top \end{aligned} \tag{3.91}$$

where the transformation matrix $\mathbf{T}$ is defined according to Eq. (3.1) with $\bar{\mathbf{e}}_i$ replaced by the beam element corotated unit vectors $\mathbf{e}_i$. The load components F_i and M_i are assigned hyper-elastic relations based on piecewise linear interpolation. The following approximation is used for the element tangent stiffness matrix,

$$\begin{aligned} &d\left(\delta W_k\right) = \delta\mathbf{v}\,\mathbf{K}\,d\mathbf{v} \qquad \mathbf{K} = \bar{\mathbf{T}}^\top\mathbf{K}^l\bar{\mathbf{T}} \\ &\mathbf{K}^l = \begin{bmatrix} k_{F1} & 0 & 0 & 0 & 0 & 0\\ 0 & k_{F2} & 0 & 0 & 0 & 0\\ 0 & 0 & k_{F3} & 0 & 0 & 0\\ 0 & 0 & 0 & k_{M1} & 0 & 0\\ 0 & 0 & 0 & 0 & k_{M2} & 0\\ 0 & 0 & 0 & 0 & 0 & k_{M3} \end{bmatrix} \qquad \begin{aligned} k_{Fi} &= \left.\tfrac{dF_i}{ds_i}\right|_{s_i} \\ k_{Mi} &= \left.\tfrac{dM_i}{d\omega_i}\right|_{\omega_i} \end{aligned} \end{aligned} \tag{3.92}$$

3.8 Additional features

The GLview Inova program [107] was used for visualization of the pipe geometry and the contact rollers. In brief, this program offers basic geometric shapes which requires only the current displacement state transferred as ASCII encoded data at selected load steps. Both the pipe and the roller surfaces were modeled as a grid of rectangular plane elements.

For the numerical studies in Paper IV, convergence failure occurred for cases where one mesh endpoint was axially fixed and the other endpoint had a prescribed axial force. An axial force control was therefore implemented where the endpoint with prescribed force was held fixed and given appropriate displacement increments to retain the axial force within a predefined interval. Several restarts throughout the analysis run would be necessary without this feature.

Restart facilities are regarded as mandatory in any nonlinear FE code. The program therefore stores element histories, result data, the displacement state and visualization data at predefined load steps. A module for reading input text files was made based on built-in MATLAB functions. Displacement boundary conditions can be imposed in the global, the nodal or the beam element coordinate systems. For efficiency purposes, the element load vectors and tangent stiffness matrices with associated transformations were expanded symbolically by means of the Maple software [108], where the entries were optimized and converted to MATLAB language with the code generator module.

3.9 Verification study and influence of tangent stiffness

To verify the implementation the 45° cantilever bend in Fig. 3.3 was considered. This example was first studied in work by Bathe and Bolourchi [109] with an updated Lagrangian beam formulation. Later, Simo and Vu-Quoc [97] and Cardona and Geradin [110] simulated the response with their geometrically exact beam models. Crisfield [111] also studied the example with his corotational beam formulation.

The bend had a radius of 100 m and was located in the xz-plane in the unloaded configuration. Eight elements with bending stiffness $K_E = 833.33$ kNm^2, torsion stiffness $GJ = 705$ kNm^2 and axial stiffness $EA = 1$ GN were employed. The load convergence

Table 3.1: $\{x, y, z\}$ coordinates of tip vs. load level

	F_y [N]		
Beam model	300	450	600
Present	58.56, 40.47, 22.18	51.99, 48.72, 18.45	46.91, 53.64, 15.65
Crisfield [111]	58.53, 40.53, 22.16	51.93, 48.79, 18.43	46.84, 53.71, 15.61
Cardona and Geradin [110]	58.64, 40.35, 22.14	52.11, 48.59, 18.38	47.04, 53.50, 15.55
Simo and Vu-Quoc [97]	58.84, 40.08, 22.33	52.32, 48.39, 18.62	47.23, 53.37, 15.79
Bathe and Bolourchi [109]	59.2, 39.5, 22.5	–	47.2, 53.4, 15.9

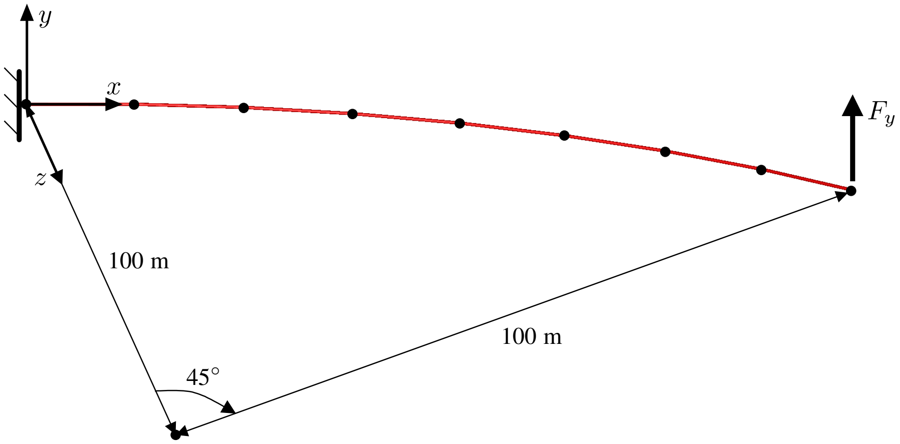

Figure 3.3: Initial configuration of 45° cantilever bend

tolerance ϵ_f in Eq. (3.11) was set to 10^{-9}. The conservative tip point load F_y was applied in a sequence of three load increments with magnitudes 300 N, 150 N and 150 N. This gives a genuinely three-dimensional response which mobilizes axial force, bending moment and torque. According to Table 3.1, the present implementation predicts a tip displacement that is well within the range of the previous studies. As expected, the corotational formulation of Crisfield which employs an identical Euler-Bernoulli beam element predicts almost identical tip displacements.

The derivation of the initial stress stiffness matrix in Section 3.5.3 opens for three different representations. Therefore, the convergence behavior of the following $\mathbf{K}_\sigma$-matrices was studied,

Case 1	The symmetric version presented in Eqs. (3.48) – (3.53).
Case 2	Similar to case 1, but includes also the local initial stress stiffness contribution as given in Eqs. (3.60) – (3.65).
Case 3	The non-symmetric version that results from Eqs. (3.40), (3.43) and (3.45).

The load convergence norm defined in Eq. (3.11) was set to 10^{-7} and 10^{-9}, where the former tolerance was found to represent the lower bound with regard to displacement accuracy. The following conservative sinusoidal load was applied at the tip,

$$F_y = F_a \sin\left(\frac{2\pi}{T}t\right) \qquad T = 3.0\text{ s} \qquad F_a = 1\,000\text{ N} \tag{3.93}$$

As seen in Fig. 3.4, a reasonable number of equilibrium iterations is achieved for cases 1 and 3 when the time step size is 0.1 s. Interestingly, the local geometric stiffness matrix included for case 2 yields more iteration cycles. This trend is present also when the iteration tolerance is increased to 10^{-9}, see Fig. 3.5. In Table 3.2, the accumulated number of iterations up to 3.0 s simulation time is presented, where X marks that convergence was not achieved within 500 iterations for a single load step. The limiting step size for case 2 is seen to be 0.15 s, while the first convergence failure for cases 1 and 3 occur for a step size of 0.35 s. None of the cases were able to achieve reliable convergence for time steps greater than 0.55 s. Observe that the non-symmetric matrix for case 3 gives slightly more iterations than the symmetric version used for case 1.

Although it is hardly scientific to make conclusions from one single example, the present study demonstrates that the non-symmetric $\mathbf{K}_\sigma$-matrix and the associated symmetrized version have fairly good convergence properties. The local initial stress stiffness matrix is in contrast not beneficial for the efficiency, however, non-trivial coupling terms which are important for instability phenomenons like torsional buckling are introduced via this matrix. The numerical studies in Paper III and IV were conducted with the local initial stress stiffness matrix included.

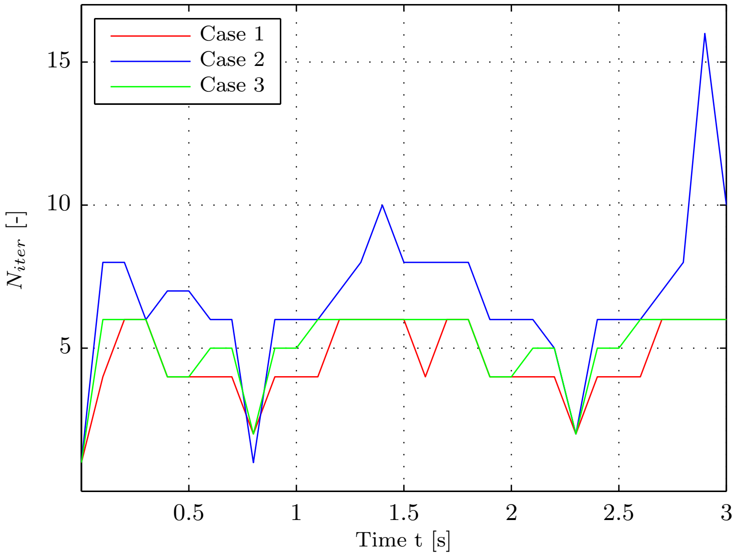

Figure 3.4: Number of iterations, $\epsilon_f = 10^{-7}$, $\Delta t = 0.1$ s

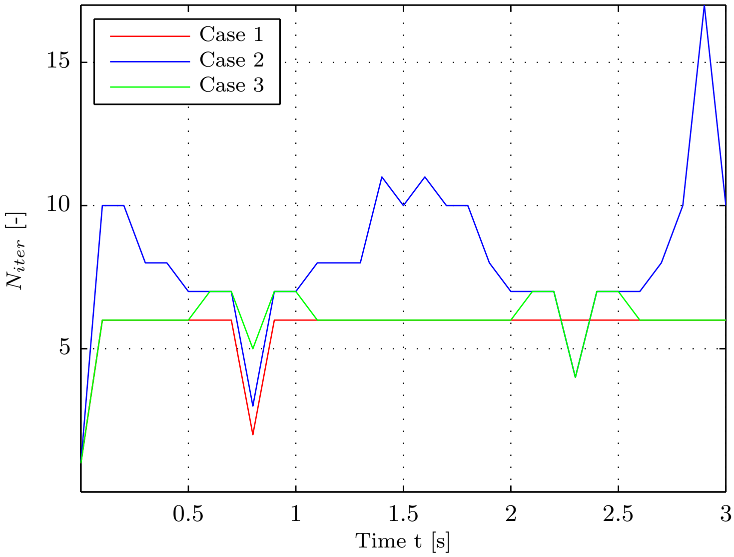

Figure 3.5: Number of iterations, $\epsilon_f = 10^{-9}$, $\Delta t = 0.1$ s

Table 3.2: Accumulated number of iterations vs. time step size Δt, $\epsilon_f = 10^{-9}$

Δt [s]	0.01	0.10	0.15	0.20	0.25	0.30	0.35	0.40	0.45	0.50	0.55
Case 1	1650	176	128	102	84	65	X	52	46	46	X
Case 2	1828	257	X	175	X	X	X	X	X	X	X
Case 3	1806	185	134	107	92	75	X	62	49	52	49

Chapter 4

Extended summary of papers

Full-length versions of the papers are appended to the main part of the thesis. The two first papers focus on the computational strategy for the trawl-pipe interaction problem, while the two last ones are concerned with the Lagrangian-Eulerian analysis strategy for reeling operations. For both topics, the first paper deals with theoretical aspects and basic performances of the developed FE formulation, while the second paper completes the developments and emphasizes application on physical problems. The novelty of the research in relation to previous work is described in a separate paragraph for each paper.

Paper I: A penalty-based contact element for pipe and 3D rigid body interaction

This paper presents a contact element tailor-made for trawl-pipeline interference simulations. The developed element is intended for prediction of the global pipe response such that several simplifying assumptions beneficial for both numerical efficiency and robustness could be utilized.

In previous beam contact publications, much effort is devoted to derivation of stiffness matrices proportional to the contact forces, but without studying the resulting convergence behavior [39, 44]. The benefit of including such matrices is therefore investigated in the present paper. The friction kinematics has previously been based on parametrizations of the beam centerline, see Ref. [43, 45]. In this work, a tangential gap measure which accounts for centerline-surface eccentricities is employed instead. Furthermore, a continuous rigid body contact geometry representation suitable for trawl gear is proposed and a small comparison study against existing model test measurements is conducted.

A rigid body model was used for the trawl gear and the pipe was represented by a corotational Euler-Bernoulli beam model. Due to the rigid body assumption, only six DOFs were needed for the trawl gear and a continuous contact geometry description was achieved by means of spherical and circular cylinder surfaces. The modeling of the contact geometry is illustrated in Fig. 4.1 where the body is represented by a three-dimensional mesh of triangular elements. The surfaces in green color are included in the contact geometry while the plane surfaces are excluded. This is regarded acceptable because the pipe is in practice approximately straight within the extent of a single triangular element. With regard to numerical robustness, the selected contact geometry description is able to provide smooth contact loads and has no issues related to dead zones in the contact search. Two-parameter surface parametrizations with computationally expensive contact searches were avoided. Instead, bounding planes as indicated in Fig. 4.1 were introduced and the body kinematic relations were expressed in terms of a single parameter. This made it possible to formulate an efficient line-line and line-point contact search strategy.

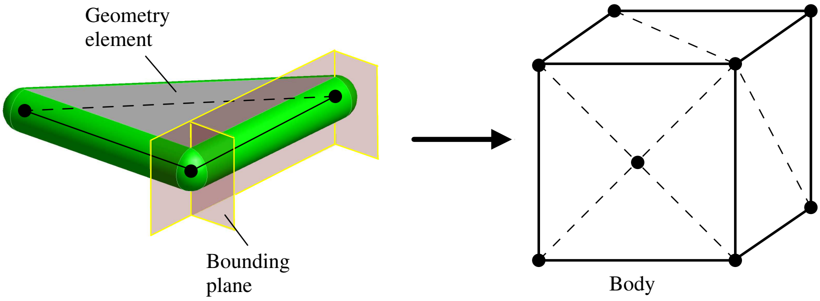

Figure 4.1: Modeling of the body contact geometry

The penalty method was selected to enforce the impenetrability constraints because it enables for representation of the pipe radial stiffness. A piecewise linear hyper-elastic relation between the normal contact force and the penetration was presumed in the implementation.

The friction kinematics was based on an alternative tangential gap measure compared to previous work on beam contact. Rather than studying the contact point displacement separately on the body and the pipe, the relative displacement on both surfaces were considered simultaneously. Surface eccentricities were taken into account such that the associated moments and cases with rolling interaction behavior could be captured. The applied Coulomb friction model was formulated in compliance with the framework of computational elasto-plasticity, in which a penalty regularization with constant stiffness was used for stick and an implicit update scheme was established for the slip case.

Terms proportional to the normal contact force were accounted for when the tangent stiffness matrices were derived. The change of the base vectors used to express the kinematic relations was neglected in order to obtain symmetric stiffness matrices. Likewise, terms proportional to the friction force and changes of the contact tangent plane base vectors were neglected. However, a non-symmetric slip tangent matrix related to coupling with the normal gap was included and artificially symmetrized. The contact virtual work contribution and the associated tangent stiffness matrices were presented on vector-matrix format suitable for computer implementation.

The ability to predict interaction responses was examined by comparison against existing trawl board and pipeline pull-over model tests. A FE model was established of a

2 600 kg polyvalent trawl board and a horizontally flexible pipe section with span height set to 1 m and 3 m. Consistent time histories were demonstrated for the horizontal pipe reaction force, the towing line tension and the pipe horizontal velocity. The interaction behavior of the trawl board itself was not studied. After publication, when access to video recordings of the tests was provided, it was realized that the characteristic board-pipe locking experienced for 3 m span height was not captured as the board rotated approximately 90° about the pipe axis prior to release, see Fig. 19 in Paper I. Consistent behavior with negligible rotation was however achieved in Paper II with improved models for the board hydrodynamic loads and the trawl gear wire configuration. This underlines the complexity of the interaction and the need to validate also the trawl board motion.

The numerical performance was examined in 84 simulation runs for various combinations of the penalty stiffness and the board-pipe friction coefficient. No significant improvement of the convergence properties was achieved by including tangent stiffness matrices that were proportional to the normal contact force. Similarly, the convergence properties did not improve when an artificially symmetrized slip tangent matrix associated with normal gap coupling was included. Regarding the overall efficiency, the ratio of simulation time to CPU time was 1:40 on a 2.66 GHz processor and the convergence rate was characterized by 2-3 Newton iterations per load step.

Paper II: Dynamic simulation of subsea pipeline and trawl board pull-over interaction

In this paper the trawl board hydrodynamic load description is addressed, which combined with the contact element developed in Paper I, completes the computational strategy for prediction of trawl board pull-over loads on subsea pipelines.

In previous work, FE models of clump weights have been validated against a limited number of model test runs and employed for comparison against design loads [10, 11]. The complex interaction behavior present for trawl boards has also been investigated, however, no validation studies were conducted and contact-related convergence problems were reported [14, 15]. In the present work, an extensive simulation work is carried out to validate the proposed computational strategy, and thereafter sensitive model parameters are identified and their influence on the pull-over loading are quantified. Thus, the novelty of the work consists of the numerical studies, the proposed trawl board load model and the application of the contact element developed in Paper I.

A six DOF rigid body model with precomputed coefficients was applied for the trawl board. To account for seabed proximity effects, the hydrodynamic mass was expressed as a function of the seabed gap and the board-seabed inclination angle. The Coriolis-centripetal loads were included for both the structural and the hydrodynamic mass. Rather than resorting to model testing, the fluid loads due to linear velocities were approximated by a simple drag force model without any contributions from transient and lift-induced effects. Possible eccentricity moments from the drag force were also neglected. This approach is regarded acceptable provided that the hydrodynamic angles of attack stay within the stall regime during the interference. Furthermore, the velocity-dependent loads are of less importance since the equilibrium balance is dominated by contact loads and inertia loads during the initial interaction phase. A pressure-induced rotational damping model based on integration of the drag forces normal to the board surface was proposed and tuned against the model test interaction behavior. Possible hydrodynamic interaction with the pipeline was neglected.

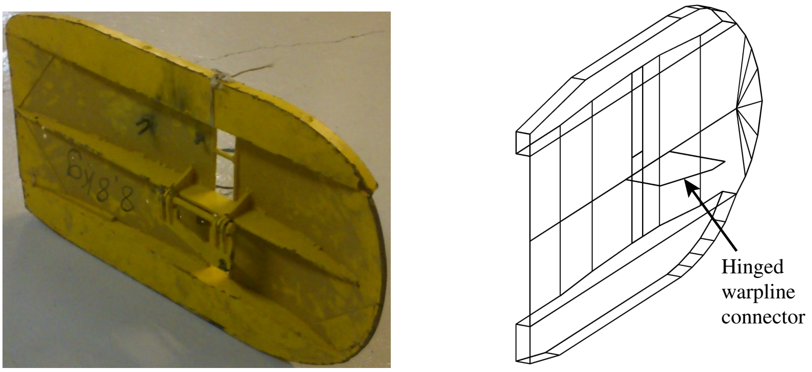

(a) Model test

(b) Contact geometry in FE model

Figure 4.2: 1900 kg polyvalent trawl board

A validation study involving 34 model test runs was carried out with variation of the pipe lateral support conditions, the span height, the towing velocity and the towing line stiffness. The FE model established in Paper I was modified such that the tension in the sweepline between the board and the trawl net could be adjusted toward the model test value. A 2 600 kg V-board and a 1 900 kg polyvalent board were included in addition to the 2 600 kg polyvalent board from Paper I. The approximation of the contact geometry for the smallest trawl board is illustrated in Fig. 4.2. The pull-over load histories were found to agree well with the model tests in terms of duration, maximum values and the build-up phase, see Fig. 4.3. This good accordance was confirmed by the simulated pull-over load impulse which in average deviated less than 10% from the reported model test impulses. Furthermore, the trawl board interaction behavior was seen to be consistent with video recordings of the laboratory test. In particular, the characteristic board-pipe locking phenomenon experienced for the two polyvalent boards and the rather smooth passings of the V-board were well captured. The proposed hydrodynamic load model and the employed body-pipe contact element were therefore concluded to be capable of describing the relevant effects of the pull-over process.

The pressure-induced rotational damping model for the trawl board was seen to be important for the interaction behavior. Use of small damping levels resulted in too large angular velocities and Coriolis-centripetal loads, which was demonstrated to give non-conservative pull-over loads. Furthermore, the Coriolis-centripetal loads were found to be important since the trawl board motion deviated from the model test behavior without these loads.

A sensitivity study involving nearly 250 simulation runs was conducted based on the

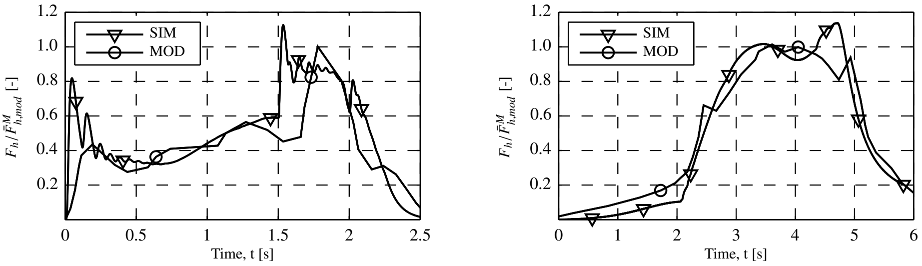

(a) 1900 kg P-board, 1 m span height, fixed pipe

(b) 2600 kg V-board, 3 m span height, flexible pipe

Figure 4.3: Horizontal pipe reaction force

validated FE model. The board-pipe friction coefficient was seen to affect the interaction behavior for low span heights, in which reduced coefficient values lead to significantly smaller load levels and durations. For span heights above 2 m, less sliding motions were present and the friction coefficient had consequently less influence. When the sweepline tension was adjusted toward zero, the pull-over load impulses reduced by $10-20\%$ and 40% for fixed and flexible pipe support conditions, respectively. This behavior must be understood by the restraining effect the sweepline tension has on the trawl board motion, which was most pronounced for flexible support conditions where the relative change of tension was largest. The opposite trend appeared when the sweepline tension increased, where some of the simulation runs experienced more than 100% increase of the pull-over load impulse. The truncated towing line used in the model test was revealed to give $20-40\%$ lower pull-over impulses than the full-length towing line. This occurred because it was unable to account for the adrupt stiffness rise provided by the line drag forces when the full-length catenary tightened up and the subsequent reduction toward the static stiffness. As opposed to the basic assumption in current design practices [7], the most severe responses did not occur when the trawling direction was perpendicular to the pipeline. When the pipe was rotated 30° about the vertical axis compared to the perpendicular base case, the maximum load and the duration became roughly twice as large for span heights above 2 m. No clear statement could be provided with regard to the degree of non-conservatism present in current design codes because the trawl board hydrodynamic angles of attack were located outside of the validity range for several seconds. Nevertheless, the simulated trends were believed to be representable for the true interaction behavior.

Paper III: A Lagrangian-Eulerian formulation for reeling analysis of history-dependent multilayered beams

Reeling operations of multilayered beams with interlayer slippage are very demanding and in some cases not feasible to simulate with conventional Lagrangian formulations.

This relates to the moving mesh which provokes contact-related convergence problems, see Refs. [18–20]. In addition, long meshes are often involved and the elements must be small and equal-sized such that a poor numerical efficiency results. In the present work, these issues are solved by utilizing a Lagrangian-Eulerian description of motion that enables the mesh to be virtually fixed in space. The novelty of the work is considered to be fairly high as the paper represents the first contribution where the Lagrangian-Eulerian viewpoint is employed for a beam with path-dependent material behavior.

The multilayered beam was represented by a constitutive model valid for a flexible pipe cross-section, see Fig. 4.4. The history-dependent bending response due to slippage between the tensile helix layers was represented by a simple Coulomb model without hardening variables. A separate constitutive model was employed for the axial-torsional response and for determination of the interlayer pressures governing the stick-slip behavior of the tensile helix layers.

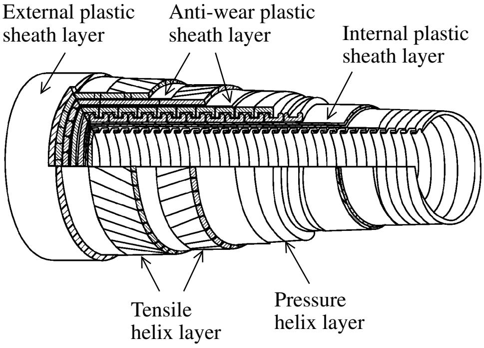

Figure 4.4: Flexible pipe cross-section

The Lagrangian-Eulerian formulation was developed by utilizing a fully coupled approach where the mesh motion, the material motion and the convective transport effects were handled simultaneously. The material motion along the centroidal line was assumed prescribed in terms of a boundary condition, while the mesh motion was computed identically as in the conventional Lagrangian approach. A quasistatic approach was utilized as reeling operations normally involve low velocities and negligible accelerations. The computational domain was represented by two-noded corotational Euler-Bernoulli beam elements.

Due to the Lagrangian-Eulerian viewpoint, convective transport terms appear in the history-dependent constitutive equations. For the bending moment and the bending curvature, the material time derivative reads as follows relative to the corotated element frames,

$$\dot{\mathbf{A}}\left(\mathcal{X},t\right)=\frac{\partial\mathbf{A}}{\partial t}+c\frac{\partial\mathbf{A}}{\partial\mathcal{X}} \tag{4.1}$$

where the first term on the right-hand side represents the change for a fixed value of the mesh arc-length parameter $\mathcal{X}$ and the second term accounts for the convective change experienced as the material travels with velocity c relative to the mesh. Numerical studies

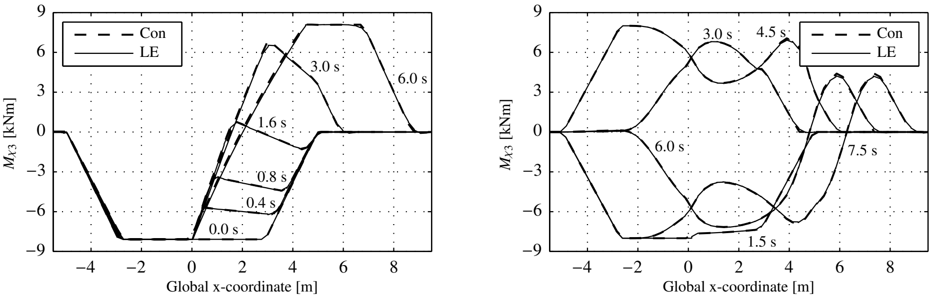

(a) 20 kN transverse load, 25 kN axial load

(b) 20 kN sinusoidal transverse load, 6 s period

Figure 4.5: Bending moment evolution, outer tensile helix layer

revealed that the approximation selected for the gradient in Eq. (4.1) strongly influenced the accuracy and the stability of the moment update algorithm, e.g. unacceptable performance resulted when the approximation was based on information from one single element. The difficulties were overcome by developing a weak form for Eq. (4.1) based on C^0-continuous shape functions between the element nodes. This enabled for communication with the neighboring elements via the boundary term by assuming continuity in the constitutive variables across the element borders. The weak form provided also an appropriate spatial weighting of the nodal values involved in the gradient approximation. To avoid spatial instabilities, a simple upwind scheme that discarded information from downstream elements was proposed.

An implicit backward Euler update scheme was formulated for the history-dependent bending response. The weak form developed for Eq. (4.1) was here utilized for both the curvature increments at the material points and the mesh-fixed bending moments needed in the beam weak formulation. A tangent stiffness that accounted for the material transport effect was derived by linearizing the moment update scheme.

Benchmark tests against the conventional Lagrangian formulation were carried out for a simply supported beam configuration with 10 m span length. Constant transverse loads and sinusoidal transverse loads giving three-dimensional responses were applied at the midspan and the axial material velocity was set to 1 m/s. Figure 4.5a displays the time evolution of the bending moment distribution for a case with 20 kN constant transverse load and 25 kN axial load. Annotation *LE* and *con* refer to the Lagrangian-Eulerian and the conventional simulation, respectively. The responses are seen to be coincident and high accuracy is achieved even at locations where the bending moment gradient undergoes large changes. Complete agreement was demonstrated also when the beam was subjected to sinusoidal loads, see Fig. 4.5b. This confirms that the developed formulation is able to handle temporal loadings and three-dimensional responses. The Lagrangian-Eulerian formulation required in general shorter elements than the conventional approach. This relates to the fact that the curvature increments are expressed in terms of the total curvature, which becomes poorly approximated when too long elements are used. The tangent stiffness associated with material transport was found to be important for the convergence properties. With this stiffness included, significantly larger time steps could be used and the number of iteration cycles reduced by almost 50% for moderate step sizes.

Paper IV: On prediction of torque in flexible pipe reeling operations using a Lagrangian-Eulerian FE framework

In this paper, the Lagrangian-Eulerian formulation from Paper III is extended into a framework for simulation of reeling operations. The key novelties of the work are the outcome of the numerical studies and the application of the Lagrangian-Eulerian formulation for a flexible load-out operation which is not feasible to simulate with existing FE software. Furthermore, simulation strategies for the analysis start-up phase and the operation start-up phase are proposed and a consistent linearization scheme for the axial-torsional constitutive model is presented.

The Lagrangian-Eulerian formulation as presented in Paper III requires use of a conventional Lagrangian simulation to establish the mesh domain. To disengage completely from the cumbersome Lagrangian analysis method, a stepwise procedure that utilizes a cubic Hermite interpolator to compute the initial mesh configuration was proposed. At analysis start-up, stabilizing springs were attached in the mesh transverse directions and the overall stiffness of the FE model was reduced. Thereafter, the interpolated mesh configuration was released and subjected to Newton-Raphson iterations until equilibrium was achieved. From the converged configuration, the internal and external loads were gradually activated and the stabilizing springs were removed. The contact constraints along the reeling route were enforced by the penalty method, which was found to be advantageous with regard to convergence during computation of the initial mesh configuration.

To enable for simulation of the operation start-up phase, where material flows through an empty mesh, moving weight factors for the constitutive stiffness and the gravity load were introduced. By means of the weight factors, the mesh was divided into regions with and without material, in which the material-filled region was gradually activated to simulate the moving material flow-front.

The Lagrangian-Eulerian framework was employed to study the torque generated during start-up in the spoolbase-vessel load-out operation seen in Fig. 4.6. The flexible pipe was modeled by corotational beam elements and assigned the same constitutive models as applied in Paper III. The main objective was to identify plausible mechanisms and to provide mitigation strategies for the torsional failures experienced by subsea contractors in recent years. Here, three different mechanisms were found to provoke torsional failure of the pipe.

The material transport effect alone exceeded a conservative estimate for the lateral buckling stress of the tensile helix tendons by more than 300% when the induced torque upstream of the turn-table acted in the stiff torsion direction. Even more severe torque responses were identified for cases with 0.1 m^{-1} residual curvature in the plastic layers and for unfavorable spool arm motions giving constrained geometric roll rotations at the turn-table inlet. The latter mechanism was regarded as the most plausible explanation for the experienced extreme torque incidents.

The identified torsional failures can be mitigated by means of operational requirements. To avoid lateral tendon buckling of the inner tensile helix layer, the pipe should be coiled onto the turn-table such that the induced torque yields torsion in the soft direction at the ship deck. Regarding unfavorable spool arm motions, the personnel must be given adequate training and a motion alarm system should be installed to keep the spool arm within the safe region. Given that the presence of a significant plastic layer residual curvature is plausible, it should be addressed in terms of storage specifications and inspection routines prior to the load-out operation.

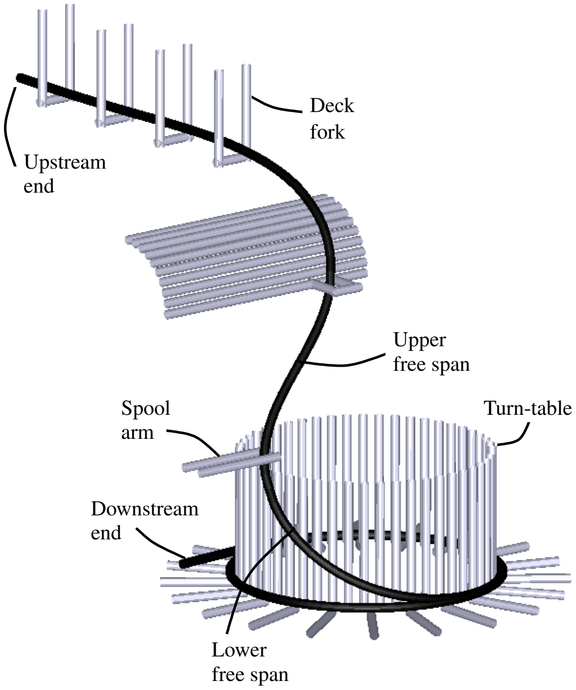

Figure 4.6: Truncated FE model of vessel turn-table and ship deck

Chapter 5

Conclusions and future work

This thesis presents original contributions with regard to development and application of FE formulations for slender marine structures subjected to contact interactions. The underlying objective has been to develop analysis methods for contact-governed problems where existing FE software suffer from lack of robustness and poor efficiency. In Section 5.1 the original contributions of the work are listed. Limitations regarding the developed models and the numerical studies are described in Section 5.2. Concluding statements, implications of the work and recommendations for future work are presented in Section 5.3 and 5.4.

5.1 Original contributions

The original contributions in this thesis can be summarized as follows,

i) The penalty-based contact element for pipe and rigid body interaction developed in Paper I. A continuous contact geometry representation was established and the formulated friction kinematics accounted for surface eccentricities with associated moments such that cases with rolling interaction behavior could be captured.

ii) A six DOF trawl board load model with precomputed hydrodynamic coefficients was established. Here, the existing hydrodynamic mass interpolation scheme in the SIMLA software [89] was re-used.

iii) Based on item i) and ii), a computational strategy for simulation of trawl board and pipeline pull-over interaction was proposed in Paper II. An extensive validation study was carried out in which the simulated response behavior was concluded to be in very good agreement with existing laboratory test results. The sensitivity of parameters important for the pull-over loading was quantified.

iv) In Paper III, a Lagrangian-Eulerian formulation for reeling analysis of history-dependent multilayered beams that enables for a virtually fixed mesh in space was developed. The proposed formulation was shown to predict responses with the same accuracy as offered by the conventional Lagrangian formulation.

v) The FE formulation in item iv) was merged into a Lagrangian-Eulerian framework for simulation of reeling operations in Paper IV. Plausible mechanisms responsible for the torsional failures experienced in spoolbase-vessel flexible pipe load-out operations were identified and strategies for avoiding the failures were proposed.

5.2 Limitations

The body-pipe contact element in Paper I was formulated by assuming a rigid trawl gear body and a corotational beam model for the pipe. Hence, information about the pipe wall denting and the trawl gear deformations cannot be obtained. However, if the contact force and the pipe radial deformation follows a hyper-elastic relation, possible influence on the global response from the initial impact can be correctly represented.

The convergence properties reported in Paper I were obtained with a symmetric equation solver. As the consistent tangent stiffness is non-symmetric, the optimal convergence rate of the Newton-Raphson method could not be utilized. Nevertheless, the presented results are valuable since most structural FE programs use symmetric solvers.

A simple drag model was used for the trawl board steady-state fluid loads in Papers I and II. Although the numerical model was shown to agree well with laboratory tests, accurate predictions of the pull-over responses cannot be guaranteed in situations where the trawl board hydrodynamic angles of attack are less than approximately 30° and for cases where the contact loads and the inertia loads do not dominate the initial equilibrium balance to the same extent.

For the specific load-out operation considered in Paper IV, the validity of the applied flexible pipe constitutive model has not been confirmed. Model deficiencies may be present in terms of end-termination effects during operation start-up, the disregarded helix longitudinal slippage interaction and the neglected additional interlayer contact pressure due to bending. The established FE model is thus applicable mainly for rough predictions, identification of extreme responses and mutual comparison of responses.

5.3 Trawl board and pipeline pull-over interaction

5.3.1 Conclusions

The proposed computational strategy was demonstrated to predict pull-over impulses within a 10% margin of the model test measurements. Furthermore, the trawl board interaction behavior was found to be consistent with video recordings from the model tests. The trawl board hydrodynamic load model and the board-pipe contact model are therefore capable of describing the relevant effects of the interaction.

The following concluding statements can be drawn based on the numerical performance tests, the validation study and the sensitivity study conducted in Papers I and II,

- The Newton convergence properties did not improve when terms proportional to the normal contact force was included in the tangent stiffness relation. Similarly, artificial symmetrization of the slip tangent matrix gave the same convergence properties as obtained when the non-symmetric tangent stiffness due to normal gap coupling was set to zero.
- Consistent pull-over loads were predicted in Paper I although the trawl board motions deviated from the model test behavior. Thus, the trawl board interaction behavior must also be examined in the validation study.
- The direct use of trawl board steady-state fluid loads in the transient interaction phase seems to be acceptable. Also, provided that the trawling direction is perpendicular to the pipeline, the choice of modeling the board as a pure drag device without eccentricity moments and lift-induced forces seems reasonable.
- Hydrodynamic board-pipe interaction can securely be neglected for pipe diameter to trawl board height ratios less than approximately 0.3.
- The hydrodynamic Coriolis-centripetal loads must be accounted for in order to achieve an interaction behavior that is consistent with model tests.
- The pressure-induced rotational damping model is important for the interaction behavior. If these damping loads are under-estimated, too large angular velocities and hydrodynamic Coriolis-centripetal loads will arise, which was demonstrated to result in non-conservative pull-over loads.
- The pull-over process was seen to be significantly influenced by the following parameters: the direction of over-trawling, the board-pipe friction coefficient, the towing line drag properties and the tension level in the wire between board and trawl net.
- A detailed contact geometry description of the interacting parts of the board is necessary, e.g. the towing line connector must be modeled accurately as it governs the board-pipe locking phenomenon that occurred for the polyvalent boards.

This work demonstrates that trawl board pull-over loads on subsea pipelines can be accurately predicted by numerical simulations. However, the simulated behavior depends strongly on some of the input parameters, such as the board-pipe friction coefficient, the pressure-induced rotational damping coefficients and the tension in the line between the board and the trawl net. A proper validation of the numerical model against experimental tests is therefore regarded as mandatory. This makes the proposed strategy too expensive for in-place design analysis of subsea pipelines. Hence, typical applications are in research-oriented work such as establishment of pull-over loads for design codes and examination of the over-trawling ability of new subsea structures.

The main benefit with combined use of model testing and numerical simulations is the possibility to remove model bias and to effectively reduce statistical uncertainty. For instance, the truncated towing line applied in the laboratory test was demonstrated to result in non-conservative loads because it failed to represent the drag-dependent stiffness of the full-length catenary configuration. This bias can readily be removed if a validated numerical model is available. Uncertainties related to lack of observations in model tests are often not feasible to reduce due to the high expenses, whereas additional test samples can easily be generated with aid of numerical simulations.

The sensitivity study revealed that the pull-over loading depends on quantities which are not explicitly accounted for in the DNV-RP-F111 code [7]. This implies that more accurate design loads can be obtained if the missing quantities are introduced as variables.

The developed contact element has been extensively used in this work. No incidents with loss of contact or convergence problems were detected. This motivates use of the contact element in other interaction problems involving rigid bodies and pipes, especially if simple hydrodynamic load models can be used, such as in simulation of clump weight over-trawling or hooking assessment of a de-stabilized trawl board towed flat on the seafloor.

5.3.2 Future work

Non-perpendicular crossings at high span heights were found to induce considerable more severe loads than perpendicular crossings. This conflicts with the basic assumption in current design practices [7], however, the degree of non-conservatism could not be quantified as the validity range for the trawl board hydrodynamic angles of attack was violated. Thus, the steady-state fluid loads at low angles of attack must be estimated in future work, considering both in-plane directions of the board.

The recommended pull-over loading used in the industry today is based on more than 20 year old model tests. A natural step in future work is therefore to examine crossings of the modern multi-foil boards considered by Teigen et al. [12]. In such a study, a further improvement of the design loads should be undertaken by including parameters such as crossing angle, board-pipe friction coefficient, span flexibility and pipe mass.

5.4 The Lagrangian-Eulerian formulation and flexible pipe load-out operations

5.4.1 Conclusions

The Lagrangian-Eulerian formulation was subjected to benchmark testing against the conventional Lagrangian method in Paper III, and thereafter employed in Paper IV to study the torque generated in a flexible pipe spoolbase load-out operation with vertical-axis vessel turn-table. The main conclusions from these studies can be summarized as follows,

- The Lagrangian-Eulerian formulation was demonstrated to provide the same accuracy as the conventional Lagrangian method for simulation cases with constant transverse loads, axial loads and temporal three-dimensional transverse loads.
- The tangent stiffness contribution from the material transport effect should be included as it significantly improves the convergence properties.

- A fully implicit integration of the convective terms is recommended in order to avoid spatial oscillations.

- The Lagrangian-Eulerian formulation requires in general smaller elements than the conventional Lagrangian method.

- Extreme torque responses giving torsional failure were identified for two different mechanisms in the considered load-out operation, namely, unfavorable operator-controlled changes of the pipe configuration and presence of plastic layer residual curvature.

- The material transport effect may alone provoke torsional failure in load-out operations and it yields also a significant contribution to the two identified extreme torque mechanisms.

- The flexible pipe constitutive model must account for interlayer pressure changes as cases with at least 50% friction moment increase relative to the initial value were observed in regions where torque was induced. Also, the upstream roll stiffness and the bi-linear torque-torsion relationship are important regarding the relative sharing of torque between the turn-table and the ship deck.

Existing FE programs suffer from poor efficiency and contact-related convergence issues in reeling simulations. The contact interactions often require use of cumbersome analysis procedures and necessitate frequent user interaction throughout the analyses. Therefore, complex reeling operations of multilayered beams, such as the one considered in Paper IV, has until now not been regarded as feasible to simulate. As demonstrated, the proposed Lagrangian-Eulerian framework is able to handle such operations without any difficulties. The present work thus contributes to a significant advance of the state of the art simulation practice for elasto-plastic beam problems involving transport of material.

The advantageous properties of the Lagrangian-Eulerian formulation are achieved solely because of the virtually fixed mesh. With regard to robustness, the contact geometry undergoes significantly less changes such that potential convergence difficulties related to the contact algorithms are mitigated. As opposed to the conventional formulation, the mesh is allowed to be non-uniform and need only to cover the region of interest, thus giving a considerable reduction of the number of DOFs. A noticeable efficiency improvement also results for the contact algorithms since the search range need only to cover a few number of beam elements. Furthermore, in situations where stationary conditions prevail, the Lagrangian-Eulerian formulation has superior efficiency as the contact loads and the beam element stress resultants hardly change.

The Lagrangian-Eulerian formulation can readily be implemented into existing FE software since it does not affect the underlying beam kinematics, the displacement update scheme or the equation solver. Only the stress-update algorithm and the associated tangent stiffness matrix for the beam model must be modified.

The developed formulation is in its current form expected to be appreciated in the field of subsea engineering, where the main applications are identification of unforeseen events prior to flexible pipe load-operations and post-analysis of failed operations. The development also opens up new possibilities for related problems involving beams and material transport. This can for instance be offshore installation of flexible pipes and cables, rigid steel pipeline laying operations or the wounding process for cross-section components in manufacturing of umbilicals and flexible pipes.

5.4.2 Future work

As mentioned in Section 5.2, the flexible pipe constitutive model applied in Paper IV has not been validated for use in load-out operations. The ability to predict the torque and possible model deficiencies should therefore be investigated in future work. A comparison study against a physical load-out operation involving validation of roll rates and torsion is recommended.

The Lagrangian-Eulerian analysis strategy represents an attractive alternative for simulation of rigid steel pipeline laying operations. Compared to the conventional approach, improved performance of the pipe-vessel contact elements is expected and the non-uniform vessel-following mesh can be terminated at the seafloor point where stationary conditions prevail. Future work should therefore aim to establish a J2-plasticity stress-update algorithm with sufficient numerical stability and similar accuracy as the conventional Lagrangian method. Dynamic analysis must further be enabled as the contributions from velocity-dependent loads and inertia loads can be significant. The convective acceleration term is not expected to introduce particular issues since the axial inertia loads are small compared to the tension.

References

[1] Turner MJ, Clough RW, Martin HC, Topp LT. Stiffness and deflection analysis of complex structures. J Aeronaut Sci 1956;25:805–23.

[2] Argyris JH, Kelsey S. Energy theorems and structural analysis. Butterworth Scientific Publications, London; 1960.

[3] Brown O. Report of the Inspector's inquiry into the loss of the fishing vessel WESTHAVEN AH 190 with four lives on 10 March 1997 in the North Sea. Marine Accident Investigation Branch of the Department of the Environment, Transport and the Regions: London; 1998.

[4] Utvikling i risikonivå - norsk sokkel, Fase 5 hovedrapport 2004 (text in Norwegian). Petroleum Safety Authority, Norway; 2004.

[5] Fyrileiv O, Spiten J. Trawl gear protection within platform safety zones. In: Proceedings of OMAE2004 23rd International Conference on Ocean, Offshore and Arctic Engineering. 2004, p. 217–23.

[6] Gómez C, Green DR. The impact of oil and gas drilling accidents on EU fisheries. European Parliament, Directorate General for Internal Policies, Policy Department B: Structural and Cohesion Policies, Fisheries; 2013.

[7] Recommended practice DNV-RP-F111, Interference between trawl gear and pipelines, October 2010. Det Norske Veritas, Høvik, Norway; 2010.

[8] Birkely S, Sandberg JH, Urke HA, Palerud R, Abelsen R, Larsen LH. Oppdatering av regional konsekvensutredning for Nordsjøen - Konsekvenser for fiskeri og oppdrettsnæringen: Aktivitet 2 og 3 - Fiskerinæringen og konsekvenser av petroleumsvirksomhet (text in Norwegian). Tech. Rep. APN-421.3484.1; Akvaplan-niva, Tromsø, Norway; 2006.

[9] Kristoffersen AS, Asklund PO, Nystrøm PR. Pipe-in-pipe global buckling and trawl design on uneven seabed. In: Proceedings of the Twenty-second (2012) International Offshore and Polar Engineering Conference. 2012, p. 166–72.

[10] Igland RT, Søreide T. Advanced pipeline trawl gear impact design. In: Proceedings of the ASME 2008 27th International Conference on Ocean, Offshore and Arctic Engineering. 2008, p. 271–7.

[11] Maalø K, Alsos HS, Sævik S. Detailed analysis of clump-weight interference with subsea pipelines. In: Proceedings of the ASME 2012 31st International Conference on Ocean, Offshore and Arctic Engineering. 2012, p. 725–32.

[12] Teigen P, Ilstad H, Levold E, Hansen K. Hydrodynamical aspects of pipeline overtrawling. In: Proceedings of the Nineteenth (2009) International Offshore and Polar Engineering Conference. 2009, p. 435–42.

[13] Reite KJ. Modeling and control of trawl systems. Ph.D. thesis; Norwegian University of Science and Technology, Trondheim, Norway; 2006.

[14] Møller MT. Simulation of interference between trawl gear and pipelines. Master's thesis; Norwegian University of Science and Technology, Trondheim, Norway; 2009.

[15] Longva V. Simulation of trawl loads on subsea pipelines. Master's thesis; Norwegian University of Science and Technology, Trondheim, Norway; 2010.

[16] Biglift shipping b.v. http://bigliftshipping.com/projects/offshore-supply-and-support/2600mt-carousel-; Accessed 20.12.14.

[17] Økland OD, Giertsen E, Sævik S, Taby J. On the use of online monitored key parameters from pipe lay operations. In: Proceedings of the ASME 2008 27th International Conference on Ocean, Offshore and Arctic Engineering. 2008, p. 301–7.

[18] Daly R, Bell M. Reeling strain analysis of a dynamic pipe in pipe riser. In: Offshore Technology Conference. 2002, 14 pages.

[19] Jukes P, Eltahler A, Sun J. The latest developments in the design and simulation of deepwater subsea oil and gas pipelines using FEA. In: Proceedings of the Third (2009) International Deep-Ocean Technology Symposium. 2009, p. 70–82.

[20] Jukes P, Wang S, Wang J. The sequential reeling and lateral buckling simulation of pipe-in-pipe flowlines using finite element analysis for deepwater applications. In: Proceedings of the Eighteenth (2008) International Offshore and Polar Engineering Conference. 2008, p. 181–8.

[21] Szczotka M. Dynamic analysis of an offshore pipe laying operation using the reel method. Acta Mech Sin 2011;27:44–55.

[22] Donea J, Ponthot JP, Rodríguez-Ferran A, Huerta A. Arbitrary Lagrangian-Eulerian Methods. In: Encyclopedia of Computational Mechanics. John Wiley & Sons Ltd. 2004.

[23] API 17B: Recommended practice for flexible pipe. American Petroleum Institute; 2012.

[24] API 17J: Specification for unbonded flexible pipe. American Petroleum Institute; 2008.

[25] API 17E: Specification for subsea umbilicals. American Petroleum Institute; 2010.

[26] Fylling I, Bech A. Effects of internal friction and torque stiffness on the global behavior of flexible risers and umbilicals. In: Proceedings of the 10th International Conference on Offshore Mechanics and Arctic Engineering. 1991, p. 489–96.

[27] Nygaard I. Trawl - Pipeline span interaction. Model tests. Final report. Tech. Rep. 511191.01-07; Norwegian Marine Technology Research Centre (MARINTEK), Trondheim, Norway; 1990.

[28] Gjørsvik O, Kjeldsen S, Lund S. Influences of bottom trawl gear on submarine pipelines. In: Seventh Annual Offshore Technology Conference. 1975, p. 337–45.

[29] Carstens T, Kjeldsen S, Gjørsvik O. The conflict between pipelines and bottom trawls - Some results from laboratory and field tests. In: Offshore North Sea Technology Conference and Exhibition. 1976, p. T–I/18: 1–28.

[30] Moshagen H, Kjeldsen S. Fishing gear loads and effects on submarine pipelines. In: Twelfth Annual Offshore Technology Conference. 1980, p. 383–92.

[31] Nygaard I. Improved design for protective subsea structures. In: Subsea ’88 International Conference. 1988.

[32] Verley RLP, Moshagen BH, Moholdt NC, Nygaard I. Trawl forces on free-spanning pipelines. Int J Offshore Polar 1992;2:24–31.

[33] Valdemarsen JW. Trawling across pipelines. Tech. Rep. 09VF01785; Directorate of Fisheries, Bergen, Norway; 1988.

[34] Valdemarsen JW. Trawling across 40" pipeline - Effects on trawl gear (text in Norwegian). In: Fisken og havet, nr. 11 - 1993. The Institute of Marine Research, Bergen, Norway; 1993.

[35] Horenberg JAG, Guijt J. An analytical and experimental analysis of trawl gear-pipeline interaction. In: Nineteenth Annual Offshore Technology Conference. 1987, p. 563–72.

[36] OTH 561 - Guidelines for trenching design of submarine pipelines. Health and Safety Executive, Norwich, United Kingdom; 1999.

[37] Abbott H, Doenhoff AEV. Theory of wing sections: Including a summary of airfoil data. McGraw-Hill Book Company, New York; 1959.

[38] Newman JN. Transient problems. In: Marine hydrodynamics. The MIT Press; 1977, p. 230–2.

[39] Wriggers P, Zavarise G. On contact between three-dimensional beams undergoing large deflections. Commun Numer Meth En 1997;13:429–38.

[40] Wriggers P. Computational contact mechanics, second edition. Springer-Verlag Berlin Heidelberg; 2006.

[41] Souza de Cursi JE. Stress unilateral analysis of mooring cables. Int J Numer Meth Eng 1992;34:279–302.

[42] Maker BN, Laursen TA. A finite element formulation for rod/continuum interactions: The one-dimensional slideline. Int J Numer Meth Eng 1994;37:1–18.

[43] Zavarise G, Wriggers P. Contact with friction between beams in 3-D space. Int J Numer Meth Eng 2000;49:977–1006.

[44] Litewka P, Wriggers P. Contact between 3D beams with rectangular cross-sections. Int J Numer Meth Eng 2002;2:2019–41.

[45] Litewka P, Wriggers P. Frictional contact between 3D beams. Comput Mech 2002;28:26–39.

[46] Litewka P. Hermite polynomial smoothing in beam-to-beam frictional contact. Comput Mech 2007;40:815–26.

[47] Konyukhov A, Schweizerhof K. Geometrically exact covariant approach for contact between curves. Comput Method Appl M 2010;199:2510–31.

[48] Courtney-Pratt JS, Eisner E. The effect of a tangential force on the contact of metallic bodies. In: Proceedings of the Royal Society of London. Series A, Mathematical and Physical Sciences; vol. 238. 1957, p. 529–50.

[49] Wriggers P, Van TV, Stein E. Finite element formulation of large deformation impact-contact problems with friction. Comput Struct 1990;37:319–31.

[50] Konyukhov A, Schweizerhof K. Computational contact mechanics - Geometrically exact theory for arbitrary shaped bodies. Springer-Verlag Berlin Heidelberg; 2013.

[51] Noh WF. A time-dependent two-space-dimensional coupled Eulerian-Lagrangian code. In: Methods in Computational Physics, Volume 3, Fundamental Methods in Hydrodynamics. Academic Press, New York; 1964, p. 117–79.

[52] Liu WK, Belytschko T, Chang H. An arbitrary Lagrangian-Eulerian finite element method for path-dependent materials. Comput Method Appl M 1986;58:227–45.

[53] Rodríguez-Ferran A, Pérez-Foguet A, Huerta A. Arbitrary Lagrangian-Eulerian (ALE) formulation for hyperelastoplasticity. Int J Numer Meth Eng 2002;53:1831–51.

[54] Bayoumi HN, Gadala MS. A complete finite element treatment for the fully coupled implicit ALE formulation. Comput Mech 2004;33:435–52.

[55] Askes H, Rodríguez-Ferran A, Huerta A. Adaptive analysis of yield line patterns in plates with the arbitrary Lagrangian-Eulerian method. Comput Struct 1999;70:257–71.

[56] Hong D, Tang J, Ren G. Dynamic modeling of mass-flowing linear medium with large amplitude displacement and rotation. J Fluid Struct 2011;27:1137–48.

[57] Hong D, Ren G. A modeling of sliding joint on one-dimensional flexible medium. Multibody Syst Dyn 2011;26:91–106.

[58] Vu-Quoc L, Li S. Dynamics of sliding geometrically-exact beams: large angle maneuver and parametric resonance. Comput Method Appl M 1995;120:65–118.

[59] Ghosh S, Kikuchi N. An arbitrary Lagrangian-Eulerian finite element method for large deformation analysis of elasto-viscoplastic solids. Comput Method Appl M 1991;86:127–88.

[60] Benson DJ. An efficient, accurate, simple ALE method for nonlinear finite element programs. Comput Method Appl M 1989;72:305–50.

[61] Rodríguez-Ferran A, Casadei F, Huerta A. ALE stress update for transient and quasistatic processes. Int J Numer Meth Eng 1998;43:241–62.

[62] Stoker HC. Developments of the arbitrary Lagrangian-Eulerian method in nonlinear solid mechanics. Applications to forming processes. Ph.D. thesis; University of Twente, Enschede, The Netherlands; 1999.

[63] Belytschko T, Liu WK, Moran B. Arbitrary Lagrangian Eulerian formulations. In: Nonlinear finite elements for continua and structures. John Wiley & Sons Ltd.; 2001, p. 393–449.

[64] Liu WK, Chang H, Chen JS, Belytschko T. Arbitrary Lagrangian-Eulerian Petrov-Galerkin finite elements for nonlinear continua. Comput Method Appl M 1988;68:259–310.

[65] Donea J. A Taylor-Galerkin method for convective transport problems. Int J Numer Meth Eng 1984;20:101–19.

[66] Donea J, Quartapelle L. An introduction to finite element methods for transient advection. Comput Method Appl M 1992;95:169–203.

[67] Huétink J, Vreede PT, van der Lugt J. Progress in mixed Eulerian-Lagrangian finite element simulation of forming processes. Int J Numer Meth Eng 1990;30:1441–57.

[68] Witz JA. A case study in the cross-section analysis of flexible risers. Mar Struct 1996;9:885–904.

[69] Féret JJ, Bournazel CL. Calculation of stresses and slip in structural layers of unbonded flexible pipes. J Offshore Mech Arct 1987;109:263–9.

[70] Féret JJ, Momplot G. CAFLEX - A program for capacity analysis of flexible pipes, Theory manual. Tech. Rep. 710668; Norwegian Marine Technology Research Centre (MARINTEK), Trondheim, Norway; 1989.

[71] Custódio AB, Vaz MA. A nonlinear formulation for the axisymmetric response of umbilical cables and flexible pipes. Appl Ocean Res 2002;24:21–9.

[72] Sævik S. Theoretical and experimental studies of stresses in flexible pipes. Comput Struct 2011;89:2273–91.

[73] Tan Z, Quiggin P, Sheldrake T. Time domain simulation of the 3D bending hysteresis behavior of an unbonded flexible riser. J Offshore Mech Arct 2009;131, 8 pages.

[74] Alfano G, Bahtui A, Bahai H. Numerical derivation of constitutive models for unbonded flexible risers. Int J Mech Sci 2009;51:295–304.

[75] Bahtui A, Alfano G, Bahai H, Hosseini-Kordkheili SA. On the multi-scale computation of un-bonded flexible risers. Eng Struct 2010;32:2287–99.

[76] Skeie G, Sødahl N, Steinkjer O. Efficient fatigue analysis of helix elements in umbilicals and flexible risers: Theory and applications. Journal of Applied Mathematics (Hindawi Publishing Corporation - open access journal) 2012;Article ID 246812, 22 pages.

[77] Vaz MA, Rizzo NAS. A finite element model for flexible pipe armor wire instability. Mar Struct 2011;24:275–91.

[78] Østergaard NH, Lyckegaard A, Andreasen JH. On modelling of lateral buckling failure in flexible pipe tensile armour layers. Mar Struct 2012;27:64–81.

[79] Sævik S, Thorsen MJ. Techniques for predicting tensile armour buckling and fatigue in deep water flexible risers. In: Proceedings of the ASME 2012 31st International Conference on Ocean, Offshore and Arctic Engineering. 2012, p. 469–82.

[80] Sævik S, Ji G. Differential equation for evaluating transverse buckling behavior of tensile armour wires. In: Proceedings of the ASME 2014 33rd International Conference on Ocean, Offshore and Arctic Engineering. 2012, 8 pages.

[81] Ramos RJ, Pesce CP. A stability analysis of risers subjected to dynamic compression coupled with twisting. J Offshore Mech Arct 2003;125:183–9.

[82] Neto AG, Martins CA. Structural stability of flexible lines in catenary configuration under torsion. Mar Struct 2013;34:16–40.

[83] Bažant ZP, Cedolin L. Spatial buckling of beams under torque and axial force. In: Stability of structures: elastic, inelastic, fracture, and damage theories. Oxford University Press, Inc.; 1991, p. 46–9.

[84] Yazdchi M, Crisfield MA. Non-linear dynamic behaviour of flexible marine pipes and risers. Int J Numer Meth Eng 2002;54:1265–308.

[85] Aguiar LL, Almeida CA, Paulino GH. A three-dimensional multilayered pipe beam element: Nonlinear analysis. Comput Struct 2014;138:142–61.

[86] Sævik S. Bflex2010 - Theory manual. Tech. Rep. 700883.00.01; Norwegian Marine Technology Research Centre (MARINTEK), Trondheim, Norway; 2010.

[87] Sævik S. Usap - Theory manual. Tech. Rep. 700254.00.01; Norwegian Marine Technology Research Centre (MARINTEK), Trondheim, Norway; 2010.

[88] Fylling I, Larsen C, Sødahl N, Ormberg H, Engseth A, Passano E, et al. Riflex theory manual. Tech. Rep. STF70 F95219; Norwegian Marine Technology Research Centre (MARINTEK), Trondheim, Norway; 1995.

[89] Sævik S. Simla - Theory manual. Tech. Rep. 700254.00.01; Norwegian Marine Technology Research Centre (MARINTEK), Trondheim, Norway; 2008.

[90] Krenk S, Vissing-Jørgensen C, Thesbjerg L. Efficient collapse analysis techniques for framed structures. Comput Struct 1999;72:481–96.

[91] Battini JM, Pacoste C. Plastic instability of beam structures using co-rotational elements. Comput Method Appl M 2002;191:5811–31.

[92] Le TN, Battini JM, Hjiaj M. Dynamics of 3D beam elements in a corotational context: A comparative study of established and new formulations. Finite Elem Anal Des 2012;61:97–111.

[93] Jensen GA, Säfström N, Nguyen TD, Fossen TI. A nonlinear PDE formulation for offshore vessel pipeline installation. Ocean Eng 2010;37:365–77.

[94] Simo JC. A finite strain beam formulation. The three-dimensional dynamic problem. Part I. Comput Method Appl M 1985;49:55–70.

[95] Reissner E. On one-dimensional finite strain beam theory: the plane problem. J Appl Math Phys 1972;23:795–804.

[96] Romero I. A comparison of finite elements for nonlinear beams: the absolute nodal coordinate and geometrically exact formulations. Multibody Syst Dyn 2008;20:51–68.

[97] Simo JC, Vu-Quoc L. A three-dimensional finite strain rod model. Part II: Computational aspects. Comput Method Appl M 1986;58:79–116.

[98] MATLAB Release 2013a, The MathWorks, Inc., Natick, Massachusetts, United States. http://mathworks.com/products/matlab/; Accessed 17.01.15.

[99] Spurier RA. Comment on "Singularity-free extraction of a quaternion from a direction-cosine matrix". J Spacecraft Rockets 1978;15:255-255.

[100] Felippa CA, Haugen B. A unified formulation of small-strain corotational finite elements: I. Theory. Comput Method Appl M 2005;194:2285–335.

[101] Mathisen KM. Large displacement analysis of flexible and rigid systems considering displacement-dependent loads and nonlinear constraints. Ph.D. thesis; The Norwegian Institute of Technology, Trondheim, Norway; 1990.

[102] Krenk S. Non-linear modeling and analysis of solids and structures. John Wiley & Sons Ltd.; 2009.

[103] Pacoste C, Eriksson A. Beam elements in instability problems. Comput Method Appl M 1997;144:163–97.

[104] Chen HH, Lin WY, Hsiao KM. Co-rotational finite element formulation for thin-walled beams with generic open section. Comput Method Appl M 2006;195:2334–70.

[105] Battini JM, Pacoste C. Co-rotational beam elements with warping effects in instability problems. Comput Method Appl M 2002;191:1755–89.

[106] Alsafadie R, Hjiaj M, Battini JM. Three-dimensional formulation of a mixed corotational thin-walled beam element incorporating shear and warping deformation. Thin Wall Struct 2011;49:523–33.

[107] Glview Inova, Ceetron AS, Trondheim, Norway. http://ceetron.com; Accessed 17.01.15.

[108] Monagan MB, Geddes KO, Heal KM, Labahn G, Vorkoetter SM, McCarron J, et al. Maple advanced programming guide. Maplesoft; 2009.

[109] Bathe KJ, Bolourchi S. Large displacement analysis of three-dimensional beam structures. Int J Numer Meth Eng 1979;14:961–86.

[110] Cardona A, Geradin M. A beam finite element non-linear theory with finite rotations. Int J Numer Meth Eng 1988;26:2403–38.

[111] Crisfield MA. A consistent co-rotational formulation for non-linear, three-dimensional, beam elements. Comput Method Appl M 1990;81:131–50.

[112] Recommended practice DNV-RP-C205, Environmental conditions and environmental loads, April 2007. Det Norske Veritas, Høvik, Norway; 2007.

[113] Reite KJ, Sørensen AJ. Mathematical modeling of the hydrodynamic forces on a trawl door. IEEE J Oceanic Eng 2006;31:432–53.

[114] Crisfield MA. Non-linear finite element analysis of solids and structures. John Wiley & Sons Ltd.; 1997.

Appended papers

Paper I

A penalty-based contact element for pipe and 3D rigid body interaction

Vegard Longva[a], Svein Sævik[a]

[a] Department of Marine Technology, Norwegian University of Science and Technology
NO-7491 Trondheim, Norway

Engineering Structures, Vol. 56, 2013, pp. 1580 – 1592

Abstract

In this paper a contact element tailor-made for global response prediction of pipelines subject to interaction with rigid 3-dimensional bodies is presented. A continuous representation of the contact geometry is applied. The contact contribution to virtual work and associated linearizations are presented on matrix format suitable for implementation into computer codes based on a corotated description of beam kinematics. Experimental tests of trawl gear and subsea pipeline interference are used to validate the performance of the element. The benefit of including a tangent stiffness matrix proportional to the normal contact force and the effect of performing artificial symmetrization of the linearized friction contribution are investigated in terms of numerical efficiency.

Keywords: Contact mechanics; Penalty method; Pipeline; Rigid body; Trawl gear

1 Introduction

Large networks of subsea pipelines for transportation of oil and gas are today in operation unprotected on the seabed. Future field developments tend to move into arctic waters especially suitable for pipeline transportation systems. Both for existing and new installations the risk of interaction with bottom-trawling fisheries cannot be disregarded. The heaviest trawl gears nowadays have a steel mass of 10 000 kg and are operated in arctic waters [1]. With a trawling velocity of $2-3$ m/s the interference loading may result in a severe utilization of the pipeline capacity. The main objective of the present effort has therefore been to develop a robust and efficient contact formulation for prediction of the pipe response. An important synergy effect arise here since collisions between bodies and other structures made of tubular elements may also be investigated.

Assessment of trawl and pipeline interference may be separated into two distinct parts [1, 2]. The first part deals with local deformations of the cross-section at the contact point, whereas the second focus on the global response of an undeformed pipe cross-section. In this paper the developed finite element (FE) formulation is restricted to capture only the latter response type. This has two important consequences for the computational efficiency,

1) Contact formulations such as the conventional node-to-surface (NTS) approach [3] used for continuum and shell elements can be avoided. Instead, a potentially much more efficient formulation based on the FE framework for beam elements can be developed.

2) The body can be assumed rigid such that its kinematical description is given by only six degrees of freedom (DOFs).

With regard to item 2) negligible conservatism is introduced for the global pipe response because the pipe flexural stiffness is small compared to the rigidity of standard trawl gears. The rigid body assumption also implies that the contact patch test can be disregarded, see e.g. [4].

3-dimensional surface representations used for contact problems have in the last decades adopted interpolation techniques from the field of computer-aided geometric design. Successful applications have been reported for meshes consisting of both triangular elements [5] and quadrilateral elements [6]. Subdivision schemes providing C^1-continuity for triangular and quadrilateral meshes have also been used [7]. With regard to application in this work it must be noted that such approaches are computationally expensive, and that a beam-to-surface contact search algorithm has to account for changes in three variables. Previously, contact detection problems for the NTS procedure with two variables have occurred when multiple candidate contact points exist or if the contact surface has been distorted [8]. In order to ensure robustness and efficiency a simpler geometry representation of the rigid body, yet providing sufficient accuracy for the global pipe response, is aimed for in this paper.

Contact problems in FE computations are usually solved by Lagrange multiplier methods [9, 10] or the penalty method [11, 12]. In this work the penalty approach was selected because it enables representation of the pipe coating stiffness via the regularized penetration constraint. An analogous representation were employed by Wriggers et al. [11] where the contact traction was expressed in terms of micro-mechanical properties of the contact interface. The applied penalty stiffness must, however, be kept within a given interval because low values can deteriorate the accuracy [13] and too large values may cause ill-conditioning of the FE equation system.

Experiments addressing friction on metallic surfaces [14] have proven that the tangential displacement during stick and slip can be decomposed into a small elastic part and a non-reversible plastic part, respectively. This advocate use of a penalty regularization for stick and a constitutive interface law for slip. With the breakthrough of return mapping algorithms in plasticity [15], consistent friction formulations for Newton-based solution schemes could be developed. Yet, the non-associative nature of the slip rules lead to non-symmetric matrices, see e.g. [11, 12, 16], which could not be consistently implemented into computer codes with symmetric solvers. This issue was remedied by Laursen and Simo [17] who used an augmented Lagrange method to obtain algorithmic symmetrization of the friction tangent matrix. Additional unknowns are, however, introduced with the Lagrange-based approach which makes implementation into existing codes more cumbersome.

In the literature only a handful of publications deals with contact involving beams. Maker and Laursen [18] presented a model for interaction between a rod and a medium modeled by continuum elements. A contact formulation for frictionless beam-to-beam contact with circular cross-sections have been given by Wriggers and Zavarise [19]. Their development were later extended in terms of a penalty-based friction formulation, but without accounting for surface eccentricity moments caused by the friction force [20]. Similarly, contacting beams with rectangular cross-sections have been addressed by Litewka and Wriggers both for frictionless behavior [21] and for a penalty-based friction formulation [22]. Much effort is put on derivation of tangent matrices proportional to the contact forces in these publications, however, the effect of discarding them was not investigated. A Hermite smoothing technique that provides contact FE equations independent of the underlying beam theory was presented by Litewka [23]. This idea was recently accomplished for arbitrary 3-dimensional curves by Konyukhov and Schweizerhof [24]. In their approach friction due to rotational interaction could be accounted for and consistent tangent matrices were derived by means of covariant derivatives.

Based on the provided background information the objectives of this paper can be summarized as follows:

- Develop a contact element within an implicit solution scheme for global response prediction of pipelines subject to interaction with a rigid body.

- Present a simple and robust way of modeling the contact geometry of 3-dimensional rigid bodies interacting with beams.

- Study the numerical performance resulting from an artificial symmetrization of the slip tangent matrix, and the effect of including a tangent matrix proportional to the normal contact force.

- Formulate a friction model which takes due account of surface eccentricities and associated moments.

Section 2 begins with a description of the body geometry representation. The kinematics of the involved geometries are thereafter presented together with the contact detection algorithm. In Section 3 the semi-discrete FE equations for the contact virtual work and the associated linearizations are presented. Results from a validation study against experimental data and numerical performance tests are given in Section 4. Conclusions and findings of the work are summarized in Section 5.

2 Body geometry representation, kinematics and contact detection

2.1 Body geometry representation

The rigid body is modeled by a 3-dimensional mesh of geometry elements. A single element is shown in Fig. 1 and consists of a plane triangular plate with thickness $2\bar{R}$ surrounded by circular-shaped edges and spherical-shaped corners with radius $\bar{R}$. To obtain a continuous description of the unit normal vector on convex surface regions the radius is set equal for all geometry elements defining the rigid body. Beam formulations for nonlinear analysis of pipelines are usually based on corotated straight elements with small local rotations, see e.g. [25–27]. With regard to global response prediction it is hence permissible to remove the flat plate surface, such that the contact geometry of a single element consists of the three edges and the three corners seen in Fig. 1.

In contrast to approaches based on 3-dimensional surface interpolation with two parameters [5–7], the selected geometry representation yields a simple kinematical description in terms of one parameter. Straight lines coincident with the locus of center points along the cylindrical-shaped edges are here used to express the contact kinematics. These lines are parametrized in terms of the initial coordinates as,

$$\bar{\mathbf{X}}(\bar{\eta}) = \frac{1-\bar{\eta}}{2}\bar{\mathbf{X}}_{\mathbf{1}} + \frac{1+\bar{\eta}}{2}\bar{\mathbf{X}}_{\mathbf{2}} \qquad -1 \leq \bar{\eta} \leq 1 \tag{1}$$

where $\bar{\mathbf{X}}_{\mathbf{1}}$ and $\bar{\mathbf{X}}_{\mathbf{2}}$ refer to the center coordinates of the corners, see Fig. 1.

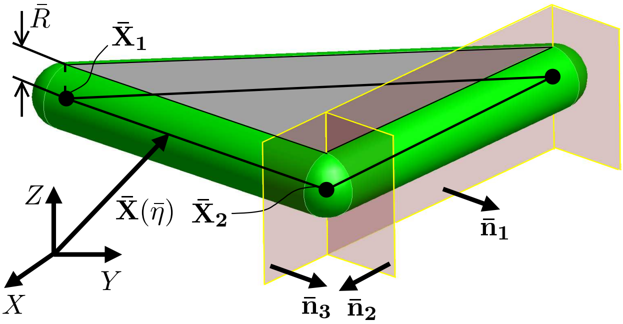

Figure 1: Body geometry element

Regarding contact detection there is no need to use explicit mathematical expressions for the edge and corner surfaces in Fig. 1. A sufficient description is obtained via Eq. (1) and by introducing bounding plane functions $\bar{H}_i$ at the corners and along the edges of the body geometry elements. The bounding planes shown in Fig. 1 are defined in terms of the outward normal vectors $\bar{\mathbf{n}}_{\mathbf{i}}$,

$$\bar{H}_i(\bar{\mathbf{P}}) = \bar{\mathbf{n}}_{\mathbf{i}} \cdot (\bar{\mathbf{P}} - \bar{\mathbf{P}}_{\mathbf{i}}) = 0 \qquad \bar{\mathbf{P}} = \begin{bmatrix} X & Y & Z \end{bmatrix} \tag{2}$$

where $\bar{\mathbf{P}}_{\mathbf{i}}$ is a coordinate point located on bounding plane $\bar{H}_i$. As illustrated in Fig. 1 two bounding planes are needed to enclose the spherical corner surfaces, while one bounding plane is sufficient for the cylindrical edge surfaces.

When a 3-dimensional body is modeled there will appear joint surfaces at corners and along edges shared by surrounding body geometry elements. To avoid multiple definitions of a single contact point these surfaces should be defined as non-overlapping regions. Contributions from the solid plate part of the body geometry elements should also be excluded. A joint surface $\partial\bar{C}$ is therefore defined as the subset of coordinate points $\bar{\mathbf{P}}$ that fulfill,

$$\partial\bar{C}: \quad \bar{\mathbf{P}} \in \partial\bar{S} \qquad \bar{H}_i(\bar{\mathbf{P}}) \geq 0 \qquad i = 1, ..., N \tag{3}$$

where $\partial\bar{S}$ refers to the spherical corner surface or the circular cylinder surface of the edge, see Fig. 2. The bounding plane functions $\bar{H}_i$ consist of N contributions as defined by Eq. (2). N is equal to the number of adjacent body geometry elements in case of an edge, whereas for a corner N is equal to twice the number of neighboring body geometry elements. Equation (3) implies that contact at concave parts of the body cannot be described. This is considered acceptable in view of the assumption of approximately straight pipe elements.

The defined geometry may contain fully encapsulated corners and edges that should be removed to speed up the contact search. This is enlightened for the rectangular box with plane facets shown in Fig. 3. The front face center node has here eight bounding plane functions, $\bar{H}_1 - \bar{H}_8$, stemming from four neighboring body geometry elements. There exist no coordinate points where all of the $\bar{H}_i$-functions are positive. Consequently, the

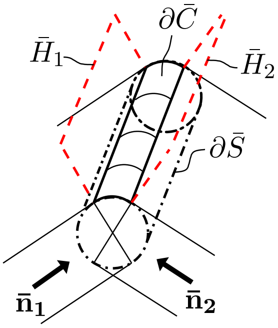

Figure 2: Joint edge surface

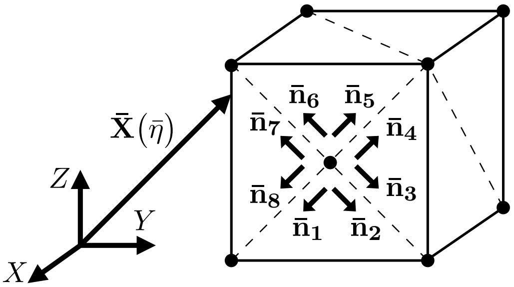

Figure 3: Contact geometry of a rectangular box

center node can be removed from the contact geometry. Based on similar arguments the six edges indicated by dashed lines in Fig. 3 can also be removed.

2.2 Kinematics

The developed contact element is 3-noded and as depicted in Fig. 4 the DOFs associated with the pipe are,

$$\mathbf{v} = \begin{bmatrix} v_1 & v_2 & v_3 & v_4 & v_5 & v_6 & v_7 & v_8 & v_9 & v_{10} & v_{11} & v_{12} \end{bmatrix}^\top \tag{4}$$

while the six DOFs that belong to the body are denoted,

$$\bar{\mathbf{v}} = \begin{bmatrix} \bar{\mathbf{v}}_\mathbf{B} \\ \bar{\boldsymbol{\theta}} \end{bmatrix} \qquad \bar{\mathbf{v}}_\mathbf{B} = \begin{bmatrix} \bar{v}_1 & \bar{v}_2 & \bar{v}_3 \end{bmatrix}^\top \qquad \bar{\boldsymbol{\theta}} = \begin{bmatrix} \bar{\theta}_1 & \bar{\theta}_2 & \bar{\theta}_3 \end{bmatrix}^\top \tag{5}$$

Due account is made for the pipe rotational DOFs to obtain a C_1-continuous pipe centroidal curve. As discussed by Litewka [23] a continuous representation is beneficial regarding convergence rate and smoothness of the solution. The contact element has been implemented into a computer code [28] where a corotated description of the pipe kinematics is applied, identical to the formulation presented by Mathisen [27]. There the pipe element centroidal displacement field relative to a straight line intersecting the nodal endpoints is expressed as,

$$\{\mathbf{u}_\mathbf{d}(\eta)\} = \{\mathbf{T}\}^\top \{\mathbf{N}^l(\eta)\}\{\mathbf{v}^l_{\boldsymbol{\theta}}\} \tag{6}$$

where $\mathbf{T}$ is a 3×3 transformation matrix for the considered pipe element. Curly brackets are introduced here to emphasize the vector-matrix notation. The non-zero components of the interpolation matrix $\mathbf{N}^l(\eta)$ are presented in Section 3.3, and $\mathbf{v}^l_{\boldsymbol{\theta}}$ contains the local deformational rotations depicted in Fig. 4,

$$\mathbf{v}^l_{\boldsymbol{\theta}} = \begin{bmatrix} 0 & 0 & 0 & \alpha_1 & \phi_1 & \psi_1 & 0 & 0 & 0 & \alpha_2 & \phi_2 & \psi_2 \end{bmatrix}^\top \tag{7}$$

The current configuration of the considered pipe element centroidal curve in global coordinates is found by adding $\mathbf{u}_\mathbf{d}(\eta)$ to the straight pipe configuration defined by the updated

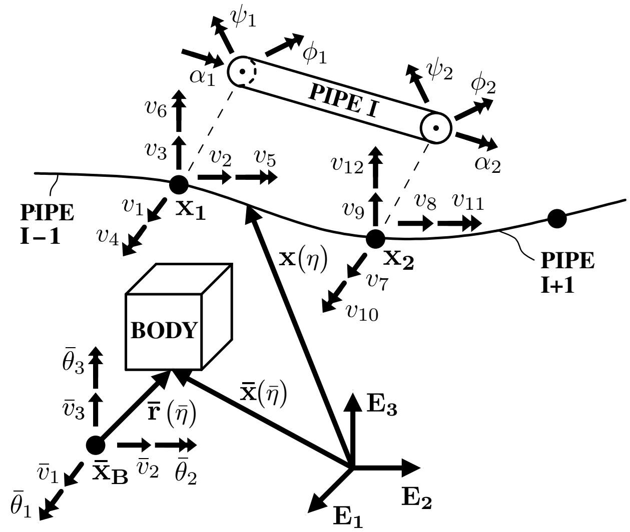

Figure 4: Current configuration of pipe and body

global coordinates of the pipe element nodes, $\mathbf{x_1}$ and $\mathbf{x_2}$,

$$\mathbf{x}(\eta) = \mathbf{u_d}(\eta) + \frac{1-\eta}{2}\mathbf{x_1} + \frac{1+\eta}{2}\mathbf{x_2} \qquad -1 \le \eta \le 1 \tag{8}$$

The updated configuration of the body contact geometry is defined by the body edge center lines. As illustrated in Fig. 4 these lines can be expressed by the updated global coordinates of the body node $\mathbf{x_B}$ and an eccentricity vector $\bar{\mathbf{r}}(\bar{\eta})$,

$$\bar{\mathbf{x}}(\bar{\eta}) = \bar{\mathbf{x}}_\mathbf{B} + \bar{\mathbf{r}}(\bar{\eta}) \qquad \bar{\mathbf{r}}(\bar{\eta}) = \bar{\mathbf{R}} \cdot \left[\bar{\mathbf{X}}(\bar{\eta}) - \bar{\mathbf{X}}_\mathbf{B}\right] \tag{9}$$

where $\bar{\mathbf{R}}$ is the body node rotation tensor. $\bar{\mathbf{X}}_\mathbf{B}$ denotes the initial coordinates of the body node and $\bar{\mathbf{X}}(\bar{\eta})$ is the initial center coordinates of the considered edge or corner as given by Eq. (1).

2.3 Contact detection

The body and the pipeline may occupy configurations with several contact points. Due to topology reasons a single contact element cannot handle more than one contact point at the same time. In Fig. 5 the contact detection algorithm for a single contact element is illustrated. If the element was inactive in the previous equilibrium state the left branch is entered, and a global contact search is performed to identify the body geometry elements that can obtain contact with the considered pipe element. A local contact search is thereafter initiated for the identified body geometry elements to check if the conditions for contact are fulfilled. If a candidate contact point is found it must also be ensured that the point is not occupied by other contact elements.

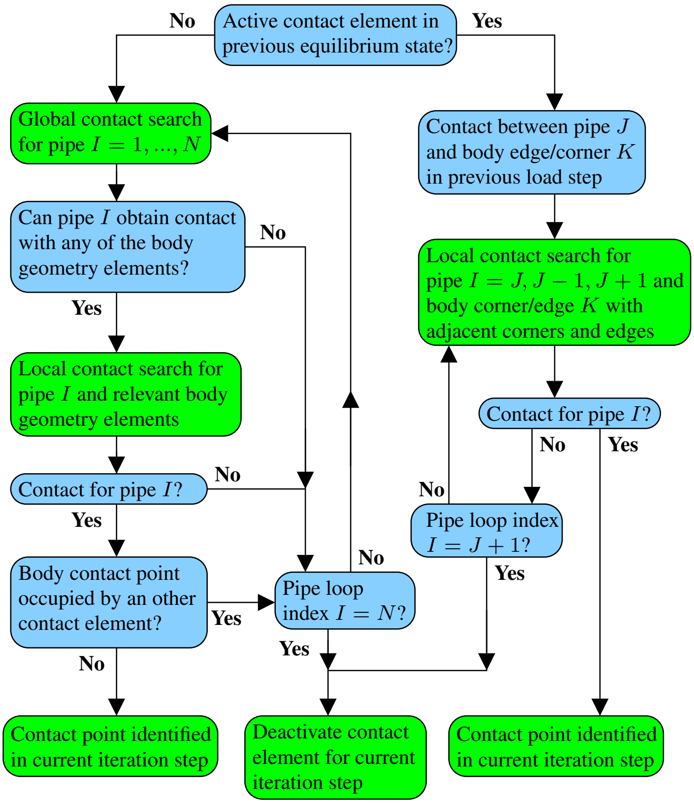

Figure 5: Contact detection algorithm

If contact was present in the previous equilibrium state this information is exploited by entering the right branch in Fig. 5. The computational effort is here reduced since the local contact search is executed only for pipe elements, edges and corners in the vicinity of the previous contact point.

2.3.1 Global contact search

The objective of the global contact search is to reduce the computing time by removal of unnecessary body geometry elements from the local contact search. At initialization joint edges and joint corners are distributed among the body geometry elements. Each of the body geometry elements is assigned a bounding sphere located at the geometric center of the element, and the radius C is set such that it encloses the edges and corners, similar to the body-based cell strategy described by Williams and O’Connor [29]. A circular cylinder geometry is used to represent the pipe element, see Fig. 6. The body geometry element is included in the local contact search if its bounding sphere intersects the considered pipe element cylinder.

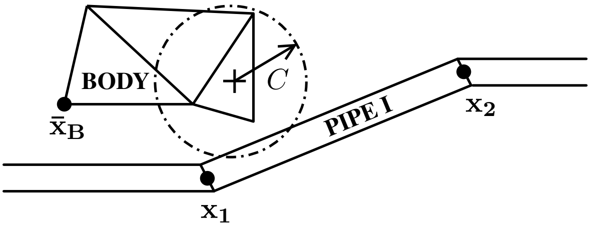

Figure 6: Global contact search

2.3.2 Local contact search

The local contact search is founded upon the assumption that contact is pointwise and occurs at the so-called minimum distance points of the pipe and the body. Since the pipe is circular and the body contact geometry is represented by cylindrical surfaces and spheres with equal radius, the minimum distance points can be found based on the center coordinates, $\mathbf{x}(\eta)$ and $\bar{\mathbf{x}}(\bar{\eta})$. The center distance is therefore minimized,

$$d = \min ||\bar{\mathbf{x}}(\bar{\eta}) - \mathbf{x}(\eta)|| \tag{10}$$

which results in the orthogonality conditions,

$$\big[\bar{\mathbf{x}}(\bar{\eta}) - \mathbf{x}(\eta)\big] \cdot \mathbf{x}_{,\eta}(\eta) = 0 \tag{11}$$

$$\big[\bar{\mathbf{x}}(\bar{\eta}) - \mathbf{x}(\eta)\big] \cdot \bar{\mathbf{x}}_{,\bar{\eta}}(\bar{\eta}) = 0 \tag{12}$$

The notation for derivatives $\frac{\partial \mathbf{x}}{\partial \eta} = \mathbf{x}_{,\eta}$ has here been introduced. If the contact search is executed for a body corner only Eq. (11) applies. Due to the term $\mathbf{u_d}(\eta)$ in Eq. (8) the orthogonality conditions are nonlinear in terms of the non-dimensional parameters. A local Newton scheme is therefore employed to find the minimum distance points. Details about formulation of the iterative scheme can be found in previous publications on beam contact [19, 21, 24].

At the converged solution of the minimum distance problem the non-dimensional parameters are denoted η_c and $\bar{\eta}_c$. If their numerical values are within the domains given in Eqs. (1) and (8), a penetration check is conducted by means of the expression,

$$g_n = ||\bar{\mathbf{x}}(\bar{\eta}_c) - \mathbf{x}(\eta_c)|| - R - \bar{R} \tag{13}$$

which henceforth will be referred to as the normal gap. The pipe radius is here denoted R. If g_n is non-positive the surface coordinate of the body candidate contact point is calculated,

$$\bar{\mathbf{x}}_\mathbf{s}(\bar{\eta}_c) = \bar{\mathbf{x}}(\bar{\eta}_c) - \bar{R}\mathbf{n} \tag{14}$$

where $\mathbf{n}$ is the pipe outward unit normal vector defined by,

$$\mathbf{n} = \frac{\bar{\mathbf{x}}(\bar{\eta}_c) - \mathbf{x}(\eta_c)}{d} \qquad d = ||\bar{\mathbf{x}}(\bar{\eta}_c) - \mathbf{x}(\eta_c)|| \tag{15}$$

Contact is then defined to be present if the following conditions hold,

$$\bar{H}_i\big(\bar{\mathbf{P}}\big) \geq 0 \qquad \bar{\mathbf{P}} = \bar{\mathbf{X}}_{\mathbf{B}} + \bar{\mathbf{R}}^{\top} \cdot \big[\mathbf{x_s}\big(\bar{\eta}\big) - \bar{\mathbf{x}}_{\mathbf{B}}\big] \qquad i = 1, ..., N \tag{16}$$

$$g_n \leq 0 \tag{17}$$

where the N bounding planes of the considered edge or corner are defined according to Eqs. (2) and (3).

3 Weak formulation, linearization and discretization

In this paper a conventional finite element approach based on the principle of virtual work is employed. Equilibrium of the pipe and the rigid body is within this principle expressed as,

$$\delta W_{INT} - \delta W_{EXT} + \delta W_{KIN} + \sum_{i}^{N_c} \left(\delta W_n^{\{i\}} + \delta W_T^{\{i\}} \right) = 0 \tag{18}$$

where δW_{EXT} and δW_{KIN} represent the pipe and body virtual work contributions from external and inertia forces, respectively, and δW_{INT} denotes the pipe virtual strain energy. These quantities will not be pursued further in this paper. $\delta W_n^{\{i\}}$ and $\delta W_T^{\{i\}}$ refer to the virtual work due to normal and frictional forces at the *i*-th contact point, respectively, defined in terms of variations of the pipe and body displacements. The variation of the centroidal displacement field associated with a single pipe element is selected as,

$$\big\{\delta \mathbf{u}\,(\eta)\,\big\} = \big\{\mathbf{T}\big\}^{\top} \big\{\mathbf{N}^l\,(\eta)\,\big\}\big\{\hat{\mathbf{T}}\big\}\big\{\delta \mathbf{v}\big\} \tag{19}$$

$\hat{\mathbf{T}}$ is here a 12×12 matrix with the pipe element transformation matrix $\mathbf{T}$ on its diagonal. The corresponding variation for the body is given by,

$$\begin{gathered} \delta\bar{\mathbf{u}}\big(\bar{\eta}\big) = \delta\bar{\mathbf{v}}_{\mathbf{B}} + \delta\bar{\mathbf{R}} \cdot \big[\bar{\mathbf{X}}\big(\bar{\eta}\big) - \bar{\mathbf{X}}_{\mathbf{B}}\big] \qquad \delta\bar{\mathbf{R}} = \mathbf{S}\big(\delta\bar{\boldsymbol{\theta}}\big) \cdot \bar{\mathbf{R}} \\ \mathbf{S}\big(\delta\bar{\boldsymbol{\theta}}\big) = \begin{bmatrix} 0 & -\delta\bar{\theta}_3 & \delta\bar{\theta}_2 \\ \delta\bar{\theta}_3 & 0 & -\delta\bar{\theta}_1 \\ -\delta\bar{\theta}_2 & \delta\bar{\theta}_1 & 0 \end{bmatrix} \qquad \delta\bar{\boldsymbol{\theta}} = \sum_{i=1}^{3} \delta\bar{\theta}_i \mathbf{E}_i \end{gathered} \tag{20}$$

In this work the implicit HHT-α scheme [30] combined with Newton's method is employed to solve Eq. (18). This necessitates establishment of tangent matrices emerging from linearization of the virtual work. All quantities that depend on the displacement state should be accounted for when the linearizations denoted by the Δ-symbol are computed, however, the transformation matrix $\mathbf{T}$ and the variation $\delta\bar{\mathbf{R}}$ will subsequently be regarded as constant quantities with respect to linearization,

$$\Delta\mathbf{T} = \mathbf{0} \qquad \Delta\big(\delta\bar{\mathbf{R}}\big) = \mathbf{0} \tag{21}$$

which is a necessity in our approach to obtain a symmetric tangent stiffness matrix for frictionless interaction.

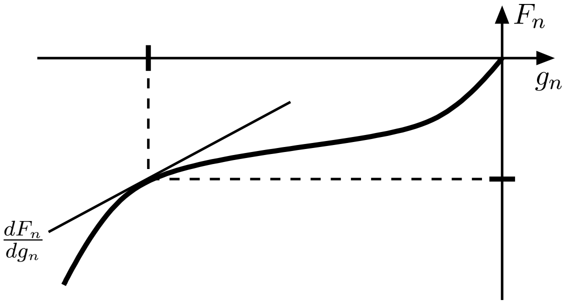

Figure 7: Force-indentation curve for coated pipe

3.1 Normal contact

In a penalty formulation the normal force virtual work contribution from a single contact point can be expressed as,

$$\delta W_n = F_n\left(g_n\right)\delta g_n \qquad F_n\left(g_n\right) \leq 0 \tag{22}$$

where $F_n\left(g_n\right)$ is a constitutive law for the normal force that may be used to incorporate stiffness properties of the pipe coating as indicated in Fig. 7.

To simplify notation the dependence on η and $\bar{\eta}$ is omitted for quantities evaluated at the current contact point, e.g. $\delta\mathbf{u} = \delta\mathbf{u}\left(\eta_c\right)$ and $\bar{\mathbf{x}} = \bar{\mathbf{x}}\left(\bar{\eta}_c\right)$. The normal gap variation is found by taking the variation of Eq. (13). Since the contact point location depends on the displacement state this quantity is expressed as,

$$\delta g_n = \left[\delta\bar{\mathbf{u}} + \bar{\mathbf{x}}_{,\bar{\eta}}\delta\bar{\eta} - \delta\mathbf{u} - \mathbf{x}_{,\eta}\delta\eta\right]\cdot\mathbf{n} \tag{23}$$

which due to the orthogonality conditions in Eqs. (11) and (12) is reduced to,

$$\delta g_n = \left[\delta\bar{\mathbf{u}} - \delta\mathbf{u}\right]\cdot\mathbf{n} \tag{24}$$

In the following a similar approach as the one presented by Wriggers and Zavarise [19] for two contacting beams with circular cross-sections will be used to establish the linearization,

$$\Delta\delta W_n = \frac{dF_n}{dg_n}\Delta g_n\delta g_n + F_n\left(g_n\right)\Delta\delta g_n \tag{25}$$

Variations and linearizations are computed in the same way, and Δg_n has therefore the same structure as δg_n given in Eq. (24),

$$\Delta g_n = \left[\Delta\bar{\mathbf{u}} - \Delta\mathbf{u}\right]\cdot\mathbf{n} \tag{26}$$

The linearization of $\Delta\delta g_n$ must be based on Eq. (23) rather than Eq. (24), because the vanishing terms leading to Eq. (24) yield non-zero tangent contributions. Due to Eq. (21)

the quantities $\Delta\big(\delta\mathbf{u}\big)$ and $\Delta\big(\delta\bar{\mathbf{u}}\big)$ will be zero such that,

$$\Delta\delta g_n \;=\; \Delta\delta g_n^{\{1\}} + \Delta\delta g_n^{\{2\}} \tag{27}$$

$$\Delta\delta g_n^{\{1\}} = [\delta\bar{\mathbf{u}} + \bar{\mathbf{x}}_{,\bar{\eta}}\delta\bar{\eta} - \delta\mathbf{u} - \mathbf{x}_{,\eta}\delta\eta] \cdot \Delta\mathbf{n} \tag{28}$$

$$\Delta\delta g_n^{\{2\}} = [\delta\bar{\mathbf{u}}_{,\bar{\eta}}\Delta\bar{\eta} + \Delta\bar{\mathbf{u}}_{,\bar{\eta}}\delta\bar{\eta} - \delta\mathbf{u}_{,\eta}\Delta\eta - \Delta\mathbf{u}_{,\eta}\delta\eta - \mathbf{x}_{,\eta\eta}\Delta\eta\delta\eta] \cdot \mathbf{n} \tag{29}$$

The linearizations, $\Delta\eta$ and $\Delta\bar{\eta}$, and the corresponding variations, $\delta\eta$ and $\delta\bar{\eta}$, are expressed in terms of the elemental DOFs in 5. If the contact point is located on a body corner Eqs. (28) and (29) simplify. In that case all terms containing $\delta\bar{\eta}$ and $\Delta\bar{\eta}$ will vanish. An expression for $\Delta\mathbf{n}$ is obtained by linearization of Eq. (15),

$$\Delta\mathbf{n} = \frac{1}{d}\,[\mathbf{I} - \mathbf{n}\otimes\mathbf{n}] \cdot [\Delta\bar{\mathbf{u}} + \bar{\mathbf{x}}_{,\bar{\eta}}\Delta\bar{\eta} - \Delta\mathbf{u} - \mathbf{x}_{,\eta}\Delta\eta] \tag{30}$$

where $\mathbf{I}$ is the identity tensor. Inserting the expression for $\Delta\mathbf{n}$ into Eq. (28) yields,

$$\begin{aligned}\Delta\delta g_n^{\{1\}} = \frac{1}{d}\,&[\delta\bar{\mathbf{u}} + \bar{\mathbf{x}}_{,\bar{\eta}}\delta\bar{\eta} - \delta\mathbf{u} - \mathbf{x}_{,\eta}\delta\eta] \cdot [\mathbf{I} - \mathbf{n}\otimes\mathbf{n}] \\ &\cdot [\Delta\bar{\mathbf{u}} + \bar{\mathbf{x}}_{,\bar{\eta}}\Delta\bar{\eta} - \Delta\mathbf{u} - \mathbf{x}_{,\eta}\Delta\eta]\end{aligned} \tag{31}$$

Information about the contact geometry is introduced via the $\Delta\delta g_n$-term. The benefit of including this information is investigated in Section 4.

3.2 Frictional contact

In previous work on beam contact the friction kinematics have been based on parametrized curves defining the deformed beam configurations [20, 22]. Such descriptions will for a large diameter pipeline parametrized by the centroidal curve yield inaccurate predictions of the sliding distance and not capture the case of rolling, i.e. a pure rotation of the body or the pipe about the instantaneous contact point. Recently, this was improved by Konyukhov and Schweizerhof [24] who introduced a kinematic measure allowing for rotational friction interaction. In the following an alternative approach that accounts for both bending and torsional moments of the pipe will be developed.

A 2-dimensional representation is employed for the friction force $\mathbf{F}_T$ and the tangential displacement of the contact point $\mathbf{g}_T$,

$$\mathbf{F}_T = F_k\mathbf{k} + F_m\mathbf{m} \tag{32}$$

$$\mathbf{g}_T = g_{Tk}\mathbf{k} + g_{Tm}\mathbf{m} \tag{33}$$

where the base vectors, $\mathbf{k}$ and $\mathbf{m}$, spanning the current tangent plane of the contacting surfaces are established by the following rules,

$$\mathbf{k} = \frac{\mathbf{x}_{,\eta}}{||\mathbf{x}_{,\eta}||} \qquad \mathbf{m} = \mathbf{n}\times\mathbf{k} \tag{34}$$

The virtual work due to friction from a single contact point can then be expressed as,

$$\delta W_T = \delta\mathbf{g}_T \cdot \mathbf{F}_T \tag{35}$$

To develop the FE equations due to friction the main task is now to express $\delta\mathbf{g}_T$ and $\mathbf{F}_T$ in terms of the pipe and body displacements.

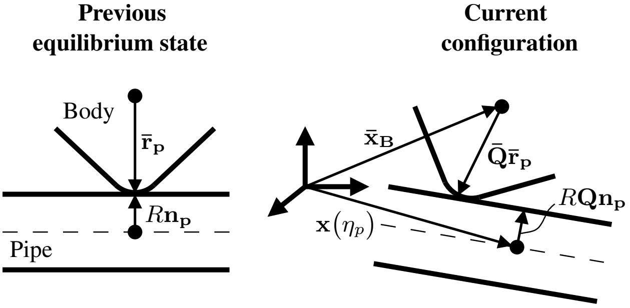

Figure 8: Relative displacement increment of previous contact points

3.2.1 Tangential displacement of the contact point

A kinematical measure of the tangential displacement may be obtained by separate considerations of the contact point motions on the body and on the pipe, similar as in the friction formulations presented previously on beam contact [20, 22, 24]. Alternatively, as adopted in this work the relative displacement of the body and the pipe contact points can be studied simultaneously. By mapping the contact points from the previous equilibrium state into the current configuration, see Fig. 8, the relative displacement increment can be defined as,

$$\mathbf{d} = \mathbf{x}(\eta_p) + R\mathbf{Q}\cdot\mathbf{n}_\mathbf{P} - \bar{\mathbf{x}}_\mathbf{B} - \bar{\mathbf{Q}}\cdot\bar{\mathbf{r}}_\mathbf{P} \tag{36}$$

The pipe centroidal coordinate of the previous contact point mapped into the current configuration is given by $\mathbf{x}(\eta_p)$. Surface eccentricities of the previous contact points are defined by the pipe outward unit normal vector $\mathbf{n}_\mathbf{P}$ and the vector $\bar{\mathbf{r}}_\mathbf{P}$, see Fig. 8. Both eccentricities refer to the previous equilibrium state and are mapped into the current configuration by the incremental rotation tensors $\mathbf{Q}$ and $\bar{\mathbf{Q}}$.

A standard multiplicative update scheme is used to compute the body incremental rotation tensor,

$$\bar{\mathbf{Q}}_{\{i+1\}} = \exp\left[\mathbf{S}(\Delta\bar{\boldsymbol{\theta}}_{\{i\}})\right]\cdot\bar{\mathbf{Q}}_{\{i\}} \qquad \bar{\mathbf{Q}}_{\{0\}} = \mathbf{I} \qquad i = 0,1,2,... \tag{37}$$

Subscript 0 refers here to the previous equilibrium state, $\mathbf{S}$ is the skew-symmetric tensor defined in Eq. (20) and $\Delta\bar{\boldsymbol{\theta}}_{\{i\}}$ denotes the body node spin obtained at the i-th iteration step in Newton's method. The exponential map of the skew-symmetric spin tensor $\mathbf{S}(\Delta\bar{\boldsymbol{\theta}})$ is approximated as,

$$\exp\left[\mathbf{S}(\Delta\bar{\boldsymbol{\theta}})\right] = \mathbf{I} + \frac{1}{1+\frac{1}{4}\Delta\bar{\boldsymbol{\theta}}\cdot\Delta\bar{\boldsymbol{\theta}}}\left[\mathbf{S}(\Delta\bar{\boldsymbol{\theta}}) + \frac{1}{2}\left[\mathbf{S}(\Delta\bar{\boldsymbol{\theta}})\right]^2\right] \tag{38}$$

The pipe incremental rotation tensor is assumed to be multiplicatively decomposed into a deformational rotation $\mathbf{Q}_\mathbf{d}$ and a rigid rotation $\mathbf{Q}_\mathbf{r}$,

$$\mathbf{Q}_{\{i\}} = \mathbf{Q}_{\mathbf{d}\{i\}}\cdot\mathbf{Q}_{\mathbf{r}\{i\}} \qquad \mathbf{Q}_{\{0\}} = \mathbf{I} \qquad i = 1,2,3,... \tag{39}$$

Updating of the rigid part is based on the pipe transformation matrix $\mathbf{T}$ which is available from the updated displacement state,

$$\left\{\mathbf{Q}_{\mathbf{r}\{i\}}\right\} = \left\{\mathbf{T}_{\{i\}}\right\}^{\top}\left\{\mathbf{T}_{\{0\}}\right\} \qquad i = 1, 2, 3, ... \tag{40}$$

The deformational part is found by interpolation with aid of Eq. (67),

$$\left\{\hat{\Delta}\boldsymbol{\theta}_{\mathbf{d}\{i\}}(\eta_p)\right\} = \left\{\mathbf{T}_{\{i\}}\right\}^{\top}\left\{\mathbf{N}_{\boldsymbol{\theta}}{}^{l}(\eta_p)\right\}\left\{\mathbf{v}^{l}_{\boldsymbol{\theta}\{i\}} - \mathbf{v}^{l}_{\boldsymbol{\theta}\{0\}}\right\} \tag{41}$$

where the changes of nodal deformational rotations are measured by the vector $\mathbf{v}^{l}_{\boldsymbol{\theta}}$ defined in Eq. (7). Assuming small increments the exponential map in Eq. (38) yields the deformational part of the incremental pipe rotation tensor,

$$\mathbf{Q}_{\mathbf{d}\{i\}} = \exp\left[\mathbf{S}\left(\hat{\Delta}\boldsymbol{\theta}_{\mathbf{d}\{i\}}\right)\right] \qquad i = 1, 2, 3, ... \tag{42}$$

Since the load increments are assumed to be small the sliding path can be approximated incrementally by straight line segments. The total tangential displacement is therefore expressed as a sum of the tangent plane projection of $\mathbf{d}$ and the tangential displacement components from the previous equilibrium state,

$$\mathbf{g}_T = \hat{\Delta}\mathbf{g}_T + g^{P}_{Tk}\mathbf{k} + g^{P}_{Tm}\mathbf{m} \qquad \hat{\Delta}\mathbf{g}_T = \left[\mathbf{k}\otimes\mathbf{k} + \mathbf{m}\otimes\mathbf{m}\right]\cdot\mathbf{d} \tag{43}$$

The variation of the tangential displacement is selected as,

$$\delta\mathbf{g}_T = \left[\mathbf{k}\otimes\mathbf{k} + \mathbf{m}\otimes\mathbf{m}\right]\cdot\delta\mathbf{d} \tag{44}$$

Noting that the non-dimensional parameter η_p is fixed the variation of $\mathbf{d}$ is given by,

$$\delta\mathbf{d} = \delta\mathbf{u}(\eta_p) + R\mathbf{S}\left[\delta\boldsymbol{\theta}(\eta_p)\right]\cdot\mathbf{Q}\cdot\mathbf{n_p} - \delta\bar{\mathbf{v}}_{\mathbf{B}} - \mathbf{S}(\delta\bar{\boldsymbol{\theta}})\cdot\bar{\mathbf{Q}}\cdot\bar{\mathbf{r}}_{\mathbf{p}} \tag{45}$$

here $\delta\boldsymbol{\theta}$ refers to the variation of the pipe centroidal rotation. The linearization $\Delta\mathbf{d}$ has the same structure as $\delta\mathbf{d}$.

3.2.2 Friction force update scheme

In analogy with classical plasticity theory the tangential displacement is assumed to be additively decomposed into an elastic part $\mathbf{g}_E$ and a plastic part $\mathbf{g}_P$,

$$\mathbf{g}_T = \mathbf{g}_E + \mathbf{g}_P \tag{46}$$

where accumulation of elastic and plastic displacements occur in the states of stick and slip, respectively. A simple constitutive relation is used to link the elastic tangential displacement to the friction force,

$$\mathbf{F}_T = c_E\mathbf{g}_E \tag{47}$$

The elastic moduli is denoted c_E and can be interpreted as a penalty regularization of the stick constraint. A Coulomb slip criterion, analogous to the yield criterion in classical plasticity theory, is used to distinguish between stick and slip states,

$$f\left(\mathbf{F}_T, F_n\right) = ||\mathbf{F}_T|| + \mu F_n\left(g_n\right) \leq 0 \tag{48}$$

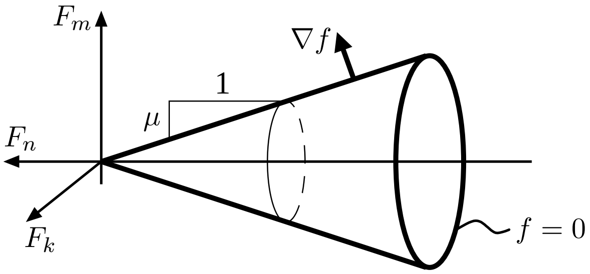

Figure 9: Coulomb slip surface

where $f = 0$ during slip, $f < 0$ indicates stick and $f > 0$ is an inadmissible state, see Fig. 9. The coefficient of friction is denoted μ and is here assumed to be independent of both sliding velocity and accumulated tangential displacement.

The principle of maximum plastic dissipation yields a so-called associated slip rule, where the slip increment is co-linear with the slip surface gradient ∇f. As pointed out by Michalowski and Mroz [31] this introduces artificial slip in the normal direction leading to loss of contact in a Coulomb friction model. Hence, a non-associated flow rule is selected as the evolution equation for slip,

$$\dot{\mathbf{g}}_P = \dot{\lambda}\frac{\partial}{\partial \mathbf{F}_T} f\left(\mathbf{F}_T, F_n\right) = \dot{\lambda}\frac{\mathbf{F}_T}{||\mathbf{F_T}||} \tag{49}$$

where the slip rate parameter is denoted $\dot{\lambda}$.

In this work the update of friction force is handled by an algorithm identical to the backward Euler stress update scheme used in plasticity models. Given a tangential displacement increment $\hat{\Delta}\mathbf{g}_T$, the first step in this algorithm is to presume stick behavior and compute the elastic trial force,

$$\mathbf{F}_T^{tr} = \mathbf{F}_T^{p} + c_E \hat{\Delta}\mathbf{g}_T \qquad \mathbf{F}_T^{p} = c_E \left[g_{Ek}^{P}\mathbf{k} + g_{Em}^{p}\mathbf{m}\right] \tag{50}$$

where $\mathbf{F}_T^p$ is the friction force at the previous equilibrium state. The assumed state is then checked according to the slip criterion in Eq. (48). In case of stick, $f\big(\mathbf{F}_T^{tr}, F_n\big) < 0$, the friction force is set equal to the elastic trial force in Eq. (50) and the update scheme is terminated.

Slip takes place if $f\big(\mathbf{F}_T^{tr}, F_n\big) > 0$, and a plastic return map must then be initiated such that the consistency condition $\dot{f} = 0$ is enforced. In general friction models a local Newton scheme is employed to update the friction force and internal variables, but for the simple Coulomb model a closed-form expression of the friction force can be found,

$$\mathbf{F}_T = -\mu F_n\left(g_n\right)\mathbf{n}^{tr} \qquad \mathbf{n}^{tr} = \frac{\mathbf{F}_T^{tr}}{||\mathbf{F}_T^{tr}||} \tag{51}$$

3.2.3 Stick

When the slip criterion in Eq. (48) indicates stick the friction force is given by the current elastic tangential displacement,

$$\mathbf{F}_T = \mathbf{F}_T^{tr} = c_E \left\{ \left[\mathbf{k} \otimes \mathbf{k} + \mathbf{m} \otimes \mathbf{m} \right] \cdot \mathbf{d} + g_{Ek}^P \mathbf{k} + g_{Em}^P \mathbf{m} \right\} \tag{52}$$

The virtual work in Eq. (35) is therefore expressed as,

$$\begin{aligned} \delta W_T = c_E \delta \mathbf{d} \cdot \Big\{ \Big[& \mathbf{k} \otimes \mathbf{k} + \mathbf{m} \otimes \mathbf{m} + (\mathbf{k} \otimes \mathbf{k}) \cdot (\mathbf{m} \otimes \mathbf{m}) \\ & + (\mathbf{m} \otimes \mathbf{m}) \cdot (\mathbf{k} \otimes \mathbf{k}) \Big] \cdot \mathbf{d} + g_{Ek}^P \mathbf{k} + g_{Em}^P \mathbf{m} \\ & + g_{Ek}^P (\mathbf{m} \otimes \mathbf{m}) \cdot \mathbf{k} + g_{Em}^P (\mathbf{k} \otimes \mathbf{k}) \cdot \mathbf{m} \Big\} \end{aligned} \tag{53}$$

which due to orthogonality simplifies to,

$$\delta W_T = c_E \delta \mathbf{d} \cdot \Big\{ \left[\mathbf{k} \otimes \mathbf{k} + \mathbf{m} \otimes \mathbf{m} \right] \cdot \mathbf{d} + g_{Ek}^P \mathbf{k} + g_{Em}^P \mathbf{m} \Big\} \tag{54}$$

$$\delta W_T = \delta \mathbf{d} \cdot \mathbf{F}_T^{tr} \tag{55}$$

The linearization of the stick virtual work should be based on Eq. (53) because the terms with orthogonal vectors yield non-zero tangent contributions, however, a simplified linearization will instead be adopted here by setting,

$$\Delta\big(\delta \mathbf{d}\big) = \mathbf{0} \qquad \Delta \mathbf{k} = \mathbf{0} \qquad \Delta \mathbf{m} = \mathbf{0} \tag{56}$$

The arguments for introducing the simplifications in Eq. (56) are as follows,

- Small increments must be applied due to Eq. (43). Requirements to numerical stability and rate of convergence can therefore be relaxed.
- The stick tangent matrix becomes symmetric.
- Setting $\Delta\big(\delta \mathbf{d}\big)$ equal to zero is consistent with the simplifications introduced in Eq. (21).

When the simplifications in Eq. (56) are imposed the linearized virtual work for stick can be expressed as,

$$\Delta \delta W_T = c_E \delta \mathbf{d} \cdot \left[\mathbf{k} \otimes \mathbf{k} + \mathbf{m} \otimes \mathbf{m} \right] \cdot \Delta \mathbf{d} \tag{57}$$

3.2.4 Slip

In case of violation of the slip criterion in Eq. (48) the virtual work is expressed according to,

$$\delta W_T = -\mu F_n \left(g_n \right) \delta \mathbf{d} \cdot \mathbf{n}^{tr} \qquad \mathbf{n}^{tr} = \frac{\mathbf{F}_T^{tr}}{||\mathbf{F}_T^{tr}||} \tag{58}$$

where $\mathbf{F}_T^{tr}$ is given by Eq. (52). The simplifications stated in Eq. (56) will also be exploited for the slip case. Hence, the linearization $\Delta\delta W_T$ can be computed as,

$$\Delta\delta W_T = \Delta\delta W_T^{\{1\}} + \Delta\delta W_T^{\{2\}} \tag{59}$$

$$\Delta\delta W_T^{\{1\}} = -\mu\frac{dF_n}{dg_n}\Delta g_n \delta\mathbf{d}\cdot\mathbf{n}^{tr} \tag{60}$$

$$\Delta\delta W_T^{\{2\}} = -\mu F_n(g_n)\,\delta\mathbf{d}\cdot\Delta\mathbf{n}^{tr} \tag{61}$$

where Δg_n is expressed in Eq. (26). The linearization of $\mathbf{n}^{tr}$ contained in Eq. (61) is given by,

$$\Delta\mathbf{n}^{tr} = \frac{1}{||\mathbf{F}_T^{tr}||}\left[\mathbf{I} - \mathbf{n}^{tr}\otimes\mathbf{n}^{tr}\right]\cdot\Delta\mathbf{F}_T^{tr} \tag{62}$$

and the linearization $\Delta\mathbf{F}_T^{tr}$ is taken as,

$$\Delta\mathbf{F}_T^{tr} = c_E\left[\mathbf{k}\otimes\mathbf{k} + \mathbf{m}\otimes\mathbf{m}\right]\cdot\Delta\mathbf{d} \tag{63}$$

Combining Eqs. (61), (62) and (63) yields,

$$\Delta\delta W_T^{\{2\}} = -\frac{c_E\mu F_n(g_n)}{||\mathbf{F}_T^{tr}||}\delta\mathbf{d}\cdot\left[\mathbf{k}\otimes\mathbf{k} + \mathbf{m}\otimes\mathbf{m} - \mathbf{n}^{tr}\otimes\mathbf{n}^{tr}\right]\cdot\Delta\mathbf{d} \tag{64}$$

3.3 Discretization of the displacement field

The linearized pipe centroidal displacement in the corotated element frame is given by the matrix relation,

$$\{\Delta\mathbf{u}^l(\eta)\} = \{\mathbf{N}^l(\eta)\}\{\Delta\mathbf{v}^l\} \qquad \{\Delta\mathbf{u}^l\} = \begin{bmatrix}\Delta u_1^l & \Delta u_2^l & \Delta u_3^l\end{bmatrix}^\top \tag{65}$$

where $\Delta\mathbf{v}^l$ is the iterative increment of the pipe local DOFs. The 3×12 interpolation matrix $\mathbf{N}^l$ is selected in accordance with Euler-Bernoulli beam theory and its non-zero components are given by,

$$\begin{aligned}
&N_{\{1,1\}}^l = \frac{1-\eta}{2} \qquad N_{\{1,7\}}^l = \frac{1+\eta}{2} && N_{\{2,2\}}^l = \frac{2+\eta^3-3\eta}{4}\\
&N_{\{2,6\}}^l = \frac{\eta^3-\eta^2-\eta+1}{8}L && N_{\{2,8\}}^l = \frac{2-\eta^3+3\eta}{4}\\
&N_{\{2,12\}}^l = \frac{\eta^3+\eta^2-\eta-1}{8}L && N_{\{3,3\}}^l = N_{\{2,2\}}^l\\
&N_{\{3,5\}}^l = -N_{\{2,6\}}^l \qquad N_{\{3,9\}}^l = N_{\{2,8\}}^l && N_{\{3,11\}}^l = -N_{\{2,12\}}^l
\end{aligned} \tag{66}$$

here L is the updated pipe element length and $\eta\in[-1,1]$. The linearized rotation of the pipe centroidal line is needed for frictional contact. In the corotated element frame this rotation is expressed as,

$$\{\Delta\boldsymbol{\theta}^l(\eta)\} = \{\mathbf{N}_{\boldsymbol{\theta}}^l(\eta)\}\{\Delta\mathbf{v}^l\} \qquad \{\Delta\boldsymbol{\theta}^l\} = \begin{bmatrix}\Delta\alpha & \Delta\phi & \Delta\psi\end{bmatrix}^\top \tag{67}$$

where the torsional angle $\Delta\alpha$ and the bending rotations $\Delta\phi$ and $\Delta\psi$, see Fig. 4, are approximated by linear interpolation along the pipe element. Strictly, the linearizations $\Delta\mathbf{u}$ and $\Delta\boldsymbol{\theta}$ should be computed in the global coordinates accounting for changes in the base vectors defining the corotated pipe element frame. In compliance with Eq. (21) this was neglected such that the global interpolation matrices $\mathbf{N}$ and $\mathbf{N}_{\boldsymbol{\theta}}$ were obtained by direct congruence transformation of the local interpolation matrices in Eqs. (65) and (67).

The linearized displacement of an edge or a corner of the body is expressed as,

$$\{\Delta\bar{\mathbf{u}}(\bar{\eta})\} = \{\bar{\mathbf{N}}(\bar{\eta})\}\{\Delta\bar{\mathbf{v}}\} \qquad \{\bar{\mathbf{N}}(\bar{\eta})\} = \left[\mathbf{I}_{3\times 3} \quad -\mathbf{S}\left[\bar{\mathbf{r}}(\bar{\eta})\right]\right] \tag{68}$$

here the vector $\Delta\bar{\mathbf{v}}$ contains the iterative increments of the body DOFs, the vector $\bar{\mathbf{r}}$ is given by Eq. (9) and the 3×3 skew-symmetric matrix $\mathbf{S}$ is defined in Eq. (20). The linearized displacement of the previous surface contact point mapped into the current configuration is needed for frictional contact,

$$\{\Delta\bar{\mathbf{u}}_{\mathbf{p}}\} = \{\bar{\mathbf{N}}_{\mathbf{p}}\}\{\Delta\bar{\mathbf{v}}\} \qquad \{\bar{\mathbf{N}}_{\mathbf{p}}\} = \left[\mathbf{I}_{3\times 3} \quad -\mathbf{S}\left[\bar{\mathbf{Q}}\cdot\bar{\mathbf{r}}_{\mathbf{p}}\right]\right] \tag{69}$$

Eccentricity of the surface point is given by $\bar{\mathbf{r}}_{\mathbf{p}}$ and $\bar{\mathbf{Q}}$ is defined in Eq. (37). These quantities are illustrated in Fig. 8.

Variations of the displacement field must also be interpolated in terms of the nodal degrees of freedom. In order to obtain symmetric FE equations the variations are interpolated by the same shape functions as used for the corresponding linearizations.

3.4 Discretization of normal contact

The variation of the normal gap in Eq. (24) is expressed in terms of the nodal degrees of freedom by the following relations,

$$\delta g_n = \{\delta\mathbf{V}\}^\top\{\mathbf{G}_1\} \qquad \{\mathbf{G}_1\} = \{\tilde{\mathbf{N}}\}^\top\{\mathbf{n}\} \tag{70}$$

The 3×18 matrix $\tilde{\mathbf{N}}$ and the 18×1 vectors $\delta\mathbf{V}$ and $\Delta\mathbf{V}$ are defined as,

$$\{\tilde{\mathbf{N}}\} = \left[-\mathbf{N}(\eta_c) \quad \bar{\mathbf{N}}(\bar{\eta}_c)\right] \qquad \{\delta\mathbf{V}\} = \begin{bmatrix}\delta\mathbf{v}\\ \delta\bar{\mathbf{v}}\end{bmatrix} \qquad \{\Delta\mathbf{V}\} = \begin{bmatrix}\Delta\mathbf{v}\\ \Delta\bar{\mathbf{v}}\end{bmatrix} \tag{71}$$

The discretization of Δg_n is given by the same matrices as used in Eq. (70). $\Delta\delta g_n^{\{1\}}$ in Eq. (31) is discretized by,

$$\Delta\delta g_n^{\{1\}} = \frac{1}{d}\{\delta\mathbf{V}\}^\top\{\mathbf{G}_2\}^\top\{\mathbf{G}_3\}\{\mathbf{G}_2\}\{\Delta\mathbf{V}\} \tag{72}$$

where the matrices $\mathbf{G}_2$ and $\mathbf{G}_3$ are defined as,

$$\{\mathbf{G}_2\} = \{\tilde{\mathbf{N}}\} + \{\bar{\mathbf{x}}_{,\bar{\eta}}\}\{\bar{\mathbf{a}}\} - \{\mathbf{x}_{,\eta}\}\{\mathbf{a}\} \qquad \{\mathbf{G}_3\} = \{\mathbf{I}\} - \{\mathbf{n}\}\{\mathbf{n}\}^\top \tag{73}$$

Here the 1×18 vectors $\mathbf{a}$ and $\bar{\mathbf{a}}$ are taken from the relation in Eq. (A.7) in case of contact along a body edge. If the contact point instead is located at a body corner, $\bar{\mathbf{a}}$ is set to zero and $\mathbf{a}$ is taken from Eq. (A.15). With this the quantity $\Delta\delta g_n^{\{2\}}$ in Eq. (29) can be discretized as,

$$\Delta\delta g_n^{\{2\}} = \{\delta\mathbf{V}\}^\top \Big\{\{\mathbf{G}_4\} + \{\mathbf{G}_4\}^\top + \{\mathbf{G}_5\}\Big\}\{\Delta\mathbf{V}\} \tag{74}$$

with $\mathbf{G}_4$ and $\mathbf{G}_5$ expressed as,

$$\{\mathbf{G}_4\} = \begin{bmatrix} -\{\mathbf{N}_{,\eta}(\eta_c)\}^\top\{\mathbf{n}\}\{\mathbf{a}\} \\ \{\bar{\mathbf{N}}_{,\bar{\eta}}(\bar{\eta}_c)\}^\top\{\mathbf{n}\}\{\bar{\mathbf{a}}\} \end{bmatrix} \qquad \{\mathbf{G}_5\} = -(\mathbf{n}\cdot\mathbf{x}_{,\eta\eta})\{\mathbf{a}\}^\top\{\mathbf{a}\} \tag{75}$$

The residual vector $\mathbf{S}_n$ containing forces and moments due to normal contact can now be obtained from the virtual work expression in Eq. (22),

$$\delta W_n = \{\delta\mathbf{V}\}^\top\{\mathbf{S}_n\} \tag{76}$$

$$\{\mathbf{S}_n\} = F_n\,(g_n)\,\{\mathbf{G}_1\} \tag{77}$$

The tangent matrix is given by the linearized virtual work in Eq. (25) and is here split into two parts, $\mathbf{K}_n^{\Delta g_n}$ and $\mathbf{K}_n^{\Delta\delta g_n}$,

$$\Delta\delta W_n = \{\delta\mathbf{V}\}^\top\Big\{\{\mathbf{K}_n^{\Delta g_n}\} + \{\mathbf{K}_n^{\Delta\delta g_n}\}\Big\}\{\Delta\mathbf{V}\} \tag{78}$$

$$\{\mathbf{K}_n^{\Delta g_n}\} = \frac{dF_n}{dg_n}\{\mathbf{G}_1\}\{\mathbf{G}_1\}^\top \tag{79}$$

$$\{\mathbf{K}_n^{\Delta\delta g_n}\} = \frac{F_n}{d}\{\mathbf{G}_2\}^\top\{\mathbf{G}_3\}\{\mathbf{G}_2\} + F_n\Big\{\{\mathbf{G}_4\} + \{\mathbf{G}_4\}^\top + \{\mathbf{G}_5\}\Big\} \tag{80}$$

The matrix $\mathbf{K}_n^{\Delta\delta g_n}$ is proportional to the normal contact force and can therefore be interpreted as an initial stress stiffness matrix. Note that both tangent matrix contributions are symmetric and that all quantities involved in Eqs. (77), (79) and (80) are evaluated at the current contact point.

3.5 Discretization of frictional contact

The linearization and the variation of the relative displacement vector $\mathbf{d}$ are discretized by identical matrices. The interpolation of $\delta\mathbf{d}$ is expressed as,

$$\{\delta\mathbf{d}\} = \{\mathbf{G}_6\}\{\delta\mathbf{V}\} \tag{81}$$

with the 3 × 18 matrix $\mathbf{G}_6$ defined by,

$$\{\mathbf{G}_6\} = \begin{bmatrix}\mathbf{N}(\eta_p) & \mathbf{0}_{3\times 6}\end{bmatrix} - \begin{bmatrix}R\{\mathbf{S}[\mathbf{Q}\cdot\mathbf{n}^p]\}\{\mathbf{N}_{\boldsymbol{\theta}}(\eta_p)\} & \bar{\mathbf{N}}_{\mathbf{p}}\end{bmatrix} \tag{82}$$

3.5.1 Stick

In the state of stick the friction residual vector $\mathbf{S}_T$ is obtained by discretization of Eq. (55),

$$\delta W_T = \{\delta\mathbf{V}\}^\top\{\mathbf{S}_T\} \tag{83}$$

$$\{\mathbf{S}_T\} = \{\mathbf{G}_6\}^\top\{\mathbf{F}_T^{tr}\} \tag{84}$$

and discretization of Eq. (57) yields the stick tangent matrix,

$$\Delta\delta W_T = \{\delta\mathbf{V}\}^\top\{\mathbf{K}_T\}\{\Delta\mathbf{V}\} \tag{85}$$

$$\{\mathbf{K}_T\} = c_E\{\mathbf{G}_6\}^\top\{\mathbf{G}_7\}\{\mathbf{G}_6\} \tag{86}$$

Where $\mathbf{G}_7$ is the tangent plane projection matrix,

$$\{\mathbf{G}_7\} = \{\mathbf{k}\}\{\mathbf{k}\}^\top + \{\mathbf{m}\}\{\mathbf{m}\}^\top \tag{87}$$

3.5.2 Slip

The discretized virtual work in Eq. (58) provides the slip residual vector $\mathbf{S}_T$,

$$\delta W_T = \{\delta\mathbf{V}\}^\top\{\mathbf{S}_T\} \tag{88}$$

$$\{\mathbf{S}_T\} = -\mu F_n\{\mathbf{G}_6\}^\top\{\mathbf{n}^{tr}\} \tag{89}$$

The slip tangent matrix is given by the linearized slip virtual work in Eqs. (60) and (64). This tangent matrix can be split into a non-symmetric part $\mathbf{K}_T^{\Delta g_n}$ related to coupling with the normal gap and a symmetric contribution $\mathbf{K}_T^{\Delta g_T}$ associated with the tangential displacement,

$$\Delta\delta W_T = \{\delta\mathbf{V}\}^\top\Big\{\{\mathbf{K}_T^{\Delta g_n}\} + \{\mathbf{K}_T^{\Delta g_T}\}\Big\}\{\Delta\mathbf{V}\} \tag{90}$$

$$\{\mathbf{K}_T^{\Delta g_n}\} = -\mu\frac{dF_n}{dg_n}\{\mathbf{G}_6\}^\top\{\mathbf{n}^{tr}\}\{\mathbf{G}_1\}^\top \tag{91}$$

$$\{\mathbf{K}_T^{\Delta g_T}\} = -\frac{c_E\mu F_n}{||\mathbf{F}^{tr}||}\{\mathbf{G}_6\}^\top\Big\{\{\mathbf{G}_7\} - \{\mathbf{n}^{tr}\}\{\mathbf{n}^{tr}\}^\top\Big\}\{\mathbf{G}_6\} \tag{92}$$

The equation solver and the matrix storage system which have been used in this work can only handle symmetric matrices. An artificial symmetrization of the non-symmetric matrix contribution was therefore applied in the implemented code,

$$\{\mathbf{K}_T^{\Delta g_n}\}_{sym} = \frac{1}{2}\Big\{\{\mathbf{K}_T^{\Delta g_n}\} + \{\mathbf{K}_T^{\Delta g_n}\}^\top\Big\} \tag{93}$$

Alternatively, the non-symmetric matrix can simply be set to zero. In Section 4 the numerical performance resulting from these two approaches is investigated.

4 Numerical examples

4.1 Trawl board pull-over tests

A comparison study against experimental tests of trawl board and pipeline interaction in 1:6 scale ratio [32] was conducted to validate the performance of the element. A full-scale FE model of the test setup in Fig. 11 was reconstructed by means of the SIMLA software [28]. The 2 600 kg trawl board was represented by a 6 DOF rigid body model taking due

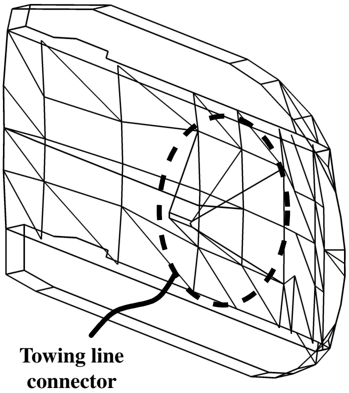

Figure 10: Contact geometry of the trawl board

account of hydrodynamic mass, structural inertia, quadratic damping and forward-speed induced loads. 205 edges and 71 corners with radius set to 0.01 m defined the board contact geometry seen in Fig. 10.

The pipe section was modeled by 40 linear-elastic corotated beam elements and had a diameter of 0.7 m and a length of 10 m. Fixed displacement boundary conditions were imposed vertically at the ends, whereas horizontal linear springs accounted for lateral pipeline flexibility. The pipe mass was set to 34 500 kg and horizontal dashpots were attached at the ends to obtain dynamic properties equivalent to a full-length pipeline.

A prescribed displacement at the upper towing line end was imposed to obtain the desired velocity of 3 m/s. Due to interaction with the pipe the lower part of the towing line was modeled with beam elements of length 100 mm. The interaction was handled by a beam-to-roller contact element [28] and the Coulomb friction coefficient was set to 0.6. The trawl net was simply represented by a nodal point with a quadratic drag coefficient in the towing direction. Fixed displacement boundary conditions were imposed vertically and in the transverse direction for both the towing node and the trawl net node. Other relevant properties of the FE model are listed in Table 1.

In case of 1 m pipe-seabed clearance the trawl board front edge initially gets into contact with the pipe, while a secondary interaction occurs between the pipe and the towing line, see Fig. 18a. During the first second the pipe accelerates to a velocity of approximately 1 m/s and the board contact points move to the towing line connector, see Figs. 18b and 18c. The connector device is shown in Fig. 10. As the towing line tension increases the board rotates about the connector and the rear part gets lifted upward as shown in Figs. 18c and 18d. The rear part of the board thereafter rotates downward due to the gravitational force acting at the board geometric centre. This brings the board to the configuration in Fig. 18e where it is released and pulled over the pipe section.

In Figs. 12 – 17 annotation "SIM" and "MOD" refer to the simulated response and the model test response, respectively. The responses for 1 m pipe-seabed clearance in Figs. 12 – 14 demonstrate that evident variations exist within the experimental tests. With this

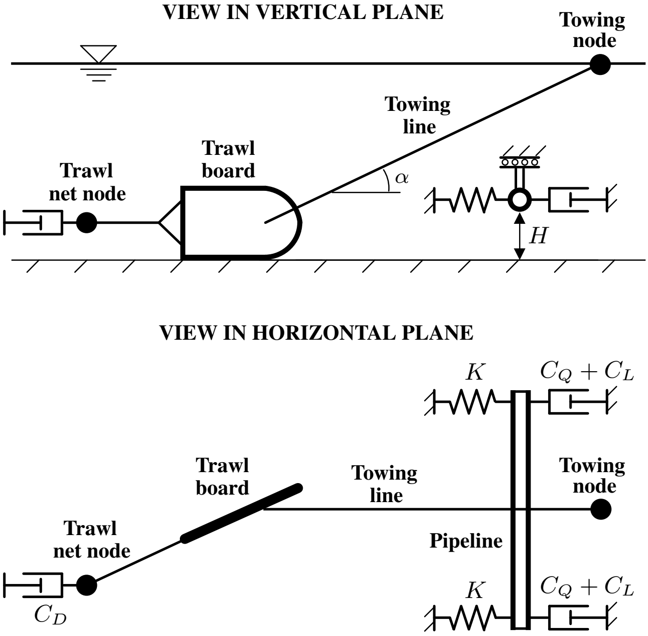

Figure 11: Model test setup

Table 1: FE model properties

Quantity	Symbol	Value	Unit
Penalty stiff. (constant)	$\frac{dF_n}{dg_n}$	24 000	kN/m
Friction coeff. body-pipe	μ	0.3	kN/m
Towing line stiffness		28	kN/m
Towing line tension		≈100	kN
Towing line inclination	α	17	deg.
Trawl board height		2.2	m
Trawl board length		4.0	m
Trawl net quad. damping	C_D	8	$\text{kN/m}^2\text{s}^{-2}$
Pipe-seabed clearance	H	$1, 3$	m
Support linear damping	C_L	10	kN/ms^{-1}
Support quad. damping	C_Q	16	$\text{kN/m}^2\text{s}^{-2}$
Support spring stiffness	K	2	kN/m

in mind the horizontal pipe reaction force in Fig. 12 is regarded as fairly well predicted by the FE simulation. The good accordance is further confirmed by the pipe velocity and the towing line tension which are coincident with the model test behavior until the board is released, see Figs. 13 and 14.

For 3 m pipe-seabed clearance the interaction is initially characterized by towing line contact, see Fig. 19a. As seen in Fig. 16 this leads to a gentle acceleration of the pipe. The board is raised from the seafloor and simultaneously rotated such that it hits into the pipe from below as shown in Fig. 19b. When the towing line tension increases a rotational motion is initiated that lifts the rear part of the board, see Figs. 19c – 19e. Note that the gravitational force does not result in the same behavior as experienced for 1 m pipe-seabed clearance. This is related to differences regarding the establishment of initial board-pipe contact and the location of contact points on the towing line connector. The board is released first when the pipe section reaches the maximum allowable displacement, see Fig. 19e.

In the case with 3 m pipe-seabed clearance the duration, maximum value and build-up of the horizontal pipe reaction force in Fig. 15 agree well with the model test. Note that the dominant force peak at 8 – 9 s interaction time appears because the test rig reached its maximum allowable displacement. Time histories of the pipe velocity and the towing line tension, see Figs. 16 and 17, further demonstrate that the simulation is consistent with the model test.

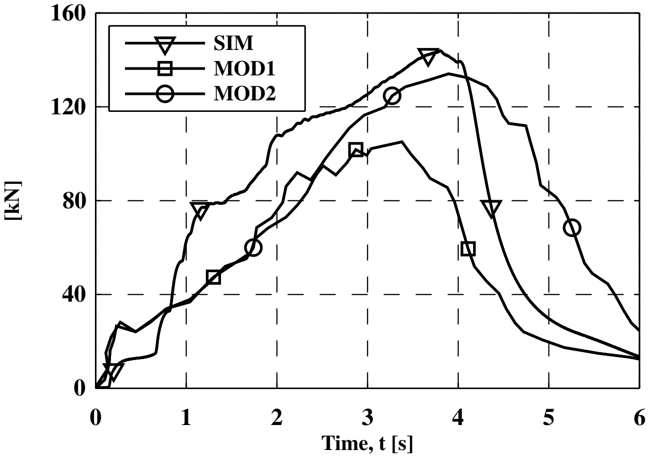

Figure 12: Horizontal pipe reaction force for H = 1 m

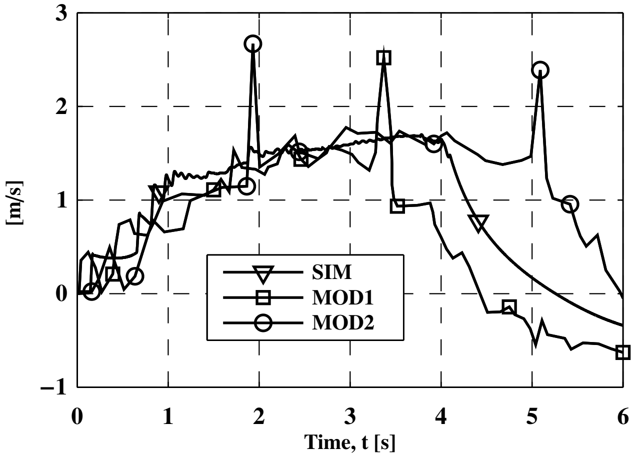

Figure 13: Horizontal pipe velocity for H = 1 m

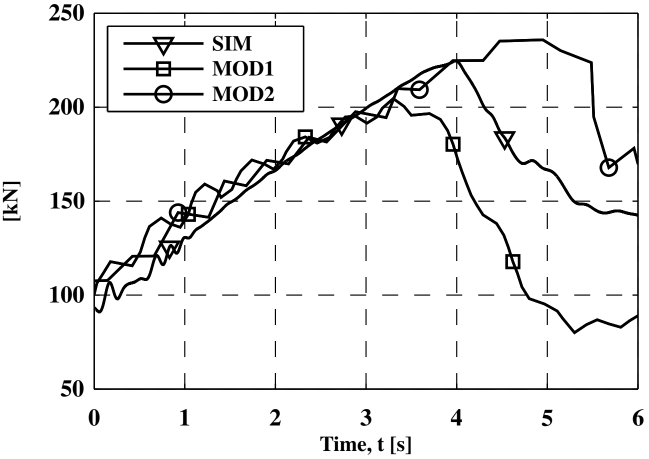

Figure 14: Towing line tension for H = 1 m

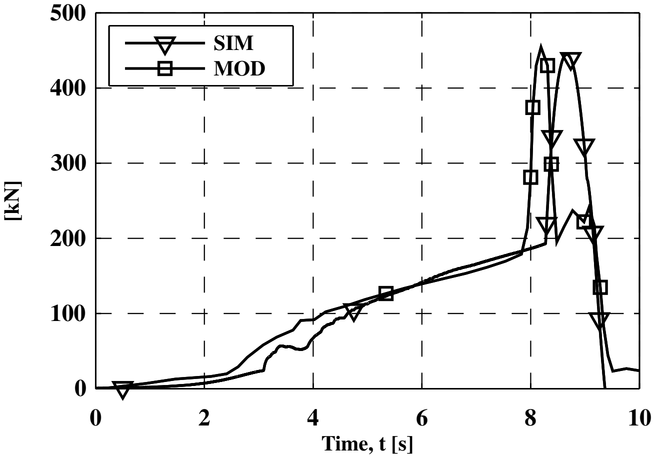

Figure 15: Horizontal pipe reaction force for H = 3 m

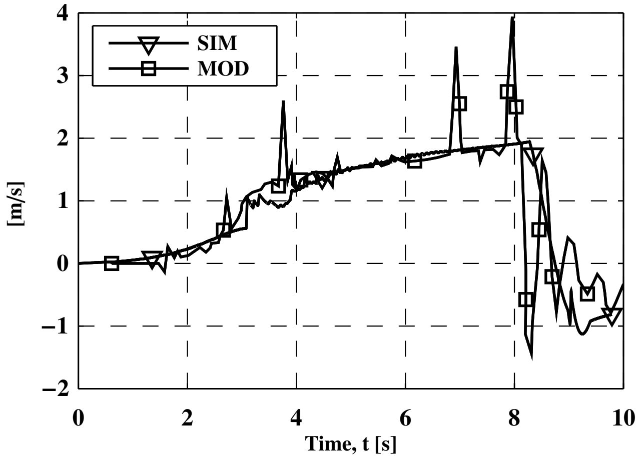

Figure 16: Horizontal pipe velocity for H = 3 m

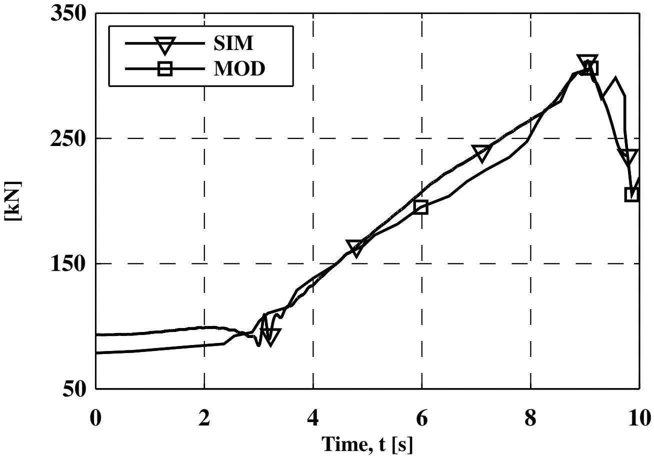

Figure 17: Towing line tension for H = 3 m

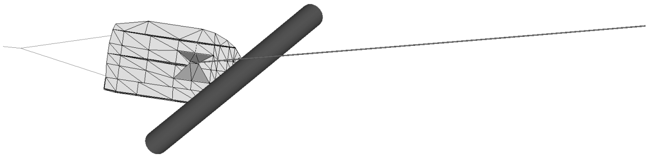

(a) $t = 0.0$ s

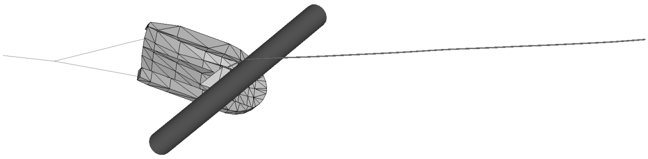

(b) $t = 0.5$ s

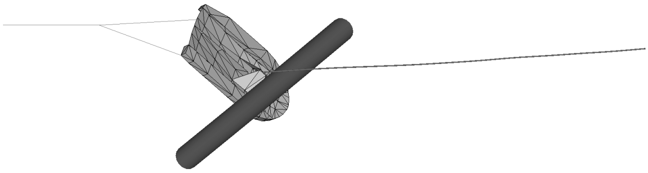

(c) $t = 1.4$ s

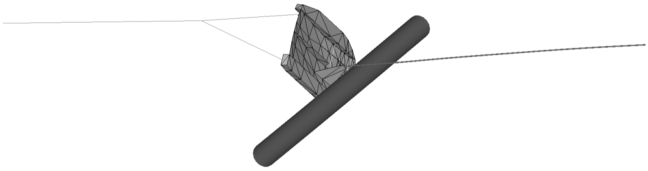

(d) $t = 3.1$ s

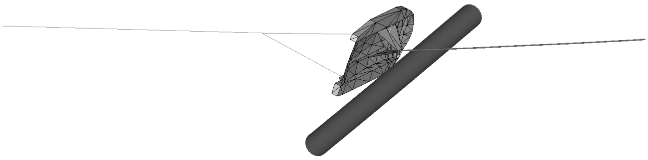

(e) $t = 4.1$ s

Figure 18: Evolution of the pull-over for H = 1 m

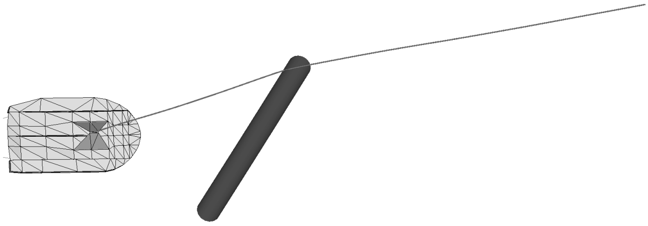

(a) $t = 0.9$ s

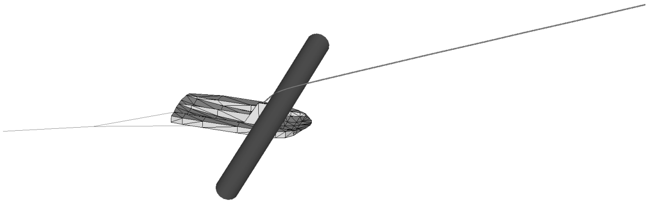

(b) $t = 3.1$ s

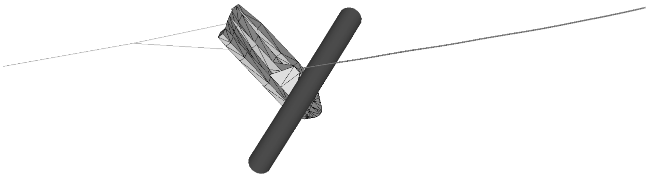

(c) $t = 4.1$ s

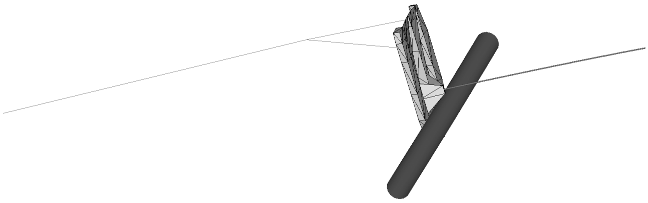

(d) $t = 6.8$ s

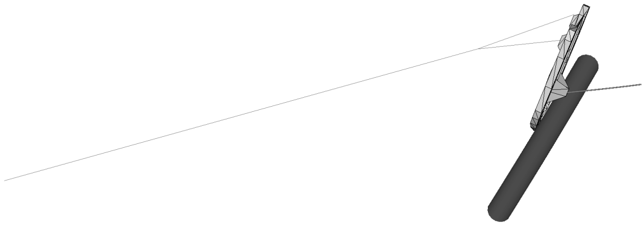

(e) $t = 9.0$ s

Figure 19: Evolution of the pull-over for H = 3 m

4.2 Initial stress stiffness matrix

The effect of the initial stress stiffness matrix $\mathbf{K}_n^{\Delta\delta g_n}$ was investigated in 48 frictionless simulations by means of the established FE model. Note that equivalent linear damping models were employed in these investigations due to issues with the tangent stiffness for the quadratic hydrodynamic loads. The choice of penalty stiffness $\frac{dF_n}{dg_n}$ and the applied interpolation functions for the pipe displacement field may be important for the convergence properties. Two different sets of pipe interpolation functions were therefore applied,

A Use linear interpolation functions for the transverse displacements in Eq. (65) :
$N^l_{\{2,2\}} = N^l_{\{3,3\}} = \frac{1-\eta}{2} \qquad N^l_{\{2,8\}}=N^l_{\{3,9\}}=\frac{1+\eta}{2}$

B Apply the interpolation functions as given in Eq. (66).

Three constant penalty stiffness values reflecting the radial stiffness range of subsea pipelines were employed. The lowest value k_1 was set equal to 3 000 kN/m and resulted in a penetration of 35 mm at initial impact. The other applied values were $k_2 = 10k_1$ and $k_3 = 100k_1$. A time step size of 0.0025 s just sufficient to capture the local eigenperiod associated with k_3 was used. Three convergence criterion norms for residual loads, iterative displacements and energy were applied simultaneously with tolerances $\epsilon_1 = 10^{-7}$ and $\epsilon_2 = 10^{-5}$. The maximum number of iterations prior to subdivision of the time step was set to 20. In Tables 2 and 3 the total number of Newton iteration cycles are listed. "ISS" refers to simulations including the initial stress stiffness matrix as given by Eq. (78), whereas "NO ISS" refers to cases using only the tangent stiffness given in Eq. (79).

Table 2: Accumulated number of iterations for H = 1 m

Case	k_1 NO ISS	k_1 ISS	k_2 NO ISS	k_2 ISS	k_3 NO ISS	k_3 ISS
A, ϵ_1	6 173	6 173	9 656	7 091	6 879	6 504
B, ϵ_1	7 121	6 173	6 706	6 716	6 204	9 025
A, ϵ_2	3 639	3 639	3 690	3 690	3 930	3 938
B, ϵ_2	3 638	3 639	3 690	3 690	3 949	3 937

Table 3: Accumulated number of iterations for H = 3 m

Case	k_1 NO ISS	k_1 ISS	k_2 NO ISS	k_2 ISS	k_3 NO ISS	k_3 ISS
A, ϵ_1	11 804	11 452	8 317	8 313	7 047	7 072
B, ϵ_1	11 804	11 452	8 499	8 313	7 037	7 020
A, ϵ_2	3 792	3 792	4 034	4 034	3 858	3 858
B, ϵ_2	3 792	3 792	4 034	4 034	3 858	3 857

Table 4: Load convergence norm for case: B, ϵ_1, k_2, NO ISS, $\mu = 0$, H = 1 m

Iter. No.	t=1.2 s	t=1.9 s	t=2.4 s	t=3.1 s
0	$3.48 \cdot 10^{-4}$	$5.05 \cdot 10^{-4}$	$4.49 \cdot 10^{-4}$	$4.48 \cdot 10^{-4}$
1	$1.92 \cdot 10^{-5}$	$3.25 \cdot 10^{-5}$	$7.33 \cdot 10^{-6}$	$3.28 \cdot 10^{-6}$
2	$2.05 \cdot 10^{-8}$	$4.23 \cdot 10^{-8}$	$2.82 \cdot 10^{-9}$	$1.30 \cdot 10^{-9}$

According to Table 2 the initial stress stiffness matrix results in both reduced and increased number of iterations when the 10^{-7} convergence tolerances are applied for the case with pipe-seabed clearance of 1 m. In case of 3 m pipe-seabed clearance the additional tangent stiffness contribution is slightly beneficial when the 10^{-7} tolerances are applied. No significant differences are present if the tolerances of 10^{-5} are applied, which yield sufficient accuracy for most applications. Representative convergence characteristics obtained without use of the initial stress stiffness matrix are displayed in Table 4. Iteration step "0" refers to the predictor step in Newton's method. The tabulated values are proportional to the Euclidian norm of the system residual load vector and demonstrate that good convergence rates are achieved. The single stiffness matrix given in Eq. (79) provides thus a satisfactorily performance for contact problems involving corotated beams and straight edges. This finding is consistent with results obtained by Konyukhov and Schweizerhof [24] for a beam with low curvature at the contact point. In their study a different expression for the initial stress stiffness matrix was applied.

4.3 Artificial symmetrization of the slip tangent matrix

The effect of using an artificial symmetrization of the slip non-symmetric tangent matrix $\mathbf{K}_T^{\Delta g_n}$ was investigated for the case with 1 m pipe-seabed clearance. The penalty parameters, time step size and convergence norms presented in Section 4.2 were used. The friction coefficients were taken in the normal range for steel-steel contact with μ_1, μ_2 and μ_3 set equal to respectively 0.2, 0.4 and 0.6. All of the simulations were conducted without the initial stress stiffness matrix. In Table 5 the total number of Newton iteration cycles are presented. "Zero" means that $\mathbf{K}_T^{\Delta g_n}$ is removed from the FE equation system and "Sym" refers to cases using the approximation given in Eq. (93).

Table 5: Accumulated number of iterations for H = 1 m

Case	k_1 Zero	k_1 Sym	k_2 Zero	k_2 Sym	k_3 Zero	k_3 Sym
μ_1, ϵ_1	5 038	5 038	5 809	6 067	8 117	7 921
μ_2, ϵ_1	4 903	4 904	7 379	7 586	8 238	9 428
μ_3, ϵ_1	6 827	6 911	10 247	10 024	8 461	9 247
μ_1, ϵ_2	3 505	3 506	3 577	3 575	3 796	3 776
μ_2, ϵ_2	3 551	3 551	4 351	4 309	3 872	3 950
μ_3, ϵ_2	3 870	3 871	5 690	5 709	4 075	4 065

Table 6: Load convergence norm for case: ϵ_1, k_2, Zero, $\mu = \mu_2$, H = 1 m

Iter. No.	t=1.2 s	t=1.9 s	t=2.4 s	t=3.1 s
0	$4.03 \cdot 10^{-4}$	$4.06 \cdot 10^{-4}$	$3.86 \cdot 10^{-4}$	$3.75 \cdot 10^{-4}$
1	$3.38 \cdot 10^{-5}$	$2.25 \cdot 10^{-6}$	$1.12 \cdot 10^{-6}$	$3.11 \cdot 10^{-6}$
2	$8.30 \cdot 10^{-8}$	$1.63 \cdot 10^{-7}$	$4.91 \cdot 10^{-8}$	$3.00 \cdot 10^{-6}$
3	-	$2.23 \cdot 10^{-9}$	-	$5.23 \cdot 10^{-8}$

According to Table 5 the symmetrization cannot be regarded as beneficial when the convergence tolerances of 10^{-7} are used. If the tolerances are set to 10^{-5} no significant differences can be observed between the two approaches. Representative values of the load convergence norm are presented in Table 6. The tabulated values indicate that the convergence rates are reduced compared to the frictionless case in Table 4. However, according to Table 5 the number of iteration cycles are acceptable when the convergence tolerances are set to 10^{-5}.

5 Conclusions

In this work a contact element for global response prediction of pipelines subject to interaction with a rigid body was developed. A continuous contact geometry representation providing numerical robustness was applied for both the body and the pipeline. The contact kinematics were expressed by means of corotated beam theory for the pipeline and straight line parametrizations for the rigid body. This lead to a robust contact search in terms of two parameters and a computationally efficient overall performance. Information about the contact geometry was included via an initial stress stiffness matrix for normal contact. Due account were made for surface eccentricities and associated moments when the friction model was formulated.

Validation against model tests of trawl-pipeline interaction demonstrated that the characteristic responses were predicted with good accuracy. Consequently, in future research the use of expensive model tests can be reduced and more accurate design loads with reduced variability as compared to current practices [1] may be obtained. The effect of including information about the contact geometry did in practice not improve the convergence rate. Thus, for contact between approximately straight beams and straight edges it is permissible to neglect terms proportional to the normal force when the linearizations are established. Similarly, artifical symmetrization of the developed slip tangent matrix gave the same convergence properties as obtained when the tangent stiffness due to normal gap coupling was set to zero. Regarding computationally efficiency the ratio of simulation time to CPU time was 1:40 during contact on a computer equipped with a 2.66 GHz processor. The convergence rate was characterized by typically 2-3 Newton iterations per time step. Compared to previous FE contact models applied by the authors in similar work [33] this represents a reduction in CPU time by a factor of at least 5.

Acknowledgements

The Norwegian Marine Technology Research Institute (MARINTEK) must be acknowledged regarding source code access and use of the SIMLA computer software. Statoil must also be acknowledged for admission to model test results of trawl board and pipeline interaction.

Appendix: Linearization, variation and discretization of the non-dimensional parameters

The approach presented by Wriggers and Zavarise [19] will now be used to express $\Delta\eta$, $\Delta\bar{\eta}$, $\delta\eta$ and $\delta\bar{\eta}$ in terms of the elemental DOFs. The starting point is to linearize the orthogonality conditions in Eqs. (11) and (12),

$$\Delta\left\{\left[\bar{\mathbf{x}}\left(\bar{\eta}_c\right)-\mathbf{x}\left(\eta_c\right)\right]\cdot\mathbf{x}_{,\eta}\left(\eta_c\right)\right\}=0 \tag{A.1}$$

$$\Delta\left\{\left[\bar{\mathbf{x}}\left(\bar{\eta}_c\right)-\mathbf{x}\left(\eta_c\right)\right]\cdot\bar{\mathbf{x}}_{,\eta}\left(\bar{\eta}_c\right)\right\}=0 \tag{A.2}$$

which yields,

$$\left[\bar{\mathbf{x}}-\mathbf{x}\right]\cdot\left[\Delta\mathbf{u}_{,\eta}+\mathbf{x}_{,\eta\eta}\Delta\eta\right]+\left[\Delta\bar{\mathbf{u}}+\bar{\mathbf{x}}_{,\bar{\eta}}\Delta\bar{\eta}-\Delta\mathbf{u}-\mathbf{x}_{,\eta}\Delta\eta\right]\cdot\mathbf{x}_{,\eta}=0 \tag{A.3}$$

and,

$$\left[\bar{\mathbf{x}}-\mathbf{x}\right]\cdot\Delta\bar{\mathbf{u}}_{,\bar{\eta}}+\left[\Delta\bar{\mathbf{u}}+\bar{\mathbf{x}}_{,\bar{\eta}}\Delta\bar{\eta}-\Delta\mathbf{u}-\mathbf{x}_{,\eta}\Delta\eta\right]\cdot\bar{\mathbf{x}}_{,\bar{\eta}}=0 \tag{A.4}$$

The quantities in Eqs. (A.3) and (A.4) are then expressed in terms of the nodal displacements and solved with respect to $\Delta\eta$ and $\Delta\bar{\eta}$. When organized on matrix format this can be expressed as,

$$\begin{Bmatrix}\Delta\eta\\ \Delta\bar{\eta}\end{Bmatrix}=\begin{Bmatrix}\mathbf{a}\\ \bar{\mathbf{a}}\end{Bmatrix}\begin{Bmatrix}\Delta\mathbf{v}\\ \Delta\bar{\mathbf{v}}\end{Bmatrix} \tag{A.5}$$

and since the variations are computed in a similar way,

$$\begin{Bmatrix}\delta\eta\\ \delta\bar{\eta}\end{Bmatrix}=\begin{Bmatrix}\mathbf{a}\\ \bar{\mathbf{a}}\end{Bmatrix}\begin{Bmatrix}\delta\mathbf{v}\\ \delta\bar{\mathbf{v}}\end{Bmatrix} \tag{A.6}$$

The 1×18 vectors $\mathbf{a}$ and $\bar{\mathbf{a}}$ are expressed by,

$$\begin{Bmatrix}\mathbf{a}\\ \bar{\mathbf{a}}\end{Bmatrix}=\left\{\mathbf{B}^{-1}\right\}\Big[\left\{\mathbf{C}\right\}\left\{\mathbf{N_1}\right\}+\left\{\mathbf{D}\right\}\left\{\mathbf{N_2}\right\}\Big] \tag{A.7}$$

Note that all matrices in Eq. (A.7) are evaluated at the current contact point. The coefficient matrix $\mathbf{B}$ has dimension 2×2 and is given by,

$$\left\{\mathbf{B}\right\}=\begin{bmatrix}\left(\bar{\mathbf{x}}-\mathbf{x}\right)\cdot\mathbf{x}_{,\eta\eta}-\mathbf{x}_{,\eta}\cdot\mathbf{x}_{,\eta} & -\mathbf{x}_{,\eta}\cdot\bar{\mathbf{x}}_{,\bar{\eta}}\\ -\bar{\mathbf{x}}_{,\bar{\eta}}\cdot\mathbf{x}_{,\eta} & \bar{\mathbf{x}}_{,\bar{\eta}}\cdot\bar{\mathbf{x}}_{,\bar{\eta}}\end{bmatrix} \tag{A.8}$$

and the 2×6 matrices $\mathbf{C}$ and $\mathbf{D}$ are expressed as,

$$\{\mathbf{C}\} = \begin{bmatrix} \{\mathbf{x}_{,\eta}\}^\top & -\{\mathbf{x}_{,\eta}\}^\top \\ \{\bar{\mathbf{x}}_{,\bar{\eta}}\}^\top & -\{\bar{\mathbf{x}}_{,\bar{\eta}}\}^\top \end{bmatrix} \tag{A.9}$$

$$\{\mathbf{D}\} = \begin{bmatrix} \{\mathbf{x}-\bar{\mathbf{x}}\}^\top & \mathbf{0}_{1\times 3} \\ \mathbf{0}_{1\times 3} & \{\mathbf{x}-\bar{\mathbf{x}}\}^\top \end{bmatrix} \tag{A.10}$$

The 6×18 matrices $\mathbf{N_1}$ and $\mathbf{N_2}$ contain the displacement interpolation matrices presented in Section 3.3 referred to global coordinates,

$$\{\mathbf{N_1}\} = \begin{bmatrix} \mathbf{N}(\eta_c) & \mathbf{0}_{3\times 6} \\ \mathbf{0}_{3\times 12} & \bar{\mathbf{N}}(\bar{\eta}_c) \end{bmatrix} \tag{A.11}$$

$$\{\mathbf{N_2}\} = \begin{bmatrix} \mathbf{N}_{,\eta}(\eta_c) & \mathbf{0}_{3\times 6} \\ \mathbf{0}_{3\times 12} & \bar{\mathbf{N}}_{,\bar{\eta}}(\bar{\eta}_c) \end{bmatrix} \tag{A.12}$$

If the contact point is located at a body corner the dimensionless parameter $\bar{\eta}$ is fixed and $\bar{\mathbf{a}}$ will vanish. The matrix relations above therefore simplifies to,

$$\{\Delta\eta\} = \{\mathbf{a}\}\begin{Bmatrix} \Delta\mathbf{v} \\ \Delta\bar{\mathbf{v}} \end{Bmatrix} \tag{A.13}$$

$$\{\delta\eta\} = \{\mathbf{a}\}\begin{Bmatrix} \delta\mathbf{v} \\ \delta\bar{\mathbf{v}} \end{Bmatrix} \tag{A.14}$$

where the 1×18 vector $\mathbf{a}$ is given by,

$$\{\mathbf{a}\} = \frac{1}{b_{11}}\Big[\{\tilde{\mathbf{C}}\}\{\mathbf{N_1}\} + \{\tilde{\mathbf{D}}\}\{\mathbf{N_2}\}\Big] \tag{A.15}$$

The coefficient b_{11} is equal to,

$$b_{11} = (\bar{\mathbf{x}} - \mathbf{x}) \cdot \mathbf{x}_{,\eta\eta} - \mathbf{x}_{,\eta} \cdot \mathbf{x}_{,\eta} \tag{A.16}$$

and the 1×6 matrices $\tilde{\mathbf{C}}$ and $\tilde{\mathbf{D}}$ are expressed by,

$$\{\tilde{\mathbf{C}}\} = \Big[\{\mathbf{x}_{,\eta}\}^\top \quad -\{\mathbf{x}_{,\eta}\}^\top\Big] \tag{A.17}$$

$$\{\tilde{\mathbf{D}}\} = \Big[\{\mathbf{x}-\bar{\mathbf{x}}\}^\top \quad \mathbf{0}_{1\times 3}\Big] \tag{A.18}$$

References

[1] Recommended practice DNV-RP-F111, Interference between trawl gear and pipelines, October 2010. Det Norske Veritas, Høvik, Norway; 2010.

[2] Bai Y, Bai Q. Trawl impact, pullover and hooking loads. In: Subsea pipelines and risers. Oxford UK: Elsevier Ltd; 2005, p. 173–948.

[3] Hallquist JO, Goudreau GL, Benson DJ. Sliding interfaces with contact-impact in large-scale Lagrangian computations. Comput Method Appl M 1985;51:107–37.

[4] El-Abassi N, Bathe KJ. Stability and patch test performance of contact discretizations and a new solution algorithm. Comput Struct 2001;79:1473–86.

[5] Krstulović-Opara L, Wriggers P, Korelc J. A C^1-continuous formulation for 3D finite deformational frictional contact. Comput Mech 2002;29:27–42.

[6] Puso MA, Laursen TA. A 3D contact smoothing method using Gregory patches. Int J Numer Meth Eng 2002;54:1161–94.

[7] Stadler M, Holzapfel GA. Subdivision schemes for smooth contact surfaces of arbitrary mesh topology in 3D. Int J Numer Meth Eng 2004;60:1161–95.

[8] Wang F, Cheng J, Yao Z. FFS contact searching algorithm for dynamic finite element analysis. Int J Numer Meth Eng 2001;52:655–72.

[9] Chaudhary AB, Bathe KJ. A solution method for static and dynamic analysis of three-dimensional contact problems with friction. Comput Struct 1986;24:855–73.

[10] Gallego FJ, Anza JJ. A mixed finite element model for the elastic contact problem. Commun Appl Numer M 1989;28:1249–64.

[11] Wriggers P, Van TV, Stein E. Finite element formulation of large deformation impact-contact problems with friction. Comput Struct 1990;37:319–31.

[12] Perić DP, Owen DRJ. Computational model for 3-D contact problems with friction based on the penalty method. Int J Numer Meth Eng 1992;35:1289–309.

[13] Nour-Omid B, Wriggers P. A note on the optimum choice for penalty parameters. Commun Appl Numer M 1987;3:581–5.

[14] Courtney-Pratt JS, Eisner E. The effect of a tangential force on the contact of metallic bodies. In: Proceedings of the Royal Society of London. Series A, Mathematical and Physical Sciences; vol. 238. 1957, p. 529–50.

[15] Simo JC, Taylor RL. Consistent tangent operators for rate-independent elastoplasticity. Comput Method Appl M 1985;48:101–18.

[16] Giannakopoulos AE. The return mapping method for the integration of friction constitutive relations. Comput Struct 1989;32:157–67.

[17] Laursen TA, Simo JC. Algorithmic symmetrization of Coulomb frictional problems using augmented Lagrangians. Comput Method Appl M 1993;108:133–46.

[18] Maker BN, Laursen TA. A finite element formulation for rod/continuum interactions: The one-dimensional slideline. Int J Numer Meth Eng 1994;37:1–18.

[19] Wriggers P, Zavarise G. On contact between three-dimensional beams undergoing large deflections. Commun Numer Meth En 1997;13:429–38.

[20] Zavarise G, Wriggers P. Contact with friction between beams in 3-D space. Int J Numer Meth Eng 2000;49:977–1006.

[21] Litewka P, Wriggers P. Contact between 3D beams with rectangular cross-sections. Int J Numer Meth Eng 2002;2:2019–41.

[22] Litewka P, Wriggers P. Frictional contact between 3D beams. Comput Mech 2002;28:26–39.

[23] Litewka P. Hermite polynomial smoothing in beam-to-beam frictional contact. Comput Mech 2007;40:815–26.

[24] Konyukhov A, Schweizerhof K. Geometrically exact covariant approach for contact between curves. Comput Method Appl M 2010;199:2510–31.

[25] Crisfield MA. A consistent co-rotational formulation for non-linear, three-dimensional, beam elements. Comput Method Appl M 1990;81:131–50.

[26] Yazdchi M, Crisfield MA. Non-linear dynamic behaviour of flexible marine pipes and risers. Int J Numer Meth Eng 2002;54:1265–308.

[27] Mathisen KM. Large displacement analysis of flexible and rigid systems considering displacement-dependent loads and nonlinear constraints. Ph.D. thesis; NTNU, Department of Structural Engineering; 1990.

[28] Sævik S. SIMLA - Theory manual. Trondheim (Norway): Norwegian Marine Technology Research Centre (MARINTEK); 2008 Jun. Report No.: 700254.00.01. Project No.: 700230.

[29] Williams JR, O'Connor R. Discrete element simulation and the contact problem. Arch Method Comput Method E 1999;6:279–304.

[30] Hilber HM, Hughes TJR, Taylor R. Improved numerical dissipation for time integration algorithms in structural dynamics. Earthquake Eng Struc 1977;5:283–92.

[31] Michalowski R, Mroz Z. Associated and non-associated sliding rules in contact friction problems. Arch Mech 1978;30:259–76.

[32] Nygaard I. Trawl - Pipeline span interaction. Model tests. Final report. Trondheim (Norway): Norwegian Marine Technology Research Centre (MARINTEK); 1990 Jun. Report No.: 511191.01-07.

[33] Longva V, Sævik S, Levold E, Ilstad H, Teigen P. Dynamic simulation of free-spanning pipeline trawl board pull-over. In: Proceedings of the ASME 2011 30th International Conference on Ocean, Offshore and Arctic Engineering; 2011 Jun 19-24; Rotterdam, The Netherlands. New York: American Society of Mechanical Engineers; 2011, p. 561–8.

Paper II

Dynamic simulation of subsea pipeline and trawl board pull-over interaction

Vegard Longva[a], Svein Sævik[a], Erik Levold[b], Håvar Ilstad[b]

[a] Department of Marine Technology, Norwegian University of Science and Technology
NO-7491 Trondheim, Norway

[b] Statoil Research Centre,
Arkitekt Ebbells vei 10, NO-7005 Trondheim, Norway

Marine Structures, Vol. 34, 2013, pp. 156 – 184

Abstract

This paper presents a novel strategy based on the finite element method for prediction of fishing gear interference loads on subsea pipelines. Trawl board pull-over interaction is addressed with emphasis on hydrodynamic load representation, handling of pipe-trawl contact and modeling of the trawl gear system. A validation study involving 34 model test runs was carried out for three trawl boards with variation of pipe span height, towing velocity, towing line stiffness and pipe support conditions. The simulated bias of the load impulse was found to be within a 10% margin of the model test measurements. Based on the validated numerical model a sensitivity analysis involving nearly 250 simulations was conducted. The interaction behavior was seen to be greatly influenced by the board-pipe friction coefficient, the tension level in the wire between board and trawl net, the towing line drag properties and the direction of over-trawling.

Keywords: Pipeline; Trawl board; Pull-over; Interference; Fishing gear

1 Introduction

Interaction between fishing gear and subsea pipelines is a crucial challenge for the coexistence of fisheries and offshore hydrocarbon exploitation. Such interacting activities exist for instance in the North Sea where large networks of pipelines have been left exposed on the seabed since the 1970s. In the near future, oil and gas field developments are expected in Arctic waters where bottom trawling is extensively used. The heaviest trawl gear operated today are used in the Arctic fisheries with steel masses up to 10 000 kg [1] and hydrodynamic masses of similar magnitude. Combined with a towing velocity of 2 – 3 m/s over-trawling events may result in a severe utilization of the pipeline capacity. During the last decades optimization of the fishery has resulted in geometry changes of the trawl gear and increased steel masses. This continuous development necessitates regular updating and calibration of the design interference loads. Model testing has traditionally been the preferred method for determination of trawl loads. Such tests suffer from high economical costs, need of truncated models, bias due to small scale ratios and poor ability to effectively reduce the statistical uncertainty. This paper attempts to avoid these drawbacks by proposing a computational strategy for prediction of interference loads between pipelines and fishing gear.

Assessment of pipelines subjected to trawl gear loads is commonly divided into three parts according to load characteristics and response analysis method [2]. The first part focuses on energy absorption and denting of the cross-section due to the initial impact load. The succeeding part is termed the pull-over phase in which the global pipe response due to the long-duration interaction forces is the main concern. This response type is dynamic and requires use of nonlinear finite element (FE) methods due to large lateral displacements, seabed contact, axial force changes and possible elasto-plastic material response. In current design practices simple physical models fitted to experimental results constitute the basis for the recommended pull-over loading. The third part is the rarely occurring hooking event where the trawl gear is assumed to get stuck between the seabed and the pipeline. Hooking design load effects may be obtained by static nonlinear FE analysis of the pipeline subjected to a prescribed vertical lifting height. With regard to current design recommendations [1], the pull-over loading seems to have the largest potential for improvements. The focus in this paper is therefore exclusively on prediction of loads and responses in the pull-over phase.

Research addressing the pull-over phase was initially based on laboratory tests and full-scale tests. Extensive testing was carried out in a Norwegian joint industry project (JIP) in the 1970s to study the interaction between pipelines and trawl gear [3–5]. Regarding pull-over of trawl boards these tests revealed that spanning pipelines were subjected to larger forces than pipelines resting on the seabed, skew passings resulted in reduced loads as compared to perpendicular crossings and that hooking could be regarded as an unlikely occurring event. Nygaard [6] conducted model tests of protective subsea structures subjected to interference with trawl boards and beam trawls, in which the behavior was found to depend on gear geometry, weight of the towed equipment and that small variations of the initial conditions could greatly change the interaction performance. An extensive model test program was conducted in 1990 [7, 8], which forms the basis for the trawl board pull-over loads recommended by DNV today [1]. Verley [9] conducted comprehensive parameter studies based on the recommended pull-over loads, and concluded that the practice of not burying pipelines with diameter larger than 0.4 m was non-conservative for pipes with large compressive axial forces. Further improvements of the recommended design procedures for pull-over interaction has been the focus in many research efforts the last decades, see e.g. Refs. [10–13]. Removal of unnecessary conservatism by use of structural reliability methods on pull-over events was recently addressed by Amdal, Røneid and Etterdal [14].

Numerical methods for response prediction of pipelines subjected to prescribed pull-over loads were introduced in work carried out by Bergan and Mollestad [15] and Guijt and Horenberg [16] in the 1980s. A 2-dimensional simulation model was proposed by Horenberg and Guijt [17] able to predict a peak pull-over load and duration within 10% margin of model test measurements for a fixed pipeline and a beam trawl. A similar 2-dimensional strategy that also allowed lateral pipeline displacements was employed in a JIP in the late 1990s, but was not able to predict realistic loads for trawl boards [18]. A far more general approach was recently used by Igland and Søreide [19] who demonstrated agreement between model tests and FE simulations of a clump weight interacting with a pipeline resting on the seabed. In their work the recommended design load was found too conservative in case of soft seabeds. Based on a similar approach Maalø, Alsos and Sævik [20] validated a clump weight FE pull-over model against model tests of a fixed pipe section at low span heights. They demonstrated that the maximum value of the recommended design load could be halved if span flexibility was accounted for. The first step towards FE simulation of the rather complex interaction between pipelines and trawl boards was initiated by Teigen, Ilstad, Levold and Hansen [21]. They investigated seabed proximity effects of the hydrodynamic mass and used flume tank experiments for determination of the forward-speed induced loads. Their work was later merged into FE simulations, but issues with the contact model between board and pipeline were reported [22]. The performance of the contact model was recently improved and consistent behavior with experimental tests was demonstrated for a handful of cases [23, 24].

This paper outlines a computational strategy which has been partly presented previously in terms of a FE formulation for frictional contact between pipelines and rigid three-dimensional bodies [24]. The present contribution focuses on FE modeling, handling of contact between trawl board and pipe, representation of trawl board hydrodynamic loads and application of the proposed strategy. The objectives of the present effort are summarized as follows,

1) Validate a numerical pull-over model for trawl boards against existing model tests considering variation of span height, towing line stiffness, board geometry, board mass, pipe support condition and towing velocity.

2) Pursue the development of the six degree of freedom (DOF) trawl board hydrodynamic load model used in previous investigations [22].

3) Apply a contact model for board-pipe interaction developed in previous work [23, 24] and validate its performance for the set of parameters listed in item 1).

4) Identify sensitive parameters not examined in previous work and study their influence on the pull-over process.

The behavior of the trawl board and the associated hydrodynamic loads during interaction are far more complex than for clump weights and beam trawls. Hence, if agreement is demonstrated for trawl boards it should be feasible also to achieve consistent behavior for other trawl gear types.

Section 2 outlines the pull-over FE model employed for validation against existing laboratory tests. In Section 3 the main ingredients of a contact element for rigid body and pipeline interaction are presented. The trawl board equation of motion with emphasis on the hydrodynamic loads is addressed in Section 4. Remarks on the proposed computational model, statistics of responses obtained in the validation study and the influence of changes in sensitive parameters are presented in Section 5. Conclusions and recommendations for future work are summarized in Section 6.

2 Pull-over model

An invariable requirement of the proposed computational strategy is that correct pipe responses and realistic trawl board motions during interaction are predicted. In Section 5.3 these features are validated against model tests carried out by MARINTEK in 1990 [7], which in spite of its old age still represent the latest test program of adequate extent for trawl board pull-over interaction. In the tests parameter variation with respect to board geometry, board mass, pipeline support condition, span height, warpline stiffness and towing velocity was conducted with 1:6 scale ratio. According to the test documentation [7] trawl board scale effects and incorrectly represented seabed friction forces could reduce the trawl net spreading force up to 40% when the scale ratio is 1:10. Such effects are of minor importance in this work as the trawl gear equilibrium configuration and the wire tension levels are to be tuned towards the model test measurements.

A full-scale reconstruction of the test setup was made by means of the SIMLA computer software [25], see Fig. 1. As opposed to the model test, only the port side trawl board was modeled and the starboard side of the gear consisted of a sweepline and a towing node at the trawl board location. The whole gear was accelerated to the considered velocities of 2 m/s and 3 m/s, and during pipe interaction the two towing nodes were assumed to maintain their prescribed velocity values. The water depth d was set to 31.2 m and a flat surface with a friction coefficient of 0.3 was used to represent the ocean basin floor. The coefficient was selected from the literature assuming steel-concrete interaction. The applied damping consisted of Rayleigh damping for the pipe with a stiffness-factor of 0.1 s^{-1} and numerical damping introduced via the recommended α-value of -0.05 for the HHT-α time integration scheme [26]. The Rayleigh damping was set equal to the largest possible damping that could be used without artificially reducing the horizontal pipe support reaction forces. Relevant parameters of the FE model which are not described in detail subsequently are given in Table 1. These parameters were chosen based on documentation and video recordings from the model tests.

In case of fixed span conditions the pipe section was not allowed to move horizontally at the supports, whereas dashpots and springs were applied for flexible support conditions

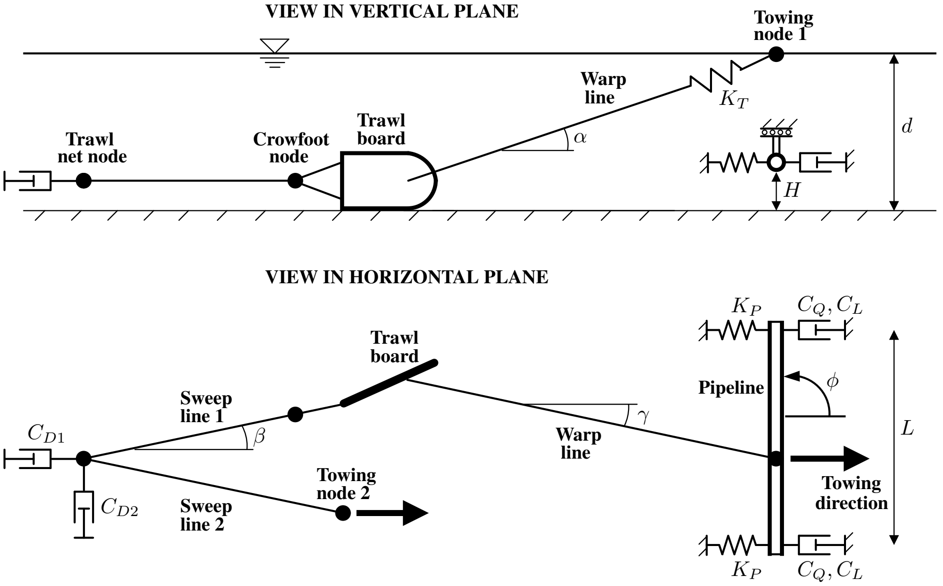

Figure 1: Configuration of FE model

to account for stiffness and damping of a full-length pipeline, see Fig. 1. Trenched support conditions were also considered in the experiments, but due to an uncertain damping level these tests have not been considered in the present work. The support damping for flexible support conditions contained both linear and quadratic contributions. The span height denoted H in Fig. 1 was set to 0 m, 1 m, 2 m, 3 m and 6 m. The pipe had a diameter of 0.7 m and was modeled by 40 corotated linear-elastic beam elements over a length L set to 10 m. The equivalent pipe mass M was 34 500 kg including added mass. Increase of added mass due to seabed proximity was accounted for in accordance with DNV-RP-C205 [27].

A truncated straight warpline was applied in the model tests with a linear spring at the upper end accounting approximately for the stiffness of a full-length warpline, see Fig. 1. The linear spring stiffness K_t was set such that the axial warp stiffness became equal to 28 kN/m and 39 kN/m. Warpline angles α of 17° and 20° were used together with the lowest and highest stiffness values, respectively. The line had a diameter D of 28 mm and an axial stiffness EA equal to 41 000 kN. Corotated beam elements with 4 m length were applied in the upper part, whereas lengths of 0.1 m were used in the lower part due to interaction with the pipe. A standard beam-to-roller contact model with a friction coefficient set to 0.6 was employed to handle the pipe-warp interaction.

To investigate the validity of the truncated warpline model the water depth was increased to 300 m and a 1 200 m warpline with diameter D equal to 28 mm was modeled. Prior to the model tests, static FE analyses of a warpline with the same length were conducted to determine the linear spring stiffness K_t at a tension level of 200 kN. Stiffness and static forces from these analyses were used as a basis for setting the submerged

Table 1: Model properties in full scale

Quantity	Symbol	Value	Unit
Support linear damping	C_L	10.0	kN/ms^{-1}
Support quad. damping	C_Q	16.0	kN/m^{2}s^{-2}
Support spring stiffness	K_P	2.0	kN/m
Pipe section quad. damping	C_P	3.5	kN/m^{2}s^{-2}
Warpline horizontal angle	γ	0.5 – 3.0	deg.
Warpline truncated length		102.5	m
Warpline tension at 3 m/s		$\approx$ 100	kN
Sweepline angle	β	10 – 20	deg.
Sweepline length		110	m
Trawl net resistance at 3 m/s		$\approx$ 150	kN
Water density	ρ	1 000	kg/m^3

weight. The Morison drag load formulation in Eqs. (1) and (2) with relative fluid velocity vector in the normal direction $\dot{\mathbf{v}}_\mathbf{N}$ and in the tangential direction $\dot{\mathbf{v}}_\mathbf{T}$ was applied. The coefficient C_N was presumed independent of inflow angle and set to 1.6 assuming a six-stranded helical wire [28]. C_T was set to 0.1 based on coefficient values for trawl warps applied by Reite [29]. By setting the submerged weight to 30.4 N/m, a chord stiffness of 28 kN/m at 200 kN pre-tension was obtained with a relative fluid velocity of 3 m/s in the towing direction.

$$\mathbf{f}_\mathbf{N} = \frac{1}{2}\rho C_N D||\dot{\mathbf{v}}_\mathbf{N}||\dot{\mathbf{v}}_\mathbf{N} \tag{1}$$

$$\mathbf{f}_\mathbf{T} = \frac{1}{2}\rho C_T D||\dot{\mathbf{v}}_\mathbf{T}||\dot{\mathbf{v}}_\mathbf{T} \tag{2}$$

The sweepline tension and the angle β in Fig. 1 are important boundary conditions for the board prior to and during pipe interaction. For validation purposes their values must be similar to those experienced in the model test. To avoid modeling of a computationally demanding trawl net structure with uncertain drag properties the simple sweepline configuration in Fig. 1 was employed instead. The sweeplines represent the physical lines and 2/3 of the trawl net such that the angle β attains a correct value. Note that the large spread of β in Table 1 is due to differences in hydrodynamic and geometrical properties of the considered trawl boards. The sweepline tension prior to interaction was tuned on a case-to-case basis by using appropriate values for the quadratic dashpot constant denoted C_{D1} in Fig. 1. Because the velocity of towing node 2 remained constant during the interference, the port side sweepline tension during interaction was passively controlled by the transverse motion of the trawl net node. A tension value close to zero in the port side sweepline was obtained by using a very large quadratic dashpot constant C_{D2} in the transverse direction, whereas maximum residual tension was achieved by removal of the transverse drag force at the trawl net node. Tension values in between these extremes were obtained on a case-to-case basis by simple tuning of the transverse drag force. Linear-elastic corotated beams with diameter 28 mm and element lengths of 2 m were employed to model both lines. To properly handle cases with zero sweepline tension, the element lengths were reduced to 0.1 m nearby the board. The vertical position of the crowfoot node in Fig. 1 is an important parameter for the trawl board orientation, and its neutral position was set to half of the board height above the seafloor. A mass of 1 665 kg was assigned to the trawl net node based on documentation from the model test.

3 Trawl board and pipeline interaction

The trawl board and pipe interaction was handled by a penalty-based contact element tailor-made for global response prediction of pipelines interacting with rigid bodies. As illustrated in Fig. 2 the element is three-noded, in which six DOFs belong to a rigid three-dimensional body and twelve DOFs are associated with a corotated beam-pipe element. The rotational DOFs of the pipe are included to get a continuous description of the circular pipe geometry, which is beneficial regarding convergence rate and smoothness of the solution [30]. The geometry of the rigid body is modeled by a three-dimensional grid consisting of plane triangular elements with equal thicknesses t_c. A single geometry element is shown in Fig. 2 where only the circular-shaped edges and the spherical-shaped corners contribute to the contact geometry. The removal of the flat top and bottom surfaces is justified because the bending curvature of the pipe elements is assumed small relative to the straight corotated reference configurations, see e.g. [31, 32].

The geometry representation is beneficial firstly in terms of numerical robustness because the contacting surfaces have a continuous description. Secondly, the involved geometries consist of circular surfaces and spherical surfaces such that the contact kinematics can be expressed in terms of the pipe centroidal line and the straight center lines of the body edges, denoted respectively by $\mathbf{x}(\eta)$ and $\bar{\mathbf{x}}(\bar{\eta})$ in Fig. 2. This enables an efficient contact detection algorithm in terms of two curve parameters for pipe-edge contact and

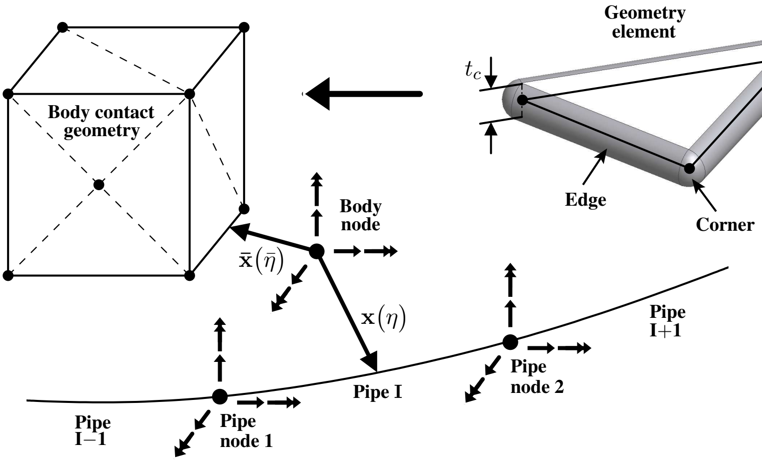

Figure 2: Contact kinematics and representation of body geometry

one curve parameter for pipe-corner contact. Further details about the contact formulation are given in [24].

The trawl boards considered in the model tests are depicted in Fig. 3. Two trawl boards were of the polyvalent type with steel masses of 1900 kg and 2600 kg. These boards are subsequently abbreviated R1900 and R2600. The third trawl board was of the V-type with 2600 kg steel mass and is abbreviated V2600 in the following. The modeled contact geometries are shown in Fig. 4. In total 111 edges and 50 corners were employed for the R1900 board, the R2600 board had 197 edges and 71 corners and the V2600 board was represented by 89 edges and 47 corners. The thickness denoted t_c in Fig. 2 was set to 0.01 m. Relevant properties of the boards are given in Table 2.

Tangential contact forces were represented by a Coulomb model with friction coefficient assumed independent of sliding distance and sliding velocity. The surfaces of the model test trawl boards were covered with paint. Surface properties of the pipe section employed in the tests are regarded as unknown. The test documentation [7] states that a

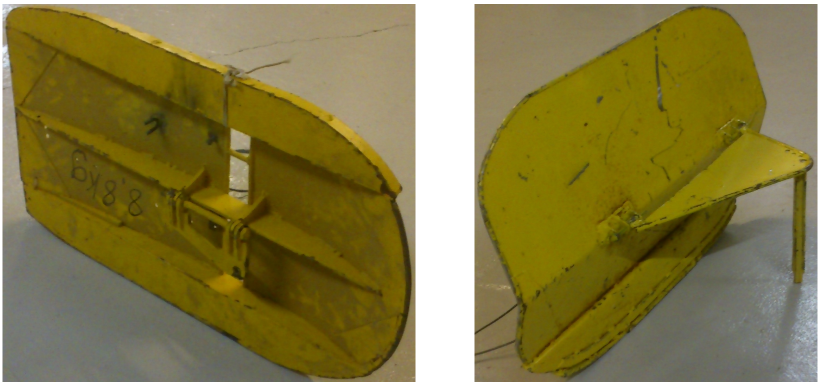

(a) R1900 (b) V2600

(c) R2600

Figure 3: Model test trawl boards

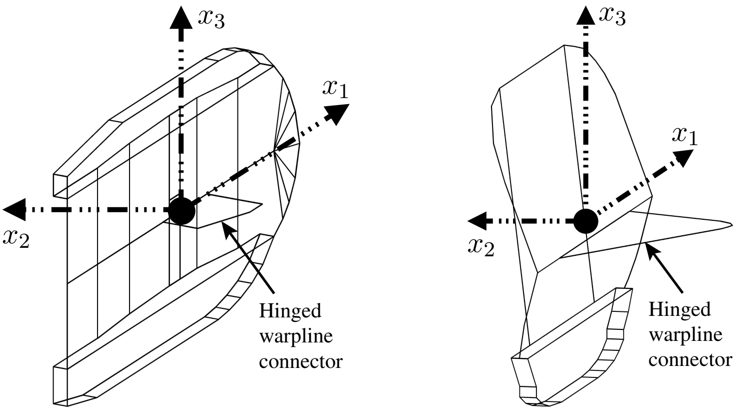

(a) R1900 (b) V2600

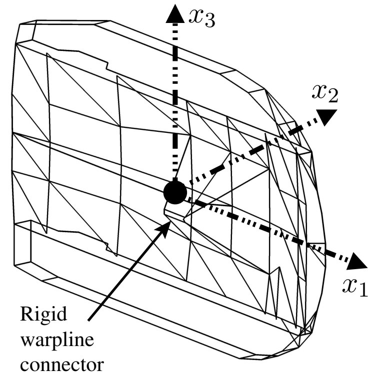

(c) R2600

Figure 4: Contact geometry of trawl boards

concrete-coated pipe was considered, but this claim was not possible to confirm by the underwater video recordings of the tests. Friction coefficients μ in the range $0.4 - 0.6$ were applied in the simulations. This range of coefficient values is considered acceptable in view of the surface degradation experienced during the tests and the different contact geometry configurations occupied in the different test runs. To avoid artificially large tangential displacements in the state of stick, the friction force was linked to the stick tangential displacement by a penalty parameter of $2.5 \cdot 10^6$ kN/m.

The normal contact force was assigned a hyper-elastic constitutive law with a gradually increasing stiffness until a force level of 170 kN was reached at 9 mm penetration. Beyond 170 kN the normal stiffness had a constant value equal to $40 \cdot 10^3$ kN/m. This stiffness is of similar magnitude as the one recommended by DNV-RP-F111 [1] for a bare steel cross-section with the same dimensions as considered in this work. A realistic stiffness characteristic is not regarded important for the pull-over responses aimed for in this work. However, micro-mechanical properties of the contacting surfaces can be represented via the normal stiffness, see e.g. [33], which might be important to take into account for very short durations. Possible damping forces proportional to the penetration velocity at the contact point were neglected as it was observed that realistic values of these forces had no influence on the interaction behavior.

4 Equation of motion for trawl board

The evolution of the pull-over is to a large extent governed by the hydrodynamic loads acting on the board. Ideally the hydrodynamic loads could be estimated in an integrated framework based on computational fluid dynamics and the structural FE method. Due to the extreme CPU resource demands such frameworks are not feasible and use of pre-computed hydrodynamic coefficients are instead favored [21]. In the following a six DOF rigid body load model for the board is outlined. All quantities refer to coordinates defined by the orthonormal base vectors $\mathbf{e_i}$ in Fig. 5 which are fixed to the geometric center of the board. Application of balance laws for linear and angular momentum yields,

$$\begin{aligned}\mathbf{T_g M_g \ddot{v}_g} + \mathbf{T_g C_g}(\mathbf{\dot{v}_g})\mathbf{\dot{v}_g} = &- \mathbf{M_a}(\Theta, \Delta)\mathbf{\ddot{v}} - \mathbf{C_a}(\Theta, \Delta, \mathbf{\dot{v}})\mathbf{\dot{v}} - \mathbf{F_{q2}}(\mathbf{\dot{v}}) \\ &- \mathbf{F_{q1}}(\Psi_1, \Psi_3, \mathbf{\dot{v}}) + \mathbf{F_c} + \mathbf{F_s} + \mathbf{F_w} + \mathbf{F_g}\end{aligned} \tag{3}$$

in which $\mathbf{M_g}$ is the rigid body mass matrix and $\mathbf{C_g}$ is the rigid body Coriolis-centripetal matrix. The corresponding hydrodynamic matrices are denoted $\mathbf{M_a}$ and $\mathbf{C_a}$, respectively. Hydrodynamic forces induced by linear velocities are contained in $\mathbf{F_{q1}}$ and rotational drag damping is included by $\mathbf{F_{q2}}$. The vector $\mathbf{F_c}$ contains contact forces due to interaction with the pipe. Seabed contact forces and trawl gear wire forces are contained in $\mathbf{F_s}$ and $\mathbf{F_w}$, respectively. Gravity and buoyancy forces are included in $\mathbf{F_g}$ with the buoyancy center assumed coincident with the center of gravity (COG). Eccentricity moments are taken into account for the load vectors $\mathbf{F_c}$, $\mathbf{F_s}$, $\mathbf{F_w}$ and $\mathbf{F_g}$. A body moving close to a wall boundary can be subjected to both attractive and repelling forces proportional to its

Table 2: Trawl board properties

Quantity	Symbol	R1900	V2600	R2600	Unit
Height	h	2.10	2.38	2.46	m
Length	l	3.60	4.13	4.44	m
Hydrodynamic thickness / ski thickness	t	0.12	0.14	0.20	m
Steel mass	m	1 900	2 600	2 600	kg
Submerged weight	W	17.7	24.5	24.5	kN
COG rotational mass about x_1-axis	I_1	1 294	1 934	1 885	kgm^2
COG rotational mass about x_2-axis	I_2	3 592	4 439	5 245	kgm^2
COG rotational mass about x_3-axis	I_3	2 298	3 385	3 358	kgm^2
COG x_1-coordinate	x_{g1}	−0.24	0.00	−0.15	m
COG x_2-coordinate	x_{g2}	0.00	0.07	0.00	m
COG x_3-coordinate	x_{g3}	−0.30	−0.42	-0.30	m

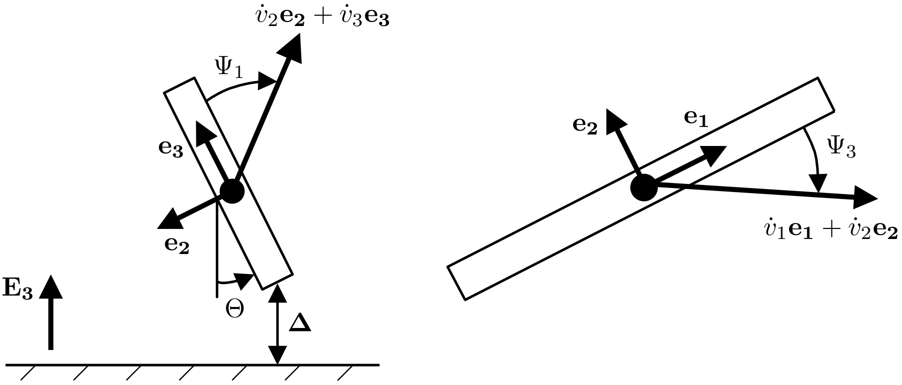

(a) Seabed inclination angle, hydrodynamic angle of attack and seabed gap

(b) Hydrodynamic angle of attack

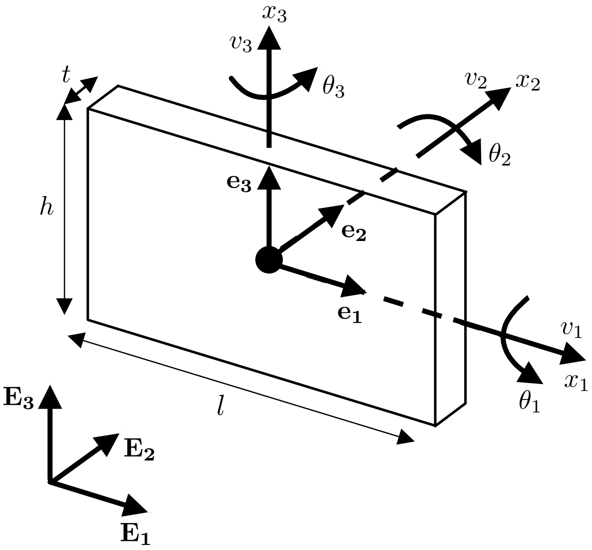

(c) Inertial base vector system ($\mathbf{E_i}$), body-fixed base vector system ($\mathbf{e_i}$), DOFs and dimensions

Figure 5: Trawl board kinematics

velocity squared, see e.g. [34, 35]. Such effects and possible hydrodynamic interaction between the pipe section and the trawl board are neglected in Eq. (3). The vector $\mathbf{v}$ contains the generalized displacements depicted in Fig. 5 and $\mathbf{v_g}$ the corresponding displacements at the COG,

$$\mathbf{v} = \begin{bmatrix} v_1 & v_2 & v_3 & \theta_1 & \theta_2 & \theta_3 \end{bmatrix}^\top \tag{4}$$

$$\mathbf{v_g} = \mathbf{T_g}^\top \mathbf{v} \tag{5}$$

where the eccentricity transformation matrix $\mathbf{T_g}$ is defined in terms of the COG coordinates $\mathbf{x_g}$,

$$\mathbf{T_g} = \begin{bmatrix} \mathbf{I}_{3\times3} & \mathbf{0}_{3\times3} \\ \mathbf{S}(\mathbf{x_g}) & \mathbf{I}_{3\times3} \end{bmatrix} \qquad \mathbf{S}(\mathbf{x_g}) = \begin{bmatrix} 0 & -x_{g3} & x_{g2} \\ x_{g3} & 0 & -x_{g1} \\ -x_{g2} & x_{g1} & 0 \end{bmatrix} \tag{6}$$

Numerical time integration with the HHT-α method [26] and Newton's method are employed to solve Eq. (3). The associated computations are executed in the inertial coordinate system defined by the $\mathbf{E_i}$-triad in Fig. 5. Velocity $\dot{\mathbf{r}}$ and acceleration $\ddot{\mathbf{r}}$ needed in the inertial coordinate system are obtained from,

$$\dot{\mathbf{v}} = \mathbf{T}\dot{\mathbf{r}} \tag{7}$$

$$\ddot{\mathbf{v}} = \dot{\mathbf{T}}\dot{\mathbf{r}} + \mathbf{T}\ddot{\mathbf{r}} \tag{8}$$

in which the 6 × 6 transformation matrix $\mathbf{T}$ and its rate of change with respect to time are given by,

$$\begin{gathered} \mathbf{T} = \begin{bmatrix} \mathbf{Q} & \mathbf{0}_{3\times3} \\ \mathbf{0}_{3\times3} & \mathbf{Q} \end{bmatrix} \qquad \dot{\mathbf{T}} = -\begin{bmatrix} \mathbf{S}(\dot{\boldsymbol{\theta}})\mathbf{Q} & \mathbf{0}_{3\times3} \\ \mathbf{0}_{3\times3} & \mathbf{S}(\dot{\boldsymbol{\theta}})\mathbf{Q} \end{bmatrix} \\ \mathbf{S}(\dot{\boldsymbol{\theta}}) = \begin{bmatrix} 0 & -\dot{\theta}_3 & \dot{\theta}_2 \\ \dot{\theta}_3 & 0 & -\dot{\theta}_1 \\ -\dot{\theta}_2 & \dot{\theta}_1 & 0 \end{bmatrix} \qquad Q_{ij} = \mathbf{e_i} \cdot \mathbf{E_j} \quad i,j = 1,2,3 \end{gathered} \tag{9}$$

The hydrodynamic mass matrix is assumed diagonal at the trawl board geometric center and is therefore expressed according to,

$$\begin{aligned} \text{Diag}\left[\mathbf{M_a}(\Theta,\Delta)\right] &= \begin{bmatrix} m_{a1} & m_{a2} & m_{a3} & I_{a1} & I_{a2} & I_{a3} \end{bmatrix} \\ m_{ai} &= m_{ai}(\Theta,\Delta) \qquad I_{ai} = I_{ai}(\Theta,\Delta) \end{aligned} \tag{10}$$

Seabed proximity effects of the hydrodynamic mass matrix are accounted for by the seabed gap Δ and the seabed inclination angle Θ, see Fig. 5. A third parameter giving the orientation of the base vector $\mathbf{e_1}$ relative to the seabed should also be included. This parameter was excluded because model tests of trawl and pipeline interaction have demonstrated that $\mathbf{e_1} \cdot \mathbf{E_3} \approx 0$ when the board is in contact or close to the seabed, see Fig. 5. A linear interpolation scheme is employed to express the hydrodynamic mass in terms of Δ and Θ. The Δ-value is taken as the minimum distance between the trawl board ski and the seabed, and the seabed inclination angle Θ is defined in terms of the seabed unit normal vector which in this work is coincident with $\mathbf{E_3}$, see Fig. 5a,

$$\Theta = \cos^{-1}\left(\mathbf{E_3} \cdot \mathbf{e_2}\right) - 90^\circ \tag{11}$$

The computation of hydrodynamic mass was carried out based on the geometry of a rectangular box with aspect ratio $\frac{h}{l}$ equal to 0.55 and thickness t set to 0.1 m. Three different gap values Δ were considered in these computations, 0.1 m, $\frac{h}{2}$ and $\frac{3}{2}h$, with the box oriented such that $\mathbf{E_3} \perp \mathbf{e_1}$, see Fig. 5. The seabed gap of $\frac{3}{2}h$ represents the unbounded fluid case in which the hydrodynamic mass is constant. Due to symmetry about $\Theta = 0°$ the computations were executed for seabed inclination angles Θ equal to $0°$, $10°$, $20°$, $30°$, $45°$, $60°$, $75°$ and $90°$. Compared to the unbounded fluid case the value of m_{a2} was found to increase 15 – 20% for $\Delta = 0.1$ m and $|\Theta| < 45°$. An identical representation of the trawl board hydrodynamic mass has previously been applied by Teigen et al. [21] and by Longva et al. [22]. The rigid body mass matrix $\mathbf{M_g}$ is assumed diagonal at the COG and hence expressed identical as in Eq. (10) with $m_{ai} = m$ and $I_{ai} = I_i$. The steel mass m and the mass moments of inertia I_i are given in Table 2 and were estimated by weight and geometric measurements of the boards applied in the laboratory tests.

The hydrodynamic Coriolis-centripetal matrix is also expressed as a function of Δ and Θ. This matrix can be written in terms of the angular velocity components as follows,

$$\mathbf{C_a}(\Theta, \Delta, \dot{\mathbf{v}}) = \begin{bmatrix} 0 & -m_{a2}\dot{\theta}_3 & m_{a3}\dot{\theta}_2 & 0 & 0 & 0 \\ m_{a1}\dot{\theta}_3 & 0 & -m_{a3}\dot{\theta}_1 & 0 & 0 & 0 \\ -m_{a1}\dot{\theta}_2 & m_{a2}\dot{\theta}_1 & 0 & 0 & 0 & 0 \\ 0 & 0 & 0 & 0 & I_{a3}\dot{\theta}_3 & -I_{a2}\dot{\theta}_2 \\ 0 & 0 & 0 & -I_{a3}\dot{\theta}_3 & 0 & I_{a1}\dot{\theta}_1 \\ 0 & 0 & 0 & I_{a2}\dot{\theta}_2 & -I_{a1}\dot{\theta}_1 & 0 \end{bmatrix}$$

$$m_{ai} = m_{ai}(\Theta, \Delta) \qquad I_{ai} = I_{ai}(\Theta, \Delta) \tag{12}$$

The $\mathbf{C_a}$-matrix together with $\dot{\mathbf{T}}$ in Eq. (8) account in a consistent way for hydrodynamic inertia loads associated with rotation of the body-fixed coordinate system. During pipe interaction large angular velocities arise which in combination with the large value of m_{a2} may result in considerable Coriolis-centripetal forces. In Section 5.2 the effect of excluding the $\mathbf{C_a}$-matrix and setting $\dot{\mathbf{T}} = \mathbf{0}$ in Eq. (8) is investigated. Munk moments arising due to linear velocities are normally included in the $\mathbf{C_a}$-matrix, see e.g. [36], but are here excluded because the inviscid flow assumption is inappropriate for flat plate geometries at large angles of attack [37]. The rigid body Coriolis-centripetal matrix $\mathbf{C_g}$ is expressed on the same format as used in Eq. (12) with $m_{ai} = m$ and $I_{ai} = I_i$.

Before pipe interaction, the tension levels of the trawl gear wires and the trawl board orientation must be similar to what were experienced in the model test. These quantities are mainly governed by the hydrodynamic force and associated eccentricity moments induced by the linear relative fluid velocity. A description of these steady-state fluid loads can be established by wind tunnel testing as employed by Reite and Sørensen [38] or by flume tank experiments as conducted by Teigen et al. [21]. Such experiments have not been considered in this work due to economic restrictions and because the boards are considered outdated for prediction of design loads from modern trawl gear. Instead, a coarse approximation of the normal force coefficient was employed based on information given in the DNV-RP-H103 code [28],

$$q_{f2}(\Psi) = hl\Gamma \cdot \begin{cases} \frac{-\,\mathrm{sign}\,(\sin\Psi)}{0.222+\frac{0.283}{\sin\Psi\,\mathrm{sign}(\sin\Psi)}} & \Psi \in [30°,150°] \cup [210°,330°] \\ 0 & \Psi = 0, 180°, 360° \end{cases} \tag{13}$$

Here Ψ refers to the hydrodynamic angles of attack Ψ_1 and Ψ_3 depicted in Fig. 5, h is the board height and l is the board length. The factor Γ accounts for 3-dimensional effects and is set to 0.6 based on the drag coefficient value for a plate with similar aspect ratio inclined 90° to the incident flow in unbounded fluid. Stalling is expected approximately at $\Psi = 30°$ and no attempt is made to predict reasonable q_{f2}-values for $\Psi \in [-30°, 30°] \cup [150°, 210°]$. On this interval the force coefficient is simply obtained by linear interpolation of the discrete values given in Eq. (13). With this the board is simply modeled as a pure drag device without contributions from lift-induced forces and moments. Hence, regarding validity of the numerical model it is a prerequisite that Ψ_1 and Ψ_3 stay within the interval $[30°, 150°] \cup [210°, 330°]$ when the board interacts with the pipe. Prior to interaction there is relative fluid motion mainly in the x_1x_2-plane, and in case of high span heights considerable velocities appear also along the x_3-axis. The loads due to linear velocities are therefore expressed as follows,

$$\mathbf{F_{q1}}(\Psi_1, \Psi_3, \dot{\mathbf{v}}) = \frac{1}{2}\rho \begin{bmatrix} q_{f1}|\dot{v}_1|\dot{v}_1 \\ q_{f2}(\Psi)U^2 \\ q_{f3}|\dot{v}_3|\dot{v}_3 \\ 0 \\ 0 \\ 0 \end{bmatrix} \qquad \begin{aligned} q_{f1} &= 2C_f hl\left(1+2\tfrac{t}{l}\right) \\ q_{f3} &= 2C_f hl\left(1+2\tfrac{t}{h}\right) + C_{p3}lt \\ \\ C_f &= 0.00615 \\ C_{p3} &= 0.5 \end{aligned} \tag{14}$$

$$\begin{aligned} \Psi &= \Psi_3 \quad , \quad U^2 = \dot{v}_1^2 + \dot{v}_2^2 \qquad \text{if} \qquad |\dot{v}_1| > |\dot{v}_3| \\ \Psi &= \Psi_1 \quad , \quad U^2 = \dot{v}_3^2 + \dot{v}_2^2 \qquad \text{if} \qquad |\dot{v}_3| > |\dot{v}_1| \end{aligned}$$

where C_f and C_{p3} are associated with skin friction and pressure drag. During pipe interaction the relative fluid motions are unsteady and rather complex due to pipeline and seabed proximity effects. Equations (13) and (14) are strictly valid only for steady-state conditions in unbounded fluid and must therefore be regarded as a rough approximation of the true hydrodynamic loads. In view of this approximation possible eccentricity moments in DOF 4 and DOF 6 are neglected in Eq. (14). This is justified since experimental tests [37, 39] have demonstrated that the normal force in DOF 2 acts nearby the geometric center for $\Psi \in [30°, 150°] \cup [210°, 330°]$. Transient lift loads are induced when there is a sudden change of the relative fluid velocity vector, see e.g. [40]. Such loads are present during the initial board-pipe interaction phase when the board decelerates and the angle of attack Ψ_3 undergoes a rapid change away from its steady value. However, as contact loads and inertia loads dominate the equilibrium balance in this phase, the contribution from transient lift loads is conveniently neglected in Eqs. (13) and (14).

A suitable rotational damping model must be employed because large angular velocities arise when the board interacts with the pipe. This damping is beneficial also for removal of unsteady motions when the trawl gear is accelerated to the desired velocity. In

DOF 5 the damping was estimated by integration of skin friction forces when considering the board subjected to a pure angular velocity $\dot{\theta}_2$, whereas a coupled damping model based on the total velocity normal to the board was applied to obtain estimates for DOF 4 and DOF 6. The damping model is summarized as follows,

$$\mathbf{F_{q2}}(\dot{\mathbf{v}}) = \frac{1}{2}\rho \begin{bmatrix} 0 \\ 0 \\ 0 \\ q_{m1} \\ q_{m2} \\ q_{m3} \end{bmatrix} \qquad \begin{aligned} q_{m1} &= -C_p \int\limits_{-h/2}^{h/2} \int\limits_{-l/2}^{l/2} x_3 \dot{v}_N \left|\dot{v}_N\right| \mathrm{d}x_1 \mathrm{d}x_3 \\ q_{m3} &= C_p \int\limits_{-h/2}^{h/2} \int\limits_{-l/2}^{l/2} x_1 \dot{v}_N \left|\dot{v}_N\right| \mathrm{d}x_1 \mathrm{d}x_3 \\ \dot{v}_N &= \dot{v}_2 + x_1 \dot{\theta}_3 - x_3 \dot{\theta}_1 \\ q_{m2} &= 2\dot{\theta}_2 |\dot{\theta}_2| C_f \int\limits_{-h/2}^{h/2} \int\limits_{-l/2}^{l/2} \left(x_1^2 + x_3^2\right)^{\frac{3}{2}} \mathrm{d}x_1 \mathrm{d}x_3 \\ C_p &= 1.7 \qquad C_f = 0.00715 \end{aligned} \tag{15}$$

where the coefficients C_f and C_p are assumed constant over the board surface. The damping in DOF 4 and DOF 6 is pressure-induced and serve as a passive magnitude control for the Coriolis-centripetal forces emerging from the $\mathbf{C_a}$-matrix and $\dot{\mathbf{T}}$, see Eqs. (8) and (12). Due to the large value of the hydrodynamic mass, m_{a2}, these forces could easily be over-predicted if the angular velocity becomes too large. The selected value of C_p in Eq. (15) was set based on comparison with video recordings and measured time histories from the experimental tests.

5 Results and discussion

The considered simulation cases are summarized in Tables 3 and 4, where ID tags A – L are used for result identification subsequently. These cases are further separated into span heights H ranging from 0.0 m to 6.0 m involving in total 34 simulation runs. Throughout this section annotation SIM designates the simulated responses and MOD refers to the model test measurements. Due to property right issues all results are normalized with respect to the averaged model test response.

5.1 Importance of the pressure-induced rotational damping model

The importance of the pressure-induced quadratic rotational damping in Eq. (15) is here demonstrated for case I in Table 4 with 1 m span height. As shown in Fig. 6a, initial contact is established at the board leading edge, and immediately a large positive rotation about the x_3-axis in Fig. 4c takes place such that the trailing edge hits into the pipe at 1.25 s interaction time, see Fig. 6b. A combined upward translation and positive rotation about the x_1-axis then follows until the board is released from the pipe as seen in Fig. 6c.

ID	Board	Pipe B.C.	Velocity [m/s]	Warp stiff. [kN/m]
A	R1900	Fixed	2.0	28.0
B	R1900	Fixed	2.0	39.0
C	R1900	Flexible	2.0	28.0
D	V2600	Fixed	2.0	28.0
E	V2600	Fixed	3.0	28.0
F	V2600	Fixed	3.0	39.0

Table 3: Identification of simulation cases

ID	Board	Pipe B.C.	Velocity [m/s]	Warp stiff. [kN/m]
G	V2600	Flexible	3.0	28.0
H	R2600	Fixed	2.0	28.0
I	R2600	Fixed	3.0	28.0
J	R2600	Fixed	3.0	39.0
K	R2600	Flexible	2.0	28.0
L	R2600	Flexible	3.0	28.0

Table 4: Identification of simulation cases

In Fig. 7 annotation WOCC refers to simulations excluding the hydrodynamic Coriolis-centripetal loads and C_p refers to Eq. (15). The force histories demonstrate that a C_p-value of 1.7 gives good agreement with the model test in terms of duration, the initial interaction phase and maximum load. A significant reduction of the duration results when the C_p-coefficient is set to 1.0. By comparison with the corresponding WOCC response in Fig. 7 it is evident that the reduced interaction time occurs due to over-prediction of the angular velocity components and the hydrodynamic Coriolis-centripetal loads. Thus, the pull-over evolution depends strongly on the pressure-induced rotational damping and non-conservative behavior may result if the C_p-coefficient is set too low. According to Fig. 7 there are small differences between the simulations denoted WOCC in spite of the distinct damping levels employed. This indicates that the damping level associated with $C_p = 1.7$ is not too conservative.

5.2 Importance of the hydrodynamic Coriolis-centripetal loads

In rigid body motions with small angular velocities, such as in seakeeping analysis of ships and floating structures, the Coriolis-centripetal loads are usually neglected, see e.g. [41]. The effect of excluding the hydrodynamic part of these loads was investigated by removing the $\mathbf{C_a}$-matrix in Eq. (3) and setting $\dot{\mathbf{T}} = \mathbf{0}$ in Eq. (8).

Without the hydrodynamic Coriolis-centripetal loads the motion of the R2600 board was found to deviate from the model test behavior for fixed support conditions with $H \geq 2.0$ m. This is illustrated in Fig. 8 where a dominant negative rotation about the x_2-

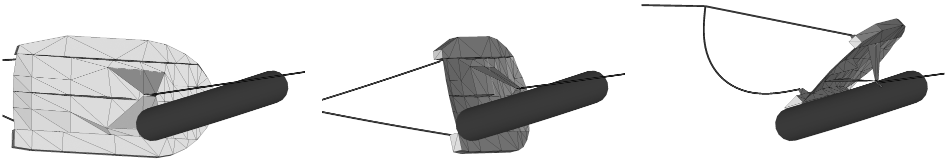

(a) 0.0 s interaction time (b) 1.1 s interaction time (c) 1.6 s interaction time

Figure 6: Evolution of pull-over, ID: I, H=1 m

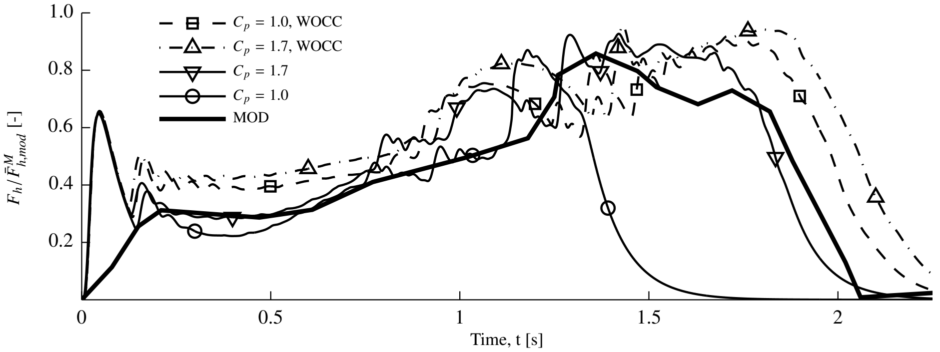

Figure 7: Horizontal pipe reaction force, ID: I, H = 1 m

axis in Fig. 4c occurs due to the lever arm between the COG and the warpline attachment point. By including hydrodynamic inertia loads associated with rotation of the body-fixed coordinate system the same motion as experienced in the model test was captured. As seen in Fig. 9 the interaction is then rather characterized by a positive rotation about the x_2-axis. The difference in interaction behavior occurs due to the Coriolis-centripetal force contribution, $m_{a2}\dot{\theta}_1\dot{v}_2$, which increases from 0 kN to 40 kN in the x_3-direction between 3.7 s and 4.8 s interaction time, see Figs. 9b and 9c. As demonstrated in Section 5.1 there is a strong interplay between the pressure-induced rotational damping and the hydrodynamic Coriolis-centripetal forces. Consequently, the board motion would deviate from the consistent behavior in Fig. 9 if the coefficient C_p in Eq. (15) is altered significantly.

In contrast the R1900 and the V2600 boards had similar motions as in the model tests regardless of the Coriolis-centripetal loads. For the R1900 board the Coriolis-centripetal loads do not affect the motion because the towing velocity is reduced to 2.0 m/s and the value of m_{a2} is reduced by 40% compared to the R2600 geometry. The interaction behavior of the V2600 board is governed by the hinged warpline connector, see Fig. 3b, and has therefore an average rotational velocity $\dot{\theta}_1$ that is approximately 50% lower than for the R2600 board.

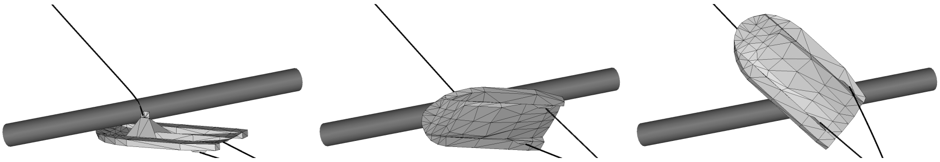

(a) 3.2 s interaction time (b) 4.2 s interaction time (c) 4.8 s interaction time

Figure 8: Pull-over evolution without hydrodynamic Coriolis-centripetal loads, ID: I, H=3 m

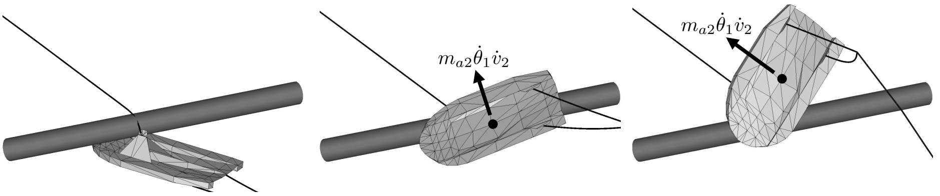

(a) 3.2 s interaction time (b) 4.2 s interaction time (c) 4.8 s interaction time

Figure 9: Pull-over evolution with hydrodynamic Coriolis-centripetal loads included, ID: I, H=3 m

5.3 Validation against model test results

The horizontal pull-over force is the primary response variable and should in principle agree with the model test in terms of duration, force build-up and maximum load level. The available data from the model tests consist of measured time histories, maximum response values and pull-over force impulses. The pull-over force was derived via measurements of the pipe acceleration in the tests. To avoid uncertainties due to the acceleration measurements the pipe reaction forces have instead been emphasized in this work. A typical time history of the total horizontal reaction force for span heights $H \geq 2$ m is shown in Fig. 10. The interaction is initially characterized by contact between the warpline and the pipe. In this phase the board is raised from the seabed and a gentle increase of the horizontal reaction force takes place. In case of fixed pipe support conditions an abrupt force increase similar as in Fig. 10 occurs when the board gets into contact with the pipe at time T_w. During the board-pipe interaction phase the warpline tension increases linearly with time and raises the total horizontal reaction force to the maximum value denoted F_h^M in Fig. 10. The time instant T_t in Fig. 10 is used to quantify the pull-over duration, and is taken at the instant when an evident drop of the horizontal force takes place. Loss of contact between board and pipe is designated by T_I and is employed for computation of the pull-over force impulses,

$$
\begin{aligned}
&I_t = \int_{0}^{T_I} \sqrt{F_{hp}^2 + F_v^2}\mathrm{d}t \qquad I_p = \int_{T_w}^{T_I} \sqrt{F_{hp}^2 + F_v^2}\mathrm{d}t \\
&F_{hp} = F_h + Ma_h + C_P|v_h|v_h
\end{aligned}
\tag{16}
$$

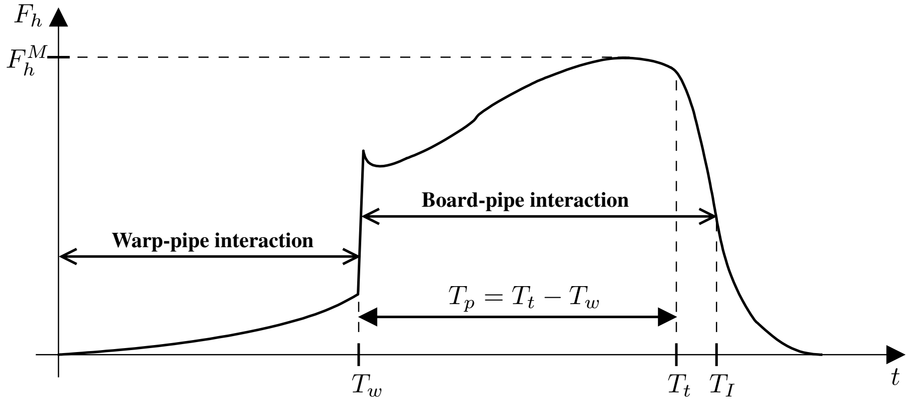

Figure 10: Definition of characteristic responses

in which F_v denotes the total vertical pipe reaction force and F_{hp} refers to the horizontal pull-over force. The acceleration a_h and the velocity v_h of the pipe are only relevant for flexible support conditions and are taken positive in the direction of over-trawling. The employed values of M and C_P are given in Section 2.

The trawl gear was not settled to the exact same steady configuration after the acceleration phase in the model tests. Differences could be observed prior to interaction for the warpline tension, hit position along the pipe and the sweepline tension level. These observations imply that the trawl board orientation also was slightly changed. In some runs small rotational board motions prior to impact were present as the boards bumped into obstacles on the ocean basin floor. These variations influence the characteristic responses and could therefore give an indication of the expected bias level for the simulation model. To quantify the variability the coefficient of variation (COV) was computed,

$$\begin{aligned} V(X_{mod}) &= 100\% \cdot \frac{S_{X,mod}}{\bar{X}_{mod}} \qquad \bar{X}_{mod} = \frac{1}{N_r}\sum_{k}^{N_r} X_{mod,k} \\ S^2_{X,mod} &= \frac{1}{N_r - 1}\sum_{k}^{N_r}\left[X_{mod,k} - \bar{X}_{mod}\right]^2 \end{aligned} \tag{17}$$

in which the generalized response parameter X_{mod} refers to either $T_{t,mod}$, $F^M_{h,mod}$ or $I_{t,mod}$. The COV was computed only for tests repeated at least three times ($N_r \geq 3$).

The bias $W\big(X\big)$ was taken as the ratio of the simulated response X_{sim} and the averaged model test response $\bar{X}_{mod}$ from Eq. (17),

$$W\big(X\big) = \frac{X_{sim}}{\bar{X}_{mod}} \tag{18}$$

The pull-over force impulse is regarded as the most important parameter for the global pipe response since it contains information of both the duration and the load level. The averaged impulse bias $\bar{W}(I)$ and its standard deviation $Z(I)$ were obtained by,

$$\bar{W}(I) = \frac{1}{N_H}\sum_{i}^{N_H}\frac{I_{sim,i}}{\bar{I}_{mod,i}} \qquad \bar{I}_{mod,i} = \frac{1}{N_r}\sum_{k}^{N_r} I_{mod,k} \tag{19}$$

$$Z^2(I) = \frac{1}{N_H - 1}\sum_{i}^{N_H}\left[W(I_i) - \bar{W}(I)\right]^2 \tag{20}$$

where N_H denotes the number of considered span heights H for the relevant test cases.

As discussed in Section 4, a prerequisite for the validation is that the hydrodynamic angles of attack Ψ_1 and Ψ_3 are kept outside the intervals $[-30°, 30°] \cup [150°, 210°]$. Representative time histories of the angles are shown in Fig. 11, where the second annotation letter refers to the span height in meters and the first letter to the ID tags in Tables 3 and 4. The runs with the V2600 board and the R2600 board are seen to be kept within the admissible range of Ψ_1 and Ψ_3 throughout the pull-over. The first occurrence of board-pipe contact corresponds to the abrupt change of attack angles in Fig. 11. Prior to the board-pipe interaction phase the simulation runs with the R1900 board violate the validity limits by about $5° - 10°$. This violation is regarded acceptable because the horizontal pull-over force is only $5 - 10$ kN in this phase, and the angles of attack are quickly brought within the admissible range when board-pipe contact is established.

The trawl board orientation just prior to the board-pipe interaction phase was realized to be important for the pull-over evolution for span heights $H \geq 2$ m. The orientation is governed by possible eccentricity moments in DOF 4 and DOF 6 associated with Eq. (14) and the attachment points of the warpline and the sweepline. As noted in Section 4 the eccentricity moments were neglected in view of the rough approximation inherent in Eqs. (13) and (14). To get the same board orientation as observed in the tests for $H \geq 2$ m, the position of the crowfoot node depicted in Fig. 1 was shifted vertically on the range ± 0.5 m away from its neutral position on a case-to-case basis. Note that no documentation was

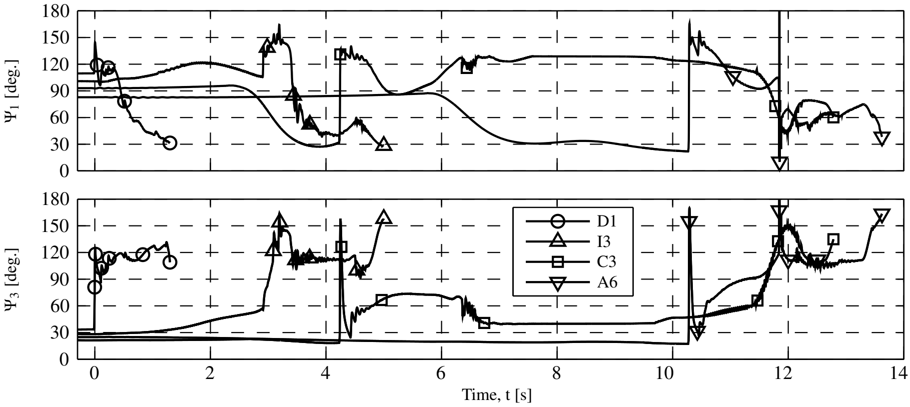

Figure 11: Hydrodynamic angles of attack

Table 5: Statistics of characteristic responses

ID	H [m]	$V(T_{t,mod})$ % [-]	$V(F_{h,mod})$ % [-]	$V(I_{t,mod})$ % [-]	$W(T_w)$ [-]	$W(T_t)$ [-]	$W(F_h)$ [-]	$W(I_t)$ [-]	$\bar{W}(I_t)$ [-]	$Z(I_t)$ [-]
A	0.0	-	3.1	-	-	-	1.076	-	1.065	0.077
	1.0	-	-	-	-	1.111	1.126	1.145		
	2.0	4.1	9.4	17.6	1.064	0.974	1.195	1.111		
	3.0	0.0	3.0	2.5	1.026	0.986	1.149	1.021		
	6.0	0.4	0.9	1.8	1.027	0.980	1.136	0.979		
B	3.0	0.8	1.4	0.5	1.069	1.005	1.143	0.991	-	-
C	0.0	-	-	-	-	-	1.021	-	-	-
	1.0	3.7	5.0	5.4	-	0.833	1.250	0.848		
	3.0	2.6	4.3	-	1.158	0.980	1.216	-		
D	6.0	1.1	1.6	3.4	1.000	1.010	1.246	1.004	-	-
E	1.0	0.0	13.0	6.8	-	1.000	0.983	0.967	0.940	0.038
	3.0	1.5	7.0	4.6	1.075	1.035	0.900	0.896		
	6.0	0.0	0.3	1.7	1.006	1.039	1.034	0.956		
F	1.0	4.0	3.4	1.1	-	1.046	1.103	1.082	1.002	0.084
	3.0	0.0	3.5	4.9	0.984	0.971	0.896	1.009		
	6.0	2.6	4.5	2.6	1.027	1.061	1.078	0.914		
G	1.0	10.2	11.3	12.7	-	0.885	1.152	0.833	0.916	0.079
	3.0	7.4	1.2	6.5	0.926	0.986	1.137	0.923		
	6.0	3.5	0.3	2.7	0.967	1.037	1.186	1.004		
H	1.0	3.8	10.1	1.3	-	0.880	1.038	1.141	0.966	0.164
	3.0	0.6	2.5	3.2	1.205	0.941	1.137	0.817		
	6.0	1.4	1.4	2.3	1.044	1.018	1.210	0.942		
I	0.0	-	1.2	-	-	-	1.146	-	1.098	0.096
	1.0	6.7	10.9	6.3	-	0.981	0.987	1.109		
	2.0	4.3	1.8	6.2	1.171	1.009	1.034	0.876		
	3.0	2.1	1.1	2.5	1.145	1.042	1.153	1.004		
	6.0	0.6	2.7	3.6	0.964	1.007	1.167	0.982		
J	1.0	3.8	2.4	9.4	-	0.919	1.012	0.895	0.901	0.049
	3.0	2.5	6.4	0.6	1.030	0.993	1.049	0.855		
	6.0	0.7	0.7	5.1	1.050	1.029	1.139	0.952		
K	6.0	-	-	-	1.076	1.005	1.207	-	-	-
L	0.0	-	9.2	-	-	-	1.047	-	-	-
	1.0	10.7	16.7	28.7	-	0.876	1.082	0.721		
	3.0	2.0	7.2	-	1.274	0.983	1.109	-		

available for the sweepline-board attachment configuration employed in the tests.

Statistics of the characteristic responses are given in Table 5 with the ID tags A – L defined in Tables 3 and 4. Duration and impulse for 0.0 m span height are not tabulated due to the short interaction time. No impulses are reported for runs where the maximum allowable pipe displacement was reached, but duration and horizontal force just prior to the pipe hitting into the end stoppers are given. According to Table 5 the model test COVs denoted by $V(X_{mod})$ are larger than 10% in 5 of 34 tests. Slight differences were present for the initial conditions prior to interaction in these tests. Since the initial conditions cannot be exactly reconstructed the simulation bias is expected to be at least 10%. Con-

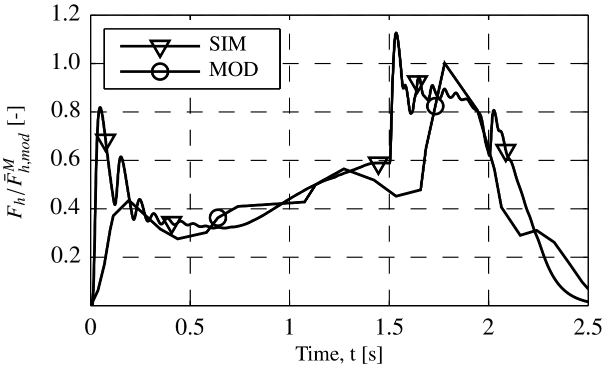

Figure 12: Horizontal pipe reaction force, ID: A, H = 1 m

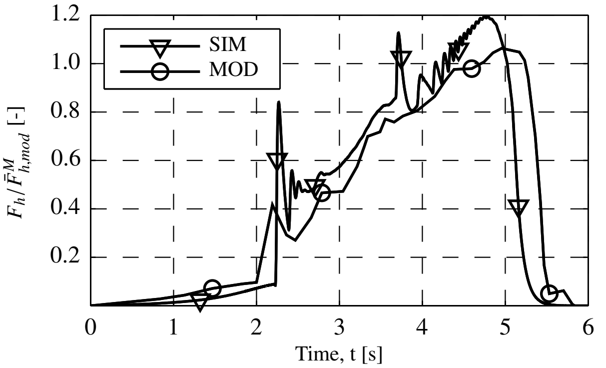

Figure 13: Horizontal pipe reaction force, ID: A, H = 2 m

sidering that the tabulated COVs are based on only three observations the variability is negligible in the majority of the tests.

According to Table 5 the bias W of the duration, the impulse and the maximum horizontal force for the R1900 board are in the range 1.15-1.20 for some of the simulations with fixed pipe supports. These bias values might be regarded as too large, but according to the force histories in Figs. 12 and 13 the model test response is actually well captured for these runs. In case of flexible pipe supports the bias is of the same magnitude, and also here the simulation predicts the behavior experienced in the tests satisfactorily, see Fig. 14. For 3 m span height the characteristic board-pipe locking phenomenon experienced in the tests is captured. This is illustrated in Fig. 15 where the warpline connector device locks onto the pipe such that the board-pipe relative motion is negligible until the instant the pipe reaches its maximum allowable displacement of 8.5 m. The force spike at 11.9 s interaction time in Fig. 14 corresponds to the instant the pipe hits into the end stopper.

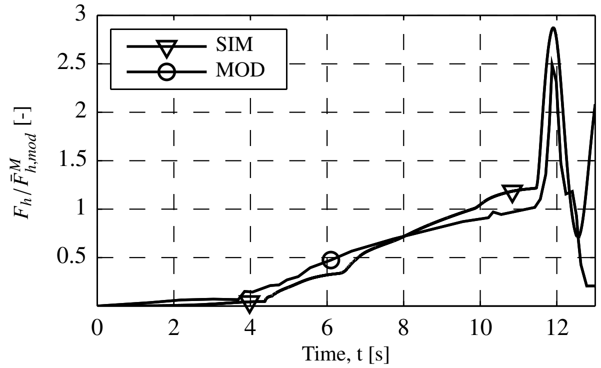

Figure 14: Horizontal pipe reaction force, ID: C, H = 3 m

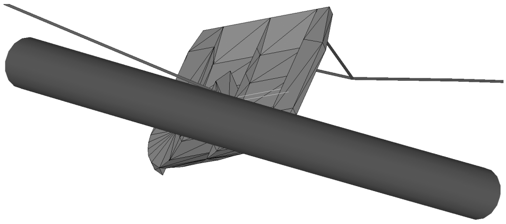

Figure 15: Board-pipe locking, ID: C, H = 3 m

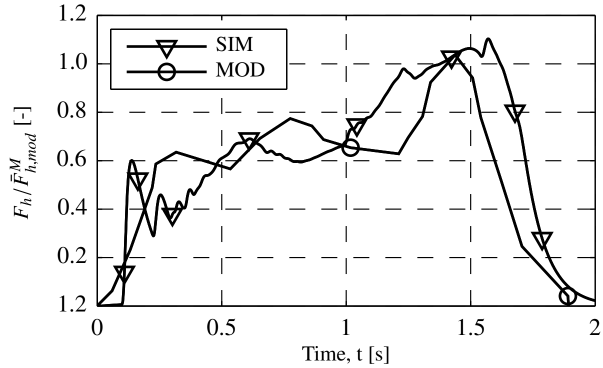

Figure 16: Horizontal pipe reaction force, ID: F, H = 1 m

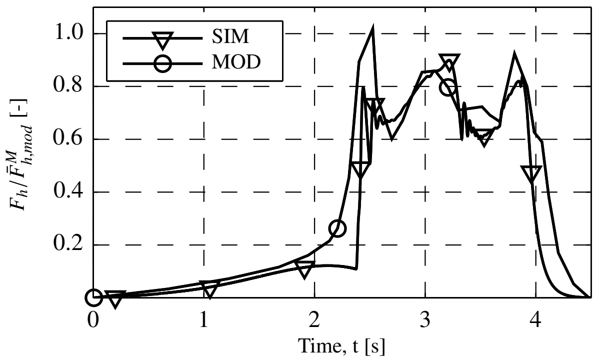

Figure 17: Horizontal pipe reaction force, ID: E, H = 3 m

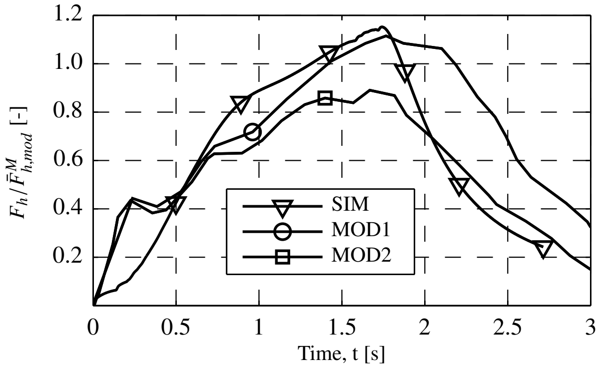

Figure 18: Horizontal pipe reaction force, ID: G, H = 1 m

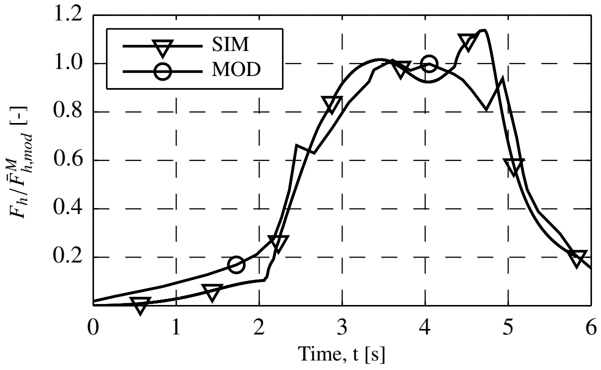

Figure 19: Horizontal pipe reaction force, ID: G, H = 3 m

In case of fixed pipe supports the bias variables W in Table 5 are in average within 10% for the V2600 board. The good accordance is confirmed by the horizontal force histories in Figs. 16 and 17. Note the nicely predicted local peaks in Fig. 17 arising when new regions of the board surface get into contact with the pipe. The simulations for flexible pipe support conditions have a slightly larger bias for the response parameters, but as shown in Figs. 18 and 19 the horizontal force is still in very good agreement with the model tests. Due to the hinged warpline connector seen in Fig. 3b, the V2600 board passed smoothly over the pipe in the model tests and induced 40% lower loads than the R2600 board [8]. The simulations confirmed these findings where the modeled warpline connector in Fig. 4b allowed the board to rotate smoothly around the pipe in the same manner as experienced in the tests. This underlines the necessity of a detailed contact geometry description when aiming for realistic predictions of the interference loads.

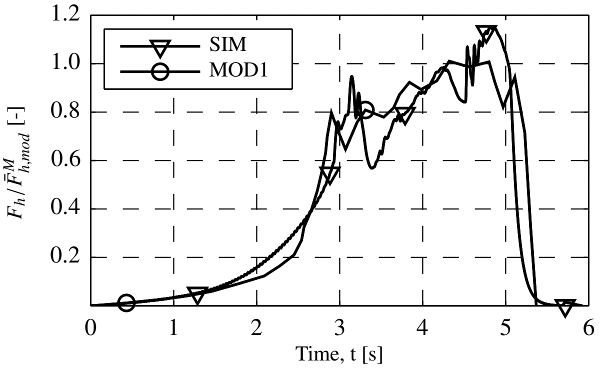

Figure 20: Horizontal pipe reaction force, ID: I, H = 3 m

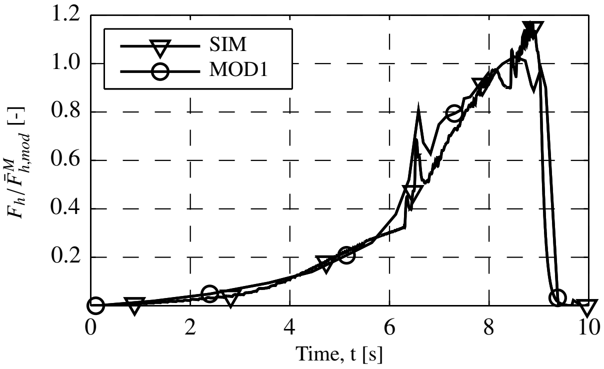

Figure 21: Horizontal pipe reaction force, ID: I, H = 6 m

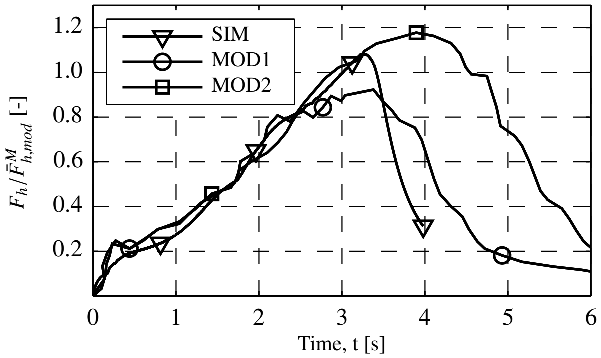

Figure 22: Horizontal pipe reaction force, ID: L, H = 1 m

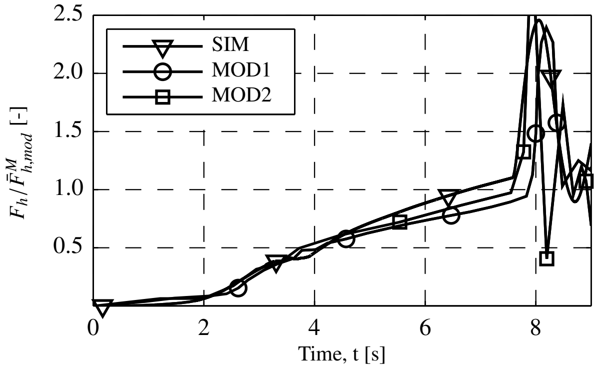

Figure 23: Horizontal pipe reaction force, ID: L, H = 3 m

According to Table 5 satisfactorily bias values W are obtained for the R2600 board in case of fixed pipe supports. This is confirmed by Figs. 20 and 21 where the simulated behavior is consistent with the model tests. Video recordings of the tests demonstrate that the R2600 board got wedged under the pipe for $H \geq 2$ m, and was released by a moment induced via the warpline tension increase and the lever arm represented by the rigid warpline connector seen in Fig. 4c. As illustrated in Fig. 9 for 3 m span height this behavior was fully captured in the simulations. For flexible supports the case with 1 m span height has a large impulse bias, but according to Fig. 22 the simulated response is within the variability of the model test runs. The characteristic locking phenomenon illustrated in Fig. 15 occurred also for the R2600 board for 3 m and 6 m span height. As seen in Fig. 23 the horizontal force is predicted fairly well for 3 m span height, where the force spike at 8.0 s interaction time corresponds to the instant the pipe hits into the end stopper. During the locking phase the exact same board orientation as observed in the model tests was persistent until the pipe reached its maximum allowable displacement. The good accordance with the laboratory tests relates to the applied contact geometry description, and points out the importance of accurate modeling of the sloping edges on the warpline connector device seen in Fig. 4c.

In view of the obtained results some comments regarding the simulation input parameters are needed. If the simulations were executed as simple blind tests it would not be possible to achieve the same level of agreement with the experimental data. This is clear from the rotational drag damping discussed in Section 5.1 and because the sweepline tension level during the board-pipe interaction phase, the crowfoot node vertical position and the board-pipe friction coefficient were tuned on a case-to-case basis. Note that the sweepline tension adjustments were made solely to get the same tension level as experienced in the tests.

The impulse is regarded as the most important parameter for pull-over events as it contains information about both the load level and the duration. Averaged values of the impulse bias $\bar{W}\big(I\big)$ are seen to be within 10% for each simulation case in Table 5. Except for the case denoted ID H the associated standard deviation $Z\big(I\big)$ is also within 10%. The simulated horizontal force histories above demonstrate that the characteristics of the pull-over interaction are consistently captured. Model test video recordings further confirm the good accordance in terms of the locking behavior for the R1900 and the R2600 boards and the smooth passings of the V2600 board. In view of the simulated bias values and the largest model test COVs in Table 5 the numerical model is therefore regarded to be successfully validated.

5.4 Influence of board-pipe friction coefficient

The friction coefficient μ between board and pipe was realized to be a sensitive parameter for the characteristic responses. Values of μ on the interval 0.4 – 0.6 were applied in the validation study in Section 5.3. Since these coefficients are regarded as upper range values, the effect of reducing the tangential contact forces was investigated. Simulated responses obtained in the validation study are regarded as benchmark values and are denoted by X_{ref}, while responses predicted with $\Delta\mu = \big\{-0.1, -0.2, -0.3\big\}$ are denoted by X. The relative change of the characteristic responses for single simulation runs D and the averaged relative changes $\bar{D}$ were computed as follows,

$$D\big(X\big) = \frac{X - X_{ref}}{X_{ref}} \qquad \bar{D}\big(X\big) = \frac{1}{N_H}\sum_{i}^{N_H} D\big(X\big) \tag{21}$$

in which X refers to either F_h^M, T_p or I_t defined in Fig. 10 and by Eq. (16). N_H denotes the number of span heights for the relevant simulation case.

The sensitivity of the friction coefficient is illustrated in Fig. 24, where labels A – L refer to the ID tags in Tables 3 and 4. The charts demonstrate that the magnitude of the averaged responses decrease when the friction coefficient is reduced. Although the predicted changes are significant, the resulting trend is expected because the frictional forces oppose the motion of the board as it slides and rotates around the pipe. The observed trend originates from the board-pipe interaction time T_p which in the extreme case with

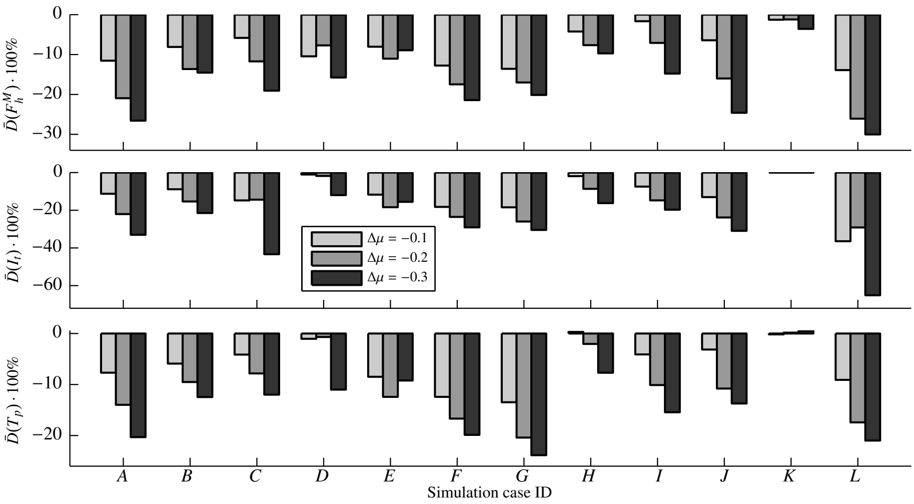

Figure 24: Overall sensitivity of board-pipe friction coefficient

$\Delta\mu = -0.3$ is reduced by $10-20\%$. The reduction of T_p limits the warpline tension increase and hence a smaller maximum horizontal force F_h^M results. Due to the combined decay of load level and interaction time the drop of pull-over impulse becomes significant. Note that $\Delta\mu = -0.3$ is perhaps too extreme as artificially large sliding motions along the pipe were present in some of the simulation runs.

The dependence on span height is reflected in Fig. 25 for $\Delta\mu = -0.2$. According to this chart the impulses are reduced by $30-60\%$ for 1 m span height, while the impulse decrease is less than 20% for higher span heights. These predictions are consistent with the trawl board motions during interaction. In case of 1 m height the board approaches the pipe horizontally and evident tangential contact point displacements occur during the pull-over, see Fig. 6, whereas for $H \geq 2$ m the board gets into contact with the pipe from beneath as seen in Fig. 9 and the interaction is rather characterized by large board rotations around the pipe with less degree of sliding. Notice that definite statements regarding the pipe support condition cannot be inferred from Fig. 25.

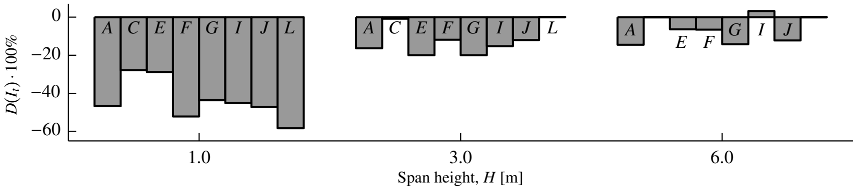

Figure 25: Span height sensitivity of board-pipe friction coefficient for $\Delta\mu = -0.2$

5.5 Effect of warpline angle, nonlinear warpline stiffness and full-length warpline

Due to space limitations in the laboratory tests a straight warpline attached to a linear spring assigned an averaged stiffness was used to represent the full-length warpline, see Fig. 1. It is a challenging task to combine a reasonable warpline angle and a constant stiffness value. The sensitivity of the warpline parameters and the validity of using a truncated warpline model were therefore investigated in terms of three cases,

- Set the warpline angle α_w to 13°. This reduces the warpline angle by approximately 4° and 7° for the axial warp stiffnesses of 28 kN/m and 39 kN/m.
- Apply a nonlinear towing spring with similar static chord stiffness characteristic as the warpline considered when the linear spring stiffness K_t in the model test was set. The employed characteristic had an axial warp stiffness of 18 kN/m and 28 kN/m at respectively 100 kN and 200 kN tension. The R1900 board was not considered since it had approximately 40 kN warpline tension prior to interaction and a maximum warp force far below 200 kN.
- Use a warpline of length 1200 m with similar static configuration and stiffness as considered in the model test to set the linear spring stiffness K_t. Details about the full-length warpline are given in Section 2.

The warp-pipe interaction phase was elongated by several seconds for high span heights when the warpline angle was set to 13°. This interaction is of no interest for comparison purposes and the impulse I_p in Eq. (16) is therefore emphasized. The change of the impulse according to Eq. (21) with $I_{p,ref}$ from Section 5.3 is shown in Fig. 26, where the IDs A – L refer to Tables 3 and 4. The four runs in Fig. 26 with the largest differences had not the same trawl gear wire tension levels and board orientation as in the reference runs in Section 5.3. A tendency of $5 - 10\%$ impulse gain is demonstrated for the other runs with minor differences in the initial conditions. The change of warpline angle alone seems therefore not to be that crucial. It is rather differences introduced via parameters depending on α_w that change the interaction performance.

The effect of a nonlinear spring at the towing node is reflected in Fig. 27. In case of fixed pipe support conditions the predicted differences are insignificant, whereas $10 - 20\%$ change of the characteristic responses results for flexible supports. No clear trend can be

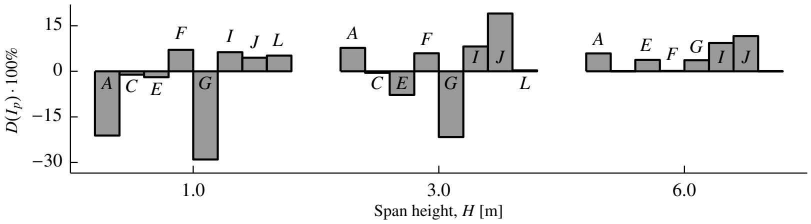

Figure 26: Warpline angle sensitivity, $\alpha_w = 13°$

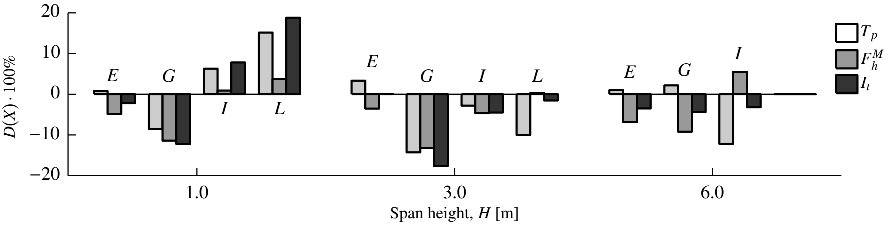

Figure 27: Effect of nonlinear warpline stiffness

inferred from these results, except that flexible supports are more susceptible for changes of the warpline stiffness. Hence, provided that an appropriate stiffness is selected the simulated results gives no reason to abandon the linear spring model applied in laboratory tests.

According to Fig. 28 a significant increase of the characteristic responses results when the full-length warpline model is employed. The impulse gain is 30% to 60% in the majority of the runs with evident rise of both maximum force F_h^M and board-pipe interaction time T_p. This trend is somewhat unexpected because both Figs. 26 and 27 dictate less influence from use of a nonlinear stiffness characteristic and a reduced warpline angle. The reason for the more severe responses stems from the normal drag forces arising when the warpline catenary configuration tightens up, which cause a significant warpline stiffness increase at the instant board-pipe contact is established. To quantify the effective stiffness a separate tow of the warpline at 3 m/s velocity with 90 kN pre-tension subjected to an immediate stop at the lower end was simulated. The resulting chord stiffness values became equal to 51.8 kN/m, 28.5 kN/m and 32.2 kN/m at tension levels of respectively 100 kN, 150 kN and 200 kN. As opposed to the static stiffness characteristic, the apparent stiffness undergoes a reduction as the warpline tension increases. This behavior explains the significant increase of the characteristic response in Fig. 28, and provide also valuable information with regard to future work relying exclusively on laboratory tests.

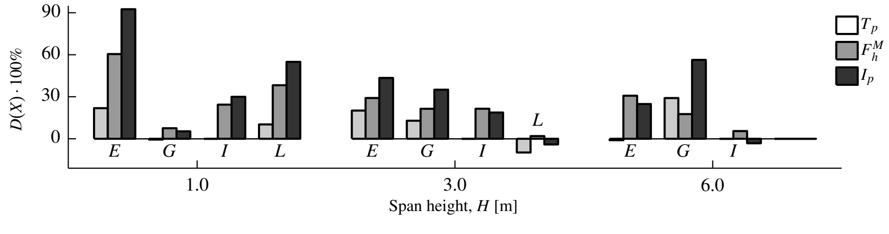

Figure 28: Effect of full-length warpline

5.6 Influence of sweepline tension during interaction

In the validation study presented in Section 5.3 the sweepline tension level during interaction was adjusted towards the model test tension by controlling the transverse motion of the trawl net node. The tests with fixed pipe supports had typically $0-15$ kN residual tension during the board-pipe interaction phase, while $0-25$ kN tension was present in the tests with flexible supports. Two extreme cases were considered to reveal the significance of the residual tension. In the first case a tension value close to zero was obtained by setting the dashpot constant denoted C_{D2} in Fig. 1 to 200 kN/m^{2}s^{-2}, whereas in the other case maximum residual tension was obtained with $C_{D2} = 0$ kN/m^{2}s^{-2}. In a realistic situation these extremes may represent turning manoeuvres of the fishing vessel that alter the port and starboard tension balance of the trawl gear.

A significant overall decrease of duration, maximum horizontal force and pull-over impulse resulted from the simulations with reduced sweepline tension. This trend is illustrated in Fig. 29 for the relative change of the impulse I_t according to Eq. (21), where annotations A – L refer to the IDs in Tables 3 and 4. For span heights $H \leq 3$ m, irrespective of the board type, the impulses decrease by $10-20\%$ for fixed pipe supports and close to 40% reduction is predicted for flexible pipe supports. This occurs because possible residual sweepline tension, which here is lost or close to zero, serve to restrain the motion of the board when it slides and rotates around the pipe. The relative decrease of sweepline tension is largest for flexible pipe supports, and the reduction of pull-over impulse is consequently more pronounced for these cases. Note the impulse decrease for ID C at 3 m span height, implying that the maximum pipe displacement was not reached and that the characteristic locking behavior illustrated in Fig. 15 was faded out. According to Fig. 29 the R2600 board predicts an impulse rise of 40% for 6 m span height and fixed pipe supports. Due to the loss of sweepline tension the board trailing edge is in this case lowered compared to the configuration shown in Fig. 9a. The board must then rotate a larger angle to get around the pipe, which in turn extend the interaction time such that a

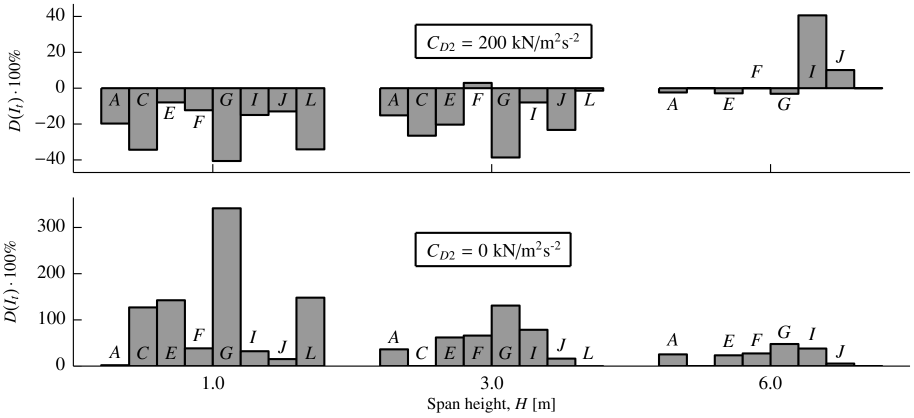

Figure 29: Influence of sweepline tension during interaction

larger maximum load is achieved.

When C_{D2} was set to zero the averaged sweepline tension became equal to $10-20$ kN for the R1900 board and $20-40$ kN for the two others during the board-pipeline interaction phase. These values are approximately $10-15\%$ of the simulated maximum warpline tension, and the horizontal balance of forces is therefore not altered much. The raised sweepline tension level resulted in an overall increase of the board-pipe interaction time with a corresponding rise of the maximum horizontal force. According to Fig. 29 the increase of impulse is significant in most of the runs, and especially pronounced for flexible support conditions. This behavior is explained by the restraining effect the sweepline tension has on the motion of the board. The motion restraint is most dominant for flexible supports because the allowance of horizontal pipe displacement leads to a higher sweepline tension level. For the R1900 board with 1 m span height the restraining effect actually made the pipe reach its maximum allowable displacement of 8.5 m. This incident and the large impulse rises in Fig. 29 indicate that the situation with zero trawl net transverse resistance is perhaps too extreme. Nevertheless, the simulated behavior identifies the sweepline tension as a crucial boundary condition for the board.

5.7 *Influence of hit angle*

In current design practices the most severe trawling direction is assumed to be perpendicular to the pipeline axis [1]. The validity of this assumption was investigated in terms of hit angles ϕ set equal to 60° and 120°, see Fig. 1. The extreme cases of zero and high transverse trawl net resistance were considered with C_{D2} in Fig. 1 set equal to respectively 0 kN/m^{2}s^{-2} and 200 kN/m^{2}s^{-2}.

When ϕ was set to 60° reductions up to 50% were obtained for both the board-pipe interaction time T_p and the maximum horizontal reaction force normal to the pipe axis F_h^M. This behavior is reflected in Fig. 30 for the relative change of the pull-over impulse I_p computed in accordance with Eq. (21). Annotations A – L refer to the IDs in Tables

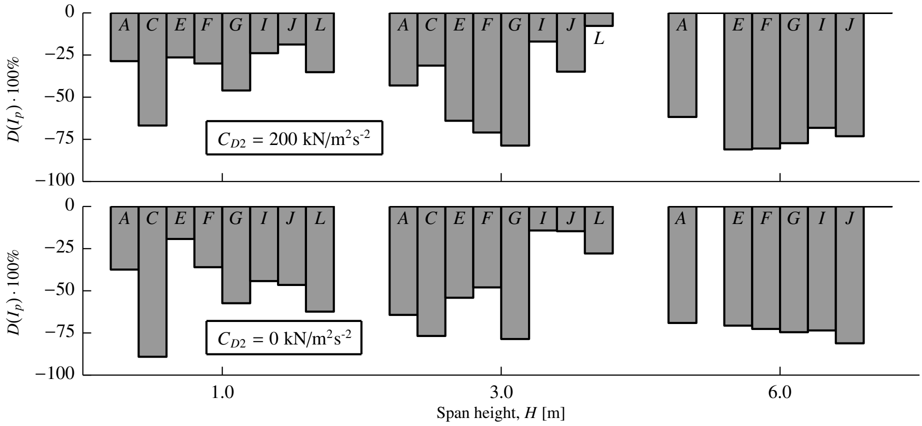

Figure 30: Relative change of impulses I_p for hit angle $\phi = 60°$

3 and 4. All of the impulses are reduced compared to the case $\phi = 90°$ with values between -30% and -70% in most of the runs. The influence of the transverse trawl net resistance is seen to be of less importance. This relates to board translatory motions along the skew pipe axis that work to prevent the sweepline from going slack, and consequently the tension level is not governed by the C_{D2}-value to the same degree as previously. Note that the R1900 and the R2600 boards have impulse drops for 3 m span height with flexible supports. In these runs the board-pipe locking behavior illustrated in Fig. 15 was more or less faded out, and for the R1900 board the maximum pipe displacement of 8.5 m was not reached. These findings are consistent with previous research [5], in which skew passings of trawl boards were found to induce less severe interaction loads than perpendicular crossings.

In case of 120° hit angle and 1 m span height with $C_{D2} = 200$ kN/m^{2}s^{-2} the maximum horizontal forces were reduced by 30% to 60%. Apart from the R1900 board which passed easy over the pipe, dominant sliding along the skew pipe occurred for approximately 10 m such that the durations were extended by up to 40%. Depending on the degree of sliding this lead to both smaller and larger impulses compared to the case with $\phi = 90°$.

With C_{d2} set to zero and $\phi = 120°$ the behavior was more or less unchanged for the R1900 and R2600 boards compared to $H = 1$ m and $C_{D2} = 200$ kN/m^{2}s^{-2}, whereas significantly more severe loads were induced by the V2600 board. For fixed pipe supports the V2600 board was restrained by a sweepline tension of about 35 kN when it rotated around the pipe. As illustrated in Fig. 31 this resulted in a nearly twice as large horizontal force compared to $\phi = 90°$. With flexible pipe supports the V2600 board was locked between the seabed and the pipe as seen in Fig. 32 until the pipe reached its maximum displacement of 8.5 m. This resulted in a 70% larger horizontal force and an impulse gain of 450%. These results are consistent with the behavior illustrated in Fig. 29 for $C_{D2} = 0$ kN/m^{2}s^{-2}, however, as noted in Section 5.6 the assumption of zero transverse trawl net resistance is perhaps too extreme. Thus, the severity of the predicted loads does

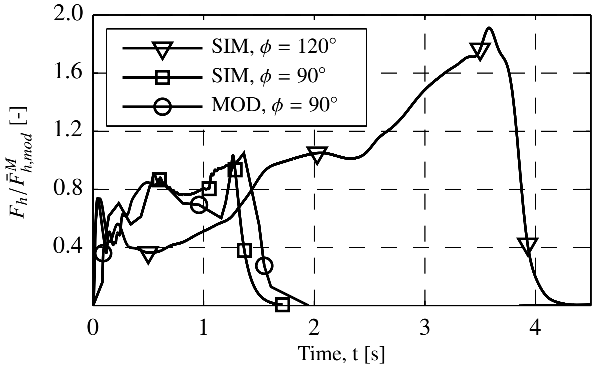

Figure 31: Horizontal pipe reaction force, ID: E, H = 1 m, $C_{D2} = 0$ kN/m^{2}s^{-2}

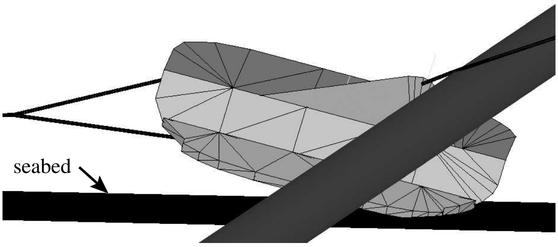

Figure 32: Board-pipe locking, ID: G, H = 1 m, $C_{D2} = 0$ kN/m^{2}s^{-2}, $\phi = 120°$

not necessarily imply that current design load recommendations are non-conservative.

A significant increase of both load level and duration were seen for span heights $H \geq$ 2 m when ϕ was set to 120° both for $C_{D2} = 0$ kN/m^{2}s^{-2} and $C_{D2} = 200$ kN/m^{2}s^{-2}. Unfortunately, the trawl board hydrodynamic angles of attack Ψ_1 and Ψ_3 were kept within the inadmissible range $[-30°, 30°] \cup [150°, 210°]$ for several seconds in these runs. The obtained responses can therefore not be regarded as fully valid, however, the authors still believe that the observed trends are representable for the true interaction behavior.

In Fig. 33 the extreme behavior for $H \geq 2$ m and $\phi \approx 120°$ is illustrated for the R2600 board. Annotation TRW refers to the truncated warpline in Fig. 1 and FLW refers to a simulation with the full-length warpline considered in Section 5.5. Both the truncated and the full-length warpline model predict a significant increase of the warpline interaction time T_w with a local force peak of $0.8 \cdot \bar{F}_h^M$ just prior to board-pipe contact, see Fig. 33. The extension of T_w occurs because the warpline slides along the skew pipe, rather than folding over the pipe and increase the local warp angle α_w at the board. This prevents board uplifting and instead a 20 m translatory board motion takes place along the skew pipe until the warpline connector wedges onto the pipe. In this wedged configuration the board trailing edge is close to being in contact with the seafloor, while in Fig. 9a the trailing edge is in comparison located 2.8 m above the seafloor. Thus, the board has to

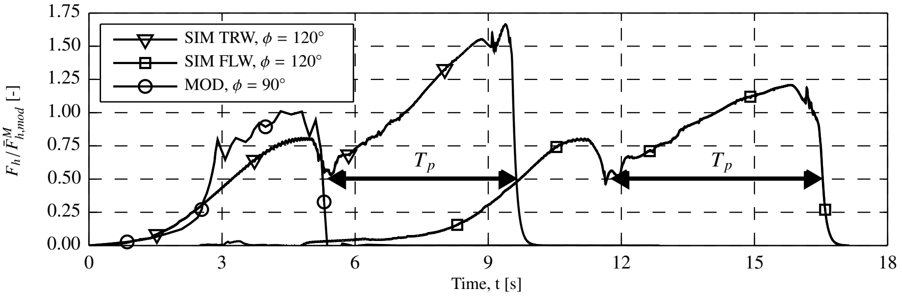

Figure 33: Horizontal pipe reaction force, ID: I, H = 3 m, $C_{D2} = 200$ kN/m^{2}s^{-2}

rotate approximately 180° about its x_3-axis to release from the pipe. This rotation takes some time, see the extended board-pipe interaction time T_p in Fig. 33, and allows large forces to build up as the warpline tension increases to 270 kN and 350 kN in the FLW and TRW runs, respectively. Compared to the model test measurement for $\phi = 90°$ the maximum horizontal forces in Fig. 33 increase respectively with 20% and 65% for the full-length and truncated warpline models.

Non-perpendicular crossings with ϕ close to 120° were considered by Moshagen, Kjeldsen and Holthe [42] in six full-scale tests for uncertain span height values between $1-4$ m. Valdemarsen [43] conducted full-scale interaction tests aiming to detect potential fishing gear damage, but only span heights less than the board height were considered. Hooking tests with ϕ set to 110° and 135° were conducted by MARINTEK [44], however, due to a short span length the interaction identified above could not develop. Thus, it seems like the setup that resulted in extreme loads, $H \geq 2$ m and $\phi \approx 120°$, has not been addressed thoroughly in previous efforts.

6 Conclusions and future work

In this contribution a novel FE-based approach for prediction of fishing gear interference loads on subsea pipelines was proposed. The rather complex interaction arising in trawl board pull-over events was addressed. Relevant issues for obtaining realistic response predictions were dealt with in terms of trawl board hydrodynamic loads, FE modeling of the trawl system and handling of contact between pipe and trawl gear. The performance of the numerical model was investigated by means of an extensive validation study, in which the pull-over load impulses were predicted within a 10% margin of the model test measurements. According to model test video recordings the characteristic interaction behavior was captured consistently for all three trawl boards. The proposed trawl board hydrodynamic load model and the employed board-pipe contact model are therefore capable of describing the relevant effects. A sensitivity analysis was conducted to identify important parameters for the simulated pull-over response. The interaction was revealed to depend upon the board-pipe friction coefficient, the sweepline tension level during interaction, the warpline drag properties and the pipeline hit angle.

Consistent interaction behavior was demonstrated in spite of the discarded hydrodynamic interaction between the trawl board and the pipeline. This indicates that for pipe diameter to trawl board height ratios less than approximately 0.3 it is acceptable to neglect the presence of the pipeline. The use of trawl board steady-state fluid loads in the rather complex and unsteady flow state present during the interaction seems to be acceptable, however, the angle of attack validity range was violated for non-perpendicular crossings with high span heights. In future work the focus should therefore be on estimation of the steady-state loads induced by the linear relative fluid velocity at low angles of attack, considering both in-plane directions of the board. In this regard flume tank experiments are favored with the seabed gap and the hydrodynamic angles of attack as independent variables, see [21].

According to the sensitivity study the pull-over process may change significantly if the governing parameters are altered. This finding is consistent with the performance seen in model test when the initial conditions prior to interaction undergo small variations [6]. The strong interplay between the hydrodynamic Coriolis-centripetal loads and the pressure-induced rotational damping poses challenges with regard to the simulation input data, even for experienced users with good knowledge about trawl board pull-over interaction. Another difficulty is introduced by the board-pipe friction coefficient sensitivity for low span heights. In future work of similar kind it is thus recommended to always conduct a proper validation of the numerical model against experimental tests.

The recommended pull-over loading used by the industry today is founded upon 20 year old model tests and assumes that perpendicular crossings induce the most severe loads. Our efforts demonstrate in contrast that non-perpendicular crossings at high span heights can induce more severe loads, however, clear statements with regard to current design practices cannot be inferred as the hydrodynamic load model validity range was violated. A natural step in further work is therefore to investigate crossings of more modern board types, e.g. the multi-foil boards considered by Teigen et al. [21], with a proper description of the steady-state hydrodynamic loads at low angles of attack. A small trawl-pipeline model test program for validation purposes is here regarded as mandatory. Use of numerical simulations is beneficial mainly for effective reduction of statistical uncertainty and to avoid use of a truncated and possible non-conservative warpline model. The current pull-over load recommendations [1] may also be extended with parameters such as trawl gear crossing angle, board-pipe friction coefficient, span flexibility and pipe mass. The dependence on these parameters is preferably obtained by numerical simulations due to the reduced parameter flexibility and the high time consumption associated with laboratory tests.

Modern trawl boards may have twice as large steel mass and surface area as those considered in this work. The computational strategy is anticipated to simulate a realistic interaction also for these boards provided that the hydrodynamic loads are well described. Modern boards are optimized with respect to lift-to-drag ratio and the geometry can be complex with openings in the board plane. Thus, simplified methods for prediction of hydrodynamic loads may be inaccurate such that separate experimental testing of the boards has to be conducted instead. The interplay between the Coriolis-centripetal loads and the rotational damping may represent a challenge also for these boards. Compared to the boards considered in this work an aspect ratio closer to unity is believed to be beneficial, because this increases the structural and hydrodynamic inertia entries I_1 and I_{a1}, such that the rotational velocity $\dot{\theta}_1$ in average becomes smaller and the interplay less pronounced.

Acknowledgements

The authors are grateful for access to model test results provided by Statoil. The Norwegian Marine Technology Research Institute (MARINTEK) must also be acknowledged regarding source code access to the SIMLA computer software and admission to the trawl boards employed in the model tests.

References

[1] Recommended practice DNV-RP-F111, Interference between trawl gear and pipelines, October 2010. Det Norske Veritas, Høvik, Norway; 2010.

[2] Bai Y, Bai Q. Trawl impact, pullover and hooking loads. In: Subsea pipelines and risers. Oxford UK: Elsevier Ltd; 2005, p. 173–948.

[3] Gjørsvik O, Kjeldsen S, Lund S. Influences of bottom trawl gear on submarine pipelines. In: Seventh Annual Offshore Technology Conference. 1975, p. 337–45.

[4] Carstens T, Kjeldsen S, Gjørsvik O. The conflict between pipelines and bottom trawls - Some results from laboratory and field tests. In: Offshore North Sea Technology Conference and Exhibition. 1976, p. T–I/18: 1–28.

[5] Moshagen H, Kjeldsen S. Fishing gear loads and effects on submarine pipelines. In: Twelfth Annual Offshore Technology Conference. 1980, p. 383–92.

[6] Nygaard I. Improved design for protective subsea structures. In: Subsea '88 International Conference. 1988.

[7] Nygaard I. Trawl - Pipeline span interaction. Model tests. Final report. Tech. Rep. 511191.01-07; Norwegian Marine Technology Research Centre (MARINTEK), Trondheim, Norway; 1990.

[8] Verley RLP, Moshagen BH, Moholdt NC, Nygaard I. Trawl forces on free-spanning pipelines. Int J Offshore Polar 1992;2:24–31.

[9] Verley R. Pipeline on a flat seabed subjected to trawling or other limited duration point loads. In: Proceedings of the Fourth (1994) International Offshore and Polar Engineering Conference. 1994, p. 128–34.

[10] Fyrileiv O, Spiten J, Mellem T, Verley R. DNV'96, Acceptance criteria for interaction between trawl gear and pipelines. In: Proceedings of the 16th International Conference on Offshore Mechanics and Arctic Engineering. 1997, p. 91–8.

[11] Fyrileiv O, Spiten J. Trawl gear protection within platform safety zones. In: Proceedings of OMAE2004 23rd International Conference on Ocean, Offshore and Arctic Engineering. 2004, p. 217–23.

[12] Fyrileiv O, Askheim DØ, Verley R, Rolsdorph H. Pipeline-trawl interaction: Effect of trawl clump weights. In: Proceedings of OMAE2006 25th International Conference on Offshore Mechanics and Arctic Engineering. 2006, p. 95–102.

[13] Askheim DØ, Fyrileiv O. New design code for interference between trawl gear and pipelines DNV-RP-F111. In: Proceedings of OMAE2006 25th International Conference on Offshore Mechanics and Arctic Engineering. 2006, p. 81–93.

[14] Amdal LW, Røneid S, Etterdal B. Optimized design of pipelines exposed to trawl pull-over. In: Proceedings of the Twenty-first (2011) International Offshore and Polar Engineering Conference. 2011, p. 130–4.

[15] Bergan PG, Mollestad E. Impact-response behavior of offshore pipelines. J Energ Resour-ASME 1982;104:325–9.

[16] Guijt J, Horenberg JAG. Recent investigations concerning the effect of bottom trawl gear crosssings on submarine pipeline integrity. In: Nineteenth Annual Offshore Technology Conference. 1987, p. 573–80.

[17] Horenberg JAG, Guijt J. An analytical and experimental analysis of trawl gear-pipeline inter-

action. In: Nineteenth Annual Offshore Technology Conference. 1987, p. 563–72.

[18] OTH 561 - Guidelines for trenching design of submarine pipelines. Health and Safety Executive, Norwich, United Kingdom; 1999.

[19] Igland RT, Søreide T. Advanced pipeline trawl gear impact design. In: Proceedings of the ASME 2008 27th International Conference on Ocean, Offshore and Arctic Engineering. 2008, p. 271–7.

[20] Maalø K, Alsos HS, Sævik S. Detailed analysis of clump-weight interference with subsea pipelines. In: Proceedings of the ASME 2012 31st International Conference on Ocean, Offshore and Arctic Engineering. 2012, p. 725–32.

[21] Teigen P, Ilstad H, Levold E, Hansen K. Hydrodynamical aspects of pipeline overtrawling. In: Proceedings of the Nineteenth (2009) International Offshore and Polar Engineering Conference. Osaka, Japan; 2009, p. 435–42.

[22] Longva V, Sævik S, Levold E, Ilstad H, Teigen P. Dynamic simulation of free-spanning pipeline trawl board pull-over. In: Proceedings of the ASME 2011 30th International Conference on Ocean, Offshore and Arctic Engineering. 2011, p. 561–8.

[23] Longva V, Sævik S. A penalty-based body-pipe contact element for simulation of pull-over events. In: Proceedings of the ASME 2012 31st International Conference on Ocean, Offshore and Arctic Engineering. 2012, p. 241–50.

[24] Longva V, Sævik S. A penalty-based contact element for pipe and 3D rigid body interaction. Eng Struct 2013;56:1580–92.

[25] Sævik S. Simla - Theory manual. Tech. Rep. 700254.00.01; Norwegian Marine Technology Research Centre (MARINTEK), Trondheim, Norway; 2008.

[26] Hilber HM, Hughes TJR, Taylor R. Improved numerical dissipation for time integration algorithms in structural dynamics. Earthquake Eng Struc 1977;5:283–92.

[27] Recommended practice DNV-RP-C205, Environmental conditions and environmental loads, April 2007. Det Norske Veritas, Høvik, Norway; 2007.

[28] Recommended practice DNV-RP-H103, Modelling and analysis of marine operations, April 2009. Det Norske Veritas, Høvik, Norway; 2009.

[29] Reite KJ. Modeling and control of trawl systems. Ph.D. thesis; Norwegian University of Technology and Science, Trondheim, Norway; 2006.

[30] Litewka P. Hermite polynomial smoothing in beam-to-beam frictional contact. Comput Mech 2007;40:815–26.

[31] Mathisen KM. Large displacement analysis of flexible and rigid systems considering displacement-dependent loads and nonlinear constraints. Ph.D. thesis; Norwegian Institute of Technology, Trondheim, Norway; 1990.

[32] Yazdchi M, Crisfield MA. Non-linear dynamic behaviour of flexible marine pipes and risers. Int J Numer Meth Eng 2002;54:1265–308.

[33] Wriggers P, Van TV, Stein E. Finite element formulation of large deformation impact-contact problems with friction. Comput Struct 1990;37:319–31.

[34] Kennard EH. Irrotational flow of frictionless fluids, mostly of invariable density. Tech. Rep. 2299; David Taylor Model Basin, Washington D.C., USA; 1967.

[35] Norrbin NH. Theory and observations on the use of a mathematical model for ship manoeuvring in deep and confined waters. Tech. Rep. 68; The Swedish State Shipbuilding Experi-

mental Tank, Göteborg, Sweden; 1971.

[36] Fossen TI. Nonlinear coriolis forces due to added mass in a rotating coordinate system. In: Handbook of marine craft hydrodynamics and motion controls. John Wiley & Sons Ltd.; 2011, p. 115–21.

[37] Fernandes AC. Fluttering and autorotation of a hinged vertical flat plate induced by uniform current. Ph.D. thesis; Federal University of Rio de Janeiro, Rio de Janeiro, Brazil; 2011.

[38] Reite KJ, Sørensen AJ. Mathematical modeling of the hydrodynamic forces on a trawl door. IEEE J Oceanic Eng 2006;31:432–53.

[39] Mueller TJ, Torres GE. Aerodynamics of low aspect ratio wings at low reynolds number with applications to micro air vehicle design and optimization. Tech. Rep. UNDAS-FR-2025; University of Notre Dame, Notre Dame, Indiana, USA; 2001.

[40] Newman JN. Transient problems. In: Marine hydrodynamics. The MIT Press; 1977, p. 230–2.

[41] Faltinsen OM. Linear wave-induced motions and loads on floating structures. In: Sea loads on ships and offshore structures. Cambridge University Press; 1990, p. 37–101.

[42] Moshagen H, Kjeldsen S, Holthe K. Influence of bottom trawl gear on submarine pipelines. Extension III: Field tests on large pipeline. Tech. Rep. STF60 F77083; River and Harbour Laboratory, Norwegian Institute of Technology, Trondheim, Norway; 1977.

[43] Valdemarsen JW. Trawling across pipelines. Tech. Rep. 09VF01785; Directorate of Fisheries, Bergen, Norway; 1988.

[44] Braaten H. Ormen lange gas pipeline - Overtrawling study. Tech. Rep. 512366.00.01; Norwegian Marine Technology Research Centre (MARINTEK), Trondheim, Norway; 2002.

Paper III

A Lagrangian-Eulerian formulation for reeling analysis of history-dependent multilayered beams

Vegard Longva[a], Svein Sævik[a]

[a] Department of Marine Technology, Norwegian University of Science and Technology
NO-7491 Trondheim, Norway

Computers & Structures, Vol. 146, 2015, pp. 44 – 58

Abstract

This paper presents a novel Lagrangian-Eulerian finite element formulation for reeling analysis of multilayered beams with gross interlayer slippage. In contrast to the conventional Lagrangian approach, the mesh becomes practically fixed in space, which yields significant benefits for the performance of the contact algorithms and the overall computational efficiency. The needed Lagrangian-Eulerian kinematic relations are derived, special attention is given to the convective transport term for the constitutive variables and an implicit update scheme for the elasto-plastic bending model is formulated. The proposed formulation is shown to predict responses with the same accuracy as offered by the conventional Lagrangian formulation.

Keywords: Lagrangian; Eulerian; Reeling; Flexible pipe; Elasto-plastic

1 Introduction

Flexible pipes and cables are widely used in the petroleum industry for fluid transport, power supply and signal transmission. Due to the compliant behavior in bending, these structures are reeled onto large carousels when transported to the production site. A typical reeling operation involves several kilometers of material, large-deformation zones, history-dependent material effects and extensive contact interactions along the reeling path. Use of the conventional finite element (FE) method to simulate such an operation is a very demanding task, however, the process is fairly steady state and the material transport occurs with low velocity along a virtually fixed route in space. This naturally points toward a quasistatic Lagrangian-Eulerian formulation in which the material and the mesh are not tied to each other. In that case the treatment of the history-dependent material behavior becomes the main challenge.

Most of the arbitrary Lagrangian-Eulerian (ALE) procedures for path-dependent materials utilize an operator split method, see e.g. Refs. [1, 2]. In such methods the time step is first simplified into a pure Lagrangian step which determines the material motion. Thereafter, the mesh velocity and the updated mesh coordinates are computed in the second step. Finally, a convection step is initiated to transfer the state variables to the new integration points established in the second step. Due to the convection step, the equilibrium is disturbed which leads to some loss of accuracy. However, greater flexibility regarding the mesh motion is allowed for [3], simpler and more robust algorithms can be developed [2] and upgrading of an existing implicit Lagrangian implementation into the ALE description is facilitated since no additional tangent stiffness contributions and global unknowns appear. Successful applications of the fully coupled approach where the mesh motion, the material motion and the convective effects are handled together have also been reported, see Refs. [4, 5].

The ALE description has been employed in three-dimensional beam problems to handle joints sliding along the beam axis [6] and to model axial mass flow [7]. Problems involving axially moving beams have been addressed with both the Eulerian description [8] and the Lagrangian-Eulerian approach [9]. In the literature for fluid conveying pipes, the Eulerian formulation is commonly applied, see the review paper by Païdoussis and Li [10] and references cited therein. Common for these applications is the focus on the dynamic behavior and the justifiable assumption of elastic structural responses. To the authors knowledge, the Lagrangian-Eulerian viewpoint has not yet been utilized in beam problems with history-dependent material behavior.

When conventional ALE formulations are used in large-deformation analysis of solids, their objective is to reduce mesh distortions without resorting to re-meshing and updating of the mesh topology. In this work, the purpose is instead to separate the mesh and the material motions such that the mesh becomes practically fixed in space. For reeling analyses this strategy yields significant benefits in terms of,

1) Use of non-uniform meshes with large elements in small-deformation regions.

2) No need to model the vast amount of material stored on the reels.

3) Improved stability performance for the contact algorithms.

4) Larger time steps due to less variations in the contact conditions.
5) Less changes in the contact element topology result in reduced time consumption for contact searches.

Regarding item 1), the overall element size in a conventional Lagrangian simulation is restricted by accuracy requirements at the most critical location along the reeling path. In contrast, a Lagrangian-Eulerian description with a nearly fixed mesh imposes restrictions only for the elements located within the large-deformation regions. This benefit yields, together with item 2) above, a significant improvement of the overall computational efficiency. With regard to item 3), contact interactions often lead to convergence problems in reeling analyses, making frequent user interaction throughout the simulation runs unavoidable. The Lagrangian-Eulerian procedure mitigates these issues as the motion of the contact geometry is significantly reduced. Furthermore, use of low-order contact elements is motivated as continuity of the contact geometry becomes less critical.

Due to the hysteretic bending behavior, significant bending-induced torques may develop in multilayered beams [11]. This phenomenon originates from interlayer friction effects, which allow the bending moment vector to be non-aligned with the normal vector of the curvature plane, such that an internal torque is needed to fulfill equilibrium. In situations with low tension, as is the case in reeling operations, the torque may provoke torsional instabilities with possible formation of loops, see Refs. [12–14]. Indeed, such incidents have been reported by subsea contractors in recent years. To obtain accurate predictions of the generated torque, all history-dependent effects that influence the reeling path configuration must be accounted for, together with the coupling between bending and axial-torsional responses introduced via the interlayer contact pressures.

Several hysteretic bending models have been developed for multilayered beams during the last years. Tan et al. [15] proposed two bending models for flexible risers that were able to account for interlayer friction effects. A more sophisticated approach able to account consistently for radial pressure loads was proposed by Alfano, Bahtui and coworkers [16, 17], who employed small-scale detailed FE simulations to calibrate elasto-plastic models for flexible risers. The disadvantage of such an approach is the considerable efforts needed to determine the material parameters. This was remedied by Sævik [18] who formulated two elasto-plastic bending models that were able to account explicitly for the radial interlayer contact pressures. The models were merged into multilayered beam elements and predicted fatigue damages for flexible pipes in good correlation with experiments. Recently, Aguiar et al. [19] proposed a multilayered beam element for flexible pipe analysis, however, explicit account was not made for the interlayer contact pressures.

Based on the background information above, the Lagrangian-Eulerian formulation must comply with the following requirements,

- Predict steady and unsteady responses with the same accuracy as offered by the conventional Lagrangian simulation.
- Properly describe the hysteretic bending behavior and the interaction between bending and axial-torsional responses.
- Provide accurate predictions of the bending-induced torque.

The developed formulation may also be advantageous for simulation of subsea pipeline and cable laying operations. In that case the mesh motion at the upper end is set equal to the motion of the surface vessel. Compared to a conventional Lagrangian simulation, the motion of the pipeline mesh relative to the surface vessel reduces significantly, such that the benefits stated above in item 1) – 5) apply. This approach is regarded as more favorable than the re-use of element strategy proposed by Økland et al. [20].

The organization of the paper is as follows: Section 2 describes the constitutive model employed for the numerical investigations. Section 3 presents the key novelties of the work, in which the kinematic relations, the treatment of convective transport effects for the constitutive variables and the update of the elasto-plastic bending model are addressed. Thereafter, the virtual work contribution is presented and the constitutive part of the tangent stiffness relation is derived. The numerical examples in Section 4 focus on benchmarking against the conventional Lagrangian approach and demonstration of basic performances. A simple reeling example is also presented to illustrate the new computational strategy offered through the developed formulation. In Section 5 the work is summarized and the conclusions are given.

2 Multilayered beam constitutive model

In Section 4 an unbonded flexible pipe is employed for benchmarking, numerical performance tests and to simulate an idealized reeling operation. This pipe represents a typical example of a multilayered beam with gross interlayer slippage. The constitutive model of the pipe is outlined in the following, with emphasis on the history-dependent bending behavior as it represents the main challenge for the Lagrangian-Eulerian formulation. The axial-torsional constitutive relations are also presented due to their coupling with the elasto-plastic bending response.

The pipe cross-section is as illustrated in Fig. 1 made of several concentric layers. With regard to load-bearing, the pressure helix layer supports radial loads, the plastic sheaths contribute mainly in bending and the tensile helix layers balance axial, torsional, bending and radial loads. Unbonded flexible pipes are categorized as slender structures with negligible shear deformations. The shear forces are consequently computed from the moment equilibrium equation, such that a constitutive description must be assigned to the axial force N, the torque M_1 and the bending moments M_2 and M_3. The generalized stress vector $\hat{\boldsymbol{\sigma}}$ and the energy-conjugate strain vector $\hat{\boldsymbol{\epsilon}}$ therefore reads,

$$\hat{\boldsymbol{\sigma}} = \sum_{i=1}^{K} \begin{bmatrix} N_i & M_{1i} & M_{2i} & M_{3i} \end{bmatrix}^\top \tag{1}$$

$$\hat{\boldsymbol{\epsilon}} = \begin{bmatrix} \epsilon & \kappa_1 & \kappa_2 & \kappa_3 \end{bmatrix}^\top \tag{2}$$

where i is the layer number, ϵ is the axial strain, κ_1 is the torsion and the bending curvature components are denoted κ_2 and κ_3. The strain components are assumed equal in all of the K layers. For flexible pipes the response due to axi-symmetric loads is usually handled by a separate constitutive model [18, 21]. The bending response for the plastic sheaths

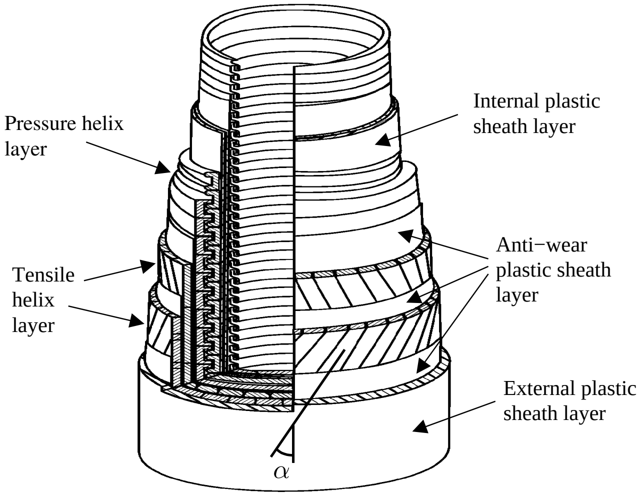

Figure 1: Unbonded flexible pipe cross-section

can be represented with a linear-elastic model, while the bending contribution from the tensile helix layers requires use of an elasto-plastic model.

2.1 Axi-symmetric model

The purpose of the axi-symmetric model is to provide axial force, torque, radial contact pressures and tangent stiffness parameters for each layer. A layer is either modeled as a tubular homogeneous sheath or as a collection of uniformly distributed helix tendons. Possible friction-induced effects, additional radial contact pressures due to bending and end-termination effects are disregarded. Further, the pipe is assumed straight with uniform strains and interlayer contact pressures within the section length considered. Rectangular uniform cross-sections are used to represent the helix tendons. The interlayer radial contact pressures and the geometry parameters involved in the model are defined in Fig. 2, where subscript i refers to the identification number of both the layer itself and the inside layer interface.

The axi-symmetric model is based on the early work of Féret and coworkers [22, 23]. The present model is extended to account for initial radial gaps between layers to ease modeling of fabrication imperfections. When developing the model, the main steps involve use of constitutive relations that link together equilibrium conditions and kinematic statements. The equilibrium equations for the helix layers are formulated by means of curved beam theory, see e.g. [24], and thin-walled shell theory is used for the sheath layers. A linear-elastic isotropic material is presumed and all kinematic relations are derived assuming linear and small motions. This results in three independent equations for each of the K layers formally expressed as,

$$h_j\left(N_i,\, \Delta r_i,\, \Delta t_i,\, p_i,\, p_{i+1},\, \epsilon,\, \kappa_1\,;\, \mathbf{z}_i\right) = 0 \qquad i = 1, ..., K \qquad j = 1, 2, 3 \tag{3}$$

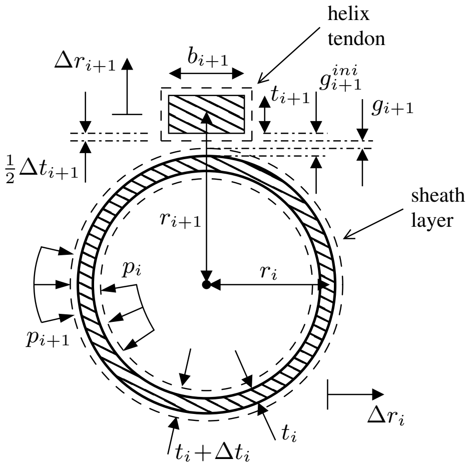

Figure 2: Geometry parameters, radial DOFs and radial pressures

in which N is the layer force in the pipe axial direction, Δ denotes the change relative to the unstressed configuration and $\mathbf{z}$ is a collection of parameters related to prescribed local pressures, material properties and geometry properties. The remaining variables are defined in Fig. 2. Notice that the generalized strain components ϵ and κ_1 are assumed equal in all layers. These strains are taken from the FE computation and are together with the radial pressure p on the internal and external pipe surfaces regarded as known quantities. The total number of unknowns in Eq. (3) is therefore equal to $4K - 1$. To obtain a solvable equation system, an interlayer continuity condition is introduced at each of the $K - 1$ interfaces,

$$\begin{aligned} &\Delta r_i - \frac{1}{2}\Delta t_i - \frac{1}{2}\Delta t_{i-1} - \Delta r_{i-1} - g_i^{\{ini\}} = g_i \qquad g_i > 0, p_i = 0 \quad i = 2, ..., K \\ &\Delta r_i - \frac{1}{2}\Delta t_i - \frac{1}{2}\Delta t_{i-1} - \Delta r_{i-1} - g_i^{\{ini\}} = 0 \qquad g_i = 0, p_i > 0 \quad i = 2, ..., K \end{aligned} \tag{4}$$

where $g^{\{ini\}}$ is the radial gap in the unloaded configuration and g is the current radial gap, see Fig. 2. The torque contribution from a sheath layer is computed separately in accordance with the St. Venant's solution for a circular cylinder, whereas the helix layer torque contribution is obtained via the associated layer axial force resulting from the solution of Eqs. (3) and (4).

An incremental constitutive relation is needed in the Newton-Raphson solution scheme. This relation is obtained from the St. Venant's solution for the sheath layer torques and by computing the partial derivative of Eqs. (3) and (4) with respect to ϵ and κ_1. For each of the partial derivatives an equation system with $4K - 1$ unknowns must be solved. The incremental relation from a single layer is formally expressed as,

$$\begin{bmatrix} dN_i \\ dM_{1i} \end{bmatrix} = \begin{bmatrix} N_{i,\epsilon} & N_{i,\kappa_1} \\ M_{1i,\epsilon} & M_{1i,\kappa_1} \end{bmatrix} \begin{bmatrix} d\epsilon \\ d\kappa_1 \end{bmatrix} \tag{5}$$

in which $M_{1,\epsilon}$ is equal to zero for sheath layers and the comma in subscript means partial derivative, e.g. $\frac{\partial N}{\partial \epsilon} = N_{,\epsilon}$.

2.2 *Elasto-plastic bending model for tensile helix layers*

The bending response of a helix layer may be explained by considering an initially straight pipe section that is gradually bent with constant interlayer radial pressures. At low curvatures, the helix tendons are kept in place by friction, and a linear relationship thus exists between the curvature and the change of tendon stress. In this situation, the bending moment is related to the curvature by a factor equal to the layer bending stiffness contribution in an equivalent cross-section not allowing for interlayer slippage. As the curvature increases, the change of tendon stress exceeds the available friction stress and slippage along the helices starts developing at the neutral axis of bending. When slippage is present around the whole circumference, the tendon stress and the resulting bending moment remain unchanged if the pipe is subjected to a further increase of the curvature. In previous work [18], this behavior was represented by a tri-linear moment-curvature relationship, however, as the transition between start of slippage to full slippage is small in terms of curvature, a bi-linear relationship corresponding to a Coulomb friction model without hardening is employed here.

The bending model is formulated in the framework of computational elasto-plasticity and is regarded valid if no significant end-termination effects are present. In order to determine whether slippage is present or not, a slip function f is defined for each of the tensile helix layers,

$$\begin{aligned} &f(\mathbf{M}_i, M_{si}) = ||\mathbf{M}_i|| - M_{si} \leq 0 \qquad \mathbf{M}_i = \begin{bmatrix} M_{2i} & M_{3i} \end{bmatrix}^\top \\ &M_{si} = M_{0i} + m_i\left(\mu_i p_i + \mu_{i+1} p_{i+1}\right) \qquad p_i, p_{i+1} \geq 0 \end{aligned} \tag{6}$$

in which $f = 0$ during slip, $f < 0$ indicates no slippage and $f > 0$ is an inadmissible state. M_0 is a constant moment stemming from the fabrication process, m is a parameter depending on the helix geometry and μ is the interface friction coefficient assumed independent of both slip rate and total curvature. In the literature, M_s is usually termed the friction moment. The radial contact pressure p is obtained from the axi-symmetric model according to Eqs. (3) and (4).

The rate of change of bending moment with respect to time is given by,

$$\dot{\mathbf{M}}_i = K_{Ei}\left(\dot{\boldsymbol{\kappa}} - \dot{\boldsymbol{\kappa}}_{pi}\right) \tag{7}$$

where a superposed dot marks that the rate is associated with a fixed set of cross-sectional material particles, K_E is the elastic modulus corresponding to the layer bending stiffness contribution in an equivalent cross-section not allowing for slippage, $\dot{\boldsymbol{\kappa}}$ is the rate of total bending curvature and $\dot{\boldsymbol{\kappa}}_p$ is the rate of bending curvature associated with slip. The latter rate is in accordance with Coulomb's friction law given by a non-associative slip rule,

$$\dot{\boldsymbol{\kappa}}_{pi} = \dot{\lambda}_i \frac{\partial}{\partial \mathbf{M}_i} f\left(\mathbf{M}_i, M_{si}\right) = \dot{\lambda}_i \frac{\mathbf{M}_i}{||\mathbf{M}_i||} \qquad \dot{\lambda}_i \geq 0 \tag{8}$$

in which $\dot{\lambda}$ is the plastic rate parameter, determined by the consistency criterion $\dot{f} = 0$ if slippage occurs and set to zero if $f < 0$.

In case of no slippage, the incremental constitutive relation is obtained by straightforward integration of Eq. (7) with $\dot{\boldsymbol{\kappa}}_p = \mathbf{0}$. When slippage occurs, the incremental relation valid for finite increments is established by linearizing the moment update scheme. If a fully implicit backward Euler scheme is employed to integrate Eqs. (7) and (8) and to satisfy Eq. (6), the linearization can be shown to result in the following algorithmic tangent operator relation,

$$\begin{aligned}
&\begin{bmatrix} dM_{2i} \\ dM_{3i} \end{bmatrix} = \mathbf{C}_\kappa\left(\mathbf{M}_i^{tr}, \mathbf{p}_i\right) \begin{bmatrix} d\kappa_2 \\ d\kappa_3 \end{bmatrix} + \mathbf{C}_p\left(\mathbf{M}_i^{tr}, \partial\mathbf{p}_i\right) \begin{bmatrix} d\epsilon \\ d\kappa_1 \end{bmatrix} \\
&\mathbf{C}_\kappa\left(\mathbf{M}_i^{tr}, \mathbf{p}_i\right) = \frac{K_{Ei} M_{si}\left(\mathbf{p}_i\right)}{||\mathbf{M}_i^{tr}||} \left[\mathbf{I}_{2\times 2} - \frac{\mathbf{M}_i^{tr}}{||\mathbf{M}_i^{tr}||} \otimes \frac{\mathbf{M}_i^{tr}}{||\mathbf{M}_i^{tr}||}\right] \\
&\mathbf{C}_p\left(\mathbf{M}_i^{tr}, \partial\mathbf{p}_i\right) = m_i \frac{\mathbf{M}_i^{tr}}{||\mathbf{M}_i^{tr}||} \left[\mu_i p_{i,\epsilon} + \mu_{i+1} p_{i+1,\epsilon} \quad \mu_i p_{i,\kappa_1} + \mu_{i+1} p_{i+1,\kappa_1}\right] \\
&\mathbf{p}_i = \left\{p_i, p_{i+1}\right\} \qquad \partial\mathbf{p}_i = \left\{p_{i,\epsilon}, p_{i,\kappa_1}, p_{i+1,\epsilon}, p_{i+1,\kappa_1}\right\}
\end{aligned} \tag{9}$$

where $\mathbf{M}^{tr}$ is the trial moment obtained by assuming no slippage during the finite curvature increment, i.e. $\dot{\boldsymbol{\kappa}}_p$ is set to zero in Eq. (7). The pressure derivatives $p_{,\epsilon}$ and $p_{,\kappa_1}$ are computed by the same procedure used for the partial derivatives in Eq. (5). Notice that the tangent operator is non-symmetric due to the coupling with ϵ and κ_1. With regard to the Lagrangian-Eulerian description in Section 3, it must be emphasized that Eqs. (6) – (9) refer to a fixed set of cross-sectional material particles.

3 The Lagrangian-Eulerian beam formulation

3.1 Basics of the FE framework

Three Lagrangian kinematic descriptions are presently used for geometrically nonlinear analysis of structures, the updated Lagrange (UL), the total Lagrange (TL) and the corotational (CR) [25]. In the TL formulation, the variables are referred back to the initial material configuration, whereas in the UL formulation they refer to a configuration which is stepwise updated throughout the analysis. Both descriptions were applied for three-dimensional beam problems in work by Bathe and Bolourchi [26], who demonstrated the equivalence of the formulations and concluded that the UL description was most efficient. In this work, the CR formulation is employed due to its successful applications for similar multilayered beam models [18, 19], and because it allows for direct implementation into existing computer software for flexible pipes and umbilical cables [27, 28].

In the applied CR formulation, each finite element has attached an orthogonal coordinate system that continuously rotates and translates together with the element. The main idea behind this approach is to separate the rigid body motion from the deformation modes. In this sense, the stress and deformation variables refer to a corotated configuration, that conceptually differs from the TL reference by the element rigid body motion. The deformations must be assumed small relative to the corotated reference configuration, which thus limit the element size, however, no restrictions are imposed on the rigid body motion. This motivates use of high-performance linear elements in a geometrical nonlinear setting, possibly with material nonlinearity incorporated. Objectivity of the constitutive variables is not an issue since the reference frame rotates together with the material. In contrast to the resembling UL formulation, the corotated reference configuration is not regarded fixed during iterative solution steps. The effect of referring the element internal loads to the corotated basis should therefore, as indicated in Section 3.7, be reflected in the tangent stiffness relation. Further details on formulation and application of corotated beams are given in Refs. [29–31].

The proposed Lagrangian-Eulerian formulation is based on a fully coupled approach where the mesh motion, the material motion and the convective transport effects are handled simultaneously. The formulation is expressed in terms of corotated beam elements, however, the development is readily convertible to other beam models such as those based on geometrically exact beam theories [32, 33]. In contrast to the conventional ALE formulations, use of the word *arbitrary* is avoided since there is no freedom of choice for the mesh motion. The motion of the mesh is instead computed similarly as in the conventional Lagrangian formulation, while the material velocity is specified by a boundary condition. The formulation reduces to a Lagrangian description if the material velocity is set equal to the mesh velocity, and the mesh becomes virtually Eulerian only when stationary conditions have settled. The primary assumptions of the developed procedure are,

- The bending curvature and the bending moment are regarded as continuous across element boundaries.
- Concentrated bending moment loads are only allowed at the endpoints.
- The mass is uniformly distributed and cannot accumulate in the mesh.

The above assumptions impose no restrictions for reeling operations. If required, concentrated bending moments may be modeled by applying a couple on a short beam element.

3.2 *Lagrangian-Eulerian kinematics*

A typical reeling operation with material transport between two reels is illustrated in Fig. 3. The spatial configuration of the beam centroidal line is referred to as the computational domain, and is represented by a three-dimensional curve in terms of the mesh arc length parameter $\mathcal{X} \in [0, L_{\mathcal{X}}]$. Here, $L_{\mathcal{X}}$ denotes the instantaneous length of material in the computational domain. The spatial configuration of the material stored on the reels is not of interest, and neither is it necessary to describe the initial configuration occupied by the

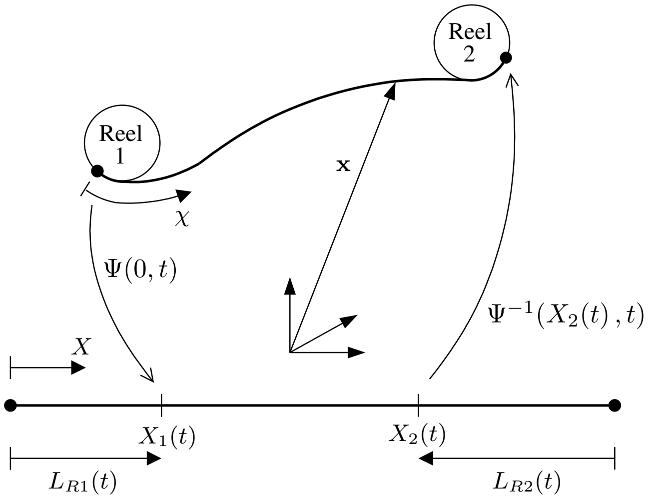

Figure 3: Lagrangian-Eulerian kinematics

material particles. However, in order to describe the kinematics, a virtual material configuration represented by the material arc length parameter $X \in [0, L_X]$ is introduced, where L_X is the unstretched length including the material present in the computational domain and the material lengths on the reels, L_{R1} and L_{R2}, see Fig. 3.

The relation between the mesh parameter and the material parameter is defined by the map,

$$X = \Psi(\chi, t) \tag{10}$$

There exists a one-to-one relationship between the material particles in the computational domain and the corresponding particles located in a bounded region of the virtual material configuration. Hence, the inverse relation of Eq. (10) can be defined,

$$\chi = \Psi^{-1}(X, t) \qquad X_1(t) \leq X \leq X_2(t) \tag{11}$$

where the bounds for X emphasize that the map is defined only for the set of material particles which happen to be in the computational domain at time t. The three-dimensional mesh motion is defined in terms of the map,

$$\mathbf{x} = \hat{\mathbf{\Phi}}(\chi, t) \tag{12}$$

in which $\mathbf{x}$ represents the coordinates of the computational domain, see Fig. 3. The motion of the material is given by,

$$\mathbf{x} = \mathbf{\Phi}(X, t) \qquad X_1(t) \leq X \leq X_2(t) \tag{13}$$

which for a fixed value of X yields the three-dimensional trajectory of a set of cross-sectional material particles in the computational domain.

The material time derivative of a quantity f is in this work denoted by a superposed dot, e.g. $\dot{f}\,(\mathcal{X},t)$. If the quantity is expressed in terms of its material representation, $f\,(X,t)$, its partial time derivative $\frac{\partial f}{\partial t}$ tacitly implies the material time derivative. To ease the notation, the independent variables of the functions in Eqs. (10) – (13) are not stated explicitly in the sequel.

The mesh velocity is obtained from Eq. (12) as follows,

$$\hat{\mathbf{V}} = \frac{\partial \hat{\mathbf{\Phi}}}{\partial t} \tag{14}$$

while the material time derivative of Eq. (11) provides the convective velocity,

$$c = \frac{\partial \Psi^{-1}}{\partial t} \tag{15}$$

which represents the material velocity along the line of centroids seen by a mesh-fixed observer. The material velocity is obtained by computing the partial time derivative of Eq. (13), or alternatively, via the material time derivative of Eq. (12),

$$\mathbf{V} = \frac{\partial \mathbf{\Phi}}{\partial t} = \frac{\partial \hat{\mathbf{\Phi}}}{\partial t} + \frac{\partial \hat{\mathbf{\Phi}}}{\partial \mathcal{X}} \frac{\partial \Psi^{-1}}{\partial t} \tag{16}$$

where $\frac{\partial \hat{\mathbf{\Phi}}}{\partial \mathcal{X}}$ is a unit vector tangent to the line of centroids in the computational domain. By inserting Eqs. (14) and (15) into Eq. (16), the following relation between the material velocity, the mesh velocity and the convective velocity is obtained,

$$\mathbf{V} = \hat{\mathbf{V}} + c \frac{\partial \hat{\mathbf{\Phi}}}{\partial \mathcal{X}} \tag{17}$$

which states that the velocity of the material is equal to the mesh velocity superposed with the convective velocity along the spatial centroidal line.

3.3 Conservation of mass

In a Lagrangian description, the conservation of mass is enforced via an algebraic equation for the mass density. This is not the case for non-Lagrangian meshes where a more elaborate treatment is required. Considering an arbitrary material region $\Omega_{\mathcal{X}}$ in the computational domain, the principle of mass conservation states that at all times,

$$\frac{\mathrm{d}}{\mathrm{d}t} \int\limits_{\Omega_{\mathcal{X}}(t)} \rho\,(\mathcal{X},t)\;\mathrm{d}\mathcal{X} = 0 \tag{18}$$

where ρ denotes the mass per unit spatial length. Since the region $\Omega_{\mathcal{X}}$ is a function of time, the differentiation and the integration in Eq. (18) cannot be interchanged. The integral is therefore pulled back to the fixed region Ω_X in the virtual material configuration, which with the Jacobian relation, $\mathrm{d}\mathcal{X} = \frac{\partial \Psi^{-1}}{\partial X}\mathrm{d}X$, is performed as follows,

$$\int\limits_{\Omega_X} \frac{\partial}{\partial t}\left(\rho\,(X,t)\,\frac{\partial \Psi^{-1}}{\partial X}\right)\mathrm{d}X = \int\limits_{\Omega_X}\left(\dot{\rho}\frac{\partial \Psi^{-1}}{\partial X} + \rho\frac{\partial c}{\partial X}\right)\mathrm{d}X = 0 \tag{19}$$

where use was made of Eq. (15). By means of Eqs. (10) and (15) and the inverse Jacobian relation, $\mathrm{d}X = \frac{\partial \Psi}{\partial \mathcal{X}}\mathrm{d}\mathcal{X}$, push-forward to the computational domain yields,

$$\int\limits_{\Omega_{\mathcal{X}}(t)} \left(\dot{\rho} + \rho \frac{\partial c}{\partial X}\frac{\partial \Psi}{\partial \mathcal{X}}\right) \mathrm{d}\mathcal{X} = \int\limits_{\Omega_{\mathcal{X}}(t)} \left(\frac{\partial \rho}{\partial t} + c\frac{\partial \rho}{\partial \mathcal{X}} + \rho\frac{\partial c}{\partial \mathcal{X}}\right) \mathrm{d}\mathcal{X} = 0 \tag{20}$$

and when recalling that the region $\Omega_{\mathcal{X}}$ is arbitrary, the local form of the principle of mass conservation follows as,

$$\frac{\partial \rho}{\partial t} + c\frac{\partial \rho}{\partial \mathcal{X}} + \rho\frac{\partial c}{\partial \mathcal{X}} = 0 \tag{21}$$

which is analogous to the continuity equation in fluid mechanic problems and can be enforced by developing a weak formulation for the mass density, see Ref. [4]. However, in this work the first term in Eq. (21) is set to zero as mass is not allowed to accumulate in the mesh, and because the change of ρ due to longitudinal straining is assumed negligible. Since the mass is uniformly distributed the second term is also zero, and the continuity equation reduces to,

$$\frac{\partial c}{\partial \mathcal{X}} = 0 \tag{22}$$

which states that the convective velocity at a given time must be constant throughout the mesh.

In view of Eq. (22), some clarifications regarding the boundary conditions for the mesh displacement and the material velocity are needed. By multiplying Eq. (17) with the unit tangent vector along the line of centroids, $\frac{\partial \hat{\boldsymbol{\Phi}}}{\partial \mathcal{X}}$, the following expression for the convective velocity is obtained,

$$c\,(t) = V\,(\mathcal{X},t) - \hat{V}\,(\mathcal{X},t) \tag{23}$$

in which V and $\hat{V}$ denote the absolute velocities of the material and the mesh along the centroidal line, respectively. When the material velocity is prescribed at a single nodal point, the convective velocity is obtained directly from Eq. (23) and the mass conservation expressed in Eq. (22) is fulfilled regardless of the applied displacement boundary conditions. However, if the material velocity is prescribed at another node in addition, one of the nodes must be regarded as constrained in terms of the other, where the velocity $\hat{V}$ of the constrained node is given according to Eq. (23) such that Eq. (22) is satisfied.

3.4 Corotational beam kinematics

The Euler-Bernoulli kinematic relations are utilized as reeling operations usually involve slender beams with negligible shear deformations. The element deformations are therefore expressed in terms of seven parameters,

$$\mathbf{v}_d^{\top} = \begin{bmatrix} u\,, & \theta_{1B} - \theta_{1A}\,, & \mathbf{v}_{db}^{\top} \end{bmatrix} \quad \mathbf{v}_{db}^{\top} = \begin{bmatrix} \theta_{2A} & \theta_{3A} & \theta_{2B} & \theta_{3B} \end{bmatrix} \tag{24}$$

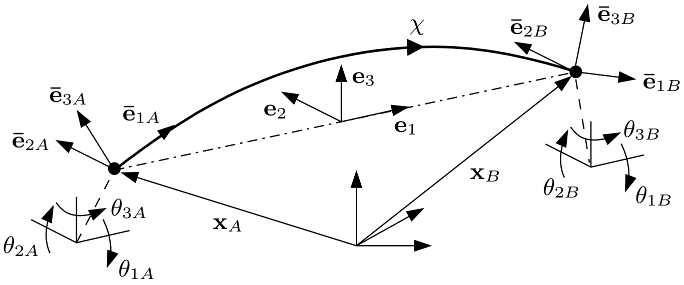

Figure 4: Beam element kinematics

where u is the axial elongation found from the secant length, the second entry is the torsion angle increment over the element, $\mathbf{v}_{db}$ is related to bending and subscript A and B refer to the element nodes. All of the parameters are referred to the coordinates associated with the element corotated unit vectors $\mathbf{e}_i$, see Fig. 4. The rotation parameters measure the rotation of the nodal triads, $\bar{\mathbf{e}}_{Ai}$ and $\bar{\mathbf{e}}_{Bi}$, relative to the $\mathbf{e}_i$-vectors, and are computed according to standard procedures given in Refs. [34, 35]. As the element deformations must be small in the CR formulation, the mesh parameter $\mathcal{X}$ of the deformed centroidal line is in the sequel not distinguished from the arc length parameter for the straight line between the element nodes.

The bending curvature at element node A and B is needed in the elasto-plastic bending model. A linear curvature distribution over the element is assumed and the nodal bending curvature is thus expressed as,

$$\begin{aligned} \boldsymbol{\kappa}_{\mathcal{X}j} &= \begin{bmatrix} \kappa_{\mathcal{X}j2} \\ \kappa_{\mathcal{X}j3} \end{bmatrix} = \mathbf{N}_{\kappa j}\mathbf{v}_{db} \qquad j = A, B \\ \mathbf{N}_{\kappa A} &= -\frac{1}{L}\begin{bmatrix} 4 & 0 & 2 & 0 \\ 0 & 4 & 0 & 2 \end{bmatrix} \qquad \mathbf{N}_{\kappa B} = \frac{1}{L}\begin{bmatrix} 2 & 0 & 4 & 0 \\ 0 & 2 & 0 & 4 \end{bmatrix} \end{aligned} \tag{25}$$

where L is the current element length and subscript $\mathcal{X}$ marks that the variable is evaluated with the mesh parameter fixed. The torsion κ_1 and the axial strain ϵ are, in line with the axi-symmetric model in Section 2.1, assumed constant within the element,

$$\kappa_1 = \frac{\theta_{1B} - \theta_{1A}}{L} \tag{26}$$

$$\epsilon = \frac{u}{L} \tag{27}$$

The mesh velocity along the centroidal line $\hat{V}$ is needed in order to determine the convective velocity in Eq. (23), and is at the element nodes computed as follows,

$$\hat{V}_j = \frac{1}{\Delta t}\left(\mathbf{x}_j - \mathbf{x}_j^p\right) \cdot \bar{\mathbf{e}}_{1j} \qquad j = A, B \tag{28}$$

where the involved vectors are defined in Fig. 4, Δt is the time step increment and superscript p refers to the previous equilibrium state.

When developing the tangent stiffness needed in the Newton-Raphson solution scheme, the element incremental nodal displacement vector $d\mathbf{v}$ is involved,

$$
\begin{aligned}
d\mathbf{v} &= \begin{bmatrix} d\mathbf{q}_A & d\mathbf{q}_B \end{bmatrix}^\top \\
d\mathbf{q}_j &= \begin{bmatrix} dx_{1j} & dx_{2j} & dx_{3j} & d\varphi_{1j} & d\varphi_{2j} & d\varphi_{3j} \end{bmatrix}
\end{aligned}
\tag{29}
$$

which is linked to the incremental deformation parameters, $d\mathbf{v}_d$, via the following expression,

$$
\begin{aligned}
d\mathbf{v}_d &= \mathbf{H}^\top d\mathbf{v} \\
\mathbf{H} &= \begin{bmatrix}
-\mathbf{e}_1 & \mathbf{0} & -\frac{1}{L}\mathbf{e}_3 & \frac{1}{L}\mathbf{e}_2 & -\frac{1}{L}\mathbf{e}_3 & \frac{1}{L}\mathbf{e}_2 \\
\mathbf{0} & -\mathbf{e}_1 & \mathbf{e}_2 & \mathbf{e}_3 & \mathbf{0} & \mathbf{0} \\
\mathbf{e}_1 & \mathbf{0} & \frac{1}{L}\mathbf{e}_3 & -\frac{1}{L}\mathbf{e}_2 & \frac{1}{L}\mathbf{e}_3 & -\frac{1}{L}\mathbf{e}_2 \\
\mathbf{0} & \mathbf{e}_1 & \mathbf{0} & \mathbf{0} & \mathbf{e}_2 & \mathbf{e}_3
\end{bmatrix}
\end{aligned}
\tag{30}
$$

where the $\mathbf{H}$-matrix also serves as a transformation operator between the corotated coordinates and the coordinates used to represent the $\mathbf{e}_i$-vectors.

3.5 Material time derivative of constitutive variables

The elasto-plastic bending model depends on the history experienced by the material particles and is hence updated by integration of the material time derivative. In contrast to a Lagrangian formulation, the mesh points do not follow the material particles such that a convective transport contribution must be accounted for. With aid of Eq. (15), the corotational material time derivative of a corotated vector $\mathbf{A}$ is therefore expressed as,

$$
\dot{\mathbf{A}}\left(\mathcal{X}, t\right) = \left.\frac{\partial \mathbf{A}}{\partial t}\right|_{[\mathcal{X}]} + c\frac{\partial \mathbf{A}}{\partial \mathcal{X}} \qquad \mathbf{A} = A_2\mathbf{e}_2 + A_3\mathbf{e}_3 \tag{31}
$$

where the notation $[*]$ emphasizes that the variable inside the brackets is held fixed. The constitutive variables in the elasto-plastic bending model are interpolated with C^0-functions between the element nodes, and the second term in Eq. (31) is therefore in general discontinuous at the element boundaries. According to numerical investigations in this work, both stability and accuracy depend strongly on the approximation selected for the gradient, e.g. unacceptable performance resulted when the gradient was approximated with nodal values from one single element only. This agrees with related work on ALE stress-update algorithms in which the treatment of the spatial gradients represents the main challenge [36]. To overcome this issue, a weak formulation for the material time derivative is developed by multiplying Eq. (31) with a test function $\delta\mathbf{A}$,

$$
\int\limits_{\Omega_m} \delta\mathbf{A} \cdot \left(\dot{\mathbf{A}} - \mathbf{A}_{,t[\mathcal{X}]} - c\mathbf{A}_{,\mathcal{X}}\right) \mathrm{d}\mathcal{X} = 0 \tag{32}
$$

where the integration is executed over element m. By rewriting the third term with aid of the product rule of differentiation, the derivative of the constitutive variable gets transferred to the test function and a boundary term emerges,

$$\int\limits_{\Omega_m} \delta\mathbf{A}\cdot\left(\dot{\mathbf{A}} - \mathbf{A}_{,t[\mathcal{X}]}\right)\mathrm{d}\mathcal{X} + \int\limits_{\Omega_m} c\,\delta\mathbf{A}_{,\mathcal{X}}\cdot\mathbf{A}\,d\mathcal{X} - c\,\delta\mathbf{A}\cdot\mathbf{A}\big|_{\partial\Omega_m} = 0 \tag{33}$$

The last term in Eq. (33) provides a natural means for setting up communication with neighboring elements. By assuming continuity of the constitutive variable across the element boundaries and using C^0-functions for $\delta\mathbf{A}$, the resulting expression reads,

$$\begin{aligned}\begin{bmatrix}\mathbf{A}_{XA,t}\\ \mathbf{A}_{XB,t}\end{bmatrix} = \begin{bmatrix}\mathbf{A}_{\mathcal{X}A,t}\\ \mathbf{A}_{\mathcal{X}B,t}\end{bmatrix} + \frac{3c}{L}\begin{bmatrix}\mathbf{A}_{\mathcal{X}A} + \mathbf{A}_{\mathcal{X}B}\\ -\mathbf{A}_{\mathcal{X}B} - \mathbf{A}_{\mathcal{X}A}\end{bmatrix} + \frac{c}{L}\begin{bmatrix}-4\tilde{\mathbf{A}}_{\mathcal{X}B}^{\{m-1\}}\\ 2\tilde{\mathbf{A}}_{\mathcal{X}B}^{\{m-1\}}\end{bmatrix}\\ + \frac{c}{L}\begin{bmatrix}-2\tilde{\mathbf{A}}_{\mathcal{X}A}^{\{m+1\}}\\ 4\tilde{\mathbf{A}}_{\mathcal{X}A}^{\{m+1\}}\end{bmatrix}\end{aligned} \tag{34}$$

where subscript A and B refer to the element nodes. Subscript X and $\mathcal{X}$ mark that the variable is evaluated by holding respectively the material parameter and the mesh parameter fixed, see Section 3.2. The superscripted curly brackets are introduced to label vectors that stem from the neighboring elements, where $m-1$ and $m+1$ refer to respectively the elements adjacent to node A and B of element m. This consecutive element numbering is assumed in the following subsections without explicit notifications. The vectors from the neighboring elements are also labeled with a superposed tilde to underline that a transformation with all three scalar components is involved,

$$\tilde{A}_r^{\{m\pm1\}} = \mathbf{e}_r\cdot\mathbf{e}_s^{\{m\pm1\}}A_s^{\{m\pm1\}} \qquad r = 2,3 \quad s = 1,2,3 \tag{35}$$

where the Einstein summation convention applies for repeated indices.

The weak form development above is beneficial since the gradient is approximated with an appropriate spatial weighting of the constitutive variables and because it comprises information from adjacent elements. Still, a direct implementation of Eq. (34) could result in spatial instabilities [37]. This can be circumvented by introducing an upwinding technique to the Galerkin-based FE method. Several examples are found in the literature, such as the streamline upwind Petrov-Galerkin method employed by Liu et al. [38] for solid mechanic problems and the Taylor-Galerkin method applied by Donea [39] for convection problems. The upwind scheme employed in this work was, however, established by means of numerical experimentation and reads,

$$\tilde{\mathbf{A}}_{\mathcal{X}B}^{\{m-1\}} = \begin{cases}\tilde{\mathbf{A}}_{\mathcal{X}B}^{\{m-1\}} & \text{if} \quad c > 0\\ \mathbf{A}_{\mathcal{X}A} & \text{if} \quad c \leq 0\end{cases} \tag{36}$$

$$\tilde{\mathbf{A}}_{\mathcal{X}A}^{\{m+1\}} = \begin{cases}\tilde{\mathbf{A}}_{\mathcal{X}A}^{\{m+1\}} & \text{if} \quad c < 0\\ \mathbf{A}_{\mathcal{X}B} & \text{if} \quad c \geq 0\end{cases} \tag{37}$$

When combining Eqs. (36) and (37) with Eq. (34), it is clear that the scheme simply prevents use of information located downstream relative to element m. Upwinding techniques are known to introduce numerical dissipation and possible effects regarding the accuracy is commented in Section 4.

3.6 Update scheme for the elasto-plastic bending model

As for conventional Lagrangian beam formulations, the internal virtual work due to bending is expressed in terms of the mesh-fixed bending moment $\mathbf{M}_{\chi}$. In contrast, the elasto-plastic model in Section 2.2 refers to the material-fixed bending moment $\mathbf{M}_{X}$. The relation between incremental values of these moments is provided by the material time derivative expression in Eq. (34). In view of the developments in Section 3.5, the integration stations are placed at element node A and B, and for the mesh moment the update reads,

$$\mathbf{M}_{\chi j} = \mathbf{M}^{p}_{\chi j} + \Delta\mathbf{M}_{\chi j} \qquad \mathbf{M}_{\chi j} = M_{\chi j 2}\mathbf{e}_2 + M_{\chi j 3}\mathbf{e}_3 \qquad j = A, B \tag{38}$$

where $\mathbf{M}^{p}_{\chi j}$ is the mesh moment in the previous equilibrium state and the Δ-symbol, both here and in the sequel, refers to an increment measured relative to the previous equilibrium state. An expression for the mesh moment increment is obtained by integration of Eq. (34) as follows,

$$\begin{aligned}
\begin{bmatrix} \Delta\mathbf{M}_{\chi A} \\ \Delta\mathbf{M}_{\chi B} \end{bmatrix} = \begin{bmatrix} \Delta\mathbf{M}_{XA} \\ \Delta\mathbf{M}_{XB} \end{bmatrix} &- \frac{\gamma c \Delta t}{L} \left\{ 3 \begin{bmatrix} \mathbf{M}_{XA} + \mathbf{M}_{XB} \\ -\mathbf{M}_{XB} - \mathbf{M}_{XA} \end{bmatrix} + \begin{bmatrix} -4\tilde{\mathbf{M}}^{\{m-1\}}_{XB} \\ 2\tilde{\mathbf{M}}^{\{m-1\}}_{XB} \end{bmatrix} \right. \\
&\left. + \begin{bmatrix} -2\tilde{\mathbf{M}}^{\{m+1\}}_{XA} \\ 4\tilde{\mathbf{M}}^{\{m+1\}}_{XA} \end{bmatrix} \right\} - \frac{(1-\gamma)\, c^{p} \Delta t}{L} \left\{ 3 \begin{bmatrix} \mathbf{M}^{p}_{XA} + \mathbf{M}^{p}_{XB} \\ -\mathbf{M}^{p}_{XB} - \mathbf{M}^{p}_{XA} \end{bmatrix} \right. \\
&\left. + \begin{bmatrix} -4\tilde{\mathbf{M}}^{p\{m-1\}}_{XB} \\ 2\tilde{\mathbf{M}}^{p\{m-1\}}_{XB} \end{bmatrix} + \begin{bmatrix} -2\tilde{\mathbf{M}}^{p\{m+1\}}_{XA} \\ 4\tilde{\mathbf{M}}^{p\{m+1\}}_{XA} \end{bmatrix} \right\} \qquad 0 \leq \gamma \leq 1
\end{aligned} \tag{39}$$

where Δt is the time increment, superscript p refers to the previous equilibrium state and γ is the temporal weight factor for the convective terms. Note that for the convective terms, the material moments $\mathbf{M}_{X}$ are employed instead of the mesh moments $\mathbf{M}_{\chi}$ to facilitate the update itself and the forthcoming linearization.

The material moment increment needed in Eq. (39) is given by,

$$\Delta\mathbf{M}_{Xj} = \mathbf{M}_{Xj} - \mathbf{M}^{p}_{\chi j} \qquad j = A, B \tag{40}$$

in which $\mathbf{M}^{p}_{\chi j}$ refers to the mesh moment in the previous equilibrium state, i.e. the initial material moment of the current time step. The material moment $\mathbf{M}_{X}$ is updated according to the interlayer friction model selected for the multilayered beam. In this work, the Coulomb model in Section 2.2 is employed and the update is performed with a fully implicit backward Euler integration scheme. For general friction models, the update requires use of a local iterative scheme, but for the simple Coulomb model the following closed form expression can be derived,

$$\mathbf{M}_{Xj} = \begin{cases} \frac{\mathbf{M}^{tr}_{Xj}}{||\mathbf{M}^{tr}_{Xj}||} M_{sj} & \text{if} \quad f\left(\mathbf{M}^{tr}_{Xj}, M_{sj}\right) \geq 0 \\ \mathbf{M}^{tr}_{Xj} & \text{if} \quad f\left(\mathbf{M}^{tr}_{Xj}, M_{sj}\right) < 0 \end{cases} \qquad j = A, B \tag{41}$$

where f is the slip function, $\mathbf{M}^{tr}_{Xj}$ is the trial material moment and M_{sj} is the slip moment computed from the nodal interlayer pressures, see Eq. (6). In Fig. 5 the slip function and

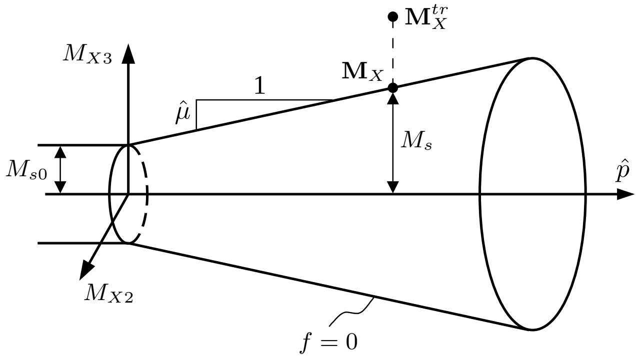

Figure 5: Coulomb slip function

the return map in Eq. (41) is illustrated. In view of the continuity assumption in Eq. (34), the nodal interlayer pressures are obtained by a spatial weighting according to,

$$\begin{aligned} p_A^{\{m\}} &= \alpha_1 p^{\{m-1\}} + \alpha_2 p^{\{m\}} & p_B^{\{m\}} &= \beta_1 p^{\{m+1\}} + \beta_2 p^{\{m\}} \\ \alpha_1 &= \frac{L^{\{m\}}}{L^{\{m\}} + L^{\{m-1\}}} & \alpha_2 &= \frac{L^{\{m-1\}}}{L^{\{m\}} + L^{\{m-1\}}} \\ \beta_1 &= \frac{L^{\{m\}}}{L^{\{m\}} + L^{\{m+1\}}} & \beta_2 &= \frac{L^{\{m+1\}}}{L^{\{m\}} + L^{\{m+1\}}} \end{aligned} \tag{42}$$

where m refers to the element number and p is the interlayer pressure which is assumed constant within the element. The trial material moment is obtained from Eq. (7) by assuming no slippage during the increment,

$$\mathbf{M}_{Xj}^{tr} = \mathbf{M}_{Xj}^{p} + K_E \Delta \boldsymbol{\kappa}_{Xj} \qquad j = A, B \tag{43}$$

where the increment of material bending curvature $\Delta \boldsymbol{\kappa}_{Xj}$ is obtained by means of Eq. (34) as follows,

$$\begin{aligned} \begin{bmatrix} \Delta \boldsymbol{\kappa}_{XA} \\ \Delta \boldsymbol{\kappa}_{XB} \end{bmatrix} = \begin{bmatrix} \Delta \boldsymbol{\kappa}_{XA} \\ \Delta \boldsymbol{\kappa}_{XB} \end{bmatrix} &+ \frac{\gamma c \Delta t}{L} \left\{ 3 \begin{bmatrix} \boldsymbol{\kappa}_{XA} + \boldsymbol{\kappa}_{XB} \\ -\boldsymbol{\kappa}_{XB} - \boldsymbol{\kappa}_{XA} \end{bmatrix} + \begin{bmatrix} -4\tilde{\boldsymbol{\kappa}}_{XB}^{\{m-1\}} \\ 2\tilde{\boldsymbol{\kappa}}_{XB}^{\{m-1\}} \end{bmatrix} \right. \\ &\left. + \begin{bmatrix} -2\tilde{\boldsymbol{\kappa}}_{XA}^{\{m+1\}} \\ 4\tilde{\boldsymbol{\kappa}}_{XA}^{\{m+1\}} \end{bmatrix} \right\} + \frac{(1-\gamma)\, c^p \Delta t}{L} \left\{ 3 \begin{bmatrix} \boldsymbol{\kappa}_{XA}^p + \boldsymbol{\kappa}_{XB}^p \\ -\boldsymbol{\kappa}_{XB}^p - \boldsymbol{\kappa}_{XA}^p \end{bmatrix} \right. \\ &\left. + \begin{bmatrix} -4\tilde{\boldsymbol{\kappa}}_{XB}^{p\{m-1\}} \\ 2\tilde{\boldsymbol{\kappa}}_{XB}^{p\{m-1\}} \end{bmatrix} + \begin{bmatrix} -2\tilde{\boldsymbol{\kappa}}_{XA}^{p\{m+1\}} \\ 4\tilde{\boldsymbol{\kappa}}_{XA}^{p\{m+1\}} \end{bmatrix} \right\} \qquad 0 \leq \gamma \leq 1 \end{aligned} \tag{44}$$

in which Δt, γ and superscript p have the same meaning as in Eq. (39). The mesh bending curvature $\boldsymbol{\kappa}_X$ at the element nodes is determined from Eq. (25), while its increment is expressed as,

$$\Delta \boldsymbol{\kappa}_{Xj} = \mathbf{N}_{\kappa j} \left[\mathbf{v}_{db} - \mathbf{v}_{db}^p \right] \qquad j = A, B \tag{45}$$

with $\mathbf{v}_{db}$ and $\mathbf{N}_{\kappa}$ defined in Eqs. (24) and (25), respectively, and superscript p refers to the previous equilibrium state.

Note that the Coulomb model applied in this work contains no hardening variables. If such internal variables are present they could be updated by similar principles as presented here. Likewise, if an elasto-plastic model is assigned to the torque or the axial force, the update algorithm may be developed along the same lines as used above.

3.7 Weak formulation and linearization

A quasistatic modeling approach is utilized as reeling operations normally involve low velocities and negligible inertia loads. The applied weak formulation contains thus contributions only from the external loads and the internal stress resultants. The latter contribution is for a single element expressed by a summation over the K load-bearing layers according to,

$$
\begin{aligned}
\delta W &= \delta \mathbf{v}^{\top} \mathbf{H}\, \mathbf{S} \\
\mathbf{S} &= \sum_{i=1}^{K} \begin{bmatrix} N_i & M_{1i} & -M_{XA2i} & -M_{XA3i} & M_{XB2i} & M_{XB3i} \end{bmatrix}^{\top}
\end{aligned}
\tag{46}
$$

where $\mathbf{H}$ is the 12×6-matrix given in Eq. (30), $\mathbf{v}$ is the element nodal displacement vector defined in Eq. (29) with incremental components and the δ-symbol refers to either virtual work or virtual displacements. The axial force N and the torque M_1 are obtained from the axi-symmetric model in Section 2.1, the plastic sheath layer bending moments are computed from their respective linear-elastic stiffness factors, while the bending moments of the tensile helix layers are obtained via the update procedure in Section 3.6.

In the Newton-Raphson solution scheme the linearization of Eq. (46) with respect to the nodal displacements is needed. This linearization provides the element tangent stiffness matrices and is expressed as,

$$
d\left(\delta W\right) = d\left(\delta \mathbf{v}^{\top}\right) \mathbf{H}\, \mathbf{S} + \delta \mathbf{v}^{\top} d\mathbf{H}\, \mathbf{S} + \delta \mathbf{v}^{\top} \mathbf{H}\, d\mathbf{S} \tag{47}
$$

where the first term appears because the variation of the rotational degrees of freedom (DOFs) is configuration-dependent. The second term accounts for the change of element length and the effect of rotating the element corotated unit vectors. The stiffness matrices associated with these terms, including also a separate local geometric stiffness contribution, are based on identical matrices as presented by Krenk et al. [31].

The constitutive stiffness contribution emerges from the third term in Eq. (47). For layers with linear-elastic bending behavior the associated stiffness relation is given by,

$$
d\mathbf{S}_i = \frac{1}{L} \begin{bmatrix}
N_{i,\epsilon} & N_{i,\kappa_1} & 0 & 0 & 0 & 0 \\
M_{1i,\epsilon} & M_{1i,\kappa_1} & 0 & 0 & 0 & 0 \\
0 & 0 & 4K_{Ei} & 0 & 2K_{Ei} & 0 \\
0 & 0 & 0 & 4K_{Ei} & 0 & 2K_{Ei} \\
0 & 0 & 2K_{Ei} & 0 & 4K_{Ei} & 0 \\
0 & 0 & 0 & 2K_{Ei} & 0 & 4K_{Ei}
\end{bmatrix} \mathbf{H}^{\top} d\mathbf{v} \tag{48}
$$

where K_{Ei} denotes the layer bending stiffness and the axial-torsional stiffness factors are obtained from Eq. (5).

The bending constitutive stiffness for the tensile helix layers is established by linearizing the moment update scheme in Section 3.6. If a consistent stiffness representation is used, the Newton-Raphson algorithm is able to provide quadratic convergence rates in the vicinity of the solution [40]. All quantities that change between the iterative solution steps must be accounted for in a consistent linearization, however, some of the involved variables can be disregarded without destroying the convergence rate. Hence, the convective velocity c and the element length L are treated as constants when the moment update scheme is linearized. The former quantity is indeed constant if the material velocity is prescribed at a node that is fixed in the beam axial direction. In addition, terms proportional to $(\Delta t)^2$ are neglected in the subsequent derivations.

Considering a single element m and a single tensile helix layer, an expression for the iterative change of the mesh moments is obtained by linearizing Eqs. (38) and (39) according to,

$$\begin{aligned} d\mathbf{M}_{\chi A} &= d\left(\Delta\mathbf{M}_{XB}\right) - \hat{\gamma}\left[3d\mathbf{M}_{XA}+3d\mathbf{M}_{XB}-4d\tilde{\mathbf{M}}_{XB}^{\{m-1\}}-2d\tilde{\mathbf{M}}_{XA}^{\{m+1\}}\right] \\ \hat{\gamma} &= \frac{\gamma c \Delta t}{L} \end{aligned} \tag{49}$$

$$d\mathbf{M}_{\chi B} = d\left(\Delta\mathbf{M}_{XB}\right) + \hat{\gamma}\left[3d\mathbf{M}_{XA}+3d\mathbf{M}_{XB}-2d\tilde{\mathbf{M}}_{XB}^{\{m-1\}}-4d\tilde{\mathbf{M}}_{XA}^{\{m+1\}}\right] \tag{50}$$

where it must be emphasized that the upwind scheme in Eqs. (36) and (37) applies for the moments that belong to the adjacent elements.

To ease the notation, the following superscripted labels are introduced for the constitutive matrix $\mathbf{C}_p$ defined in Eq. (9),

$${}^{\{a\}}\mathbf{C}_{pj}^{\{b\}} = \mathbf{C}_p\left(\mathbf{M}_{Xj}^{tr\{a\}}, \partial\mathbf{p}^{\{b\}}\right) \qquad j = A, B \tag{51}$$

in which $\{a\}$ refers to the element where the trial moment is computed and $\{b\}$ denotes the element where the pressure derivatives are defined. A similar notation is used for the constitutive matrix $\mathbf{C}_\kappa$ defined in Eq. (9),

$$\mathbf{C}_{\kappa j}^{\{a\}} = \mathbf{C}_\kappa\left(\mathbf{M}_{Xj}^{tr\{a\}}, \mathbf{p}_j^{\{a\}}\right) \qquad j = A, B \tag{52}$$

while the axial strain and the torsion are collected in the vector,

$$d\boldsymbol{\omega} = \begin{bmatrix} d\epsilon & d\kappa_1 \end{bmatrix}^\top \tag{53}$$

The first term in Eqs. (49) and (50) represents the iterative change of the material moments. An expression for this change is obtained from the algorithmic tangent relation in Eq. (9) and by linearizing the material curvature increment in Eq. (44). Since the interlayer contact pressures are weighted according to Eq. (42), the result is expressed as follows,

$$\begin{aligned} d\left(\Delta\mathbf{M}_{XA}\right) = \mathbf{C}_{\kappa A}^{\{m\}} d\boldsymbol{\kappa}_{\chi A}^{\{m\}} &+ \alpha_1{}^{\{m\}}\mathbf{C}_{pA}^{\{m-1\}} d\boldsymbol{\omega}^{\{m-1\}} + \alpha_2{}^{\{m\}}\mathbf{C}_{pA}^{\{m\}} d\boldsymbol{\omega}^{\{m\}} \\ &+ \hat{\gamma}\mathbf{C}_{\kappa A}^{\{m\}}\left[3d\boldsymbol{\kappa}_{\chi A}^{\{m\}} + 3d\boldsymbol{\kappa}_{\chi B}^{\{m\}} - 4d\tilde{\boldsymbol{\kappa}}_{\chi B}^{\{m-1\}} - 2d\tilde{\boldsymbol{\kappa}}_{\chi A}^{\{m+1\}}\right] \end{aligned} \tag{54}$$

$$\begin{aligned} d\left(\Delta \mathbf{M}_{XB}\right) = {} & \mathbf{C}_{\kappa B}^{\{m\}} d\boldsymbol{\kappa}_{XB}^{\{m\}} + {\beta_1}^{\{m\}} \mathbf{C}_{pB}^{\{m+1\}} d\boldsymbol{\omega}^{\{m+1\}} + {\beta_2}^{\{m\}} \mathbf{C}_{pB}^{\{m\}} d\boldsymbol{\omega}^{\{m\}} \\ & - \hat{\gamma} \mathbf{C}_{\kappa B}^{\{m\}} \left[3 d\boldsymbol{\kappa}_{XA}^{\{m\}} + 3 d\boldsymbol{\kappa}_{XB}^{\{m\}} - 2 d\tilde{\boldsymbol{\kappa}}_{XB}^{\{m-1\}} - 4 d\tilde{\boldsymbol{\kappa}}_{XA}^{\{m+1\}} \right] \end{aligned} \tag{55}$$

where the upwind scheme in Eqs. (36) and (37) applies for the curvature terms that stem from the neighboring elements. These terms are due to the transformation in Eq. (35), obtained from the following matrix relation,

$$\begin{aligned} d\tilde{\boldsymbol{\kappa}}_{Xj}^{\{m\pm1\}} = {} & \mathbf{G}\left(\boldsymbol{\kappa}_{Xj}^{\{m\pm1\}}\right) \boldsymbol{\Omega}^{\{m\pm1\}} d\mathbf{v}^{\{m\pm1\}} - \mathbf{G}\left(\boldsymbol{\kappa}_{Xj}^{\{m\pm1\}}\right) \boldsymbol{\Omega}^{\{m\}} d\mathbf{v}^{\{m\}} \\ & + \mathbf{T}_{2\times3}^{\{m\pm1\}} \begin{bmatrix} d\kappa_1^{\{m\pm1\}} \\ d\boldsymbol{\kappa}_{Xj}^{\{m\pm1\}} \end{bmatrix} \qquad j = A, B \end{aligned} \tag{56}$$

where a detailed derivation of the expression above and definitions of the matrices $\mathbf{G}$, $\boldsymbol{\Omega}$ and $\mathbf{T}$ are presented in 5.

The remaining terms in Eqs. (49) and (50) are associated with convective effects, and should in principle be represented by relations similar to those given in Eqs. (54) – (55). However, as contributions proportional to $(\Delta t)^2$ are neglected, the following expressions are used instead,

$$d\mathbf{M}_{XA} = \mathbf{C}_{\kappa A}^{\{m\}} d\boldsymbol{\kappa}_{XA}^{\{m\}} + {\alpha_1}^{\{m\}} \mathbf{C}_{pA}^{\{m-1\}} d\boldsymbol{\omega}^{\{m-1\}} + {\alpha_2}^{\{m\}} \mathbf{C}_{pA}^{\{m\}} d\boldsymbol{\omega}^{\{m\}} \tag{57}$$

$$d\mathbf{M}_{XB} = \mathbf{C}_{\kappa B}^{\{m\}} d\boldsymbol{\kappa}_{XB}^{\{m\}} + {\beta_1}^{\{m\}} \mathbf{C}_{pB}^{\{m+1\}} d\boldsymbol{\omega}^{\{m+1\}} + {\beta_2}^{\{m\}} \mathbf{C}_{pB}^{\{m\}} d\boldsymbol{\omega}^{\{m\}} \tag{58}$$

while the terms that stem from the neighboring elements are expressed by means of the same matrix relation used in Eq. (56),

$$\begin{aligned} d\tilde{\mathbf{M}}_{Xj}^{\{m\pm1\}} = {} & \mathbf{G}\left(\mathbf{M}_{Xj}^{\{m\pm1\}}\right) \boldsymbol{\Omega}^{\{m\pm1\}} d\mathbf{v}^{\{m\pm1\}} - \mathbf{G}\left(\mathbf{M}_{Xj}^{\{m\pm1\}}\right) \boldsymbol{\Omega}^{\{m\}} d\mathbf{v}^{\{m\}} \\ & + \mathbf{T}_{2\times3}^{\{m\pm1\}} \begin{bmatrix} dM_1^{\{m\pm1\}} \\ d\mathbf{M}_{Xj}^{\{m\pm1\}} \end{bmatrix} \qquad j = A, B \end{aligned} \tag{59}$$

where the incremental moments in the third term are given by,

$$dM_1^{\{m\pm1\}} = \begin{bmatrix} \frac{M_{1,\epsilon}^{\{m\pm1\}}}{L^{\{m\pm1\}}} & \frac{M_{1,\kappa_1}^{\{m\pm1\}}}{L^{\{m\pm1\}}} \end{bmatrix} d\boldsymbol{\omega}^{\{m\pm1\}} \tag{60}$$

$$\begin{aligned} d\mathbf{M}_{XB}^{\{m-1\}} = {} & \mathbf{C}_{\kappa B}^{\{m-1\}} d\boldsymbol{\kappa}_{XB}^{\{m-1\}} + {\alpha_1}^{\{m-1\}} \mathbf{C}_{pB}^{\{m-1\}} d\boldsymbol{\omega}^{\{m-1\}} \\ & + {\alpha_2}^{\{m-1\}} \mathbf{C}_{pB}^{\{m\}} d\boldsymbol{\omega}^{\{m\}} \end{aligned} \tag{61}$$

$$\begin{aligned} d\mathbf{M}_{XA}^{\{m+1\}} = {} & \mathbf{C}_{\kappa A}^{\{m+1\}} d\boldsymbol{\kappa}_{XA}^{\{m+1\}} + {\beta_1}^{\{m+1\}} \mathbf{C}_{pA}^{\{m+1\}} d\boldsymbol{\omega}^{\{m+1\}} \\ & + {\beta_2}^{\{m+1\}} \mathbf{C}_{pA}^{\{m\}} d\boldsymbol{\omega}^{\{m\}} \end{aligned} \tag{62}$$

The stiffness associated with Eq. (49) and (50) is obtained by relating the above expressions to the nodal displacements. Hence, by means of the $\mathbf{H}$-matrix defined in Eq.

(29), and the relations between the generalized strains and the element deformation parameters in Eqs. (25) – (27), the stiffness relation associated with bending of a tensile helix layer can be expressed on 4×12 format as,

$$\begin{aligned}\begin{bmatrix} -d\mathbf{M}_{\chi A} \\ d\mathbf{M}_{\chi B} \end{bmatrix} &= \mathbf{K}_{\kappa}^{\{m\}} d\mathbf{v}^{\{m\}} + \mathbf{K}_{p}^{\{m-1\}} d\mathbf{v}^{\{m-1\}} + \mathbf{K}_{p}^{\{m\}} d\mathbf{v}^{\{m\}} \\ &+ \mathbf{K}_{p}^{\{m+1\}} d\mathbf{v}^{\{m+1\}} + \hat{\gamma}\Big[\mathbf{K}_{LE}^{\{m-1\}} d\mathbf{v}^{\{m-1\}} + \mathbf{K}_{LE}^{\{m\}} d\mathbf{v}^{\{m\}} \\ &+ \mathbf{K}_{LE}^{\{m+1\}} d\mathbf{v}^{\{m+1\}}\Big]\end{aligned} \tag{63}$$

where the four first matrices stem from the three first terms in Eqs. (54) and (55), and are identical to those present in an equivalent Lagrangian formulation. The matrices related to the Lagrangian-Eulerian description are labeled with subscript LE. These matrices account for convective effects as they are scaled by the length of material transported during a time step. In Section 4.4 the effect of discarding the $\mathbf{K}_{LE}$-matrices is examined for various incremental step sizes. Note that the stiffness relation is non-symmetric, even for the case when the convective velocity is equal to zero. In case of no slippage at a node, the stiffness relation in Eq. (63) remains valid, provided that the corresponding nodal $\mathbf{C}_p$-matrix is set to zero and a matrix with the layer elastic bending stiffness K_E on its diagonal is introduced in place of $\mathbf{C}_\kappa$.

The developed equations were implemented into a static nonlinear finite element code written in MATLAB. For efficiency purposes, all stiffness matrices were expanded symbolically by means of the Maple software, where the expressions for the matrix entries were optimized and converted to MATLAB language by means of the code generator module.

4 Numerical examples

The performance of the Lagrangian-Eulerian formulation is demonstrated for an unbonded flexible pipe, whose cross-sectional properties are listed consecutively from the innermost layer to the outermost layer in Tab. 1. The elastic modulus is denoted E, ν is Poisson's ratio, N_T is the number of layer tendons and the remaining parameters are defined in Figs. 1 and 2. The constitutive parameters related to bending are presented in Tab. 2, where the abbreviations THL1 and THL2 refer to respectively the inner and the outer tensile helix layers.

In all simulations the time step size, Δt, was set to 0.01 s and the temporal weight factor for the convective terms, γ, was set to 1.0. Frictionless three-noded penalty-based contact elements were employed to model the pipe supports. One of the nodes was attached to a cylindrical roller with diameter 0.3 m, while the two other nodes belonged to a beam element whose geometry was represented by a cylindrical roller. No contact loads were thus present for the beam rotational DOFs, such that the continuity assumption utilized in connection with Eq. (34) remained intact. The same low-order contact elements were also used to model earth-fixed point loads. In that case, the loads were applied to the roller nodes which were attached to linear 1 kN/m springs in the load directions.

Table 1: Cross-section layer data

Layer type	t [mm]	r [mm]	b [mm]	E [MPa]	ν [-]	α [deg.]	N_T [-]
Plastic sheath	25	107.0		3 000	0.45		
Pressure helix	10	124.5	12.5	210 000	0.30	−89	1
Plastic sheath	2	130.5		300	0.45		
Tensile helix	5	134.0	12.5	210 000	0.30	40	49
Plastic sheath	2	137.5		300	0.45		
Tensile helix	5	141.0	12.5	210 000	0.30	−40	51
Plastic sheath	25	156.0		300	0.45		

Table 2: Bending constitutive parameters

Quantity	Symbol	Value	Unit
Elastic bending stiffness - THL1	K_E	3 388	kNm^2
Elastic bending stiffness - THL2	K_E	3 905	kNm^2
Fabr. fric. moment - THL1, THL2	M_{s0}	8 000	Nm
Geometry parameter - THL1	m	0.008786	m^3
Geometry parameter - THL2	m	0.010237	m^3
Friction coefficient - THL1, THL2	μ	0.1	
Total bending stiff. sheath layers		400	kNm^2

Moment distributions for the outer tensile helix layer and curvature distributions at selected time instants are presented in Sections 4.1 – 4.5. The reported time is measured from the instant the material transport is initiated. Abbreviation *Con* and *LE* refer to responses obtained with the conventional Lagrangian approach and the Lagrangian-Eulerian formulation, respectively.

4.1 Performance for increasing curvature and effect of axial force

The simply supported configuration in Fig. 6 with material transport in the positive x-direction was considered. At the downstream-end, the torsional DOF was fixed and the axial DOF was assigned a prescribed displacement u_t. The prescribed displacement was activated after the external loads were ramped to their desired levels. In the conventional

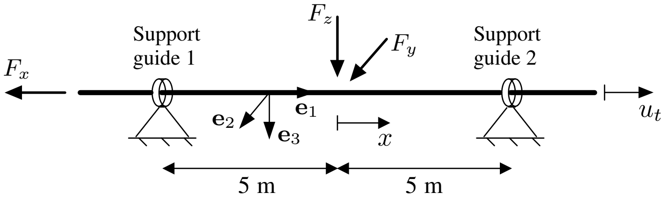

Figure 6: Simply supported axially sliding beam

simulation, u_t was set such that the material velocity became equal to 1 m/s, while the same effect was introduced in the Lagrangian-Eulerian simulation with u_t set to zero and the material velocity V prescribed to 1 m/s at the downstream-end. The pipe was modeled by 80 elements with lengths of 0.25 m.

The accuracy for increasing curvature was examined with the earth-fixed point load F_y in Fig. 6 set equal to 10 kN, 20 kN and 30 kN. In Figs. 7 – 9 the bending moment evolution histories are presented, while the curvature evolution for the medium load level is shown in Fig. 10. The maximum curvature for the smallest and the largest load was equal to 0.02 m^{-1} and 0.16 m^{-1}, respectively. By comparing the moment responses for positive x-coordinates, the speed of evolution is seen to increase with respect to the curvature level.

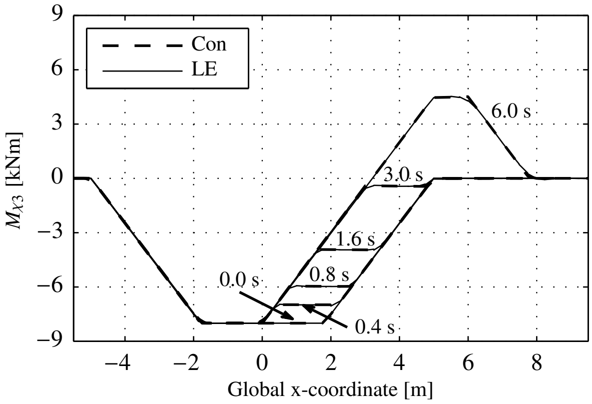

Figure 7: Bending moment evolution, THL2, F_y=10 kN

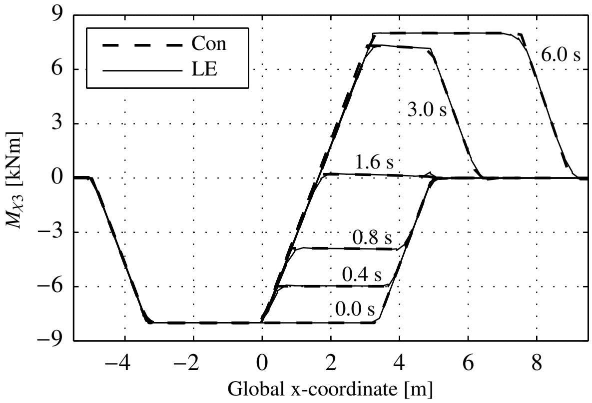

Figure 8: Bending moment evolution, THL2, F_y=20 kN

For negative x-coordinates, there are no evident changes for the bending moment, as no reversal of curvature takes place when material is transported through the mesh. Also, the accuracy seems to be unaffected by potential dissipation introduced via the upwind scheme proposed in Eqs. (36) and (37).

As seen in Figs. 7 and 8, the bending moment evolution obtained with the proposed formulation and the conventional Lagrangian formulation are coincident. The good correlation seen for the curvature evolution in Fig. 10 implies that the displacement state is correctly predicted as well. Notice that the responses are accurately predicted also at locations where large changes occur for the curvature and the moment gradients.

According to Fig. 9, the bending moment for the largest curvature level is satisfacto-

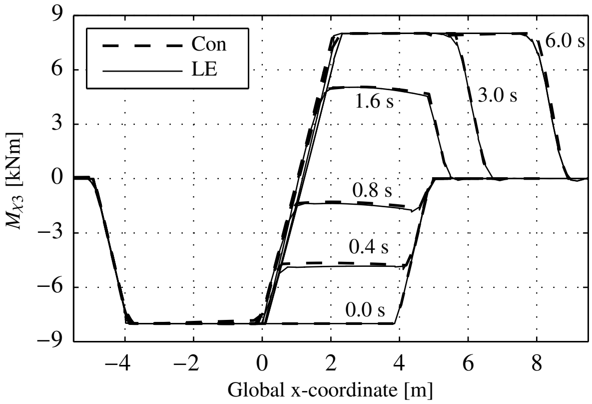

Figure 9: Bending moment evolution, THL2, F_y=30 kN

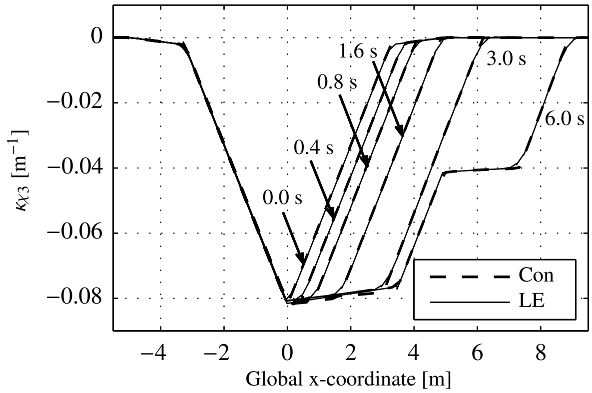

Figure 10: Curvature evolution, F_y=20 kN

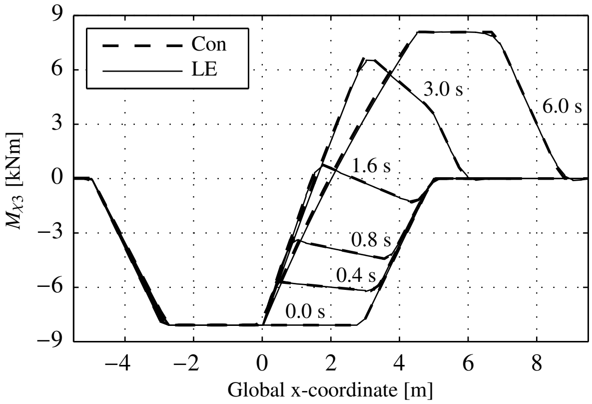

Figure 11: Bending moment evolution, THL2, F_y=20 kN, F_x=25 kN

rily predicted, however, a small offset is present at 0.4 s and the steep slope at midspan is shifted slightly rightwards at 6.0 s. Numerical testing revealed that these offsets were related to the presence of large displacements and the low-order contact formulation. At midspan, the deflection was about 1.5 m and the rotations at the supports were approximately 20°. Hence, a compressive axial force of 4 – 5 kN appeared at the midspan, whose value was sensitive to the direction of the support forces and the midspan contact load. For example, if the initial pipe configuration was moved axially 0.05 m the axial force changed by 0.5 kN, which gave a change in the bending moment larger than the offsets present in Fig. 9. For the curvature levels selected, the proposed formulation is therefore regarded to predict responses with the same accuracy as the conventional Lagrangian approach.

The behavior when subjected to an elemental axial end-force F_x of 25 kN, see Fig. 6, was examined for the case with F_y equal to 20 kN. Without the axial end-force, the midspan deflection was 0.56 m and the rotations at the supports were 8° prior to initiation of the material transport. According to Fig. 11, the bending moment evolution is in complete agreement with the conventional simulation. The slip moment is seen to remain at about 8 kNm, which implies that the increase of interlayer contact pressures due to the axial force is negligible. By comparison with the response in Fig. 8, it is clear that the axial end-force affects the equilibrium configuration and the evolution of the bending moment. In view of this, the developed formulation is regarded to give predictions with the same accuracy as offered by the Lagrangian formulation also when axial forces are present.

4.2 Influence of element size

The same example as considered in Section 4.1 was examined for element lengths L set to 0.25 m, 0.5 m, 0.75 m and 1.0 m. The pipe was subjected to an earth-fixed point load

F_y of 20 kN and the reference solution was taken as the one obtained with $L = 0.25$ m.

According to Fig. 12, the bending moment evolution is predicted with satisfactory accuracy when 0.5 m element lengths are used. Only minor differences can be observed as compared to the case with $L = 0.25$ m. Deviations from the reference solution appear first when elements with 0.75 m length are used, see Fig. 13. In that case, inaccuracies develop at locations where the moment gradient undergoes large changes, including also the sharp transition between stick and slip at $x \approx -3.5$ m.

A further increase of the element length to 1.0 m amplifies the inaccuracies, see Fig. 14. In this case, the slope at 8 m x-coordinate is not accurately represented and evident discontinuities are present at the element boundaries. As continuity is assumed in con-

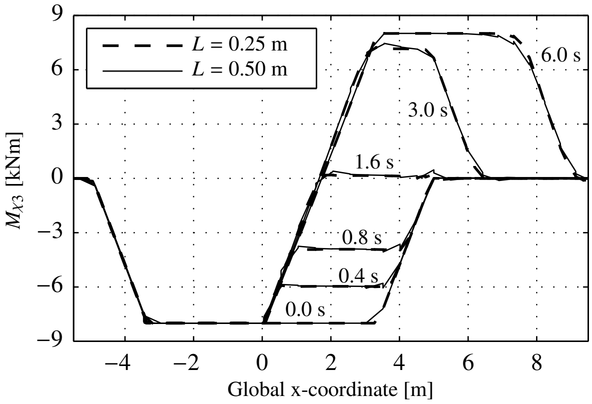

Figure 12: Bending moment evolution, THL2, F_y=20 kN

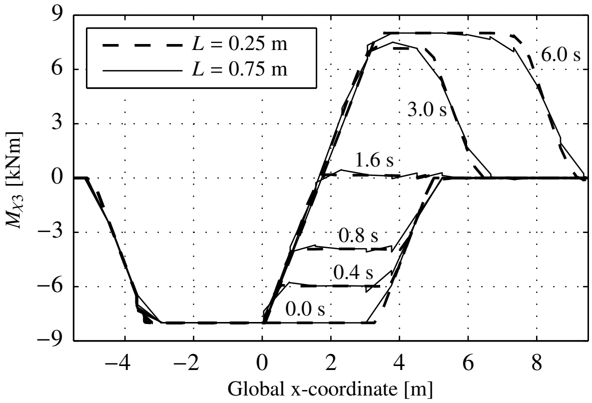

Figure 13: Bending moment evolution, THL2, F_y=20 kN

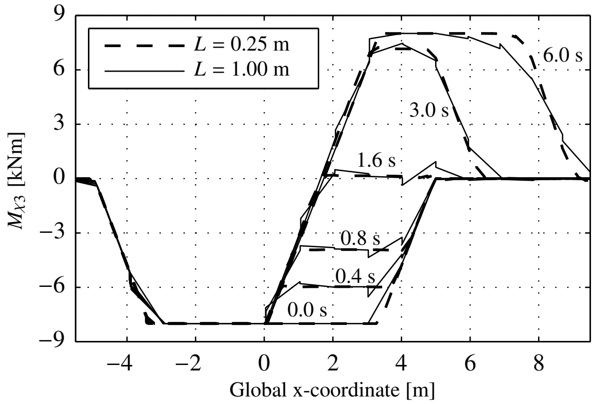

Figure 14: Bending moment evolution, THL2, F_y=20 kN

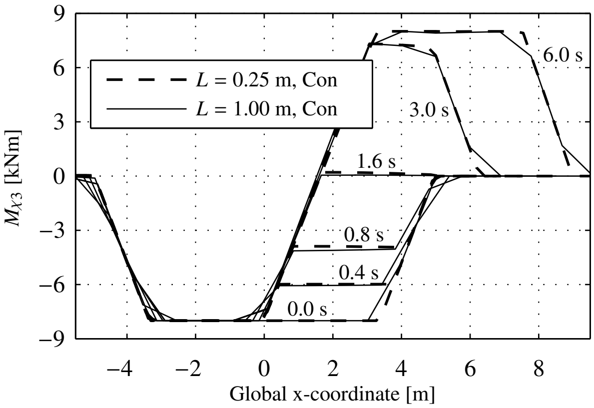

Figure 15: Bending moment evolution, THL2, F_y=20 kN

nection with Eq. (34), this solution is unacceptable and the maximum element length is regarded as exceeded. The corresponding solution obtained with the conventional Lagrangian method is seen in Fig. 15. This solution contains also inaccuracies at locations where the change of the moment gradient is large, but the deviations are in general less severe when compared against the reference solution. The Lagrangian-Eulerian procedure seems therefore to require shorter elements than the conventional approach. This behavior is indeed expected, because the curvature increments in Eq. (44) are expressed in terms of the total curvature, which becomes poorly approximated when too large elements are used.

4.3 Performance with temporal three-dimensional loads and prediction of bending-induced torque

The ability to handle three-dimensional time-varying point loads was examined for the simply supported configuration in Fig. 6. Two earth-fixed sinusoidal point loads were applied at the midspan according to,

$$F_y(t) = F_a \sin\left(\frac{2\pi}{T}t\right) H(t) \tag{64}$$

$$F_z(t) = F_a \sin\left(\frac{2\pi}{T}t - \frac{\pi}{2}\right) H\left(t - \frac{T}{4}\right) \tag{65}$$

where H is the Heaviside-function, T denotes the load period and t is the time measured from initiation of the material transport. The load amplitude F_a was set to 14 142 N and the pipe was modeled by 80 elements with lengths of 0.25 m. Note that the reported response is not realistic since the inertia loads were disregarded in the analysis.

Figure 16 displays the $M_{\chi 3}$-moment obtained with a load period T of 2 s and a material velocity V of 1 m/s. The predictions from the Lagrangian-Eulerian procedure and the conventional approach are seen to coincide in the region between the supports, whereas amplitude errors are present for $x > 5$ m. According to Fig. 17, the deviations reduce significantly when the material velocity is increased to 2.0 m/s, and vanish if the load period is increased to 6 s, see Fig. 18. In these cases, a quarter wavelength is represented by four and six elements, respectively, rather than just by two elements. Thus, the observed amplitude errors appear because the element length is not adapted to the load period and the material velocity. The proposed formulation is therefore able to predict responses from temporal loads with sufficient accuracy, provided that a proper element size is selected. Also, the responses indicate that shorter elements as compared to the Lagrangian approach are required. This is in line with the behavior demonstrated in Section 4.2.

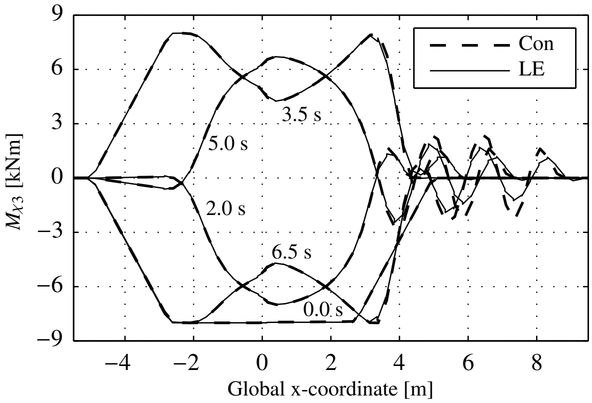

Figure 16: Bending moment evolution, THL2, T=2 s, V=1 m/s

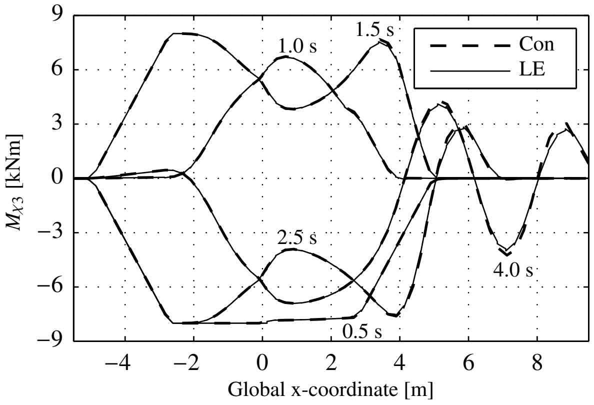

Figure 17: Bending moment evolution, THL2, T=2 s, V=2 m/s

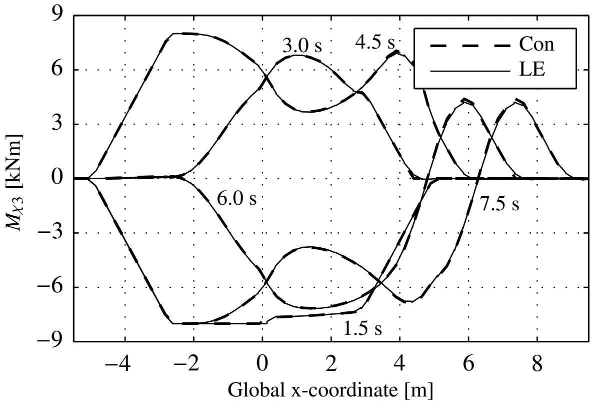

Figure 18: Bending moment evolution, THL2, T=6 s, V=1 m/s

Since the load components are out of phase, a non-alignment is introduced between the normal vector of the bending curvature plane and the bending moment vector of the tensile helix layers. Hence, a torque must be induced to satisfy the moment equilibrium conditions. As demonstrated in Fig. 19 for a load period T of 6 s and a material velocity V of 1 m/s, the bending-induced torques predicted in the two approaches are coincident. Note that the plotted saw-tooth behavior relates to the assumption of constant torque within the elements. This good correspondence indicates that the three-dimensional mesh motion is accurately predicted as well. The same degree of agreement was present also for the case with 2 s load period, which is not surprising as the torque is generated in the midspan region where the bending moment evolution is accurately predicted.

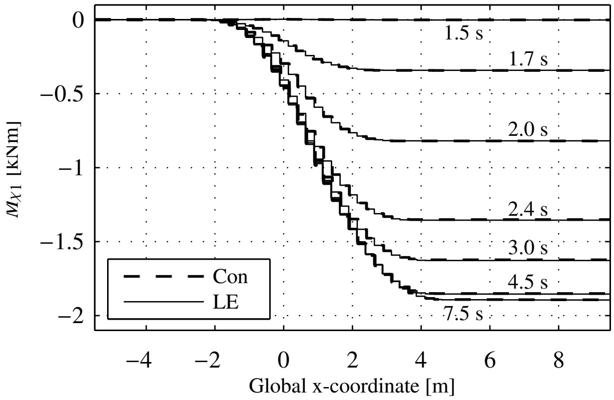

Figure 19: Torque evolution, THL2, T=6 s, V=1 m/s

4.4 *Importance of the tangent stiffness and the γ-parameter*

The effect of disregarding the $\mathbf{K}_{LE}$-matrices in Eq. (63) was examined for the example considered in Section 4.3. A load period T of 2 s was used and the material velocity V was set to 1 m/s. The following convergence tolerance defined in terms of the external loads $\mathbf{R}_{EXT}$ and the internal loads $\mathbf{R}_{INT}$ on system level was applied,

$$r = \frac{||\mathbf{R}_R||}{\frac{1}{2}||\mathbf{R}_{EXT}|| + \frac{1}{2}||\mathbf{R}_{INT}||} < 10^{-7} \qquad \mathbf{R}_R = \mathbf{R}_{EXT} - \mathbf{R}_{INT} \tag{66}$$

where $||*||$ refers to the Euclidean norm of the unconstrained translatory DOFs. The maximum number of iterations prior to subdivision of a time step was set to 20.

In Tab. 3 the mean number of iteration cycles per time step obtained with Δt in the range $0.005 - 0.02$ s are presented. The iterations were sampled during the first 4 s after the material transport was initiated, including cycles accumulated during potential time step subdivisions. Time steps of 0.001 s were used for 0.1 s intervals when the load components were reversed. No cycles were counted during these time intervals. Abbreviation WLE refers to cases using the stiffness representation as given in Eq. (63), while NLE refers to simulation runs where the stiffness related to material transport is deactivated. The tabulated values demonstrate that the WLE runs can manage larger incremental steps, and that the savings in terms of iteration cycles are nearly 50% for moderate step sizes. Similar trends were observed for the cases with constant loads considered in Section 4.1.

Considering the residual norms $||\mathbf{R}_R^L||$ obtained in the three last iteration cycles, with L as the last, the following fraction is used to quantify the load convergence rate,

$$\zeta = \frac{\log\left(\frac{||\mathbf{R}_R^{L}||}{||\mathbf{R}_R^{L-1}||}\right)}{\log\left(\frac{||\mathbf{R}_R^{L-1}||}{||\mathbf{R}_R^{L-2}||}\right)} \tag{67}$$

Table 3: Iteration cycles and subdivisions vs. time step size

Case	Δt	Subdivisions	Mean iter./step
WLE	0.005	0	4.5
NLE	0.005	0	6.4
WLE	0.010	0	5.8
NLE	0.010	0	10.1
WLE	0.015	0	7.6
NLE	0.015	23	14.2
WLE	0.020	62	11.7
NLE	0.020	142	13.0

where the convergence rate is regarded quadratic for $\zeta > 2$ and linear when ζ is close to unity. In Fig. 20 the convergence rates obtained with $\Delta t = 0.01$ s are presented. The NLE run indicates that the convergence behavior is linear, whereas the convergence rates are in the range $1.2-2.2$ when the stiffness relation in Eq. (63) is utilized. Notice that the discontinuities present at every 0.5 s correspond to reversals of the load components, where time steps of 0.001 s were used, not giving representable convergence rates.

For the case considered in Section 4.1 with $F_y = 20$ kN, the temporal weight factor for the convective terms, γ, was reduced to 0.0 and 0.5 in two simulation runs with $\Delta t = 0.02$ s. Satisfactory predictions were then obtained in the region between the supports, whereas oscillations appeared for $x > 5$ m, especially for the case with $\gamma = 0.0$. When the time step was reduced to 0.005 s, the oscillations disappeared and no differences could be observed compared to the run with $\gamma = 1.0$. This indicates that the value of γ should be set equal to 1.0 regardless of the applied time step size.

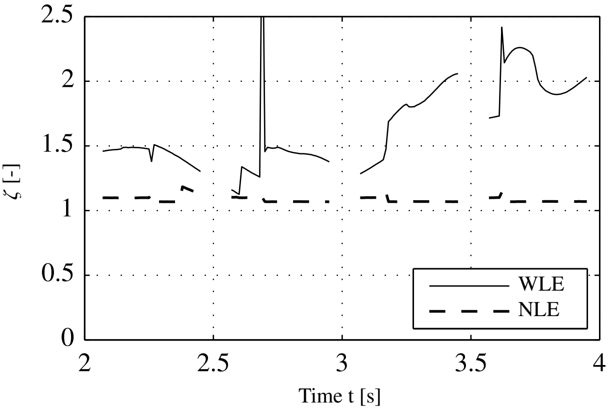

Figure 20: Load convergence rate, $\Delta t = 0.01$ s

In view of the presented results, the stiffness associated with the material transport should be included as it significantly improves the convergence properties. The observed characteristics are not directly comparable to those obtained in a conventional Lagrangian simulation, as the behavior is governed by the contact interactions when the mesh is tied to the material. Nevertheless, the convergence properties associated with the stiffness relation in Eq. (63) are, according to the authors impression, similar to the ones present in a conventional simulation. For cases where steady state conditions dominate, the proposed formulation has of course superior convergence characteristics compared to the Lagrangian approach.

4.5 Simple reeling analysis

The planar reeling operation in Fig. 21 was considered during the unsteady start-up phase. Each reel was modeled with 25 cylindrical support rollers placed equidistantly around a sector of 180°. The out-of-plane rotational DOF at the inlet node and at the outlet node were set such that the pipe curvature became equal to the reel curvature. All translatory DOFs and the torsional DOF were fixed at the outlet node, whereas the pipe was free to move axially and to rotate about the pipe axis at the inlet node. The distance between the reel centers and the support roller nodes was set to 4.0 m. Element lengths of 0.5 m were employed for the pipe parts that rested on the reels. In the regions with length s_A, the element size was increased gradually to L_B toward the free-span region, see Fig. 21. Throughout the region with length s_B, the element size was kept at L_B.

The analysis was initiated from a stressfree straight pipe configuration. An intermediate reeling configuration was established with the tensile helix layer bending moments set to zero. In this configuration the axial force F_x, see Fig. 21, was set to 50 kN such that the majority of the reel supports were in contact with the pipe. Thereafter, the elasto-plastic bending model was activated with the material velocity V set to 1 m/s at the outlet node.

In Figs. 22 and 23 the evolution of the moment and the curvature are presented as a function of the mesh parameter χ, see Fig. 21. The change of curvature is seen to be negligible throughout the simulation. Hence, the additional bending moments introduced when the elasto-plastic bending model is activated, are balanced mainly by moments caused by

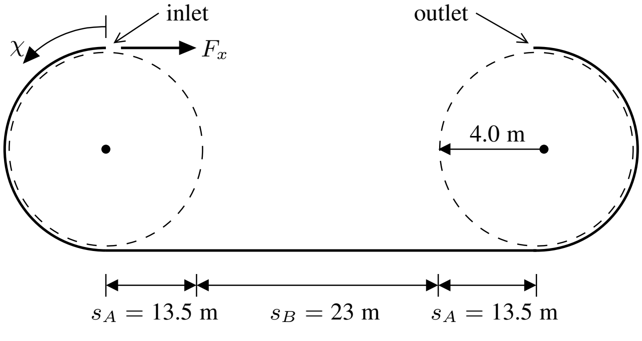

Figure 21: Reeling configuration

the axial force via free-span deflections. The regions with -0.23 m^{-1} curvature indicate that the pipe rests on the reels and is not of interest. For the unconstrained parts of the mesh, full slippage regions of 10 m develop rapidly at both ends during the first second, see Fig. 22. Thereafter, the slippage region at reel 1 spreads toward reel 2 with approximately the same velocity as the material, until it stops midway between the reels at 15 s. After this, only small changes takes place in the stick region, 30 m $< X <$ 60 m, as the moment distribution approaches its steady state solution.

Use of 0.5 m and 3.0 m element lengths in the free-span region yields practically the same moment distributions, see Fig. 22. In order to obtain accurate predictions, the mesh must be able to capture variations of the curvature and the moment at all times. The curvature is here the governing quantity since it acts as the driving mechanism in the moment evolution. In this example, the essential is to capture a sharp curvature half-wave with amplitude 0.004 m^{-1} and 14 m half-length that propagates toward reel 2 with the material velocity. If elements longer than 3.0 m are used, the curvature wave is not properly captured and deviations appear. In addition, the steep curvature gradients close to the reels must be captured, e.g. evident inaccuracies appeared when elements with length 2.0 m were used in this region. These observations underline the necessity of mesh convergence studies of the problem at hand, even for cases where the selected mesh is indeed able to represent the steady state solution.

This example demonstrates three prominent benefits of the proposed Lagrangian-Eulerian formulation. Namely, there is no need to model the material stored on the reels and the free-spanning region can be represented with six times larger elements than those required in a conventional Lagrangian simulation. These two benefits considerably reduce the computational efforts. Also, once the initial reeling path is established, there are no concerns for convergence related to the contact interactions.

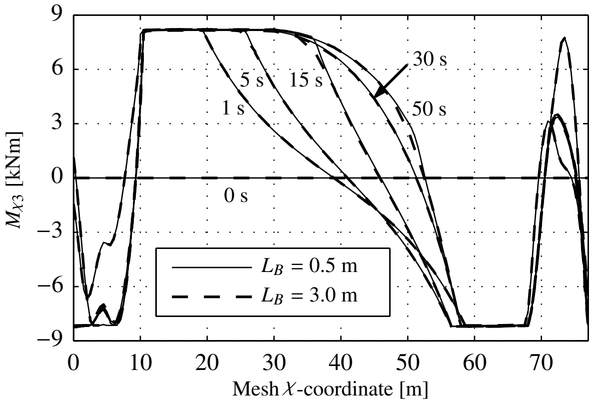

Figure 22: Bending moment evolution, THL2

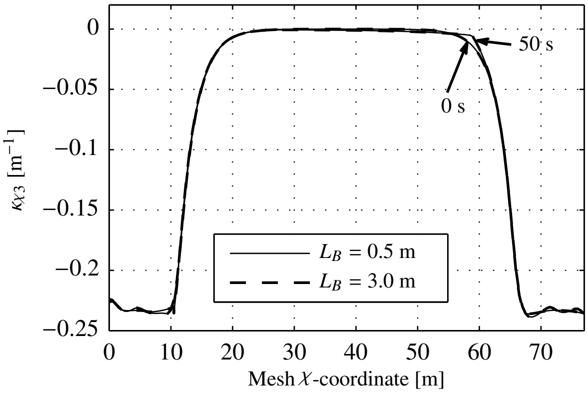

Figure 23: Curvature evolution

5 Conclusions

In this work a Lagrangian-Eulerian formulation intended for reeling analysis of multilayered beams with interlayer slippage was developed. A fully coupled approach that handles the material motion, the mesh motion and the convective transport effects simultaneously were employed. Kinematic relations for the mesh motion and the material motion were derived, along with the restriction imposed by the principle of mass conservation. Regarding the elasto-plastic bending model, an expression for the gradient of the constitutive variables was developed, an upwinding scheme was proposed and a backward Euler update scheme was formulated. The developed equations were merged into the virtual work equation for a conventional corotated beam formulation, and a tangent stiffness that accounted for the transport of material was derived.

Numerical studies were conducted with focus on benchmarking against the conventional Lagrangian approach and demonstration of basic performance characteristics. The proposed formulation was found to predict responses with satisfactory accuracy both for constant and temporal three-dimensional loads. Use of a tangent stiffness that accounted for the material transport effects was demonstrated to give considerable benefits with regard to the numerical efficiency. A simple reeling analysis was executed in which the small-deformation region could be modeled with significantly larger elements than those required to capture deformations and contact interactions at the reels. Also, due to the nearly fixed mesh in space, no convergence problems related to the contact interactions were encountered.

Appendix: Linearization of corotated vectors from adjacent elements

A matrix expression representing the linearization of Eq. (35) is needed when the element tangent stiffness matrices are developed. The linearization is established by performing a differentiation according to,

$$\begin{aligned} d\tilde{A}_r^{\{m\pm1\}} &= d\mathbf{e}_r\cdot\mathbf{e}_s^{\{m\pm1\}}A_s^{\{m\pm1\}} + \mathbf{e}_r\cdot d\mathbf{e}_s^{\{m\pm1\}}A_s^{\{m\pm1\}} \\ &\quad + \mathbf{e}_r\cdot\mathbf{e}_s^{\{m\pm1\}}dA_s^{\{m\pm1\}} \qquad r=2,3 \quad s=1,2,3 \end{aligned} \tag{A.1}$$

where the change of the unit vectors is associated with a rotation $d\boldsymbol{\phi}$ of the beam element. This change can therefore be expressed by the relation,

$$d\mathbf{e}_r = -\mathbf{S}(\mathbf{e}_r)\cdot d\boldsymbol{\phi} \qquad \mathbf{S}(\mathbf{e}_r) = \begin{bmatrix} 0 & -(\mathbf{e}_r)_3 & (\mathbf{e}_r)_2 \\ (\mathbf{e}_r)_3 & 0 & -(\mathbf{e}_r)_1 \\ -(\mathbf{e}_r)_2 & (\mathbf{e}_r)_1 & 0 \end{bmatrix} \tag{A.2}$$

in which $(\mathbf{e}_r)_k$ refers to component k of $\mathbf{e}_r$ in the coordinate representation used for the dot product in Eq. (A.1). By geometrical reasoning the rotation $d\boldsymbol{\phi}$ is expressed as follows,

$$d\boldsymbol{\phi} = \frac{1}{2}(d\theta_{1A}+d\theta_{1B})\,\mathbf{e}_1 + \frac{1}{L}\mathbf{S}(\mathbf{e}_1)\,[d\mathbf{x}_B - d\mathbf{x}_A] \tag{A.3}$$

where the involved quantities are defined in Fig. 4 and in Eq. (29). The rotation can be represented on matrix format in terms of the element displacement vector $d\mathbf{v}$ and the 3×12-matrix $\boldsymbol{\Omega}$ according to,

$$d\boldsymbol{\phi} = \boldsymbol{\Omega}\,d\mathbf{v} \qquad \boldsymbol{\Omega} = \begin{bmatrix} -\frac{1}{L}\mathbf{S}(\mathbf{e}_1) & \frac{1}{2}\mathbf{e}_1\otimes\mathbf{e}_1 & \frac{1}{L}\mathbf{S}(\mathbf{e}_1) & \frac{1}{2}\mathbf{e}_1\otimes\mathbf{e}_1 \end{bmatrix} \tag{A.4}$$

By means of Eq. (A.2) the first term in Eq. (A.1) can be expressed as,

$$d\mathbf{e}_r\cdot\mathbf{e}_s^{\{m\pm1\}}A_s^{\{m\pm1\}} = -\mathbf{A}^{\{m\pm1\}}\cdot\mathbf{S}(\mathbf{e}_r)\cdot d\boldsymbol{\phi} \quad \mathbf{A}^{\{m\pm1\}} = A_s^{\{m\pm1\}}\mathbf{e}_s^{\{m\pm1\}} \tag{A.5}$$

likewise, the second term in Eq. (A.1) is given by,

$$\begin{aligned} \mathbf{e}_r\cdot d\mathbf{e}_s^{\{m\pm1\}}A_s^{\{m\pm1\}} &= -\mathbf{e}_r\cdot\mathbf{S}\left(\mathbf{A}^{\{m\pm1\}}\right)\cdot d\boldsymbol{\phi}^{\{m\pm1\}} \\ &= \mathbf{A}^{\{m\pm1\}}\cdot\mathbf{S}(\mathbf{e}_r)\cdot d\boldsymbol{\phi}^{\{m\pm1\}} \end{aligned} \tag{A.6}$$

where use was made of the skew-symmetric property of the tensor $\mathbf{S}$. By inserting Eq. (A.4) into Eqs. (A.5) and (A.6), the sought matrix relation can be expressed as,

$$\begin{aligned} \begin{bmatrix} d\tilde{A}_2 \\ d\tilde{A}_3 \end{bmatrix} &= \mathbf{G}\left(\mathbf{A}^{\{m\pm1\}}\right)\boldsymbol{\Omega}^{\{m\pm1\}}\,d\mathbf{v}^{\{m\pm1\}} - \mathbf{G}\left(\mathbf{A}^{\{m\pm1\}}\right)\boldsymbol{\Omega}\,d\mathbf{v} \\ &\quad + \mathbf{T}_{2\times3}^{\{m\pm1\}}\begin{bmatrix} dA_1^{\{m\pm1\}} \\ dA_2^{\{m\pm1\}} \\ dA_3^{\{m\pm1\}} \end{bmatrix} \\ T_{rs}^{\{m\pm1\}} &= \mathbf{e}_r\cdot\mathbf{e}_s^{\{m\pm1\}} \quad \mathbf{G}\left(\mathbf{A}^{\{m\pm1\}}\right) = \begin{bmatrix} \mathbf{A}^{\{m\pm1\}}\cdot\mathbf{S}(\mathbf{e}_2) \\ \mathbf{A}^{\{m\pm1\}}\cdot\mathbf{S}(\mathbf{e}_3) \end{bmatrix} \end{aligned} \tag{A.7}$$

where the scalar components dA_r and $dA_s^{\{m\pm1\}}$ are represented in the coordinates associated with the unit vectors $\mathbf{e}_r$ and $\mathbf{e}_s^{\{m\pm1\}}$, respectively. The matrices in the two first terms of Eq. (A.7) are not restricted to a specific coordinate representation, however, to avoid unnecessary transformations the involved vectors are expressed in the same coordinates as used for the system FE equations.

References

[1] Benson DJ. An efficient, accurate, simple ALE method for nonlinear finite element programs. Comput Method Appl M 1989;72:305–508.

[2] Rodríguez-Ferran A, Casadei F, Huerta A. ALE stress update for transient and quasistatic processes. Int J Numer Meth Eng 1998;43:241–62.

[3] Stoker HC. Developments of the arbitrary Lagrangian-Eulerian method in non-linear solid mechanics. Applications to forming processes. Ph.D. thesis; University of Twente, Enschede, The Netherlands; 1999.

[4] Liu WK, Belytschko T, Chang H. An arbitrary Lagrangian-Eulerian finite element method for path-dependent materials. Comput Method Appl M 1986;58:227–45.

[5] Bayoumi HN, Gadala MS. A complete finite element treatment for the fully coupled implicit ALE formulation. Comput Mech 2004;33:435–52.

[6] Hong D, Tang J, Ren G. Dynamic modeling of mass-flowing linear medium with large amplitude displacement and rotation. J Fluid Struct 2011;27:1137–48.

[7] Hong D, Ren G. A modeling of sliding joint on one-dimensional flexible medium. Multibody Syst Dyn 2011;26:91–106.

[8] Wickert JA. Non-linear vibration of a traveling tensioned beam. Int J Nonlinear Mech 1992;27:503–17.

[9] Vu-Quoc L, Li S. Dynamics of sliding geometrically-exact beams: large angle maneuver and parametric resonance. Comput Method Appl M 1995;120:65–118.

[10] Païdoussis MP, Li GX. Pipes conveying fluid: A model dynamical problem. J Fluid Struct 1993;7:137–204.

[11] Fylling I, Bech A. Effects of internal friction and torque stiffness on the global behavior of flexible risers and umbilicals. In: Proceedings of the 10th International Conference on Offshore Mechanics and Arctic Engineering. 1991, p. 489–96.

[12] Coyne J. Analysis of the formation and elimination of lops in twisted cables. IEEE J Oceanic Eng 1990;15:72–83.

[13] Miyazaki Y, Kondo K. Analytical solution of spatial elastica and its application to kinking problem. Int J Solids Struct 1997;34:3619–36.

[14] Neto AG, Martins CA. Structural stability of flexible lines in catenary configuration under torsion. Mar Struct 2013;34:16–40.

[15] Tan Z, Quiggin P, Sheldrake T. Time domain simulation of the 3D bending hysteresis behavior of an unbonded flexible riser. J Offshore Mech Arct 2009;131. 8 pages.

[16] Alfano G, Bahtui A, Bahai H. Numerical derivation of constitutive models for unbonded flexible risers. Int J Mech Sci 2009;51:295–304.

[17] Bahtui A, Alfano G, Bahai H, Hosseini-Kordkheili SA. On the multi-scale computation of un-bonded flexible risers. Eng Struct 2010;32:2287–99.

[18] Sævik S. Theoretical and experimental studies of stresses in flexible pipes. Comput Struct 2011;89:2273–91.

[19] Aguiar LL, Almeida CA, Paulino GH. A three-dimensional multilayered pipe beam element: Nonlinear analysis. Comput Struct 2014;138:142–61.

[20] Økland OD, Giertsen E, Sævik S, Taby J. On the use of online monitored key parameters

from pipe lay operations. In: Proceedings of the ASME 2008 27th International Conference on Ocean, Offshore and Arctic Engineering. 2008, p. 301–7.

[21] Custódio AB, Vaz MA. A nonlinear formulation for the axisymmetric response of umbilical cables and flexible pipes. Appl Ocean Res 2002;24:21–9.

[22] Féret JJ, Bournazel CL. Calculation of stresses and slip in structural layers of unbonded flexible pipes. J Offshore Mech Arct 1987;109:263–9.

[23] Féret JJ, Momplot G. CAFLEX - A program for capacity analysis of flexible pipes, Theory manual. Tech. Rep. 710668; Norwegian Marine Technology Research Centre (MARINTEK), Trondheim, Norway; 1989.

[24] Sævik S. On stresses and fatigue in flexible pipes. Ph.D. thesis; Norwegian Institute of Technology, Trondheim, Norway; 1992.

[25] Felippa CA, Haugen B. A unified formulation of small-strain corotational finite elements: I. Theory. Comput Method Appl M 2005;194:2285–335.

[26] Bathe KJ, Bolourchi S. Large displacement analysis of three-dimensional beam structures. Int J Numer Meth Eng 1979;14:961–86.

[27] Sævik S. Bflex2010 - Theory manual. Tech. Rep. 700883.00.01; Norwegian Marine Technology Research Centre (MARINTEK), Trondheim, Norway; 2010.

[28] Sævik S. Usap - Theory manual. Tech. Rep. 700254.00.01; Norwegian Marine Technology Research Centre (MARINTEK), Trondheim, Norway; 2010.

[29] Crisfield MA. A consistent co-rotational formulation for non-linear, three-dimensional, beam elements. Comput Method Appl M 1990;81:131–50.

[30] Battini JM, Pacoste C. Plastic instability of beam structures using co-rotational elements. Comput Method Appl M 2002;191:5811–31.

[31] Krenk S, Vissing-Jørgensen C, Thesbjerg L. Efficient collapse analysis techniques for framed structures. Comput Struct 1999;72:481–96.

[32] Reissner E. On one-dimensional finite strain beam theory: the plane problem. J Appl Math Phys 1972;23:795–804.

[33] Simo JC. A finite strain beam formulation. The three-dimensional dynamic problem. Part I. Comput Method Appl M 1985;49:55–70.

[34] Crisfield MA. A co-rotational framework for three-dimensional beam elements. In: Non-linear finite element analysis of solids and structures. John Wiley & Sons Ltd.; 1997, p. 213–26.

[35] Krenk S. Co-rotating beam elements. In: Non-linear modeling and analysis of solids and structures. John Wiley & Sons Ltd.; 2009, p. 100–41.

[36] Donea J, Ponthot JP, Rodríguez-Ferran A, Huerta A. Arbitrary Lagrangian-Eulerian methods. In: Encyclopedia of Computational Mechanics. John Wiley & Sons Ltd.; 2004,.

[37] Belytschko T, Liu WK, Moran B. Arbitrary Lagrangian Eulerian formulations. In: Nonlinear finite elements for continua and structures. John Wiley & Sons Ltd.; 2001, p. 393–449.

[38] Liu WK, Chang H, Chen JS, Belytschko T. Arbitrary Lagrangian-Eulerian Petrov-Galerkin finite elements for nonlinear continua. Comput Method Appl M 1988;68:259–310.

[39] Donea J. A Taylor-Galerkin method for convective transport problems. Int J Numer Meth Eng 1984;20:101–19.

[40] Bathe KJ. Solution of nonlinear equations. In: Finite element procedures. Prentice Hall; 1996, p. 754–67.

Paper IV

On prediction of torque in flexible pipe reeling operations using a Lagrangian-Eulerian FE framework

Vegard Longva[a], Svein Sævik[a]

[a] Department of Marine Technology, Norwegian University of Science and Technology
NO-7491 Trondheim, Norway

Submitted for journal publication, 2015

Abstract

In this paper a new framework for FE simulation of reeling operations that utilizes a Lagrangian-Eulerian description of the beam kinematics is proposed. Compared to the conventional Lagrangian formulation, significant benefits are achieved for the performance of the contact algorithms and the overall numerical efficiency as the mesh is virtually fixed in space. The main ingredients of the Lagrangian-Eulerian framework and the applied flexible pipe model are presented. An idealized spoolbase-vessel load-out operation was considered in order to gain insight into the torsional failure incidents experienced by subsea contractors in recent years. Here, three different mechanisms were found to provoke torsional failure of the pipe. Strategies to avoid the torsional failure incidents and FE modeling remarks are provided.

Keywords: Flexible pipe; Reeling; Load-out; Torque; Lagrangian-Eulerian; Beam

1 Introduction

Flexible pipes are nowadays widely used in riser and flowline transport systems for offshore hydrocarbon resources. Due to their compliant bending behavior, these pipes are coiled onto large reels, carousels or turn-tables when transported to the production site. In recent years, subsea contractors have experienced torsional failure incidents at the spoolbase when the pipes are being loaded aboard the cargo vessel. More precisely, the failures have occurred for vessels equipped with vertical-axis turn-tables placed in confined cargo holds. The pipe must therefore undergo severe curvature deformations and large rotations of the curvature plane before it enters the turn-table. In such situations, the hysteretic bending response is known to introduce significant torque responses [1]. As the load-out operation is conducted with low tension, the bending-induced torque may provoke torsional instabilities with possible loop formations at free spans, see Fig. 1a.

Torsional failure has also been reported in reeling operations of umbilical cables. Such a failure is depicted in Fig. 1b, where the helical displacement pattern indicates the presence of a significant torque, however, in this case the torque is not necessarily related to rotations of the curvature plane. Endal et al. [2] studied a similar situation for S-lay installation of subsea steel pipes, where residual curvature in the underbend region was found to provoke instabilities characterized by large roll rotations and negligible transverse displacements. The tension is considerably lower in a reeling operation, and it is therefore plausible that residual curvature effects could lead to out-of-plane displacements similar to those seen in Fig. 1b. Flexible pipes may develop a curvature set in the plastic layers when subjected to long-term storage [3], which arguably relates to fabrication residual stresses or material creep effects.

(a) Indication of loop formation at free span between vessel and quay in a flexible pipe load-out operation

(b) Severe helical deformations of an umbilical cable during installation

Figure 1: Torsional failure in reeling operations

Instabilities related to loop formation of risers have been studied in work by Ramos and Pesce [4], who derived analytical formulas for the onset of instability and concluded that Greenhill's equation [5] could be used also for curved configurations. Recently, Neto et al. [6] conducted an extensive numerical simulation work and provided formulas for prediction of loop formation in flexible catenary lines. Flexible pipes subjected to severe torsion may also fail by local buckling of the tensile armor tendons in the radial and lateral directions [7]. These failure modes have been studied in work by Vaz and Rizzo [8] with aid of detailed finite element analysis, and by Østergaard et al. [9] who developed a mathematical model able to represent the lateral tendon instability mode which was merged into a global model for limit load prediction. If the torsion yields compressive stresses in the inner tensile helix layer, its tendons may buckle radially through accumulated openings in the outer tensile helix layer. This failure mode is henceforth referred to as herniation buckling and has been detected in a load-out operation, however, no one has hitherto addressed it in the open literature. In the present work, the failure modes themselves are less emphasized and the focus is rather on prediction of the torque response.

Design codes for flexible pipes [3, 10] provide no guidance on how to avoid the torsional failure experienced in load-out operations, simply because the mechanisms driving the extreme torque have not yet been identified. Numerical simulations are regarded as the preferred approach for providing more insight into the phenomenon. Most load-out operations involve several kilometres of material, numerous contact interactions along the reeling path, large-deformation zones and history-dependent material effects. In simulation of such operations, the conventional Lagrangian finite element formulation suffer from time-consuming computations, as the mesh must be rather uniform and small elements are needed in regions with large deformations. The contact interactions are also prone to give convergence issues due to the large mesh motions involved. To avoid these drawbacks, a Lagrangian-Eulerian beam formulation that enables for a virtually fixed mesh in space was recently developed [11]. In the present paper, this development is extended into a framework for simulation of reeling operations.

With regard to prediction of the generated torque, the constitutive model must account for the hysteretic bending behavior and the interlayer radial contact pressure changes. Several flexible pipe bending models that account for the stick-slip behavior of the tensile helix tendons have been proposed in recent years. Tan et al. [12] proposed a simple model based on a predefined moment-curvature relationship and a detailed model utilizing a multiple tendon approach. More advanced models formulated in the framework of computational elasto-plasticity were proposed by Bahtui and coworkers [13, 14], who employed detailed FE analysis to calibrate flexible riser constitutive models. Their approach provides high accuracy for the selected cross-section, however, considerable efforts are needed to determine the material parameters. This was remedied in work by Sævik [15], where two elasto-plastic bending models valid for generic flexible pipe cross-sections were proposed and coupled together with a separate axi-symmetric model for determination of the interlayer pressures. Both models were successfully validated against laboratory fatigue tests.

In view of the background information above, the main objectives of the current work are as follows,

- Extend the Lagrangian-Eulerian formulation developed in previous work [11] with the functionality required for robust and efficient simulation of reeling operations.
- Identify the source for the extreme torque responses experienced in flexible pipe load-out operations.
- Propose strategies to avoid torsional failure incidents and provide insight into numerical simulations of load-out operations.

The proposed Lagrangian-Eulerian framework is applicable also for simulation of flexible pipe and cable installation operations. Compared to the conventional Lagrangian approach, a significant reduction of the degrees of freedom (DOFs) is achieved as the vessel-following mesh can be terminated at the seafloor point where stationary conditions prevail. The development may also be applied for rigid steel pipe laying simulations if a J2 plasticity stress-update algorithm is formulated.

2 Flexible pipe model

Both geometric and constitutive coupling effects must be accounted for in order to capture the bending-induced torque in flexible pipe reeling operations. The constitutive coupling is associated with the bending moment contribution from the tensile helix layers, as the helix tendon slippage is governed by the interlayer radial pressures which depend on the axial-torsional strain state. Further, the hysteretic bending behavior allows the bending moment vector to be non-aligned with the normal vector of the principal curvature plane. This non-alignment induces a torque in order to satisfy the torsional equilibrium equation, and is thus responsible for a geometric coupling effect, see Ref. [1]. The pipe model must also account for the bi-linear torque-torsion relationship and allow for three-dimensional motions with large rotations and displacements. A quasistatic modeling approach is regarded appropriate as reeling operations are conducted at low velocities with negligible accelerations.

To capture the effects described above, a corotational beam formulation with an elastoplastic bending model that accounts for the axial-torsional coupling is selected. This beam model has previously been demonstrated to predict fatigue damage of flexible pipes in good correlation with experimental tests [15].

2.1 Corotational Euler-Bernoulli beam element

In the applied corotational formulation, each beam element has attached an orthogonal coordinate system that continuously translates and rotates with the element rigid body motion. In this way, the deformation parameters can readily be extracted from the total element motion, which combined with the assumption of small deformations relative to the element frames, enables for straightforward use of linear beam elements in geometrically nonlinear analyses. Further details on corotational beams may be found in Ref. [16, 17].

In this work, the corotational beam formulation proposed by Krenk [18] is employed. The Euler-Bernoulli kinematic relations are utilized as negligible shear deformations arise in flexible pipes. Thus, the shear forces are obtained via the bending moment equilibrium

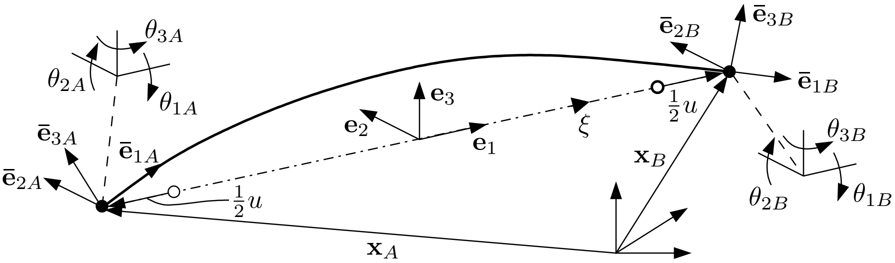

Figure 2: Beam element kinematics

equations and only centerline translation quantities are needed in the kinematic description. As illustrated in Fig. 2, the element deformational DOFs consist of an axial elongation variable u and the rotation parameters, θ_{jA} and θ_{jB}, which measure the rotation of the nodal unit triads, $\bar{\mathbf{e}}_{jA}$ and $\bar{\mathbf{e}}_{jB}$, relative to the corotated element unit vectors $\mathbf{e}_j$. The axial strain ϵ and the torsion κ_1 are assumed constant within the element according to,

$$\epsilon = \frac{u}{L} \tag{1}$$

$$\kappa_1 = \frac{\theta_{1B} - \theta_{1A}}{L} \tag{2}$$

while the bending curvature components, κ_2 and κ_3, are interpolated with linear shape functions,

$$\kappa_j = \frac{3\xi - 1}{L}\theta_{jA} + \frac{3\xi + 1}{L}\theta_{jB} \qquad j = 2,3 \qquad -1 \leq \xi \leq 1 \tag{3}$$

Due to the assumption of small deformations relative to the element frames, sufficiently short elements must be used in regions with large deformations. An additional restriction for the element size appears in this work, because the straight two-noded beam elements must capture the geometric effect responsible for the bending-induced torque solely by the nodal equilibrium conditions.

2.2 Axi-symmetric model

The purpose of the axi-symmetric model is to provide torque, axial force, interlayer pressures and tangent stiffness parameters for each layer. The model is based on the early work of Féret and coworkers [19, 20], where a layer is either modeled as a collection of uniformly distributed tendons or as a thin tubular sheath. The axi-symmetric response is assumed unaffected by friction-induced effects, additional interlayer contact pressure due to bending and end-termination effects. Furthermore, the axial strain ϵ and the torsion κ_1 are assumed equal in all layers within a single beam element. The layer types, the geometric parameters and the layer DOFs are defined in Fig. 3, where subscript i refers to both the layer itself and the inside layer interface.

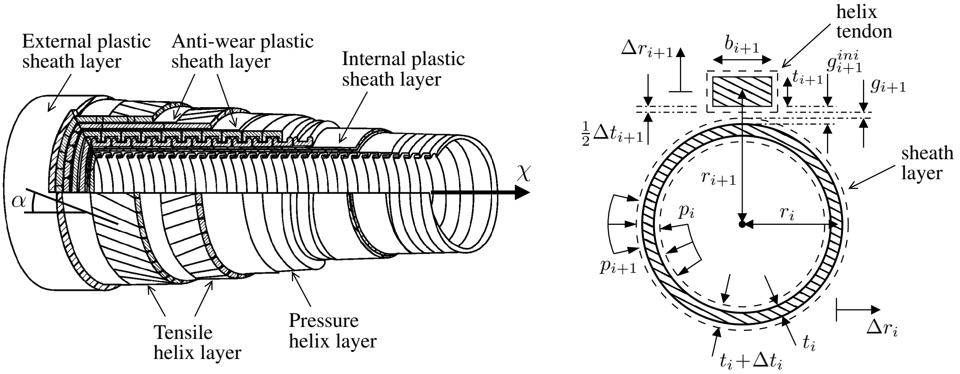

Figure 3: Definition of layers, geometric parameters and axi-symmetric variables

The governing equations for the helix layers are based on curved beam theory, see Ref. [15]. A linear-elastic isotropic material law is applied and the helix kinematics is established by assuming linear and small motions. Local torque and bending moments along the helices are neglected as they have no significant influence on the response of flexible pipes [21]. For a single helix layer, the following equations govern the axi-symmetric behavior,

$$\tan^2 \alpha_i \, N_i - 2\pi r_i^2 \, (p_i - p_{i+1}) = 0 \tag{4}$$

$$\frac{\Delta t_i}{t_i} + \frac{\nu_i \, N_i}{n_i b_i t_i E_i \cos\alpha_i} + \frac{p_i + p_{i+1}}{2E_i f} = 0 \qquad f = \frac{n_i b_i}{2\pi r_i \cos\alpha_i} \tag{5}$$

$$\frac{N_i}{n_i b_i t_i E_i \cos\alpha_i} - \frac{\sin\alpha_i \, \Delta r_i}{r_i} - \cos^2\alpha_i \, \epsilon - r_i \cos\alpha_i \sin\alpha_i \, \kappa_1 + \nu_i \frac{p_i + p_{i+1}}{2E_i f} = 0 \tag{6}$$

where the geometric quantities are defined in Fig. 3, N is the layer axial force, p denotes the interlayer radial pressure, n denotes the number of tendons, ν is Poisson's ratio and E denotes the elastic modulus. The helix layer torque is obtained by the relation,

$$M_{1i} = N_i r_i \tan\alpha_i \tag{7}$$

Regarding the sheath layers, a linear-elastic isotropic material law is assumed and the governing equations are based on thin-walled shell theory and St. Venant's solution for a circular cylinder subjected to torque, see Ref. [20].

The set of active gap constraints is determined from the following interlayer continuity relations,

$$\Delta r_i - \frac{1}{2}\Delta t_i - \Delta r_{i-1} - \frac{1}{2}\Delta t_{i-1} - g_i^{\{ini\}} = g_i \qquad g_i > 0, p_i = 0 \qquad i = 2, ..., K \tag{8}$$

$$\Delta r_i - \frac{1}{2}\Delta t_i - \Delta r_{i-1} - \frac{1}{2}\Delta t_{i-1} - g_i^{\{ini\}} = 0 \qquad g_i = 0, p_i > 0 \qquad i = 2, ..., K \tag{9}$$

in which $g_i^{\{ini\}}$ denotes the interlayer radial gap in the unloaded state, which normally is equal to zero. With this, the assembled equation system for all K layers and the P active gap constraints reads,

$$\begin{bmatrix} \mathbf{A}_{3K\times(3K+P)} & \mathbf{A}^{\epsilon}_{3K\times 1} & \mathbf{A}^{\kappa_1}_{3K\times 1} \\ \mathbf{G}_{P\times(3K+P)} & \mathbf{0}_{P\times 1} & \mathbf{0}_{P\times 1} \end{bmatrix} \begin{bmatrix} \mathbf{s} \\ \boldsymbol{\lambda} \\ \epsilon \\ \kappa_1 \end{bmatrix} = \begin{bmatrix} \mathbf{p}_{3K\times 1} \\ \mathbf{g}^{\{ini\}} \end{bmatrix}$$
$$\mathbf{s} = \begin{bmatrix} \Delta r_1 & \Delta t_1 & N_1 & ... & \Delta r_i & \Delta t_i & N_i & ... & \Delta r_K & \Delta t_K & N_K \end{bmatrix}^\top$$
$$\boldsymbol{\lambda} = \begin{bmatrix} p_{\{1\}} & \cdots & p_{\{P\}} \end{bmatrix}^\top \qquad \mathbf{g}^{\{ini\}} = \begin{bmatrix} g^{\{ini\}}_{\{1\}} & \cdots & g^{\{ini\}}_{\{P\}} \end{bmatrix}^\top \tag{10}$$

where the subscripted brackets for the pressure and the initial gap are introduced to avoid confusion with the interface index. In the solution procedure, the axial strain ϵ and the torsion κ_1 represent known values obtained from the FE computation. The matrix $\mathbf{G}$ holds the constraints in Eq. (9) for the P interfaces with gap closure, the vector $\boldsymbol{p}$ is associated with prescribed pressure loads, while $\mathbf{A}$, $\mathbf{A}^{\epsilon}$ and $\mathbf{A}^{\kappa_1}$ contain coefficients from the layer governing equations, see Eqs. (4) – (6).

The bending behavior is coupled to the axi-symmetric response via the interlayer pressures. In situations with pressure variations, the global Newton-Raphson solution procedure is known to perform poorly if this coupling is omitted in the tangent stiffness relation. Ad-hoc solutions are often employed to tackle this issue, e.g. the stiffness coupling is neglected and the current pressure values are replaced by those obtained in the previous equilibrium state. Such approaches are not desirable and a consistent stiffness representation is therefore proposed here. The sought linearization of Eq. (10) is consistently obtained as follows,

$$\begin{bmatrix} \mathbf{A}_{3K\times(3K+P)} \\ \mathbf{G}_{P\times(3K+P)} \end{bmatrix} \begin{bmatrix} \mathbf{s}_{,D} \\ \boldsymbol{\lambda}_{,D} \end{bmatrix} = - \begin{bmatrix} \mathbf{A}^{D}_{3K\times 1} \\ \mathbf{0}_{P\times 1} \end{bmatrix} \qquad D = \epsilon, \kappa_1 \tag{11}$$

where the comma in subscript denotes the partial derivative, e.g. $\boldsymbol{\lambda}_{,\epsilon} = \frac{\partial \boldsymbol{\lambda}}{\partial \epsilon}$. The coupling of $p_{,\epsilon}$ and $p_{,\kappa_1}$ with the bending response is described in Section 2.4. Once Eq. (11) is solved, the axial force entries needed in the tangent constitutive stiffness matrix are available from $N_{,\epsilon}$ and $N_{,\kappa_1}$, while the helix layer torque entries $M_{1,\epsilon}$ and M_{1,κ_1} are readily obtained via Eq. (7). In this way, the iterative changes of interlayer pressure, layer radius and layer thickness are consistently accounted for in the global solution procedure. For a given strain state, the linearization in Eq. (11) yields a weakly unsymmetric axial-torsional tangent stiffness matrix.

2.3 Plastic sheath layer bending model

A standard linear-elastic bending model is applied for the plastic sheath layers. To account for residual curvature effects the constitutive relation reads,

$$\begin{aligned}
&\mathbf{M}_i = K_{Ei}\left(\boldsymbol{\kappa} - \boldsymbol{\kappa}_i^{\{0\}}\right) \qquad \boldsymbol{\kappa} = \left[\begin{array}{cc} \kappa_2 & \kappa_3 \end{array}\right]^\top \\
&K_{Ei} = \frac{\pi}{4}\left[\left(r_i + \frac{t_i}{2}\right)^4 - \left(r_i - \frac{t_i}{2}\right)^4\right] E_i
\end{aligned} \tag{12}$$

where the geometric parameters are defined in Fig. 3, E denotes the elastic modulus and $\boldsymbol{\kappa}^{\{0\}}$ represents a constant residual bending curvature.

2.4 Coulomb bending model for tensile helix layers

The applied bending model was developed by Sævik [15], who employed a Coulomb friction model to describe the stick-slip behavior of the tensile helix tendons, resulting in a three-linear bending-curvature relationship. As the transition between stick and full slip is small in terms of curvature, the bending response is instead approximated with a bi-linear relationship here, which is equivalent to a Coulomb friction model without hardening. The model is regarded valid if no significant end-termination effects are present and if the longitudinal communication along the helix tendons due to slippage is not too dominant.

The governing equations are formulated in compliance with the framework of computational elasto-plasticity. Hence, to determine whether slippage is present or not, a slip function f is defined for each of the tensile helix layers,

$$\begin{aligned}
&f\left(\mathbf{M}_i, M_{si}\right) = ||\mathbf{M}_i|| - M_{si} \leq 0 \qquad \mathbf{M}_i = \left[\begin{array}{cc} M_{2i} & M_{3i} \end{array}\right]^\top \\
&M_{si} = M_{0i} + m_i\left(\mu_i p_i + \mu_{i+1} p_{i+1}\right) \qquad m_i = \frac{4r_i^3 \cos\alpha_i}{\tan|\alpha_i|}
\end{aligned} \tag{13}$$

in which $f = 0$ during slip, $f < 0$ indicate no slippage and $f > 0$ is an inadmissible state. The geometric parameters are defined in Fig. 3, M_s is termed the friction moment, M_0 is a constant moment stemming from the fabrication process and μ is the interface friction coefficient assumed independent of both slip rate and total curvature. The contact pressure p is obtained from the axi-symmetric model according to Eq. (10). The rate of change of the bending moment with respect to time is given by the elastic relation,

$$\dot{\mathbf{M}}_i = K_{Ei}\left(\dot{\boldsymbol{\kappa}} - \dot{\boldsymbol{\kappa}}_{pi}\right) \qquad \boldsymbol{\kappa} = \left[\begin{array}{cc} \kappa_2 & \kappa_3 \end{array}\right]^\top \qquad K_{Ei} = \frac{1}{2}E_i n_i b_i t_i r_i^2 \cos^3\alpha_i \tag{14}$$

where the superposed dot denotes the material time derivative. In Fig. 3 the geometric parameters are defined, n_i is the number of tendons, E denotes the elastic modulus, $\dot{\boldsymbol{\kappa}}$ is the rate of total bending curvature and $\dot{\boldsymbol{\kappa}}_p$ represents the rate of bending curvature associated with slip. The latter rate is in accordance with Coulomb's friction law given by a non-associative slip rule,

$$\dot{\boldsymbol{\kappa}}_{pi} = \dot{\lambda}_i \frac{\partial}{\partial \mathbf{M}_i} f\left(\mathbf{M}_i, M_{si}\right) = \dot{\lambda}_i \frac{\mathbf{M}_i}{||\mathbf{M}_i||} \qquad \dot{\lambda}_i \geq 0 \tag{15}$$

in which $\dot{\lambda}$ is the plastic rate parameter, determined by the consistency criterion $\dot{f} = 0$ if slippage occurs and set to zero if $f < 0$.

In case of no slippage, the incremental constitutive relation is obtained by straightforward integration of Eq. (14) with $\dot{\boldsymbol{\kappa}}_p = \mathbf{0}$. If slippage occurs, the incremental relation should be obtained from a consistent linearization of the moment update scheme. However, for brevity the continuum tangent relation valid for infinitesimal increments is instead emphasized here, which for the selected slip function, elastic relation and slip rule reads as follows,

$$\begin{aligned}
&\dot{\mathbf{M}}_i = \mathbf{C}_{\kappa i}\,\dot{\boldsymbol{\kappa}} + \mathbf{C}_{pi}\,\dot{\boldsymbol{\omega}} \qquad \boldsymbol{\omega} = \begin{bmatrix} \epsilon & \kappa_1 \end{bmatrix}^\top \\
&\mathbf{C}_{pi} = m_i \frac{\mathbf{M}_i}{||\mathbf{M_i}||} \begin{bmatrix} \mu_i p_{i,\epsilon} + \mu_{i+1} p_{i+1,\epsilon} & \mu_i p_{i,\kappa_1} + \mu_{i+1} p_{i+1,\kappa_1} \end{bmatrix} \\
&\mathbf{C}_{\kappa i} = K_{Ei} \left[\mathbf{I}_{2\times 2} - \tfrac{\mathbf{M}_i}{||\mathbf{M}_i||} \otimes \tfrac{\mathbf{M}_i}{||\mathbf{M}_i||} \right]
\end{aligned} \tag{16}$$

where the pressure derivatives $p_{,\epsilon}$ and $p_{,\kappa_1}$ introduce a coupling with the axial-torsional response such that the tangent operator becomes non-symmetric. These derivatives are obtained in a consistent way by means of Eq. (11). With regard to the Lagrangian-Eulerian description in Section 3, it must be emphasized that Eqs. (13) – (16) refer to a fixed set of cross-sectional material particles.

3 The Lagrangian-Eulerian framework

3.1 Basics of the formulation

A detailed presentation of the Lagrangian-Eulerian beam formulation is given in Ref. [11] where it is demonstrated to provide similar accuracy as the conventional Lagrangian formulation. For completeness of the present work, the basic ideas and the assumptions are repeated below, and in Section 3.3 the governing equations for the history-dependent bending response are stated.

The main idea behind the developed formulation is to separate the mesh and the material motion in such a way that the mesh becomes practically fixed in space. Compared to the conventional Lagrangian approach, this strategy yields significant benefits for the overall computational efficiency and the performance of the contact algorithms. The number of DOFs reduces considerably because the mesh need only to extend between the inlet and the outlet of the reels. As opposed to the conventional formulation, non-uniform meshes can be employed which thus enable use of large elements in small-deformation regions. The contact element topology changes less frequently, which implies that potential convergence issues related to the contact algorithms are mitigated and more efficient contact searches can be executed. Also, larger time steps may be used due to less variations in the contact conditions.

The formulation is based on a fully coupled approach where the material motion, the mesh motion and the convective transport effects are handled simultaneously. The mesh motion is computed similarly as in the conventional Lagrangian formulation, while the material motion is given in terms of a single prescribed boundary condition. The development is founded upon the following assumptions,

- The bending curvature and the bending moment are continuous across element boundaries.
- Concentrated bending moment loads are only allowed at the endpoints.
- The mass is uniformly distributed and cannot accumulate in the mesh.
- Inertia and velocity-dependent loads are disregarded.

None of the above assumptions impose restrictions for prediction of responses in reeling operations. If required, concentrated moments may be modeled by a couple acting on a short beam element.

3.2 Computational domain

The computational domain in a typical reeling operation is illustrated in Fig. 4, where the centroidal line of the transported product is represented by a three-dimensional curve in terms of the mesh arc length parameter χ. A conventional Lagrangian analysis can be employed to establish the initial computational domain, however, such an approach is cumbersome and spoils the advantages offered by the Lagrangian-Eulerian procedure. Hence, a cubic Hermite spline interpolator is introduced to compute the initial nodal coordinates, the unstretched beam element lengths and the initial nodal rotation parameters.

As seen in Fig. 4, the interpolated region is parametrized in terms of a local coordinate $\eta \in [-1, 1]$, which extends between the midpoints of two straight segments with end coordinates $\hat{\mathbf{x}}^{\{m-1\}}$, $\hat{\mathbf{x}}^{\{m\}}$ and $\hat{\mathbf{x}}^{\{m+1\}}$. Global C^1-continuity is ensured as the spline

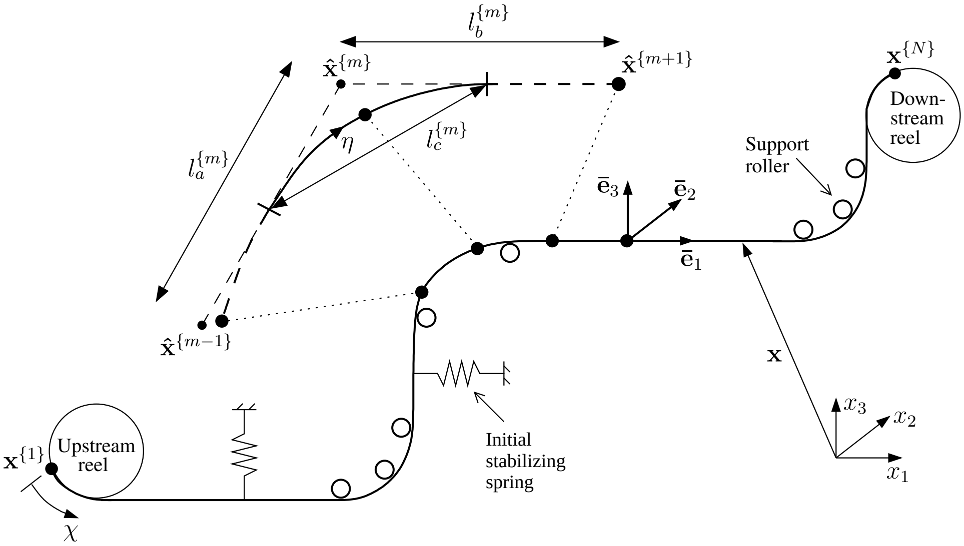

Figure 4: Initial computational domain

passes through and is tangent to the midpoint of the straight control lines. For a mesh with N nodes, the piecewise spline interpolation is defined by the following formulae,

$$\mathbf{x}\left(\eta\right) = \mathbf{X}\,\mathbf{A}\,\mathbf{B}\,\mathbf{n}(\eta) \qquad \mathbf{X} = \begin{bmatrix} \hat{x}_1^{\{m-1\}} & \hat{x}_1^{\{m\}} & \hat{x}_1^{\{m+1\}} \\ \hat{x}_2^{\{m-1\}} & \hat{x}_2^{\{m\}} & \hat{x}_2^{\{m+1\}} \\ \hat{x}_3^{\{m-1\}} & \hat{x}_3^{\{m\}} & \hat{x}_3^{\{m+1\}} \end{bmatrix}$$

$$\mathbf{A} = \frac{1}{2}\begin{bmatrix} 1 & 0 & -\frac{l_c^{\{m\}}}{l_a^{\{m\}}} & 0 \\ 1 & 1 & \frac{l_c^{\{m\}}}{l_a^{\{m\}}} & -\frac{l_c^{\{m\}}}{l_b^{\{m\}}} \\ 0 & 1 & 0 & \frac{l_c^{\{m\}}}{l_b^{\{m\}}} \end{bmatrix} \qquad \mathbf{B} = \frac{1}{4}\begin{bmatrix} 1 & 0 & -3 & 2 \\ -1 & 0 & 3 & 2 \\ 1 & -1 & -1 & 1 \\ 1 & 1 & -1 & -1 \end{bmatrix} \tag{17}$$

$$l_a^{\{m\}} = \left|\left|\hat{\mathbf{x}}^{\{m\}} - \hat{\mathbf{x}}^{\{m-1\}}\right|\right| \qquad l_b^{\{m\}} = \left|\left|\hat{\mathbf{x}}^{\{m+1\}} - \hat{\mathbf{x}}^{\{m\}}\right|\right|$$

$$l_c^{\{m\}} = \left|\left|\frac{\hat{\mathbf{x}}^{\{m-1\}} + \hat{\mathbf{x}}^{\{m\}}}{2} - \frac{\hat{\mathbf{x}}^{\{m\}} + \hat{\mathbf{x}}^{\{m+1\}}}{2}\right|\right| \qquad m = 2, ..., N-1$$

$$\mathbf{x} = \begin{bmatrix} x_1 & x_2 & x_3 \end{bmatrix}^\top \qquad \mathbf{n} = \begin{bmatrix} \eta^3 & \eta^2 & \eta & 1 \end{bmatrix}^\top \qquad -1 \leq \eta \leq 1$$

The orientation of the unit triads $\bar{\mathbf{e}}_j$ at the beam element nodes, see Fig. 2, is obtained by integration of the Serret-Frenet differential formula. In the initial configuration, the elements are assumed to have zero torsion such that the differential change along the mesh of the unit triads is given by,

$$\frac{\mathrm{d}\bar{\mathbf{e}}_j}{\mathrm{d}\mathcal{X}} = \boldsymbol{\Omega}\,\bar{\mathbf{e}}_j \qquad \boldsymbol{\Omega} = \mathbf{Q}\begin{bmatrix} 0 & -\kappa_\nu & 0 \\ \kappa_\nu & 0 & -\kappa_\zeta \\ 0 & \kappa_\zeta & 0 \end{bmatrix}\mathbf{Q}^\top \qquad \mathbf{Q} = \begin{bmatrix} \boldsymbol{\zeta} & \boldsymbol{\nu} & \boldsymbol{\beta} \end{bmatrix}$$
$$j = 1, 2, 3 \tag{18}$$

where the geometric torsion κ_ζ, the principal curvature κ_ν and the Serret-Frenet unit vectors, $\boldsymbol{\zeta}$, $\boldsymbol{\beta}$ and $\boldsymbol{\nu}$, are obtained according to,

$$\kappa_\zeta = \frac{\left(\mathbf{x}_{,\eta} \times \mathbf{x}_{,\eta\eta}\right) \cdot \mathbf{x}_{,\eta\eta\eta}}{||\mathbf{x}_{,\eta} \times \mathbf{x}_{,\eta\eta}||^2} \qquad \kappa_\nu = \frac{||\mathbf{x}_{,\eta} \times \mathbf{x}_{,\eta\eta}||}{||\mathbf{x}_{,\eta}||^3} \qquad \boldsymbol{\zeta} = \frac{\mathbf{x}_{,\eta}}{||\mathbf{x}_{,\eta}||}$$
$$\boldsymbol{\beta} = \frac{\mathbf{x}_{,\eta} \times \mathbf{x}_{,\eta\eta}}{||\mathbf{x}_{,\eta} \times \mathbf{x}_{,\eta\eta}||} \qquad \boldsymbol{\nu} = \boldsymbol{\beta} \times \boldsymbol{\zeta} \tag{19}$$

In the implementation, Eq. (18) is integrated numerically from a nodal point with known orientation. The integration is performed by means of the matrix exponential map to preserve orthogonality of the unit triads $\bar{\mathbf{e}}_j$ as follows,

$$\bar{\mathbf{e}}_j\left(\mathcal{X} + \Delta\mathcal{X}\right) = \mathbf{R}_{\Delta\mathcal{X}}\,\bar{\mathbf{e}}_j\left(\mathcal{X}\right) \qquad \mathbf{R}_{\Delta\mathcal{X}} = \exp\left[\frac{\Delta\mathcal{X}}{2}\Big\{\boldsymbol{\Omega}\left(\mathcal{X}\right) + \boldsymbol{\Omega}\left(\mathcal{X} + \Delta\mathcal{X}\right)\Big\}\right]$$
$$\Delta\mathcal{X} = \frac{J\left(\eta\right) + J\left(\eta + \Delta\eta\right)}{2}\Delta\eta \qquad J = ||\mathbf{x}_{,\eta}|| \tag{20}$$

The quantities κ_ζ, $\boldsymbol{\beta}$ and $\boldsymbol{\nu}$ in Eq. (19) are not well-behaved if the principal curvature approaches zero. In such cases the orthogonal matrix $\mathbf{R}_{\Delta\mathcal{X}}$ is simply replaced with the identity matrix.

The initial computational domain is released at analysis start-up and subjected to Newton-Raphson iterations until equilibrium is achieved. Recommendations on how to ensure convergence are given in Section 3.6. The update of the mesh displacement state and the beam deformation parameters are throughout the analysis handled identically as in the conventional Lagrangian formulation.

3.3 Path-dependent material responses

The axi-symmetric response and the plastic sheath layer bending response require no specific treatment as they depend solely on the current strain state. The Coulomb bending model depends in contrast on the history experienced by the material particles and its evolution is therefore obtained by integration of the material time derivative. As the mesh points are not tied to the material particles, a convective transport contribution appears in the material rate equations. Hence, relative to the corotational element frames, the material time derivative of the bending moment and the bending curvature reads,

$$\dot{\mathbf{M}}\,(\mathcal{X},t) = \mathbf{M}_{,t[\mathcal{X}]} + c\,\mathbf{M}_{,\mathcal{X}} \tag{21}$$

$$\dot{\boldsymbol{\kappa}}\,(\mathcal{X},t) = \boldsymbol{\kappa}_{,t[\mathcal{X}]} + c\,\boldsymbol{\kappa}_{,\mathcal{X}} \tag{22}$$

where the notation $[\mathcal{X}]$ emphasizes that the mesh arc length parameter is held fixed. The convective velocity is denoted c and represents the material velocity seen by a mesh-fixed observer. As the mass density per unit length is assumed constant, the principle of mass conservation implies that c at a given time is constant throughout the mesh. The convective velocity is obtained via the following relation,

$$c\,(t) = V\,(\mathcal{X},t) - \hat{V}\,(\mathcal{X},t) \tag{23}$$

in which V and $\hat{V}$ denote the absolute velocities of the material and the mesh along the centroidal line. The material velocity V is given in terms of a prescribed boundary condition at a single mesh point, while the nodal mesh velocity is computed as,

$$\hat{V}_j = \mathbf{x}_{j,t} \cdot \bar{\mathbf{e}}_{1j} \qquad j = A, B \tag{24}$$

where the involved vectors are defined in Fig. 2.

The bending moment components in Eq. (16) refer to material-fixed points, whereas the mesh-fixed bending moments are needed in the beam weak formulation. In Eq. (21) the mesh-fixed moments are represented by the partial time derivative term. These moments are computed by a fully implicit backward Euler integration scheme in the implementation, but for the sake of brevity, the mesh-fixed continuum tangent relation valid for infinitesimal increments is instead emphasized here. This relation emerges when Eqs. (21) and (22) are inserted into the material continuum tangent relation in Eq. (16),

$$\mathbf{M}_{i,t[\mathcal{X}]} = \mathbf{C}_{\kappa i}\,\boldsymbol{\kappa}_{,t[\mathcal{X}]} + \mathbf{C}_{pi}\,\dot{\boldsymbol{\omega}} + c\,\mathbf{C}_{\kappa i}\,\boldsymbol{\kappa}_{,\mathcal{X}} - c\,\mathbf{M}_{i,\mathcal{X}} \tag{25}$$

in which the two first terms are pure Lagrangian contributions and the two last ones appear because of the Lagrangian-Eulerian viewpoint. The components of the axi-symmetric strain vector $\boldsymbol{\omega}$ and the bending curvature $\boldsymbol{\kappa}$ are readily obtained from Eqs. (1) – (3). The convective terms containing the gradients $\boldsymbol{\kappa}_{,\chi}$ and $\mathbf{M}_{,\chi}$ need a careful treatment to achieve similar accuracy as in the conventional Lagrangian formulation. In previous work, simple gradient approximations were seen to suffer from poor accuracy and spatial instabilities. These issues were solved by means of a gradient approximation with a suitable spatial weighting of the constitutive variables and an upwind scheme that discarded information from downstream elements. Further details about the gradient approximation, an implicit moment update scheme and the incorporation with the corotational beam formulation are given in Ref. [11].

3.4 Roller contact formulation

In reeling operations, the product is transported on rigid rollers with negligible rotational resistance. Sliding motions along the roller axes are usually limited, as the roller normal contact interaction constrains the product in both of its transverse directions at numerous points along the route. A frictionless contact model is therefore selected for the roller interaction.

Due to the frictionless assumption, the contact kinematics is expressed identically as for the Lagrangian description of motion. Although the mesh is practically fixed in space, cases where the contact points travel across element boundaries can occur. The beam geometry is hence interpolated by the conventional Hermite shape functions [22] such that dead zones in the contact search and issues with the transfer of the contact force are avoided. Thus, the contact element consists of two beam nodes with 12 DOFs and a single node with 6 DOFs attached to the roller geometry. The contact loads for the beam rotational DOFs are set equal to zero to comply with the continuity assumption stated in Section 3.1. This implies that the contact tangent stiffness matrix becomes non-symmetric, which has no practical consequence as the stiffness contributions associated with Eq. (25) and the axial-torsional response in Eqs. (7) and (10) are also non-symmetric.

In FE computations, the impenetrability constraints are normally enforced by either the penalty method or the Lagrange multiplier methods [23]. For the analysis procedure outlined in Section 3.6, the standard Lagrange multiplier method resulted in convergence difficulties at start-up, which hence made the penalty method to an obvious choice in this work. The penalty method regularizes the contact force at the cost of not fulfilling the impenetrability constraints exactly, where the degree of regularization is governed by the so-called penalty parameter. This feature was seen to be beneficial with regard to convergence during computation of the equilibrated initial mesh configuration.

3.5 Mesh stiffness and load factors

The computational domain illustrated in Fig. 4 represents the situation when material is being transported between the reels. For the operation start-up phase, where the pipe-end is guided toward and attached to the destination reel, an initial Lagrangian simulation could be applied. However, that represents a cumbersome approach and it is desirable to rather utilize the established computational domain. Hence, by assuming that the pipe-end follows the path defined by the current mesh configuration, its motion can be simulated by means of moving weight factor distributions for the constitutive stiffness and the gravity loads. For a single beam element with K layers, the bending stiffness parameters defined in Section 2 and the distributed mass m_g are therefore scaled according to,

$$\bar{K}_{Ei} = \gamma_i K_{Ei} \qquad \bar{m}_{gi} = \gamma_i m_{gi} \qquad i = 1, ..., K \tag{26}$$

where the moving mesh weight factor is defined in terms of the Heaviside step function H as follows,

$$\begin{aligned} \gamma_i\left(\chi_{cg}^{\{m\}}, t\right) = {} & \frac{\chi_{1i} - \chi_{cg}^{\{m\}}}{\chi_{2i} - \chi_{1i}} \left[H\left(\chi_{cg}^{\{m\}} - \chi_{1i}\right) - H\left(\chi_{cg}^{\{m\}} - \chi_{2i}\right)\right] \\ & - H\left(\chi_{cg}^{\{m\}} - \chi_{2i}\right) + 1.0 \\ \chi_{ji}\left(t\right) = {} & \int_0^t c\,\mathrm{d}t + \chi_{ji}\left(0\right) \quad j = 1, 2 \end{aligned} \tag{27}$$

which yields a linear increase of stiffness and gravity in the material flow-front region, $\chi_1 < \chi < \chi_2$. The convective velocity c is obtained from Eq. (23) and $\chi_{cg}^{\{m\}}$ denotes the mesh coordinate at the midpoint of beam element m. The region with no material, $\chi > \chi_2$, is assigned a low bending stiffness K_{E0} to ensure a non-singular FE equation system. This stiffness parameter is scaled similarly as in Eq. (26) by the following weight factor,

$$\begin{aligned} \gamma_0\left(\chi_{cg}^{\{m\}}, t\right) = {} & \frac{\chi_{cg}^{\{m\}} - \chi_1}{\chi_2 - \chi_1} \left[H\left(\chi_{cg}^{\{m\}} - \chi_1\right) - H\left(\chi_{cg}^{\{m\}} - \chi_2\right)\right] \\ & - H\left(\chi_{cg}^{\{m\}} - \chi_2\right) \\ \chi_j\left(t\right) = {} & \int_0^t c\,\mathrm{d}t + \chi_j\left(0\right) \quad j = 1, 2 \end{aligned} \tag{28}$$

No scaling is applied for the axial and torsional stiffness parameters, as this could give large interlayer contact pressures at the flow-front region leading to an artificial high friction moment capacity. Notice that the flow-front region is defined independently for each layer. This allows for a delayed activation of the Coulomb bending model, such that numerical issues due to the low stiffness at $\chi > \chi_2$ are avoided and the flow-front curvature discontinuity can be taken mainly by the plastic sheath layers. Comparison against the conventional Lagrangian approach for the simply supported beam examples considered in Ref. [11] indicated that a delayed activation of one and two element lengths had no significant influence on the accuracy.

3.6 Analysis execution

At analysis initiation, the mesh is released from the configuration described in Section 3.2 with relevant DOFs at the endpoints held fixed. This abrupt release introduces large unbalanced loads prone to preclude convergence at the initial load step if the constitutive models in Section 2 are activated. Hence, the analysis is initiated with a soft initial linear-elastic constitutive model, small contact penalty parameters and with stabilizing springs in the mesh transverse directions, see Fig. 4. The internal and the external loads are thereafter activated in a stepwise manner, the penalty parameters are increased to their appropriate values and the stabilizing springs are removed. The selected approach involves the following sequence of steps,

1) Establish the initial computational domain as described in Section 3.2. Attach stabilizing springs in the beam transverse direction and set the contact roller penalty parameters to a lower bound value.

2) Compute the equilibrated initial computational domain by using an initial linear-elastic constitutive model with stiffness properties set sufficiently low to handle the iterative strain variations encountered during the initial load step.

3) Apply the gravity loads.

4) Increase the contact roller penalty parameters to their desired values.

5) Apply the loads from the axi-symmetric model, the plastic sheath layer bending loads and the K_{E0}-bending loads associated with Eq. (28).

6) Remove the stabilizing transverse springs and the loads from the initial linear-elastic constitutive model.

7) Apply relevant boundary conditions at the mesh endpoints.

8) Adjust the tension level to the desired value.

9) Activate the elasto-plastic bending model and initiate the material transport.

The appropriate stiffness properties of the stabilizing springs, the initial penalty parameters and the initial linear-elastic constitutive model are interrelated. In this work, a reasonable initial linear-elastic model was defined, thereafter the stiffness of the stabilizing springs was set sufficiently soft to avoid slow convergence and yet stiff enough to avoid large mesh displacements, and at last the initial penalty parameters were adjusted toward a lower bound value.

Due to the non-linearity present in the model, the established configuration depends in principle on the order of the steps 1) – 9) above. In practice, there is yet no concern regarding the solution uniqueness, because the numerous contact constraints along the transport route preclude large differences in the computed equilibrium state.

4 Generation of torque in flexible pipe load-out operation

The bending-induced torque generated in an idealized flexible pipe load-out operation from an onshore spool base to a cargo vessel was investigated. The main contributions are generated aboard the vessel where the bending curvature vector is large and undergoes significant direction changes. A truncated FE model was therefore created of the onboard turn-table and the load-out path on the ship deck, see Fig. 5. The turn-table has an angular velocity in the physical operation. In the simulation, this rotation is conveniently avoided due to the Lagrangian-Eulerian viewpoint. Regarding loop formation, the free span between the turn-table and the ship deck in Fig. 5 is not of major concern as it is short, constrained by the spool arm and already has the shape of a helix. It is rather at free spans located upstream of the ship deck the loops are prone to occur, e.g. the free span between the vessel and the quay seen in Fig. 1a. The simulated torque is largest at the ship deck and is therefore regarded as the target response parameter.

All contact interactions along the load-out path was modeled by frictionless rollers with 0.3 m diameter. The configuration of the rollers is seen in Fig. 5, where all labeled distances refer to the center points. On the ship deck the load-out path was defined by four fork supports, and ten rollers placed along a quarter-circle of radius 2.0 m were employed for the overbend support. Fifty rollers placed equidistantly around a 8.0 m diameter circle were used to represent the turn-table hub, while the floor was modeled by twenty

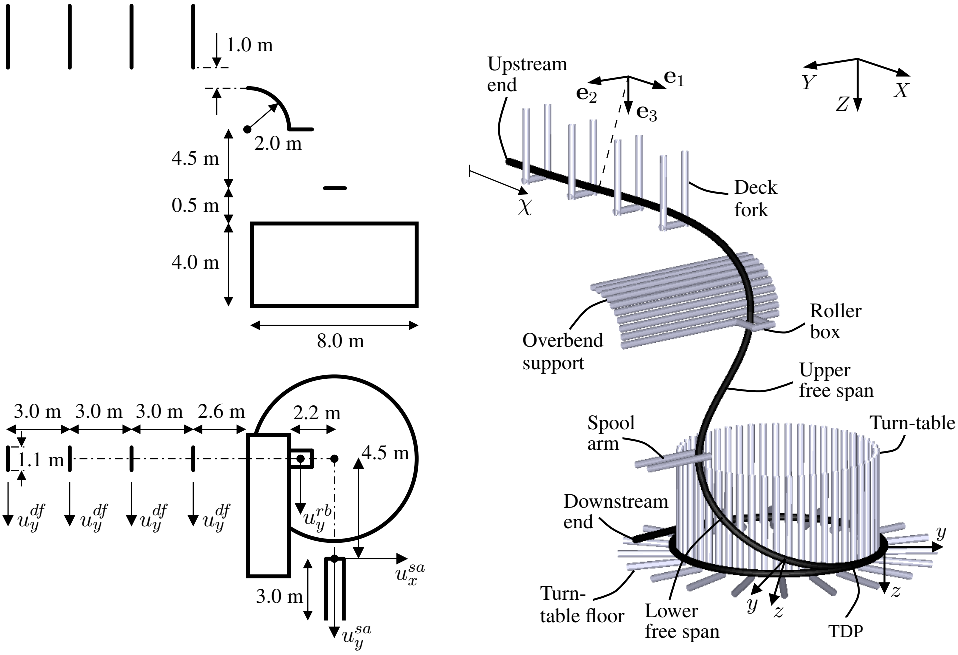

Figure 5: FE model

equidistant rollers spanning outwards from the hub. The spool arm and the roller box are operated by the vessel crew such that the pipe enters the turn-table in the desired way. A fork was used to represent the spool arm with center distance between the long edges set to 0.8 m. The roller box was attached to the overbend support and had centerline dimensions 1.2 m × 0.8 m.

At the turn-table inlet where most of the torque is generated, the assumption of zero friction is indeed regarded acceptable. This is because the deck tensioner and the turn-table operate with slight speed variations, giving fluctuations in the touchdown point (TDP) tension with associated axial slippage that reduces the ability to fix the roll DOF. Consequently, the torque at the ship deck may be underestimated if friction resistance is included. Additionally, a couple of metres downstream of the TDP there will be negligible roll rotations due to the high roll stiffness provided by the Coulomb bending model. Possible missing friction forces are of no importance for the axial and the bending responses.

The mesh consisted of 154 corotated beam elements with lengths set to 0.5 m. At the turn-table, the mesh extended about 1.5 coils downstream of the TDP, with a free end of 3.0 m used for feed-in when adjusting the axial force, see Fig. 5. Self-contact for the coiled part of the mesh was not modeled. The transverse DOFs at the downstream-end were held fixed, while the axial DOF was given appropriate displacement increments to keep the tension in the coiled part between 5 – 15 kN throughout the simulation. All translatory DOFs were kept fixed at the upstream-end. To obtain conservative predictions of the ship deck torque, the roll DOF at the downstream-end was free to rotate, while the one at the upstream-end was held fixed. These boundary conditions represent the situation during start-up of the operation, provided that the end of the pipe is connected to the turn-table by a torque-free joint. Nevertheless, as will be indicated later, potential roll stiffness at the downstream-end is of no importance if the mesh is terminated sufficiently far away from the TDP.

The constitutive parameters of the flexible pipe are given in Table 1 with symbols and parameters as defined in Section 2. Abbreviations THL1 and THL2 refer to respectively the inner and the outer tensile helix layers. Material and geometric properties of the composite cross-section are listed consecutively from the innermost layer to the outermost layer in Table 2 with parameters as defined in Section 2.2. Each of the tensile helix layer fabrication friction moments were set to 15% of the total friction moment capacity at 20 MPa internal pressure based on laboratory test trends [24]. Regarding the torque stiffness, soft and stiff directions are associated with torsion that yields respectively radial separation and radial compression of the tensile helix layers. The selected friction coefficient represents an upper bound value as measured coefficients are normally in the range 0.07 – 0.2 [25].

The simulations were executed according to the procedure outlined in Section 3.6. The material velocity V was set to 1.0 m/s at the upstream-end. Prior to initiation of the material transport, the flow-front region was set to χ_1=11.5 m and χ_2=12.0 m, see Fig. 5. A delayed activation of the Coulomb bending model corresponding to one element length was employed with K_{E0} set to 40 kNm^{-2}, see Section 3.5. Time steps of 0.005 s had to be used during the unsteady start-up phase, while a step size of 0.02 s was applied when stationary conditions started to settle.

Table 1: Flexible pipe properties

Quantity	Symbol	Value	Unit
Elastic modulus - THL1	K_E	2 596	kNm^{-2}
Elastic modulus - THL2	K_E	2 991	kNm^{-2}
Fabrication friction moment - THL1, THL2	M_0	8 000	Nm
Geometry parameter - THL1	m	0.008786	m^3
Geometry parameter - THL2	m	0.010237	m^3
Friction coefficients - THL1, THL2	μ	0.2	
Total bending stiffness sheath layers		400	kNm^2
Total torque stiffness - stiff direction		$\approx$8 000	kNm^2
Total torque stiffness - soft direction		$\approx$1 440	kNm^2
Total distributed mass	m_g	100	kg/m

Table 2: Cross-section layer data

Layer type	t [mm]	r [mm]	b [mm]	E [MPa]	ν [-]	α [deg.]	n_i [-]
Plastic sheath	25	107.0		3 000	0.45		
Pressure helix	10	124.5	12.5	210 000	0.30	-89	1
Plastic sheath	2	130.5		300	0.45		
Tensile helix	5	134.0	12.5	210 000	0.30	$\pm$40	49
Plastic sheath	2	137.5		300	0.45		
Tensile helix	5	141.0	12.5	210 000	0.30	$\pm$40	51
Plastic sheath	25	156.0		300	0.45		

In Section 4.1 – 4.3 the simulated responses are presented. Regarding the sign convention, both torque and roll rotation are defined positive in the clockwise direction when looking downstream.

4.1 Importance of free span shape and tensile helix lay angle direction

The torque induced by the material transport effect during operation start-up was simulated for several free span configurations by varying the position of the spool arm, the roller box and the deck fork supports. Table 3 presents the bending-induced torque at the upstream-end, M_1^{ue}, at the spool arm, M_1^{sa}, and the maximum value at the turn-table inlet, M_1^{cs}. All torque values were sampled when approximately three coils of material had been transported to the turn-table, which for most of the simulation runs coincided with the steady-state value. The lay angles of the inner and the outer tensile helix layers are denoted by α_5 and α_7, respectively. The displacement components u_x and u_y in Table 3 are defined in Fig. 5. A selection of torque response plots for the steady-state configuration is presented in Figs. 6 – 9, where abbreviations SA and RB refer to the spool arm and the roller box, respectively.

The driving mechanism for the torque is found in the lower free span and at the turn-table inlet. In this region the y-axis curvature is gradually reduced, while the curvature is

Table 3: Torque due to material transport versus free span shape and tensile helix lay angle direction

Case	u_y^{rb} [m]	u_x^{sa} [m]	u_y^{sa} [m]	u_y^{df} [m]	α_5 [deg]	α_7 [deg]	M_1^{ue} [kNm]	M_1^{sa} [kNm]	M_1^{cs} [kNm]
1	0.0	−2.0	−0.5	0.0	40	−40	−80.9	−49.6	9.5
2					−40	40	−44.6	−21.4	30.8
3	0.0	1.0	−0.5	0.0	40	−40	−80.6	−53.3	6.3
4					−40	40	−45.6	−24.5	29.2
5	0.0	4.0	−0.5	0.0	40	−40	−46.4	−22.3	0.9
6					−40	40	−27.9	−9.4	12.4
7	2.0	−2.0	0.0	0.0	40	−40	−46.0	−37.2	11.1
8					−40	40	−30.4	−24.1	23.1
9	2.0	1.0	0.0	0.0	40	−40	−64.3	−55.1	−2.0
10					−40	40	−31.6	−26.4	25.5
11	2.0	4.0	0.0	0.0	40	−40	−45.6	−33.5	2.5
12					−40	40	−21.7	−13.7	20.3
13	4.0	−2.0	1.5	0.0	40	−40	−9.9	−27.7	5.5
14					−40	40	−3.6	−21.1	12.7
15	4.0	1.0	1.5	0.0	40	−40	−26.1	−42.2	10.8
16					−40	40	−7.5	−23.0	24.5
17	4.0	4.0	1.5	0.0	40	−40	−16.9	−19.8	3.6
18					−40	40	−6.2	−10.3	13.4
19	4.0	−2.0	0.0	4.0	40	−40	−67.7	−52.4	2.6
20					−40	40	−44.8	−34.8	18.9
21	4.0	1.0	0.0	4.0	40	−40	−66.3	−54.8	6.1
22					−40	40	−42.2	−35.8	22.9
23	4.0	4.0	0.0	4.0	40	−40	−53.7	−38.6	10.6
24					−40	40	−23.6	−14.3	30.3

constrained by the turn-table and kept rather constant about the z-axis, see Fig. 5. With the presence of material transport, this causes a moment about the negative y-axis of approximately 8 – 10 kNm for 10 – 15 metres in each of the tensile helix layers, which thus yields a positive rise of torque in the lower free span and at the turn-table inlet, see Figs. 6 – 9. The torque rise, $M_1^{cs} - M_1^{sa}$, is according to Table 3 between 23 – 61 kNm. A few metres downstream of the TDP, the bending curvature gradient about the y-axis is close to zero, see Fig. 5, such that the material transport effect is unable to maintain the moment about the negative y-axis. The torque therefore decays to zero over a couple of metres distance, in which it transfers into a small positive y-axis bending moment in the tensile helix layers with negligible increase of the associated curvature. Further downstream, only small fluctuations around the zero level are present for the torque and the y-axis bending moment. This implies that potential roll stiffness at the downstream-end is of minor importance if the mesh terminates sufficiently far away from the TDP. A few simulation runs with the downstream-end roll DOF held fixed confirmed this observation.

The torque values in Table 3 depend strongly on the tensile helix lay angle directions, in which $\alpha_5 = 40°$ and $\alpha_7 = -40°$ are seen to give the largest upstream-end torque. For a given free span shape, the lay angle directions have no significant influence on the torque rise, $M_1^{cs} - M_1^{sa}$. However, as exemplified in Fig. 8, the torque distributions undergo a shift that reduces the upstream torque for the cases with $\alpha_5 = -40°$ and $\alpha_7 = 40°$. This shift must be understood in terms of the stiff and soft torsion directions, see Table 1, the high turn-table roll stiffness provided by the Coulomb bending model and the gradual activation of the tensile helix layer bending stiffness as the material flow-front moves. For the lay angles $\alpha_5 = 40°$ and $\alpha_7 = -40°$, the induced torque is counteracted mainly by upstream torque. This occurs because the torsion in the upstream region acts in the stiff direction, whereas the torsion downstream of the TDP works in the soft direction. When the lay angles are reversed, the upstream region counteracts instead with torsion in the soft direction, and a major part of the turn-table inlet region undergoes a stiffness increase as the pipe there counteracts with torsion in the stiff direction. This relative change of stiffness therefore shifts a significant part of the upstream torque toward the turn-table, see Fig. 8.

According to Table 3, the position of the roller box affects the torque to a much larger degree than the spool arm position. The responses obtained for cases 13 – 18 demonstrate that there exist favorable roller box positions which reduce the upstream-end torque. This becomes apparent by comparing Fig. 6 against Fig. 7 where the upstream torque is seen to magnify and reduce, respectively. The cancellation behavior relates to the pipe configuration in the upper free span and at the overbend, which has the shape of a positive helix that acts to cancel the torque induced in the lower free span and at the turn-table inlet. For the cases considered, a favorable roller box position reduces the ship deck torque by up to 70 kNm, see Table 3. Cancellation effects due to roller box displacements have indeed been witnessed in load-out operations.

As seen in Fig. 6, case 5 with spool arm position $u_x^{sa} = 4.0$ m has a reduced upstream torque compared to case 3 where $u_x^{sa} = 1.0$ m. Similar trends, but less pronounced, are present for the other cases as well, see Table 3. This occurs because the selected spool arm position reduces the y-axis curvature gradient for a couple of metres downstream of the spool arm. Consequently, the negative y-axis moment in the tensile helix layers, which is the driving mechanism for the torque, vanishes for a few metres.

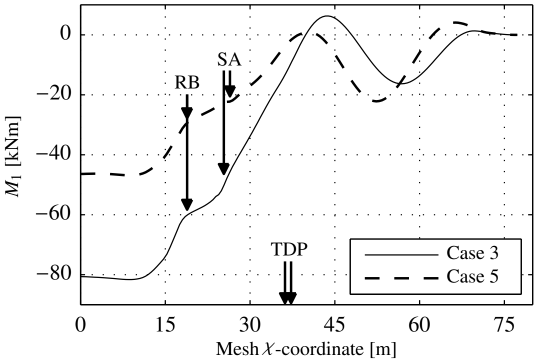

Figure 6: Torque distribution

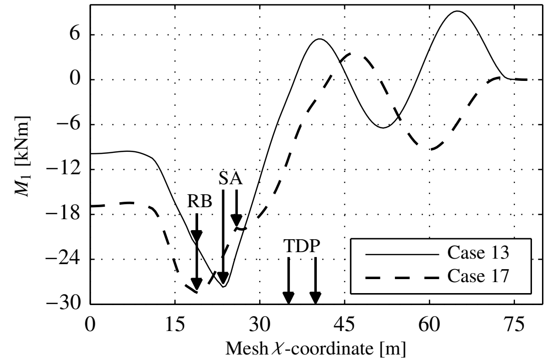

Figure 7: Torque distribution

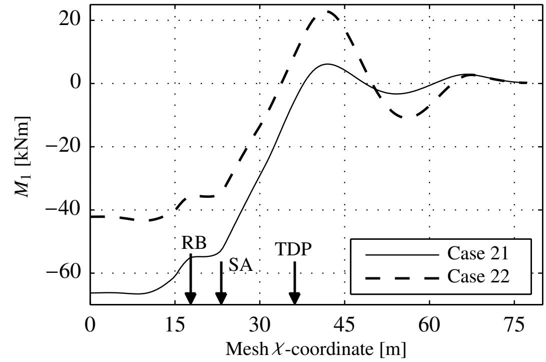

Figure 8: Torque distribution

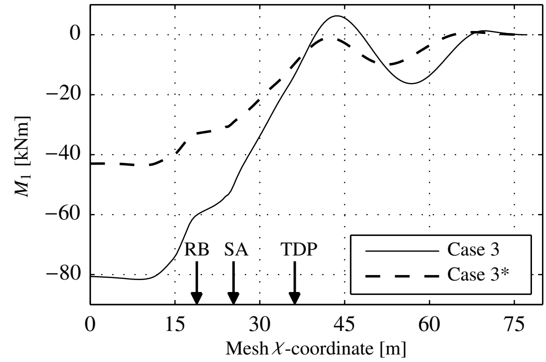

Figure 9: Torque distribution

The effect of reducing the fabrication friction moment to 4 000 Nm in both of the tensile helix layers was examined. The simulated torque distribution is denoted case 3* in Fig. 9, and is seen to be roughly halved compared to case 3. This implies that the induced torque is roughly proportional to the fabrication friction moment, which is also expected as the contact pressures are small and the torque is not sufficiently large to alter the pipe path.

4.2 Influence of spool arm motion

The influence of a 6 m spool arm displacement in the positive X-direction was considered for the cases listed in Table 4, with tensile helix lay angles $\alpha_5 = 40°$ and $\alpha_7 = -40°$. The spool arm was kept at rest in the initial configuration defined by ${}^0u_y^{rb}$, ${}^0u_x^{sa}$, ${}^0u_y^{sa}$ and ${}^0u_y^{df}$, see Fig. 5, until a material length corresponding to three coils had been transported to the turn-table. Thereafter, the spool arm was assigned the velocity history in Table 3. An extended mesh of length 96 m was used to ensure that the torque decayed to zero before the mesh endpoint. In Figs. 10 and 12, the torque distributions are presented at the instant the maximum torque was attained. The torque evolution at the upstream-end is shown in Figs. 11 and 13 with the time measured from the instant the spool arm motion was initiated.

Table 4: Initial position and velocity history for the spool arm

Case	${}^0u_y^{rb}$ [m]	${}^0u_x^{sa}$ [m]	${}^0u_y^{sa}$ [m]	${}^0u_y^{df}$ [m]	Spool arm velocity [m/s]
25	0.0	−2.0	−0.5	0.0	v_x^{sa}=0.8 for $t \in \langle 0.0$ s, 7.5 s$]$
26	0.0	−2.0	−0.5	0.0	v_y^{sa}=0.8 for $t \in \langle 0.0$ s, 5.0 s$]$ $\rightarrow$ v_x^{sa}=0.8 for $t \in \langle 5.0$ s, 12.5 s$]$
27	4.0	−2.0	0.0	4.0	v_x^{sa}=0.8 for $t \in \langle 0.0$ s, 7.5 s$]$
28	4.0	−2.0	0.0	4.0	v_y^{sa}=0.8 for $t \in \langle 0.0$ s, 5.0 s$]$ $\rightarrow$ v_x^{sa}=0.8 for $t \in \langle 5.0$ s, 12.5 s$]$

When the spool arm is moved directly with 0.8 m/s velocity in the positive X-direction for 6 m, the torque increases approximately linearly until the peak value is attained after 6 s, see Figs. 11 and 13. The maximum values at the upstream-end are 184 kNm for case 25 and 193 kNm for case 27, respectively. For cases 26 and 28, the spool arm is first displaced 4 m in the positive Y-direction, which results in a far less torque rise during the X-displacement.

The extreme response for cases 25 and 27 occurs because the part coiled on the turn-table mobilizes a considerable torque to counteract the TDP geometric roll rotation imposed by the change in free span shape. This effect relates to the Coulomb bending model, which allows the bending moment vector of the tensile helix layers to rotate rapidly such that it becomes perpendicular to the turn-table-constrained pipe curvature vector. Thus, large torques can be mobilized even for small roll rotations at the turn-table inlet. For the present cases, the rotation of the tensile helix layer bending moment vectors spreads gradually downstream on the turn-table. The friction moment capacity in each tensile helix layer is between 8 – 12 kNm in the coiled part throughout the process, which implies

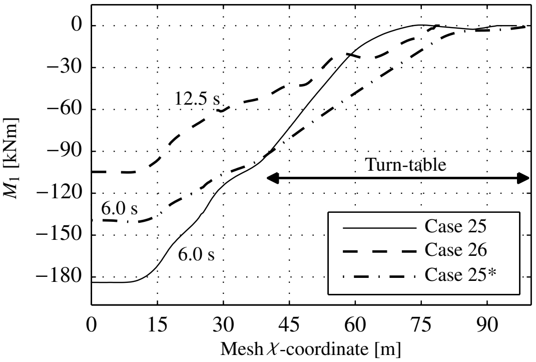

Figure 10: Torque distribution

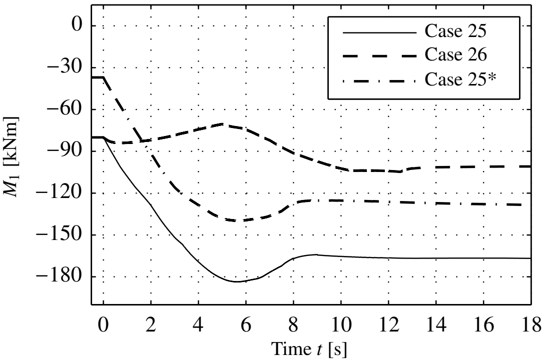

Figure 11: Torque at upstream-end

that the contact pressures provide a noticeable contribution. For case 27, the maximum contact pressure between the tensile helix layers is 4.6 MPa and occurs at the ship deck. In contrast to the cases in Section 4.1, approximately half of the torque is induced at the turn-table, see Figs. 10 and 12. Observe that the torque in Figs. 11 and 13 undergoes a drop about 1.5 s before the final spool arm position is reached. This occurs because the material transport effect counteracts with a larger torque than the one induced by the TDP roll rotation. For case 25, the X-direction contact force on the spool arm changed from 40 kN to -25 kN during the prescribed displacement.

A test run was conducted for case 25 to examine the degree of roll restraint provided by the Coulomb bending model. About 10 m downstream of the TDP, the roll rotation was 53° when the Coulomb model was deactivated, whereas 3° rotation occurred with the bending model activated. Thus, the Coulomb bending model gives a significant roll stiffness contribution at the turn-table.

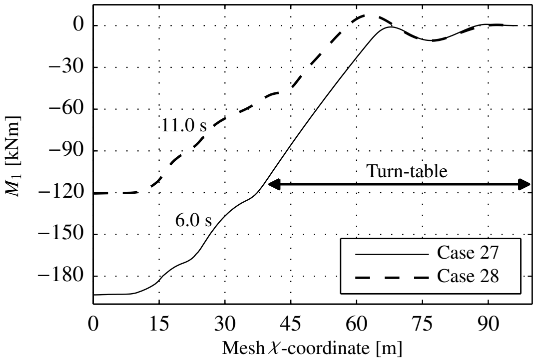

Figure 12: Torque distribution

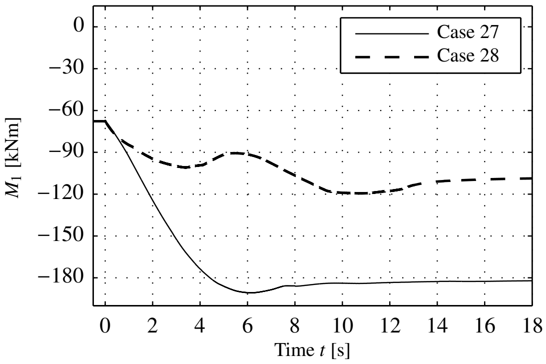

Figure 13: Torque at upstream-end

The torque response was simulated for a fabrication friction moment of 4 000 Nm in both of the tensile helix layers, see case 25* in Figs. 10 and 11. An extended mesh with length 144 m was used such that the torque could decay to zero before the mesh endpoint. As expected, the torque prior to the spool arm displacement reduces approximately by 50%. According to Fig. 11, the maximum value is attained at the same instant and the torque rise is of similar magnitude as for case 25. The main difference is that the material transport contribution is roughly halved and that the rotation process of the tensile helix layer bending moment vector spreads further downstream on the turn-table to mobilize more torque.

The 4 m initial displacement in the positive Y-direction which was prescribed for cases 26 and 28 resulted in a different change of the free span shape during the positive X-displacement. The mesh motion at the turn-table was then characterized by bending action rather than constrained geometric roll rotation. Consequently, less torque was induced in the coiled part such that the upstream-end maximum values reduced by approximately 40% compared to cases 25 and 27, see Figs. 11 and 13. This implies that the extreme torque for cases 25 and 27 can be mitigated by using a spool arm motion path that minimizes the pipe roll rotation at the turn-table inlet.

Some investigations were carried out for spool arm displacements from ${}^{0}u_x^{sa} = 4$ m to $u_x^{sa} = -2$ m with lay angles $\alpha_5 = -40°$ and $\alpha_7 = 40°$. In that case, the magnitude of the torque rise during the spool arm displacement phase was similar to the cases in Table 4.

4.3 Effect of residual bending curvature for plastic sheath layers

The unsteady operation start-up phase was simulated for the cases listed in Table 5, where the index numbers refer to the layers subjected to residual curvature, numbered consecutively according to Table 2 from the innermost to the outermost layer. The cross-section orientation is defined by the $\mathbf{e}_i$-vectors in Fig. 5, while the residual curvature and the resulting layer moment are defined according to Eqs. (3) and (12). The position of the deck forks, the roller box and the spool arm was identical to cases 23 and 24, see Table 3. In Figs. 14 – 17, the torque distributions are shown at the instant the material flow-front reached the mesh termination point.

Table 5: Lay angle directions and residual curvature for plastic sheath layers

Case	α_5 [deg]	α_7 [deg]	$\kappa_{2i}^{\{0\}}$ [m^{-1}]	$\kappa_{3i}^{\{0\}}$ [m^{-1}]	Layer index i for $\boldsymbol{\kappa}_i^{\{0\}}$
29	−40	40	0.1	0.0	1, 3, 5, 7
30	−40	40	0.1	0.0	7
31	40	−40	−0.1	0.0	1, 3, 5, 7
32	40	−40	−0.1	0.0	7
33	40	−40	0.0	0.1	1, 3, 5, 7
34	40	−40	0.0	0.1	7
35	−40	40	0.0	−0.1	1, 3, 5, 7
36	−40	40	0.0	−0.1	7

For case 29, the pipe residual curvature vector has approximately the same direction as the curvature constraint defined by the contact rollers at the overbend region and at the turn-table. As seen in Fig. 14, the torque is therefore induced mainly in the free span region and is of similar magnitude as the cases in Section 4.1.

An extreme torque response appears for case 31 where the upstream-end torque is close to -300 kNm, see Fig. 15. The residual curvature vector and the contact roller curvature constraints are here misaligned approximately by 180°. This mesh configuration is not stable when the plastic sheath layer bending loads are activated. Consequently, a roll rotation was initiated when the material flow-front reached the turn-table inlet, which continued as the material coiled its way around the turn-table, giving an upstream-end torque rise of about 180 kNm and a total roll rotation of 130 – 140° at the downstream-end. The resulting non-alignment between the bending curvature and the bending moment, which induces the torque, is therefore a compromise of the residual curvature, the roll rotation

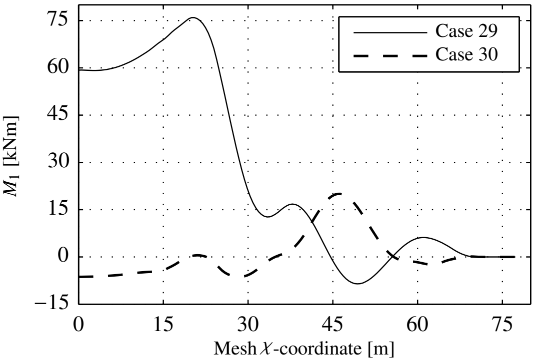

Figure 14: Torque distribution

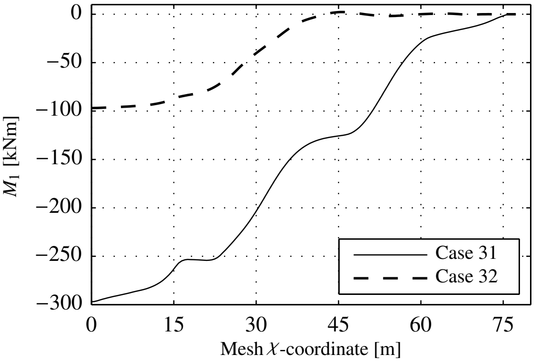

Figure 15: Torque distribution

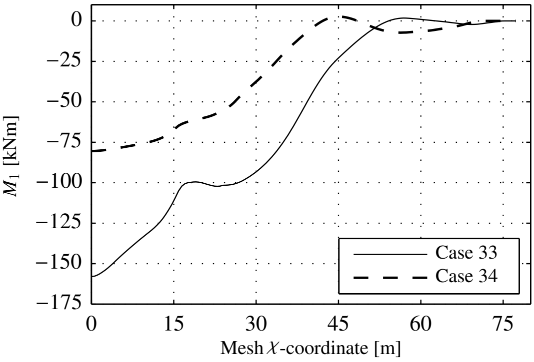

Figure 16: Torque distribution

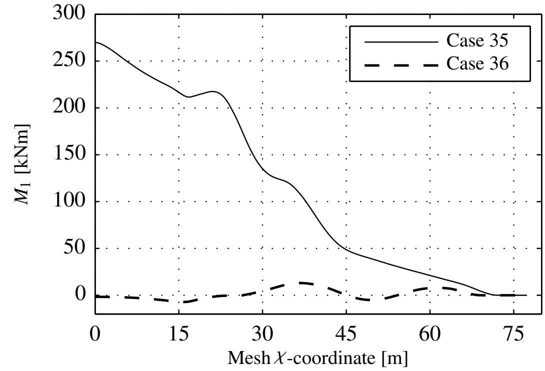

Figure 17: Torque distribution

restraint provided by the Coulomb bending model and the material transport effect. Observe in Fig. 15 that the turn-table and the region upstream of the TDP contribute about equally to the induced torque. The same behavior was present also for cases 33 and 35, where the upstream-end torque was respectively -160 kNm and 270 kNm, see Fig. 16 and 17, with downstream-end roll rotations of about 45° and $-60°$.

Regarding the evolution in time, the torque distributions presented for cases 29 and 33 coincide with the steady-state solution. For cases 31 and 35, the upstream-end torque still increased at the end of the simulation, implying that the responses in Figs. 15 and 17 will become more severe as more material is coiled onto the turn-table.

The extreme responses reduce significantly or vanish when residual curvature is present only in the external plastic layer, see the dashed lines in Figs. 15 – 17. No evident roll rotation took place when the material was coiled around the turn-table, which means that the selected residual curvature was not sufficiently large to change the configuration into a state with significant torsion. Note that for cases 32 and 34, the upstream-end torque values still represent an increase of approximately 30 kNm and 50 kNm compared to the cases without residual curvature in Section 4.1.

5 Discussion

The simulated results must be seen in light of the conservatism incorporated for the boundary conditions and the Coulomb bending model parameters. Regarding the former, the upstream-end roll stiffness is governed by the length to the onshore turn-table and the placement of low-radius bends along the load-out route. If the load-out path is long and rather straight all the way from the onshore turn-table, the predicted upstream torque would reduce drastically. Contrarily, if several bends are located nearby the ship deck, which normally is the case due to limited space, the Coulomb bending model may provide considerable roll stiffness such that the upstream-end roll DOF could be regarded fixed. Furthermore, critical situations may just as well occur in later phases of the operation not considered in this work.

For the cases in Section 4.1 with $\alpha_5 = -40^\circ$ and $\alpha_7 = 40^\circ$, the largest compressive tendon stress in the outer tensile helix layer due to axial straining, torsion and bending was 27 MPa. This is far below the critical stress for the radial failure modes described in Ref. [26], provided that an anti-buckling tape with realistic properties is applied. Significantly larger compressive tendon stresses occurred with $\alpha_5 = 40^\circ$ and $\alpha_7 = -40^\circ$, in which cases 1 and 19 had compressive tendon stresses in the inner layer of 165 MPa and 138 MPa, respectively. In absence of interlayer friction, the tendon lateral buckling stress is 52 MPa according to Ref. [27]. Although friction may increase the capacity by at least a factor of two [26, 27], the authors believe that lateral tendon instability can be provoked solely by the material transport effect when the torque acts in the stiff direction upstream of the turn-table.

Extreme responses were identified in cases with unfavorable spool arm displacements and plastic layer residual curvature. For cases 25 and 27, the largest tensile helix compressive stress was respectively 364 MPa and 391 MPa, which severely exceed the tendon lateral buckling capacity of 52 MPa. Failure would probably occur also if the tensile helix lay angle direction was reversed, as high compressive stresses then would arise for large spool arm displacements in the opposite direction. The tendon lateral buckling stress is clearly exceeded also for the cases with plastic layer residual curvature. Herniation buckling of the inner tensile helix tendons, see Section 1, was evaluated based on the buckling load for a clamped straight beam with span length taken as the largest possible accumulated gap of the outer tensile helix layer. In accordance to Ref. [28], this resulted in a collapse load close to the yield strength, which arguably can be trigged by the simulated maximum compressive inner tendon stress of 614 MPa that occurred in case 31, provided that sufficient friction is mobilized to prevent lateral tendon buckling. Considering the free span configuration in Fig. 1a, loop formation may be naively predicted by Greenhill's equation with $k \in [1, 1.58]$, see Ref. [5]. Hence, in case of zero tension, 400 kNm^2 bending stiffness and 190 kNm torque, the resulting critical span length is on the interval $L \in [6.6 \text{ m}, 8.3 \text{ m}]$. Loop formation should therefore not be disregarded for the extreme torque levels in Sections 4.2 and 4.3.

Large spool arm displacements are likely to occur several times during the operation. For instance, when a layer of the turn-table has been filled, the subsequent layer must be coiled in the opposite direction, either inward or outward. To ensure good packing in this phase, the spool arm is arguably displaced in the X-direction to push the pipe against the turn-table hub, the already stacked coils or the turn-table outer wall. Also, the spool arm is throughout the operation actively used to counteract for tension variations and to adjust the free span shape as the TDP migrates in the turn-table radial direction. Regarding the presence of residual curvature, the pipe must be subjected to long-term storage and the stress relaxation must take place throughout the thick internal plastic layer. In view of these considerations, the authors believe that the extreme torque responses experienced in load-out operations relate solely to the aggregate effect of unfavorable spool arm displacements and material transport.

The failures identified above and the extreme torque responses can be avoided or mitigated by means of operational requirements. With regard to lateral tendon buckling of the inner tensile helix layer, the turn-table inlet side should be selected so that the induced torque yields torsion in the soft direction at the ship deck. Regarding the spool arm, it cannot be permitted to displace such that large constrained roll rotations occur at the turn-table inlet. This calls for personnel training and installation of a motion alarm system for the spool arm. Potential issues due to residual curvature can be avoided with aid of storage specifications and inspection routines prior to the operation. Regardless of the effect that induces the torque, a long and straight load-out route upstream of the cargo hold is favored, torsion in the soft direction at the ship deck is beneficial and the pipe should preferably be given a helix shape at the overbend and in the upper free span that cancels the torque induced in the lower free span.

The torque response and the governing failure mode depend on the actual case that is considered. Simplified response prediction methods are clearly not feasible. Hence, to ensure sufficient safety of load-out operations, numerical simulations should be applied on a case-to-case basis. Regarding FE modeling of flexible pipe load-out processes, the most important implications from the present study can be summarized as follows,

- The material transport effect must be properly accounted for as it may alone provoke torsional failure. It yields also a noticeable contribution to the extreme torque levels in Sections 4.2 and 4.3.
- Cases with at least 50% friction moment increase relative to the initial value were observed in regions where torque was induced. Hence, the constitutive model must account for interlayer pressure changes.
- The roll boundary condition at the downstream-end has no influence on the generated torque, provided that the coiled mesh length allows the torque to decay to zero before the endpoint.
- The bi-linear torque-torsion relationship must be represented as it affects the relative sharing of torque between the turn-table and the ship deck. Here, the roll stiffness at the upstream-end is also important.
- The torque induced by material transport is roughly proportional to the fabrication friction moment M_0 in cases with low interlayer contact pressures. However, the M_0-parameter is of less importance for the extreme torque rise associated with constrained roll rotation at the turn-table inlet.
- Regarding prediction of loop formation, the actual free spans along the load-out route should be modeled such that sag effects, the stick-slip bending stiffness and the support conditions are correctly represented.

6 Conclusions and further work

In this work a Lagrangian-Eulerian framework for simulation of flexible pipe reeling operations was presented. The bending response of the tensile helix layers was represented by a Coulomb model and account was made for interlayer pressure variations due to axial straining and torsion. A consistent linearization scheme for the axial-torsional response and the interlayer pressures was presented. Guidelines for the Lagrangian-Eulerian analysis strategy were provided and an interpolator method for the initial mesh configuration was proposed. A truncated finite element model of an idealized flexible pipe load-out operation with material transport from an onshore spoolbase to a cargo vessel was established. The torque response at operation start-up was examined in terms of reeling path, tensile helix lay angle direction, prescribed spool arm motions and presence of residual curvature in the plastic layers. Unfavorable spool arm motions and residual curvature effects were found to cause failure, in which the former was regarded as the most plausible source for the extreme torques experienced in load-out operations. Failure solely due to the material transport effect was detected for cases where the torque upstream of the turntable acted in the stiff torsion direction. Strategies to avoid the torsional failures were proposed and implications for the FE modeling were given.

At present the numerical model is applicable primarily for rough torque predictions, identification of extreme torque events and for mutual comparison of simulated responses. The validity of the modeling assumptions and the applied constitutive model should therefore be examined in future work. A comparison study against physical reeling operations with validation of roll rates and torsion is recommended. Measurements of the fabrication friction moment M_0 are also encouraged as the torque due to material transport is roughly proportional to M_0 for small contact pressures. Such a study enables also a more accurate evaluation of the torsional failure utilization factors. For that purpose it is desirable to improve the current tendon lateral buckling criterions [26, 27] with regard to the resisting effect provided by interlayer friction. The Lagrangian-Eulerian framework has provided robust and efficient simulations throughout this work and is highly recommended to use also in future studies.

Acknowledgements

The authors are grateful for the research efforts of Dr. Philippe Mainçon on torsional failure in flexible pipe load-out operations. Findings and reflections from his engagement in industrial research projects have been the main motivation for developing the Lagrangian-Eulerian formulation. In this work, Dr. Philippe Mainçon is acknowledged for fruitful discussions and FE modeling advices.

References

[1] Fylling I, Bech A. Effects of internal friction and torque stiffness on the global behavior of flexible risers and umbilicals. In: Proceedings of the 10th International Conference on Offshore Mechanics and Arctic Engineering. 1991, p. 489–961.

[2] Endal G, Ness O, Verley R, Holthe K, Remseth S. Behaviour of offshore pipelines subjected to residual curvature during laying. In: Proceedings of the 14th International Conference on Offshore Mechanics and Arctic Engineering. 1995, p. 513–23.

[3] API Recommended Practice 17B. American Petroleum Institute; 2012.

[4] Ramos RJ, Pesce CP. A stability analysis of risers subjected to dynamic compression coupled with twisting. J Offshore Mech Arct 2003;125:183–9.

[5] Bažant ZP, Cedolin L. Spatial buckling of beams under torque and axial force. In: Stability of structures: elastic, inelastic, fracture, and damage theories. Oxford University Press, Inc.; 1991, p. 46–9.

[6] Neto AG, Martins CA. Structural stability of flexible lines in catenary configuration under torsion. Mar Struct 2013;34:16–40.

[7] Bectarte F, Coutarel A. Instability of tensile armour layers of flexible pipes under external pressure. In: Proceedings of OMAE2004 23rd International Conference on Offshore Mechanics and Arctic Engineering. 2004, p. 155–61.

[8] Vaz MA, Rizzo NAS. A finite element model for flexible pipe armor wire instability. Mar Struct 2011;24:275–91.

[9] Østergaard NH, Lyckegaard A, Andreasen JH. On modelling of lateral buckling failure in flexible pipe tensile armour layers. Mar Struct 2012;27:64–81.

[10] API Specification 17J. American Petroleum Institute; 2008.

[11] Longva V, Sævik S. A Lagrangian-Eulerian formulation for reeling analysis of history-dependent multilayered beams. Comput Struct 2015;146:44–58.

[12] Tan Z, Quiggin P, Sheldrake T. Time domain simulation of the 3D bending hysteresis behavior of an unbonded flexible riser. J Offshore Mech Arct 2009;131, 8 pages.

[13] Alfano G, Bahtui A, Bahai H. Numerical derivation of constitutive models for unbonded flexible risers. Int J Mech Sci 2009;51:295–304.

[14] Bahtui A, Alfano G, Bahai H, Hosseini-Kordkheili S. On the multi-scale computation of un-bonded flexible risers. Eng Struct 2010;32:2287–99.

[15] Sævik S. Theoretical and experimental studies of stresses in flexible pipes. Comput Struct 2011;89:2273–91.

[16] Crisfield MA. A co-rotational framework for three-dimensional beam elements. In: Non-linear finite element analysis of solids and structures. John Wiley & Sons Ltd.; 1997, p. 213–26.

[17] Krenk S. Co-rotating beam elements. In: Non-linear modeling and analysis of solids and structures. John Wiley & Sons Ltd.; 2009, p. 100–41.

[18] Krenk S, Vissing-Jørgensen C, Thesbjerg L. Efficient collapse analysis techniques for framed structures. Comput Struct 1999;72:481–96.

[19] Féret JJ, Bournazel CL. Calculation of stresses and slip in structural layers of unbonded flexible pipes. J Offshore Mech Arct 1987;109:263–9.

[20] Féret JJ, Momplot G. CAFLEX - A program for capacity analysis of flexible pipes, Theory manual. Tech. Rep. 710668; Norwegian Marine Technology Research Centre (MARINTEK), Trondheim, Norway; 1989.

[21] Sævik S. On stresses and fatigue in flexible pipes. Ph.D. thesis; Norwegian Institute of Technology, Trondheim, Norway; 1992.

[22] Bathe KJ, Bolourchi S. Large displacement analysis of three-dimensional beam structures. Int J Numer Meth Eng 1979;14:961–86.

[23] Wriggers P. Contact boundary value problem and weak form. In: Computational contact mechanics. Springer-Verlag Berlin Heidelberg; 2006, p. 109–56.

[24] Skallerud B. Structural Damping in a Wellstream pipe. Tech. Rep. STF71 F91059; SINTEF,

Structural Engineering, Trondheim, Norway; 1991.

[25] Féret JJ, Bournazel CL, Rigaud J. Evaluation of flexible pipes' life expectancy under dynamic conditions. In: Proceedings of the Eighteenth Annual Offshore Technology Conference. 1986, p. 83–90.

[26] Sævik S, Thorsen MJ. Techniques for predicting tensile armour buckling and fatigue in deep water flexible risers. In: Proceedings of the ASME 2012 31st International Conference on Ocean, Offshore and Arctic Engineering. 2012, p. 469–82.

[27] Sævik S, Ji G. Differential equation for evaluating transverse buckling behavior of tensile armour wires. In: Proceedings of the ASME 2014 33rd International Conference on Ocean, Offshore and Arctic Engineering. 2012, 8 pages.

[28] Eurocode 3: Design of steel structures - Part 1-1: General rules and rules for buildings, May 2005. European Committee for Standardization, Brussels, Belgium; 2005.

Previous PhD theses published at the Departement of Marine Technology (earlier: Faculty of Marine Technology) NORWEGIAN UNIVERSITY OF SCIENCE AND TECHNOLOGY

Report No.	Author	Title
	Kavlie, Dag	Optimization of Plane Elastic Grillages, 1967
	Hansen, Hans R.	Man-Machine Communication and Data-Storage Methods in Ship Structural Design, 1971
	Gisvold, Kaare M.	A Method for non-linear mixed -integer programming and its Application to Design Problems, 1971
	Lund, Sverre	Tanker Frame Optimalization by means of SUMT-Transformation and Behaviour Models, 1971
	Vinje, Tor	On Vibration of Spherical Shells Interacting with Fluid, 1972
	Lorentz, Jan D.	Tank Arrangement for Crude Oil Carriers in Accordance with the new Anti-Pollution Regulations, 1975
	Carlsen, Carl A.	Computer-Aided Design of Tanker Structures, 1975
	Larsen, Carl M.	Static and Dynamic Analysis of Offshore Pipelines during Installation, 1976
UR-79-01	Brigt Hatlestad, MK	The finite element method used in a fatigue evaluation of fixed offshore platforms. (Dr.Ing. Thesis)
UR-79-02	Erik Pettersen, MK	Analysis and design of cellular structures. (Dr.Ing. Thesis)
UR-79-03	Sverre Valsgård, MK	Finite difference and finite element methods applied to nonlinear analysis of plated structures. (Dr.Ing. Thesis)
UR-79-04	Nils T. Nordsve, MK	Finite element collapse analysis of structural members considering imperfections and stresses due to fabrication. (Dr.Ing. Thesis)
UR-79-05	Ivar J. Fylling, MK	Analysis of towline forces in ocean towing systems. (Dr.Ing. Thesis)
UR-80-06	Nils Sandsmark, MM	Analysis of Stationary and Transient Heat Conduction by the Use of the Finite Element Method. (Dr.Ing. Thesis)
UR-80-09	Sverre Haver, MK	Analysis of uncertainties related to the stochastic modeling of ocean waves. (Dr.Ing. Thesis)

UR-81-15	Odland, Jonas	On the Strength of welded Ring stiffened cylindrical Shells primarily subjected to axial Compression
UR-82-17	Engesvik, Knut	Analysis of Uncertainties in the fatigue Capacity of Welded Joints
UR-82-18	Rye, Henrik	Ocean wave groups
UR-83-30	Eide, Oddvar Inge	On Cumulative Fatigue Damage in Steel Welded Joints
UR-83-33	Mo, Olav	Stochastic Time Domain Analysis of Slender Offshore Structures
UR-83-34	Amdahl, Jørgen	Energy absorption in Ship-platform impacts
UR-84-37	Mørch, Morten	Motions and mooring forces of semi submersibles as determined by full-scale measurements and theoretical analysis
UR-84-38	Soares, C. Guedes	Probabilistic models for load effects in ship structures
UR-84-39	Aarsnes, Jan V.	Current forces on ships
UR-84-40	Czujko, Jerzy	Collapse Analysis of Plates subjected to Biaxial Compression and Lateral Load
UR-85-46	Alf G. Engseth, MK	Finite element collapse analysis of tubular steel offshore structures. (Dr.Ing. Thesis)
UR-86-47	Dengody Sheshappa, MP	A Computer Design Model for Optimizing Fishing Vessel Designs Based on Techno-Economic Analysis. (Dr.Ing. Thesis)
UR-86-48	Vidar Aanesland, MH	A Theoretical and Numerical Study of Ship Wave Resistance. (Dr.Ing. Thesis)
UR-86-49	Heinz-Joachim Wessel, MK	Fracture Mechanics Analysis of Crack Growth in Plate Girders. (Dr.Ing. Thesis)
UR-86-50	Jon Taby, MK	Ultimate and Post-ultimate Strength of Dented Tubular Members. (Dr.Ing. Thesis)
UR-86-51	Walter Lian, MH	A Numerical Study of Two-Dimensional Separated Flow Past Bluff Bodies at Moderate KC-Numbers. (Dr.Ing. Thesis)
UR-86-52	Bjørn Sortland, MH	Force Measurements in Oscillating Flow on Ship Sections and Circular Cylinders in a U-Tube Water Tank. (Dr.Ing. Thesis)
UR-86-53	Kurt Strand, MM	A System Dynamic Approach to One-dimensional Fluid Flow. (Dr.Ing. Thesis)

UR-86-54	Arne Edvin Løken, MH	Three Dimensional Second Order Hydrodynamic Effects on Ocean Structures in Waves. (Dr.Ing. Thesis)
UR-86-55	Sigurd Falch, MH	A Numerical Study of Slamming of Two-Dimensional Bodies. (Dr.Ing. Thesis)
UR-87-56	Arne Braathen, MH	Application of a Vortex Tracking Method to the Prediction of Roll Damping of a Two-Dimension Floating Body. (Dr.Ing. Thesis)
UR-87-57	Bernt Leira, MK	Gaussian Vector Processes for Reliability Analysis involving Wave-Induced Load Effects. (Dr.Ing. Thesis)
UR-87-58	Magnus Småvik, MM	Thermal Load and Process Characteristics in a Two-Stroke Diesel Engine with Thermal Barriers (in Norwegian). (Dr.Ing. Thesis)
MTA-88-59	Bernt Arild Bremdal, MP	An Investigation of Marine Installation Processes – A Knowledge - Based Planning Approach. (Dr.Ing. Thesis)
MTA-88-60	Xu Jun, MK	Non-linear Dynamic Analysis of Space-framed Offshore Structures. (Dr.Ing. Thesis)
MTA-89-61	Gang Miao, MH	Hydrodynamic Forces and Dynamic Responses of Circular Cylinders in Wave Zones. (Dr.Ing. Thesis)
MTA-89-62	Martin Greenhow, MH	Linear and Non-Linear Studies of Waves and Floating Bodies. Part I and Part II. (Dr.Techn. Thesis)
MTA-89-63	Chang Li, MH	Force Coefficients of Spheres and Cubes in Oscillatory Flow with and without Current. (Dr.Ing. Thesis
MTA-89-64	Hu Ying, MP	A Study of Marketing and Design in Development of Marine Transport Systems. (Dr.Ing. Thesis)
MTA-89-65	Arild Jæger, MH	Seakeeping, Dynamic Stability and Performance of a Wedge Shaped Planing Hull. (Dr.Ing. Thesis)
MTA-89-66	Chan Siu Hung, MM	The dynamic characteristics of tilting-pad bearings
MTA-89-67	Kim Wikstrøm, MP	Analysis av projekteringen for ett offshore projekt. (Licenciat-avhandling)
MTA-89-68	Jiao Guoyang, MK	Reliability Analysis of Crack Growth under Random Loading, considering Model Updating. (Dr.Ing. Thesis)
MTA-89-69	Arnt Olufsen, MK	Uncertainty and Reliability Analysis of Fixed Offshore Structures. (Dr.Ing. Thesis)

MTA-89-70	Wu Yu-Lin, MR	System Reliability Analyses of Offshore Structures using improved Truss and Beam Models. (Dr.Ing. Thesis)
MTA-90-71	Jan Roger Hoff, MH	Three-dimensional Green function of a vessel with forward speed in waves. (Dr.Ing. Thesis)
MTA-90-72	Rong Zhao, MH	Slow-Drift Motions of a Moored Two-Dimensional Body in Irregular Waves. (Dr.Ing. Thesis)
MTA-90-73	Atle Minsaas, MP	Economical Risk Analysis. (Dr.Ing. Thesis)
MTA-90-74	Knut-Aril Farnes, MK	Long-term Statistics of Response in Non-linear Marine Structures. (Dr.Ing. Thesis)
MTA-90-75	Torbjørn Sotberg, MK	Application of Reliability Methods for Safety Assessment of Submarine Pipelines. (Dr.Ing. Thesis)
MTA-90-76	Zeuthen, Steffen, MP	SEAMAID. A computational model of the design process in a constraint-based logic programming environment. An example from the offshore domain. (Dr.Ing. Thesis)
MTA-91-77	Haagensen, Sven, MM	Fuel Dependant Cyclic Variability in a Spark Ignition Engine - An Optical Approach. (Dr.Ing. Thesis)
MTA-91-78	Løland, Geir, MH	Current forces on and flow through fish farms. (Dr.Ing. Thesis)
MTA-91-79	Hoen, Christopher, MK	System Identification of Structures Excited by Stochastic Load Processes. (Dr.Ing. Thesis)
MTA-91-80	Haugen, Stein, MK	Probabilistic Evaluation of Frequency of Collision between Ships and Offshore Platforms. (Dr.Ing. Thesis)
MTA-91-81	Sødahl, Nils, MK	Methods for Design and Analysis of Flexible Risers. (Dr.Ing. Thesis)
MTA-91-82	Ormberg, Harald, MK	Non-linear Response Analysis of Floating Fish Farm Systems. (Dr.Ing. Thesis)
MTA-91-83	Marley, Mark J., MK	Time Variant Reliability under Fatigue Degradation. (Dr.Ing. Thesis)
MTA-91-84	Krokstad, Jørgen R., MH	Second-order Loads in Multidirectional Seas. (Dr.Ing. Thesis)
MTA-91-85	Molteberg, Gunnar A., MM	The Application of System Identification Techniques to Performance Monitoring of Four Stroke Turbocharged Diesel Engines. (Dr.Ing. Thesis)

MTA-92-86	Mørch, Hans Jørgen Bjelke, MH	Aspects of Hydrofoil Design: with Emphasis on Hydrofoil Interaction in Calm Water. (Dr.Ing. Thesis)
MTA-92-87	Chan Siu Hung, MM	Nonlinear Analysis of Rotordynamic Instabilities in Highspeed Turbomachinery. (Dr.Ing. Thesis)
MTA-92-88	Bessason, Bjarni, MK	Assessment of Earthquake Loading and Response of Seismically Isolated Bridges. (Dr.Ing. Thesis)
MTA-92-89	Langli, Geir, MP	Improving Operational Safety through exploitation of Design Knowledge - an investigation of offshore platform safety. (Dr.Ing. Thesis)
MTA-92-90	Sævik, Svein, MK	On Stresses and Fatigue in Flexible Pipes. (Dr.Ing. Thesis)
MTA-92-91	Ask, Tor Ø., MM	Ignition and Flame Growth in Lean Gas-Air Mixtures. An Experimental Study with a Schlieren System. (Dr.Ing. Thesis)
MTA-86-92	Hessen, Gunnar, MK	Fracture Mechanics Analysis of Stiffened Tubular Members. (Dr.Ing. Thesis)
MTA-93-93	Steinebach, Christian, MM	Knowledge Based Systems for Diagnosis of Rotating Machinery. (Dr.Ing. Thesis)
MTA-93-94	Dalane, Jan Inge, MK	System Reliability in Design and Maintenance of Fixed Offshore Structures. (Dr.Ing. Thesis)
MTA-93-95	Steen, Sverre, MH	Cobblestone Effect on SES. (Dr.Ing. Thesis)
MTA-93-96	Karunakaran, Daniel, MK	Nonlinear Dynamic Response and Reliability Analysis of Drag-dominated Offshore Platforms. (Dr.Ing. Thesis)
MTA-93-97	Hagen, Arnulf, MP	The Framework of a Design Process Language. (Dr.Ing. Thesis)
MTA-93-98	Nordrik, Rune, MM	Investigation of Spark Ignition and Autoignition in Methane and Air Using Computational Fluid Dynamics and Chemical Reaction Kinetics. A Numerical Study of Ignition Processes in Internal Combustion Engines. (Dr.Ing. Thesis)
MTA-94-99	Passano, Elizabeth, MK	Efficient Analysis of Nonlinear Slender Marine Structures. (Dr.Ing. Thesis)
MTA-94-100	Kvålsvold, Jan, MH	Hydroelastic Modelling of Wetdeck Slamming on Multihull Vessels. (Dr.Ing. Thesis)
MTA-94-102	Bech, Sidsel M., MK	Experimental and Numerical Determination of Stiffness and Strength of GRP/PVC Sandwich Structures. (Dr.Ing. Thesis)

MTA-95-103	Paulsen, Hallvard, MM	A Study of Transient Jet and Spray using a Schlieren Method and Digital Image Processing. (Dr.Ing. Thesis)
MTA-95-104	Hovde, Geir Olav, MK	Fatigue and Overload Reliability of Offshore Structural Systems, Considering the Effect of Inspection and Repair. (Dr.Ing. Thesis)
MTA-95-105	Wang, Xiaozhi, MK	Reliability Analysis of Production Ships with Emphasis on Load Combination and Ultimate Strength. (Dr.Ing. Thesis)
MTA-95-106	Ulstein, Tore, MH	Nonlinear Effects of a Flexible Stern Seal Bag on Cobblestone Oscillations of an SES. (Dr.Ing. Thesis)
MTA-95-107	Solaas, Frøydis, MH	Analytical and Numerical Studies of Sloshing in Tanks. (Dr.Ing. Thesis)
MTA-95-108	Hellan, Øyvind, MK	Nonlinear Pushover and Cyclic Analyses in Ultimate Limit State Design and Reassessment of Tubular Steel Offshore Structures. (Dr.Ing. Thesis)
MTA-95-109	Hermundstad, Ole A., MK	Theoretical and Experimental Hydroelastic Analysis of High Speed Vessels. (Dr.Ing. Thesis)
MTA-96-110	Bratland, Anne K., MH	Wave-Current Interaction Effects on Large-Volume Bodies in Water of Finite Depth. (Dr.Ing. Thesis)
MTA-96-111	Herfjord, Kjell, MH	A Study of Two-dimensional Separated Flow by a Combination of the Finite Element Method and Navier-Stokes Equations. (Dr.Ing. Thesis)
MTA-96-112	Æsøy, Vilmar, MM	Hot Surface Assisted Compression Ignition in a Direct Injection Natural Gas Engine. (Dr.Ing. Thesis)
MTA-96-113	Eknes, Monika L., MK	Escalation Scenarios Initiated by Gas Explosions on Offshore Installations. (Dr.Ing. Thesis)
MTA-96-114	Erikstad, Stein O., MP	A Decision Support Model for Preliminary Ship Design. (Dr.Ing. Thesis)
MTA-96-115	Pedersen, Egil, MH	A Nautical Study of Towed Marine Seismic Streamer Cable Configurations. (Dr.Ing. Thesis)
MTA-97-116	Moksnes, Paul O., MM	Modelling Two-Phase Thermo-Fluid Systems Using Bond Graphs. (Dr.Ing. Thesis)
MTA-97-117	Halse, Karl H., MK	On Vortex Shedding and Prediction of Vortex-Induced Vibrations of Circular Cylinders. (Dr.Ing. Thesis)

MTA-97-118	Igland, Ragnar T., MK	Reliability Analysis of Pipelines during Laying, considering Ultimate Strength under Combined Loads. (Dr.Ing. Thesis)
MTA-97-119	Pedersen, Hans-P., MP	Levendefiskteknologi for fiskefartøy. (Dr.Ing. Thesis)
MTA-98-120	Vikestad, Kyrre, MK	Multi-Frequency Response of a Cylinder Subjected to Vortex Shedding and Support Motions. (Dr.Ing. Thesis)
MTA-98-121	Azadi, Mohammad R. E., MK	Analysis of Static and Dynamic Pile-Soil-Jacket Behaviour. (Dr.Ing. Thesis)
MTA-98-122	Ulltang, Terje, MP	A Communication Model for Product Information. (Dr.Ing. Thesis)
MTA-98-123	Torbergsen, Erik, MM	Impeller/Diffuser Interaction Forces in Centrifugal Pumps. (Dr.Ing. Thesis)
MTA-98-124	Hansen, Edmond, MH	A Discrete Element Model to Study Marginal Ice Zone Dynamics and the Behaviour of Vessels Moored in Broken Ice. (Dr.Ing. Thesis)
MTA-98-125	Videiro, Paulo M., MK	Reliability Based Design of Marine Structures. (Dr.Ing. Thesis)
MTA-99-126	Mainçon, Philippe, MK	Fatigue Reliability of Long Welds Application to Titanium Risers. (Dr.Ing. Thesis)
MTA-99-127	Haugen, Elin M., MH	Hydroelastic Analysis of Slamming on Stiffened Plates with Application to Catamaran Wetdecks. (Dr.Ing. Thesis)
MTA-99-128	Langhelle, Nina K., MK	Experimental Validation and Calibration of Nonlinear Finite Element Models for Use in Design of Aluminium Structures Exposed to Fire. (Dr.Ing. Thesis)
MTA-99-129	Berstad, Are J., MK	Calculation of Fatigue Damage in Ship Structures. (Dr.Ing. Thesis)
MTA-99-130	Andersen, Trond M., MM	Short Term Maintenance Planning. (Dr.Ing. Thesis)
MTA-99-131	Tveiten, Bård Wathne, MK	Fatigue Assessment of Welded Aluminium Ship Details. (Dr.Ing. Thesis)
MTA-99-132	Søreide, Fredrik, MP	Applications of underwater technology in deep water archaeology. Principles and practice. (Dr.Ing. Thesis)
MTA-99-133	Tønnessen, Rune, MH	A Finite Element Method Applied to Unsteady Viscous Flow Around 2D Blunt Bodies With Sharp Corners. (Dr.Ing. Thesis)

MTA-99-134	Elvekrok, Dag R., MP	Engineering Integration in Field Development Projects in the Norwegian Oil and Gas Industry. The Supplier Management of Norne. (Dr.Ing. Thesis)
MTA-99-135	Fagerholt, Kjetil, MP	Optimeringsbaserte Metoder for Ruteplanlegging innen skipsfart. (Dr.Ing. Thesis)
MTA-99-136	Bysveen, Marie, MM	Visualization in Two Directions on a Dynamic Combustion Rig for Studies of Fuel Quality. (Dr.Ing. Thesis)
MTA-2000-137	Storteig, Eskild, MM	Dynamic characteristics and leakage performance of liquid annular seals in centrifugal pumps. (Dr.Ing. Thesis)
MTA-2000-138	Sagli, Gro, MK	Model uncertainty and simplified estimates of long term extremes of hull girder loads in ships. (Dr.Ing. Thesis)
MTA-2000-139	Tronstad, Harald, MK	Nonlinear analysis and design of cable net structures like fishing gear based on the finite element method. (Dr.Ing. Thesis)
MTA-2000-140	Kroneberg, André, MP	Innovation in shipping by using scenarios. (Dr.Ing. Thesis)
MTA-2000-141	Haslum, Herbjørn Alf, MH	Simplified methods applied to nonlinear motion of spar platforms. (Dr.Ing. Thesis)
MTA-2001-142	Samdal, Ole Johan, MM	Modelling of Degradation Mechanisms and Stressor Interaction on Static Mechanical Equipment Residual Lifetime. (Dr.Ing. Thesis)
MTA-2001-143	Baarholm, Rolf Jarle, MH	Theoretical and experimental studies of wave impact underneath decks of offshore platforms. (Dr.Ing. Thesis)
MTA-2001-144	Wang, Lihua, MK	Probabilistic Analysis of Nonlinear Wave-induced Loads on Ships. (Dr.Ing. Thesis)
MTA-2001-145	Kristensen, Odd H. Holt, MK	Ultimate Capacity of Aluminium Plates under Multiple Loads, Considering HAZ Properties. (Dr.Ing. Thesis)
MTA-2001-146	Greco, Marilena, MH	A Two-Dimensional Study of Green-Water Loading. (Dr.Ing. Thesis)
MTA-2001-147	Heggelund, Svein E., MK	Calculation of Global Design Loads and Load Effects in Large High Speed Catamarans. (Dr.Ing. Thesis)
MTA-2001-148	Babalola, Olusegun T., MK	Fatigue Strength of Titanium Risers – Defect Sensitivity. (Dr.Ing. Thesis)

MTA-2001-149	Mohammed, Abuu K., MK	Nonlinear Shell Finite Elements for Ultimate Strength and Collapse Analysis of Ship Structures. (Dr.Ing. Thesis)
MTA-2002-150	Holmedal, Lars E., MH	Wave-current interactions in the vicinity of the sea bed. (Dr.Ing. Thesis)
MTA-2002-151	Rognebakke, Olav F., MH	Sloshing in rectangular tanks and interaction with ship motions. (Dr.Ing. Thesis)
MTA-2002-152	Lader, Pål Furset, MH	Geometry and Kinematics of Breaking Waves. (Dr.Ing. Thesis)
MTA-2002-153	Yang, Qinzheng, MH	Wash and wave resistance of ships in finite water depth. (Dr.Ing. Thesis)
MTA-2002-154	Melhus, Øyvin, MM	Utilization of VOC in Diesel Engines. Ignition and combustion of VOC released by crude oil tankers. (Dr.Ing. Thesis)
MTA-2002-155	Ronæss, Marit, MH	Wave Induced Motions of Two Ships Advancing on Parallel Course. (Dr.Ing. Thesis)
MTA-2002-156	Økland, Ole D., MK	Numerical and experimental investigation of whipping in twin hull vessels exposed to severe wet deck slamming. (Dr.Ing. Thesis)
MTA-2002-157	Ge, Chunhua, MK	Global Hydroelastic Response of Catamarans due to Wet Deck Slamming. (Dr.Ing. Thesis)
MTA-2002-158	Byklum, Eirik, MK	Nonlinear Shell Finite Elements for Ultimate Strength and Collapse Analysis of Ship Structures. (Dr.Ing. Thesis)
IMT-2003-1	Chen, Haibo, MK	Probabilistic Evaluation of FPSO-Tanker Collision in Tandem Offloading Operation. (Dr.Ing. Thesis)
IMT-2003-2	Skaugset, Kjetil Bjørn, MK	On the Suppression of Vortex Induced Vibrations of Circular Cylinders by Radial Water Jets. (Dr.Ing. Thesis)
IMT-2003-3	Chezhian, Muthu	Three-Dimensional Analysis of Slamming. (Dr.Ing. Thesis)
IMT-2003-4	Buhaug, Øyvind	Deposit Formation on Cylinder Liner Surfaces in Medium Speed Engines. (Dr.Ing. Thesis)
IMT-2003-5	Tregde, Vidar	Aspects of Ship Design: Optimization of Aft Hull with Inverse Geometry Design. (Dr.Ing. Thesis)
IMT-2003-6	Wist, Hanne Therese	Statistical Properties of Successive Ocean Wave Parameters. (Dr.Ing. Thesis)
IMT-2004-7	Ransau, Samuel	Numerical Methods for Flows with Evolving Interfaces. (Dr.Ing. Thesis)

IMT-2004-8	Soma, Torkel	Blue-Chip or Sub-Standard. A data interrogation approach of identity safety characteristics of shipping organization. (Dr.Ing. Thesis)
IMT-2004-9	Ersdal, Svein	An experimental study of hydrodynamic forces on cylinders and cables in near axial flow. (Dr.Ing. Thesis)
IMT-2005-10	Brodtkorb, Per Andreas	The Probability of Occurrence of Dangerous Wave Situations at Sea. (Dr.Ing. Thesis)
IMT-2005-11	Yttervik, Rune	Ocean current variability in relation to offshore engineering. (Dr.Ing. Thesis)
IMT-2005-12	Fredheim, Arne	Current Forces on Net-Structures. (Dr.Ing. Thesis)
IMT-2005-13	Heggernes, Kjetil	Flow around marine structures. (Dr.Ing. Thesis
IMT-2005-14	Fouques, Sebastien	Lagrangian Modelling of Ocean Surface Waves and Synthetic Aperture Radar Wave Measurements. (Dr.Ing. Thesis)
IMT-2006-15	Holm, Håvard	Numerical calculation of viscous free surface flow around marine structures. (Dr.Ing. Thesis)
IMT-2006-16	Bjørheim, Lars G.	Failure Assessment of Long Through Thickness Fatigue Cracks in Ship Hulls. (Dr.Ing. Thesis)
IMT-2006-17	Hansson, Lisbeth	Safety Management for Prevention of Occupational Accidents. (Dr.Ing. Thesis)
IMT-2006-18	Zhu, Xinying	Application of the CIP Method to Strongly Nonlinear Wave-Body Interaction Problems. (Dr.Ing. Thesis)
IMT-2006-19	Reite, Karl Johan	Modelling and Control of Trawl Systems. (Dr.Ing. Thesis)
IMT-2006-20	Smogeli, Øyvind Notland	Control of Marine Propellers. From Normal to Extreme Conditions. (Dr.Ing. Thesis)
IMT-2007-21	Storhaug, Gaute	Experimental Investigation of Wave Induced Vibrations and Their Effect on the Fatigue Loading of Ships. (Dr.Ing. Thesis)
IMT-2007-22	Sun, Hui	A Boundary Element Method Applied to Strongly Nonlinear Wave-Body Interaction Problems. (PhD Thesis, CeSOS)
IMT-2007-23	Rustad, Anne Marthine	Modelling and Control of Top Tensioned Risers. (PhD Thesis, CeSOS)
IMT-2007-24	Johansen, Vegar	Modelling flexible slender system for real-time simulations and control applications

IMT-2007-25	Wroldsen, Anders Sunde	Modelling and control of tensegrity structures. (PhD Thesis, CeSOS)
IMT-2007-26	Aronsen, Kristoffer Høye	An experimental investigation of in-line and combined inline and cross flow vortex induced vibrations. (Dr. avhandling, IMT)
IMT-2007-27	Gao, Zhen	Stochastic Response Analysis of Mooring Systems with Emphasis on Frequency-domain Analysis of Fatigue due to Wide-band Response Processes (PhD Thesis, CeSOS)
IMT-2007-28	Thorstensen, Tom Anders	Lifetime Profit Modelling of Ageing Systems Utilizing Information about Technical Condition. (Dr.ing. thesis, IMT)
IMT-2008-29	Berntsen, Per Ivar B.	Structural Reliability Based Position Mooring. (PhD-Thesis, IMT)
IMT-2008-30	Ye, Naiquan	Fatigue Assessment of Aluminium Welded Box-stiffener Joints in Ships (Dr.ing. thesis, IMT)
IMT-2008-31	Radan, Damir	Integrated Control of Marine Electrical Power Systems. (PhD-Thesis, IMT)
IMT-2008-32	Thomassen, Paul	Methods for Dynamic Response Analysis and Fatigue Life Estimation of Floating Fish Cages. (Dr.ing. thesis, IMT)
IMT-2008-33	Pákozdi, Csaba	A Smoothed Particle Hydrodynamics Study of Two-dimensional Nonlinear Sloshing in Rectangular Tanks. (Dr.ing.thesis, IMT/ CeSOS)
IMT-2007-34	Grytøyr, Guttorm	A Higher-Order Boundary Element Method and Applications to Marine Hydrodynamics. (Dr.ing.thesis, IMT)
IMT-2008-35	Drummen, Ingo	Experimental and Numerical Investigation of Nonlinear Wave-Induced Load Effects in Containerships considering Hydroelasticity. (PhD thesis, CeSOS)
IMT-2008-36	Skejic, Renato	Maneuvering and Seakeeping of a Singel Ship and of Two Ships in Interaction. (PhD-Thesis, CeSOS)
IMT-2008-37	Harlem, Alf	An Age-Based Replacement Model for Repairable Systems with Attention to High-Speed Marine Diesel Engines. (PhD-Thesis, IMT)
IMT-2008-38	Alsos, Hagbart S.	Ship Grounding. Analysis of Ductile Fracture, Bottom Damage and Hull Girder Response. (PhD-thesis, IMT)

IMT-2008-39	Graczyk, Mateusz	Experimental Investigation of Sloshing Loading and Load Effects in Membrane LNG Tanks Subjected to Random Excitation. (PhD-thesis, CeSOS)
IMT-2008-40	Taghipour, Reza	Efficient Prediction of Dynamic Response for Flexible amd Multi-body Marine Structures. (PhD-thesis, CeSOS)
IMT-2008-41	Ruth, Eivind	Propulsion control and thrust allocation on marine vessels. (PhD thesis, CeSOS)
IMT-2008-42	Nystad, Bent Helge	Technical Condition Indexes and Remaining Useful Life of Aggregated Systems. PhD thesis, IMT
IMT-2008-43	Soni, Prashant Kumar	Hydrodynamic Coefficients for Vortex Induced Vibrations of Flexible Beams, PhD thesis, CeSOS
IMT-2009-43	Amlashi, Hadi K.K.	Ultimate Strength and Reliability-based Design of Ship Hulls with Emphasis on Combined Global and Local Loads. PhD Thesis, IMT
IMT-2009-44	Pedersen, Tom Arne	Bond Graph Modelling of Marine Power Systems. PhD Thesis, IMT
IMT-2009-45	Kristiansen, Trygve	Two-Dimensional Numerical and Experimental Studies of Piston-Mode Resonance. PhD-Thesis, CeSOS
IMT-2009-46	Ong, Muk Chen	Applications of a Standard High Reynolds Number Model and a Stochastic Scour Prediction Model for Marine Structures. PhD-thesis, IMT
IMT-2009-47	Hong, Lin	Simplified Analysis and Design of Ships subjected to Collision and Grounding. PhD-thesis, IMT
IMT-2009-48	Koushan, Kamran	Vortex Induced Vibrations of Free Span Pipelines, PhD thesis, IMT
IMT-2009-49	Korsvik, Jarl Eirik	Heuristic Methods for Ship Routing and Scheduling. PhD-thesis, IMT
IMT-2009-50	Lee, Jihoon	Experimental Investigation and Numerical in Analyzing the Ocean Current Displacement of Longlines. Ph.d.-Thesis, IMT.
IMT-2009-51	Vestbøstad, Tone Gran	A Numerical Study of Wave-in-Deck Impact usin a Two-Dimensional Constrained Interpolation Profile Method, Ph.d.thesis, CeSOS.
IMT-2009-52	Bruun, Kristine	Bond Graph Modelling of Fuel Cells for Marine Power Plants. Ph.d.-thesis, IMT

IMT 2009-53	Holstad, Anders	Numerical Investigation of Turbulence in a Sekwed Three-Dimensional Channel Flow, Ph.d.-thesis, IMT.
IMT 2009-54	Ayala-Uraga, Efren	Reliability-Based Assessment of Deteriorating Ship-shaped Offshore Structures, Ph.d.-thesis, IMT
IMT 2009-55	Kong, Xiangjun	A Numerical Study of a Damaged Ship in Beam Sea Waves. Ph.d.-thesis, IMT/CeSOS.
IMT 2010-56	Kristiansen, David	Wave Induced Effects on Floaters of Aquaculture Plants, Ph.d.-thesis, CeSOS.
IMT 2010-57	Ludvigsen, Martin	An ROV-Toolbox for Optical and Acoustic Scientific Seabed Investigation. Ph.d.-thesis IMT.
IMT 2010-58	Hals, Jørgen	Modelling and Phase Control of Wave-Energy Converters. Ph.d.thesis, CeSOS.
IMT 2010- 59	Shu, Zhi	Uncertainty Assessment of Wave Loads and Ultimate Strength of Tankers and Bulk Carriers in a Reliability Framework. Ph.d. Thesis, IMT/ CeSOS
IMT 2010-60	Shao, Yanlin	Numerical Potential-Flow Studies on Weakly-Nonlinear Wave-Body Interactions with/without Small Forward Speed, Ph.d.thesis,CeSOS.
IMT 2010-61	Califano, Andrea	Dynamic Loads on Marine Propellers due to Intermittent Ventilation. Ph.d.thesis, IMT.
IMT 2010-62	El Khoury, George	Numerical Simulations of Massively Separated Turbulent Flows, Ph.d.-thesis, IMT
IMT 2010-63	Seim, Knut Sponheim	Mixing Process in Dense Overflows with Emphasis on the Faroe Bank Channel Overflow. Ph.d.thesis, IMT
IMT 2010-64	Jia, Huirong	Structural Analysis of Intect and Damaged Ships in a Collission Risk Analysis Perspective. Ph.d.thesis CeSoS.
IMT 2010-65	Jiao, Linlin	Wave-Induced Effects on a Pontoon-type Very Large Floating Structures (VLFS). Ph.D.-thesis, CeSOS.
IMT 2010-66	Abrahamsen, Bjørn Christian	Sloshing Induced Tank Roof with Entrapped Air Pocket. Ph.d.thesis, CeSOS.
IMT 2011-67	Karimirad, Madjid	Stochastic Dynamic Response Analysis of Spar-Type Wind Turbines with Catenary or Taut Mooring Systems. Ph.d.-thesis, CeSOS.
IMT - 2011-68	Erlend Meland	Condition Monitoring of Safety Critical Valves. Ph.d.-thesis, IMT.

IMT – 2011-69	Yang, Limin	Stochastic Dynamic System Analysis of Wave Energy Converter with Hydraulic Power Take-Off, with Particular Reference to Wear Damage Analysis, Ph.d. Thesis, CeSOS.
IMT – 2011-70	Visscher, Jan	Application of Particla Image Velocimetry on Turbulent Marine Flows, Ph.d.Thesis, IMT.
IMT – 2011-71	Su, Biao	Numerical Predictions of Global and Local Ice Loads on Ships. Ph.d.Thesis, CeSOS.
IMT – 2011-72	Liu, Zhenhui	Analytical and Numerical Analysis of Iceberg Collision with Ship Structures. Ph.d.Thesis, IMT.
IMT – 2011-73	Aarsæther, Karl Gunnar	Modeling and Analysis of Ship Traffic by Observation and Numerical Simulation. Ph.d.Thesis, IMT.
IMT – 2011-74	Wu, Jie	Hydrodynamic Force Identification from Stochastic Vortex Induced Vibration Experiments with Slender Beams. Ph.d.Thesis, IMT.
IMT – 2011-75	Amini, Hamid	Azimuth Propulsors in Off-design Conditions. Ph.d.Thesis, IMT.
IMT – 2011-76	Nguyen, Tan-Hoi	Toward a System of Real-Time Prediction and Monitoring of Bottom Damage Conditions During Ship Grounding. Ph.d.thesis, IMT.
IMT-2011-77	Tavakoli, Mohammad T.	Assessment of Oil Spill in Ship Collision and Grounding, Ph.d.thesis, IMT.
IMT-2011-78	Guo, Bingjie	Numerical and Experimental Investigation of Added Resistance in Waves. Ph.d.Thesis, IMT.
IMT-2011-79	Chen, Qiaofeng	Ultimate Strength of Aluminium Panels, considering HAZ Effects, IMT
IMT-2012-80	Kota, Ravikiran S.	Wave Loads on Decks of Offshore Structures in Random Seas, CeSOS.
IMT-2012-81	Sten, Ronny	Dynamic Simulation of Deep Water Drilling Risers with Heave Compensating System, IMT.
IMT-2012-82	Berle, Øyvind	Risk and resilience in global maritime supply chains, IMT.
IMT-2012-83	Fang, Shaoji	Fault Tolerant Position Mooring Control Based on Structural Reliability, CeSOS.
IMT-2012-84	You, Jikun	Numerical studies on wave forces and moored ship motions in intermediate and shallow water, CeSOS.

IMT-2012-85	Xiang, Xu	Maneuvering of two interacting ships in waves, CeSOS
IMT-2012-86	Dong, Wenbin	Time-domain fatigue response and reliability analysis of offshore wind turbines with emphasis on welded tubular joints and gear components, CeSOS
IMT-2012-87	Zhu, Suji	Investigation of Wave-Induced Nonlinear Load Effects in Open Ships considering Hull Girder Vibrations in Bending and Torsion, CeSOS
IMT-2012-88	Zhou, Li	Numerical and Experimental Investigation of Station-keeping in Level Ice, CeSOS
IMT-2012-90	Ushakov, Sergey	Particulate matter emission characteristics from diesel enignes operating on conventional and alternative marine fuels, IMT
IMT-2013-1	Yin, Decao	Experimental and Numerical Analysis of Combined In-line and Cross-flow Vortex Induced Vibrations, CeSOS
IMT-2013-2	Kurniawan, Adi	Modelling and geometry optimisation of wave energy converters, CeSOS
IMT-2013-3	Al Ryati, Nabil	Technical condition indexes doe auxiliary marine diesel engines, IMT
IMT-2013-4	Firoozkoohi, Reza	Experimental, numerical and analytical investigation of the effect of screens on sloshing, CeSOS
IMT-2013-5	Ommani, Babak	Potential-Flow Predictions of a Semi-Displacement Vessel Including Applications to Calm Water Broaching, CeSOS
IMT-2013-6	Xing, Yihan	Modelling and analysis of the gearbox in a floating spar-type wind turbine, CeSOS
IMT-7-2013	Balland, Océane	Optimization models for reducing air emissions from ships, IMT
IMT-8-2013	Yang, Dan	Transitional wake flow behind an inclined flat plate - Computation and analysis, IMT
IMT-9-2013	Abdillah, Suyuthi	Prediction of Extreme Loads and Fatigue Damage for a Ship Hull due to Ice Action, IMT
IMT-10-2013	Ramìrez, Pedro Agustìn Pèrez	Ageing management and life extension of technical systems- Concepts and methods applied to oil and gas facilities, IMT

IMT-11-2013	Chuang, Zhenju	Experimental and Numerical Investigation of Speed Loss due to Seakeeping and Maneuvering. IMT
IMT-12-2013	Etemaddar, Mahmoud	Load and Response Analysis of Wind Turbines under Atmospheric Icing and Controller System Faults with Emphasis on Spar Type Floating Wind Turbines, IMT
IMT-13-2013	Lindstad, Haakon	Strategies and measures for reducing maritime CO2 emissons, IMT
IMT-14-2013	Haris, Sabril	Damage interaction analysis of ship collisions, IMT
IMT-15-2013	Shainee, Mohamed	Conceptual Design, Numerical and Experimental Investigation of a SPM Cage Concept for Offshore Mariculture, IMT
IMT-16-2013	Gansel, Lars	Flow past porous cylinders and effects of biofouling and fish behavior on the flow in and around Atlantic salmon net cages, IMT
IMT-17-2013	Gaspar, Henrique	Handling Aspects of Complexity in Conceptual Ship Design, IMT
IMT-18-2013	Thys, Maxime	Theoretical and Experimental Investigation of a Free Running Fishing Vessel at Small Frequency of Encounter, CeSOS
IMT-19-2013	Aglen, Ida	VIV in Free Spanning Pipelines, CeSOS
IMT-1-2014	Song, An	Theoretical and experimental studies of wave diffraction and radiation loads on a horizontally submerged perforated plate, CeSOS
IMT-2-2014	Rogne, Øyvind Ygre	Numerical and Experimental Investigation of a Hinged 5-body Wave Energy Converter, CeSOS
IMT-3-2014	Dai, Lijuan	Safe and efficient operation and maintenance of offshore wind farms ,IMT
IMT-4-2014	Bachynski, Erin Elizabeth	Design and Dynamic Analysis of Tension Leg Platform Wind Turbines, CeSOS
IMT-5-2014	Wang, Jingbo	Water Entry of Freefall Wedged – Wedge motions and Cavity Dynamics, CeSOS
IMT-6-2014	Kim, Ekaterina	Experimental and numerical studies related to the coupled behavior of ice mass and steel structures during accidental collisions, IMT
IMT-7-2014	Tan, Xiang	Numerical investigation of ship’s continuous-mode icebreaking in leverl ice, CeSOS

IMT-8-2014	Muliawan, Made Jaya	Design and Analysis of Combined Floating Wave and Wind Power Facilities, with Emphasis on Extreme Load Effects of the Mooring System, CeSOS
IMT-9-2014	Jiang, Zhiyu	Long-term response analysis of wind turbines with an emphasis on fault and shutdown conditions, IMT
IMT-10-2014	Dukan, Fredrik	ROV Motion Control Systems, IMT
IMT-11-2014	Grimsmo, Nils I.	Dynamic simulations of hydraulic cylinder for heave compensation of deep water drilling risers, IMT
IMT-12-2014	Kvittem, Marit I.	Modelling and response analysis for fatigue design of a semisubmersible wind turbine, CeSOS
IMT-13-2014	Akhtar, Juned	The Effects of Human Fatigue on Risk at Sea, IMT
IMT-14-2014	Syahroni, Nur	Fatigue Assessment of Welded Joints Taking into Account Effects of Residual Stress, IMT
IMT-1-2015	Bøckmann, Eirik	Wave Propulsion of ships, IMT
IMT-2-2015	Wang, Kai	Modelling and dynamic analysis of a semi-submersible floating vertical axis wind turbine, CeSOS
IMT-3-2015	Fredriksen, Arnt Gunvald	A numerical and experimental study of a two-dimensional body with moonpool in waves and current. CeSOS
IMT-4-2015	Jose Patricio Gallardo Canabes	Numerical studies of viscous flow around bluff bodies, IMT
IMT-5-2015	Vegard Longva	Formulation and application of finite element techniques for slender marine structures subjected to contact interactions, IMT